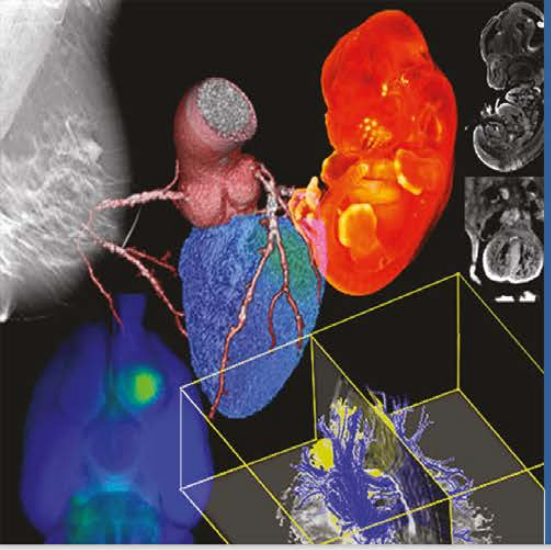

13th Imaging Network Ontario Symposium

March 30th & 31st 2015

London Convention Centre
London Ontario

PROCEEDINGS OF THE 13th ImNO SYMPOSIUM

March 30-31, 2015

TABLE OF CONTENTS

Keynote Speaker Biographies

Stephen Aylward, PhD
Senior Director of Operations at Kitware

Stephen R. Aylward, Ph.D. is founder and Senior Director of Operations at Kitware's North Carolina office. Kitware provides consultation in medical imaging, computer vision, and high-performance computing. Kitware also manages several open-source software packages for medical data analysis and visualization and for medical application development. Those freely available software tools are downloaded over 100,000 times per month. Stephen is also an adjunct professor in computer science at The University of North Carolina, serves on numerous advisory panels and organizing committees in academia and industry, and is a member of the MICCAI Society Board of Directors. As PI on multiple R01s and SBIRs, he is also investigating methods for the automated analysis of low-cost ultrasound images for in-field applications and methods for the characterization of vascular networks for cancer assessment.

Frank M. Bengel, MD, FAHA
Professor and Director of Nuclear Medicine, Hannover Medical School

Dr. Bengel received his medical degree from the Friedrich-Alexander University Erlangen / Germany and pursued training in Nuclear Medicine and Nuclear Cardiology at the Technical University of Munich / Germany, under the mentorship of Dr. Markus Schwaiger. He joined the faculty of the Technical University in Munich in 2002, before moving to Johns Hopkins University in December 2005. At Johns Hopkins, Dr. Bengel served on the faculty as an Associate Professor of Radiology and Medicine and as the Director of Cardiovascular Nuclear Medicine for 5 years. On January 1st, 2011, he started his term as the Director of Nuclear Medicine at Hannover Medical School, Hannover/Germany, one of the best funded medical institutions in Germany. There, he runs an academic imaging program which has a strong focus on translational work, guiding novel probes from preclinical to clinical application.

Dr. Bengel has contributed pioneering scientific work to the field of positron emission tomography and molecular imaging. His research focus is on the development and implementation of molecular-targeted imaging approaches for specific characterization of biologic mechanisms and for monitoring of novel gene- and cell-based therapies in the cardiovascular system. He has published numerous original contributions to peer-reviewed journals, incl. leading journals such as the New England Journal of Medicine. Dr. Bengel is on several editorial boards, incl. the Journal of the American College of Cardiology, Circulation Cardiovascular Imaging, JACC Cardiovascular Imaging and the Journal of Nuclear Medicine. Additionally, he holds several honorary positions on boards of national and international societies active in molecular imaging.

Christopher Contag, Professor,
Departments of Pediatrics, Microbiology & Immunology, and Radiology, Assoc. Chief, Neonatology, Co-director, Molecular Imaging Program at Stanford (MIPS)

Dr. Contag is a Professor in the Departments of Pediatrics, Radiology and Microbiology & Immunology at Stanford University, and a member of the BioX Faculty for interdisciplinary sciences. Dr. Contag received his B.S. in Biology in 1982, and his Ph.D. in Microbiology in 1988 from the University of Minnesota where he studied viral infections of the central nervous system. He was a postdoctoral fellow at Stanford University from 1990-1994 in the Department of Microbiology where he studied mother-to-infant transmission of HIV, and then joined the Stanford faculty in 1995. Dr. Contag is the Associate Chief of Neonatal and Developmental Medicine, director of Stanford's Center for Innovation in In Vivo Imaging and co-director of the Molecular Imaging Program at Stanford. For his fundamental contributions to imaging, Dr. Contag was awarded the Achievement Award from the Society for Molecular Imaging and is a Fellow and president elect of WMIS. The research mission of the Contag laboratory is to develop and use noninvasive imaging tools that can simultaneously reveal the nuances of biological processes and provide an overall picture of disease states for the purpose of developing and refining novel interventions. These tools are sensitive and image over a range of scales from micro- to macroscopic, and are well-suited for the in vivo study of cellular and molecular biology including miniaturized microscopes that can reach inside the body to interrogate disease states. This is enabling point-of-care microscopy that is changing the diagnostic paradigm from biopsy and histopathology to in vivo pathology.

Robert J. Gillies, PhD
Chair, Cancer Imaging & Metabolism
Vice-Chair, Radiology
Director, Center of Excellence in Cancer Imaging & Technology

Dr. Robert J. Gillies is Chairman of the Department of Cancer Imaging and Metabolism; Director of the Center of Excellence in Cancer Imaging and Technology; Vice-chair for Research in the Department of Radiology; and Scientific Director of the Small Animal Imaging Lab (SAIL) at the H. Lee Moffitt Cancer Center and Research Institute in Tampa, FL.

In addition to authoring over 200 peer-reviewed manuscripts, Dr. Gillies has received numerous local, national, and international awards for his teaching and research, including; Researcher of the Year-2012 (Moffitt Cancer Center), the Furrow Award for Innovative Teaching (U. Arizona), the Yuhas Award for Radiation Oncology Research (U. Penn), the TEFAF professorship (U. Maastricht), and the award for Distinguished Basic Scientist of 2009 from the Academy of Molecular Imaging.

Dr. Gillies' vision for the Moffitt imaging initiative includes development of new applications to diagnose, predict and monitor therapy response using noninvasive imaging. This work spans from molecular and chemical, from animal studies to human clinical trials and patient care. Dr. Gillies also leads a post-doctoral/resident training program in cancer imaging. His research is focused on functional and molecular imaging of cancer, specifically with an emphasis on the use of imaging to inform evolutionary models of carcinogenesis and response to therapy.

Commercialization Session Chair Biography

Chair: Lisa Cechetto, WORLDiscoveries
Executive Director

Lisa comes to WORLDiscoveries® with over ten years of patent and business development related experience. She has worked in both industry and academia and her most recent appointment was at Institut Pasteur Korea where she was the Director of Business Development and Intellectual Property. In this role she was responsible for the commercialization of the institute's research inputs while balancing the interests of key stakeholders including government, faculty and third parties. Prior to this role, she worked as the Patent Manager and Project Leader at ARIUS Research Inc., a biotech company subsequently acquired by Roche. Lisa obtained her Honors Bachelor of Science from the University of Guelph and her Master's of Science from McMaster University. She also graduated at the top of her class from a dual degree executive MBA program at the Kelley School of Business, Indiana University and Sungkyunkwan University.

Commercialization Session Speaker Biographies

Ian Haase, Propel
Director of Entrepreneurship at Western University

Ian Haase is the Director of Entrepreneurship at Western University, and manages Propel, the on-campus business accelerator and co-working space. The centre provides mentorship, seed funding, connections and education/training for youth entrepreneurs aged 18-29. Prior to his role at Western, Ian spent 4 years working at the Regional Innovation Centre (RIC) TechAlliance, assisting numerous early-stage technology companies while managing the day-to-day operations of the Startup Services team. Throughout his career Ian has personally assisted more than 300 startup companies, and was the founder and CEO of Spatial Solutions, a successful software company based in Montreal. Ian plays an active role on a number of organizations and committees in London, Ontario with respect to entrepreneurship and local economic development. He is also an avid triathlete, completing 2 Ironman distance races in recent years. Ian holds an MBA from the Richard Ivey School of Business, a MSc. from McGill University and a BA from Western University.

Deniz Temelli, TechAlliance
Manager, Measured Innovation and Business Services

Deniz is a Biomedical Engineer who gained industry experience by working as an R&D Engineer at Baylis Medical, a medical device company, for 4 years. There she was responsible for developing a novel product and overseeing all aspects of the commercialization including manufacturing, regulatory, validation, packaging and more. Deniz graduated with an MBA from the Ivey School of Business in 2012 and since then has been mentoring entrepreneurs as a Business Analyst at TechAlliance.

John Pollock, Southwestern Ontario Angel Group

John Pollock (MBA UWO 1984) is a seasoned entrepreneur with sales experience in Africa, construction and property development experience in Ontario and sailing miles logged in the Caribbean. John helped to launch and operate a student entrepreneurship program at Western University and Fanshawe College in 2010 which surfaced and supported more than 400 student ventures and resulted in the launch and operation of more than 70 new business ventures.
John is the Managing Director of the Southwestern Ontario Angel Group where he continues to support the regional entrepreneurial ecosystem.
The Southwestern Ontario Angel Group is one of 12 Provincial Angel groups and one of 36 such groups Nationwide which share expertise and best practices. Angel investors are committed to community development, and building lasting enterprises.

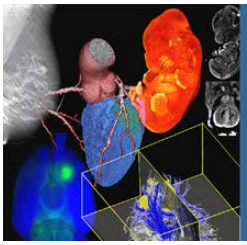

13th Imaging Network Ontario Symposium

March 30th & 31st 2015

London Convention Centre
London Ontario

Symposium Committees

Scientific Committee

Graham Wright (Chair), OCICT
Aaron Fenster (Co-Chair), OICR ITP
Jerry Battista, CINO
Gabor Fichtinger, CINO
Stuart Foster, OPIC
Richard Frayne, MITNEC/CAIN
Stewart Gaede, OCAIRO
Terry Peters, OCICT and Simulation
Frank Prato, OCICT
Giles Santyr, OPIC
Christopher Schlachta, Simulation
Aaron Ward, OICR ITP
Martin Yaffe, OICR SIP

Organizing Committee

SM+i

Ann Corbitt
Deborah Bowers
Heather Timm

Robarts Research Institute

Janette Wallace
Johanne Langford

Consortium-affiliated Administration

Carol Richardson (OICR ITP)
Jean Rookwood (OCICT)
Yulia Yerofeyeva (OICR SIP)
Connie Marano (CINO)
Sherri Couto (OICR ITP)
Janet Binding (OPIC)
Pamela Wilkinson, (MITNEC/CAIN)

Acknowledgements

We thank the following consortia for serving as Platinum Sponsors:

Medical Imaging Trials Network of Canada / Canadian Atherosclerosis Imaging Network (MITNEC/CAIN)

Cancer Imaging Network of Ontario, Cancer Care Ontario (CINO)

Ontario Consortium in Imaging for Cardiovascular Therapeutics (OCICT)

OICR Imaging Translation Program (OICR ITP)

OICR Smarter Imaging Program (OICR SIP)

Ontario Preclinical Imaging Consortium (OPIC)

Effective Systems for Procedure Specific Healthcare Simulation (Simulation)

We would like to thank our government and private sector partners, the Canadian Institutes of Health Research, the Ministry of Research and Innovation, the Ministry of Health and Long-Term Care, The University of Western Ontario, Robarts Research Institute, the Ontario Institute for Cancer Research and Cancer Care Ontario for their contributions to, and their participation in, the above mentioned consortia.

Poster Awards

We would like to thank Ontario Preclinical Imaging Consortium (OPIC) as a major supporter of the Poster Awards.

Key Sponsors

Commercialization Session Sponsor

CIMTEC builds and tests clinical prototypes in the broad areas of 3D visualization, image analysis and mechatronics design. Through technology development, business advice, and clinical testing, we help researchers, startups and small to medium-sized companies commercialize their medical imaging innovations.

Silver Sponsors

GE Healthcare provides transformational medical technologies and services to meet the demand for increased access, enhanced quality and more affordable healthcare around the world. GE works on things that matter -great people and technologies taking on tough challenges. From medical imaging, software & IT, patient monitoring and diagnostics to drug discovery, biopharmaceutical manufacturing technologies and performance improvement solutions, GE Healthcare helps medical professionals deliver great healthcare to their patients. www.gehealthcare.com

A leader in multimodality and programmable; physiological flow pumps, heart motion phantoms and respiratory tumor motion, as well as QA phantoms for MRI, ultrasound & micro-CT. New Products: CT/MRI/PET compatible DCE Perfusion Flow Phantom, MRI compatible motion controllers/stages & a Mixed Plaque CTCA phantom.

Responsibility, excellence and innovation have been the basis for Siemens' success for over 160 years. Siemens Magnetic Resonance innovates to advance human health – in every hospital or practice or lab or university. Whether you are just beginning to work with MRI or you are at the forefront of research.

VisualSonics is a manufacturer of realtime, in vivo, high-resolution micro-imaging systems designed specifically for preclinical research. VisualSonics' imaging technologies allow researchers at pharmaceutical and biotechnology companies, hospitals and universities to conduct research in cardiovascular, cancer, neurobiology and developmental biology areas. The micro-imaging technologies support research applications that include genetic research, phenotypic studies and drug development. VisualSonics is based out of Toronto, Ontario, Canada with operations in more than 30 countries. European operations are conducted out of Science Park, Amsterdam, Netherlands and Asia Pacific operations out of Singapore.

Bronze Sponsors

Celebrating 15 years of providing confidence to over 1,800 leading treatment centres worldwide with more than 3,000 QUASAR™ phantoms in clinical use

Philips is one of the world's leading healthcare technology companies. We are committed to understanding patients' and caregivers' needs and improving the experience of Care.

Exhibitors

Abstract Reviewers

We would also like to thank the volunteer abstract reviewers.

Mitchell Albert
Jerry Battista
Jeff Carson
Elvis Chen
Ralph Da Costa
Rob deKemp
Paula Foster
Stuart Foster
Richard Frayne
Stewart Gaede
Jim Lacefield
Andras Lasso
Len Luyt
Christopher Macgowan
John More
Grace Parraga
Terry Peters
Tom Purdie
Giles Santyr
Tim Scholl
Marshall Sussman
Marie-Claude Villeneuve
Aaron Ward
Martin J. Yaffe

MARCH 30, 2015

7:00 – 8:00 REGISTRATION (BALLROOM 2367 FOYER)

8:00 – 8:10 OPENING REMARKS (BALLROOM 2367)
GRAHAM WRIGHT, AARON FENSTER

Keynote Lectures (BALLROOM 2367)

8:10 – 9:00 ***INSERTABLE, IMPLANTABLE AND WEARABLE MICRO-OPTICAL DEVICES FOR DETECTION OF EARLY CANCER***
Christopher H. Contag, Stanford University School of Medicine

9:00 – 9:50 ***RADIO(GENO)MICS***
Robert Gillies, Moffitt Cancer Center

9:50 – 10:35 POSTER VIEWING & BREAK (BALLROOM 5)
(Please see page 16 for Adjudication Schedule)

10:35 - 12:05 SESSION 1 (BALLROOM 2367)

PERFUSION, METABOLIC AND HYPOXIA IMAGING
Chair: Frank Prato
Lawson Health Research Institute

10:35 Quantitative functional and molecular imaging in cardiac and cancer studies
Ting Lee, Robarts Research Institute

10:50 Simultaneous Measurement of Perfusion and Hypoxia in Pancreatic Cancers
Ivan Yeung, Princess Margaret Cancer Centre

11:05 Evaluation of CT Perfusion as an Imaging Biomarker of Tumor Hypoxia
Qi Qi, Western University

11:20 Comparison of small (~800 Da) and large (65,000 Da) contrast agent CT perfusion to quantify blood-tumor-barrier permeability following focused ultrasound and microbubble treatment in a C6 rat glioma model.
Hassaan Ahmed, Robarts Research Institute

11:35 Visualizing Ipsilateral Activation in patients with Cervical Myelopathy using Functional Magnetic Resonance Imaging
Kayla Ryan, Robarts Research Institute

11:50 Non-invasive quantification of coronary (fractional) flow reserve to direct optimal therapies
Rob deKemp, University of Ottawa Heart Institute

10:35 - 12:05 SESSION 2 (BALLROOM 4)

IMAGE-GUIDED INTERVENTION
Chair: Terry Peters
Robarts Research Institute/Western University

10:35 Towards integrated image guidance for endoscopic sinus and skull-base surgery
David Adair, University of Calgary

10:50 Visual feedback mounted on surgical tool
Kaci Carter, Queen's University

11:05 Open source software for intracranial blood clot measurement
Maggie Hess, Queen's University

11:20 Respiratory motion model based correction for MRI-guided intracardiac electrophysiology procedures
Robert Xu, University of Toronto

11:35 Positron Detector for Intra-Operative Surgical Margin Evaluation in Breast Cancer
John Dillon, Odette Cancer Centre

11:50 Taking advantage of artifacts: Coherent half field of view replication passive tracking technique for controllable susceptibility devices for magnetic resonance imaging in the presence of motion
Justin Lau, University of Toronto

12:05 – 1:05 LUNCH (BALLROOM 5)

MARCH 30, 2015 CONTINUED

1:05 – 2:35 SESSION 3 (BALLROOM 2367)

PRECLINICAL IMAGING HIGHLIGHT REEL
Chair: Stuart Foster
Sunnybrook Research Institute

1:05 OPIC and the Development of a Commercialized Photoacoustic Imaging Platform
Stuart Foster, Sunnybrook Research Institute

1:20 Mouse Models of Human Diseases
Mark Henkelman, Toronto Centre for Phengenomics

1:35 Anatomical, Functional and Metabolic MRI of Lung Injury using Hyperpolarized Nuclei
Giles Santyr, Hospital for Sick Children

1:50 Pre-Clinical Imaging for Models of Musculoskeletal Disease
David Holdsworth, Robarts Research Institute

2:05 Hyperpolarized 13C Imaging: from Rats to Humans
Chuck Cunningham, Sunnybrook Research Institute

2:20 Micro-MRI Techniques for Cellular and Metabolic Imaging at 3 Tesla
Paula Foster, Robarts Research Institute

1:05 - 2:35 SESSION 4 (BALLROOM 4)

QUANTITATIVE IMAGING
Chair: Grace Parraga
Robarts Research Institute

1:05 Comparison of Functional Lung Imaging using Inert Fluorinated Gas and Hyperpolarized 3He MRI
Marcus Couch, Lakehead University

1:20 Generation of high-contrast single-slice susceptibility weighted images in the brain at 7T
Zahra Hosseini, Robarts Research Institute

1:35 Next-generation MRI of the human spinal cord: Translating measures of microarchitecture and function to clinical utilization
Allan Martin, Institute of Medical Science, University of Toronto

1:50 Quantitative Functional Imaging of Prostate Cancer with Improved Kinetics Modeling of Hybrid 18F-Fluorocholine PET-CT Imaging
Adam Blais, Western University

2:05 Principal Component Analysis of the CT Density Histogram to Generate Parametric Response Maps of COPD
Nanxi Zha, Western University

2:20 Ventilation Defect Clusters: MRI Measurements of Regional Ventilation Heterogeneity
Dante Capaldi, Robarts Research Institute

2:35 – 3:20 POSTER VIEWING & BREAK (BALLROOM 5)

(Please see page 16 for Adjudication Schedule)

MARCH 30, 2015 CONTINUED

3:20 – 4:50 SESSION 5 (BALLROOM 2367)

TARGETED PROBE DEVELOPMENT
Chair: Martin Yaffe & Len Luyt
Sunnybrook Research Institute/Centre for Imaging Technology Commercialization & Western University

3:20 New Approaches for Functionalizing and Targeting Ultrasound Microbubbles
John Valliant, McMaster University

3:35 Panitumumab modified with metal chelating polymers (MCPs) for dual labeling with 111In and 177Lu as a potential theranostic for pancreatic cancer
Sadaf Aghevlian, University of Toronto

3:50 Molecular Modeling Studies for Rational Design of GHSR-1a Agonist for Prostate Cancer Diagnosis Using PET
Jinqiang Hou, London Health Sciences Center

4:05 In Vivo Whole-Body Spin-Lattice Relaxation Dispersion at 1.5 Tesla using Delta Relaxation Enhanced Magnetic Resonance (dreMR) Imaging
Yonathan Araya, Western University, Robarts Research Institute

4:20 Influence of MagA Expression on MRI Relaxation Rates in Different Cell Types
Donna Goldhawk, Lawson Health Research Institute / Western University

4:35 Development of Bipyridine-Containing Peptide Imaging Probes for SPECT Imaging
William Turnbull, Western University

3:20 – 4:50 SESSION 6 (BALLROOM 4)

VISUALIZATION AND IMAGE ANALYSIS
Chair: Aaron Ward
Western University

3:20 Automated segmentation of whole-slide histology for vessel morphology comparison
Yiwen Xu, Western University

3:35 Image-based Personalized Analysis and Modeling of Cardiac Structure and Function: A Robust Method for Automatic Left-Ventricular Infarct Segmentation
Eranga Ukwatta, University of Toronto

3:50 Three-Dimensional Pulmonary 1H MRI Multi-Region Segmentation Using Convex Optimization
Fumin Guo, Robarts Research Institute

4:05 Deep Neural Network Based Segmentation of Lesions in Breast DCE-MRI
Hongbo Wu, University of Toronto

4:20 Three dimensional retrospective motion correction in MRI using spherical navigator echoes (SNAV)
Patricia Johnson, Robarts Research Institute

4:35 Optical CT scanning for skeletal imaging in an optically cleared mouse
Kurtis Dekker, Department of Medical Biophysics, Western University

5:00 – 7:00 POSTER SESSION & RECEPTION (BALLROOM 5)
(Please see page 16 for Adjudication Schedule)

MARCH 31, 2015

7:00 – 8:00 REGISTRATION (BALLROOM 2367 FOYER)
8:00 – 8:10 OPENING REMARKS (BALLROOM 2367)

Keynote Lectures (BALLROOM 2367)

8:10 – 9:00 ***BRIDGING ACADEMIA AND INDUSTRY WITH OPEN SOURCE***
Stephen Aylward, Kitware Inc.

9:00 – 9:50 ***CARDIOVASCULAR MOLECULAR IMAGING: PAST, PRESENT, FUTURE***
Frank Bengel, Hannover Medical School

9:50 – 10:35 **POSTER VIEWING & BREAK (BALLROOM 5)**
(Please see page 16 for Adjudication Schedule)

10:35 – 12:05 (BALLROOM 2367)

SESSION 7 COMMERCIALIZATION
Chair: Lisa Cechetto, WORLDiscoveries

SPEAKERS
10:35 – 11:05 Ian Haase, Propel - *An overview of the services and programs available through the Ontario Network of Entrepreneurs (ONE)*

11:05 – 11:35 Deniz Temelli, TechAlliance - *Medical Technology Commercialization*

11:35 – 12:05 John Pollock, Southwestern Ontario Angel Group - *Seeking Angel Investment*

12:05 – 1:05 **Lunch (BALLROOM 5)**

MARCH 31, 2015 CONTINUED

1:05 – 2:35 SESSION 8 (BALLROOM 2367)

CLINICAL IMAGING
Chair: Richard Frayne
Seaman Family MR Centre

1:05 Precise and Rapid assessment of collaterals using multi-phase CTA in the triage of patients with acute ischemic stroke for Intra-Arterial Therapy (PRove-IT)
Christopher d'Esterre, University of Calgary

1:20 Carotid atherosclerosis and cerebral small vessel disease.
Navneet Singh, CAIN (Canadian Atherosclerosis Imaging Network): Sunnybrook

1:35 Carotid plaque texture: toward a biological meaning of mathematical algorithms in 3D carotid ultrasound
David Spence, Stroke Prevention & Atherosclerosis Research Centre, Robarts Research Institute

1:50 Reproducibility of Quantitative Susceptibility Mapping in Healthy Brains
Armin Eilaghi, University of Calgary

2:05 Site qualification standards for Tc-99m-SPECT perfusion imaging in a multi-centre study of MITNEC (Medical Imaging Trials Network of Canada)
Jennifer Renaud, University of Ottawa Heart Institute

2:20 Predicting the Impact of Surgery on Quality of Life and Risk Management in Patients Afflicted with Glioblastoma Multiforme
Luca Li, University of Calgary

1:05 – 2:35 SESSION 9 (BALLROOM 4)

INSTRUMENTATION/DEVICES
Chair: Aaron Fenster
Western University/Centre for Imaging Technology Commercialization

1:05 Development of fast 3D photoacoustic imaging
Jeffrey Carson, Lawson Health Research Institute

1:20 A Novel Nasopharyngeal Method for Rapid Selective Brain Cooling in a Rabbit Model
Mohammad Fazel, Robarts Research Institute

1:35 Current sensing for navigated electrosurgery
Kaci Carter, Queen's University

1:50 The effect of matching layers as an acoustic lens in a staring transducer array in photo acoustic imaging
Madeleine Van de Kleut, Lawson Health Research Institute

2:05 Phase-matched 4DCT for AC in 4D gated PET
Julia Publicover, Techna Institute, University Health Network

2:20 Design, Development and in vivo Evaluation of a Remote Catheter Navigation System with 3-Degrees-of-Freedom
Mohammad Tavallaei, Robarts Research Institute

2:35 – 2:50 Afternoon Break (BALLROOM 5)

March 31, 2015 Continued

2:50 – 4:20 Session 10 (Ballroom 2367)

IMAGING/SIMULATION FOR THERAPY PLANNING AND RESPONSE
Chair: Gabor Fichtinger
Queens University

2:50 Dosimetric Analysis of Respiratory-Induced Cardiac Intrafraction Motion in Left-sided Breast Cancer Radiotherapy
Omar El-Sherif, Western University

3:05 The Effect of the Chemotherapy Agent Methotrexate on the Developing Brain
Leigh Spencer Noakes, The Hospital for Sick Children

3:20 Response Monitoring Using Texton-Based Approach in Locally Advanced Breast Cancer
Mehrdad Gangeh, Sunnybrook Health Sciences Center

3:35 Early prediction of lung cancer recurrence after stereotactic radiotherapy using texture analysis of automatic graph cuts segmentations
Sarah Mattonen, Western University

3:50 Personalized Treatment Selection for Brain Metastases Using MRI Radiomics
Timothy Yeung, Western University

4:05 [19]Fluorine cellular magnetic resonance imaging to monitor in vivo therapeutic cell migration
Corby Fink, Robarts Research Institute, Western University

2:50 – 4:20 Session 11 (Ballroom 4)

IMAGING BIOMARKERS
Chair: Giles Santyr
Hospital for Sick Children

2:50 Gd-Free MRI Contrasts Agents Based on Manganese Porphyrin: a Sensitive and Versatile Platform for Diverse Applications at High Clinical Fields
Xaio-An Zhang, University of Toronto

3:05 In Vivo Sodium MRI of Human Prostate Cancer
Justin Peterson, Western University

3:20 Development of an image based classification method for the interventional treatment of preterm neonates with intraventricular hemorrhage using 3D ultrasound
Jessica Kishimoto, Western University

3:35 How do Exercise Responses Relate to 3He Magnetic Resonance Imaging Apparent Diffusion Coefficients in Older Never-Smokers?
Khadija Sheikh, Robarts Research Institute

3:50 Roemer-Optimal Reconstruction of Hyperpolarized 13C Cardiac Images with an 8 Channel Coil
William Dominquez, Sunnybrook Research Institute

4:20 – 4:45 Poster Awards (Ballroom 2367)

4:45 – 5:00 Closing Remarks

POSTER COMPETITION ADJUDICATION SCHEDULE

Poster presenters need to be at their posters during the times specified in the schedule below.
Judges will judge posters by visiting each poster and talking with the presenter. If the presenter is not present when the judge arrives, this counts against the overall judgement.

Group A: Poster numbers 3 – 81
Group B: Poster numbers 82 - 151

DAY 1, March 30

AM poster viewing/networking break **9:50 to 10:35 am**
Adjudicated poster time for Group **A**: 20 min - **9:55 to 10:15 am**
Adjudicated poster time for Group **B**: 20 min - **10:15 to 10:35 am**

PM poster viewing/networking break **2:35 to 3:20 pm**
Adjudicated poster time for Group **A**: 20 min - **2:40 to 3:00 pm**
Adjudicated poster time for Group **B**: 20 min - **3:00 to 3:20 pm**

Evening poster viewing session **5:10 to 7:00 pm**
Adjudicated poster time for Group **A**: 20 min - **5:15 to 5:35 pm**
Adjudicated poster time for Group **B**: 20 min - **5:35 to 5:55 pm**

DAY 2, March 31

AM poster viewing/networking time **9:50 to 10:35 am**
Adjudicated poster time for Group **A**: 20 min - **9:55 to 10:15 am**
Adjudicated poster time for Group **B**: 20 min - **10:15 to 10:35 am**

TOTAL Adjudicated time per group during the two days is 80 min.

Canadian Atherosclerosis Imaging Network

CAIN

&

Medical Imaging Trial Network of Canada

MITNEC

Oral Presentation and Poster Abstracts

Towards integrated image guidance for endoscopic sinus and skull-base surgery

David Adair*, David G Gobbi, Richard Frayne, and Yves P Starreveld
Medical Imaging Trial Network of Canada
Biomedical Engineering, Clinical Neurosciences, Radiology and Hotchkiss Brain Institute, University of Calgary, Calgary, Alberta
Calgary Image Processing and Analysis Centre, Foothills Medical Centre, Calgary, Alberta, Canada

Introduction: Approximately 400,000 endoscopic sinus surgeries are performed annually in the United States, 45% of which are performed using image guidance systems (IGSs) (1). IGSs provide intraoperative localization of surgical targets by tracking an image guidance probe (through optical or electromagnetic tracking) and displaying the position and orientation of the probe tip on triplanar pre- or intra-procedural image sets (Fig 1). IGSs are considered state-of-the-art technology (2, 3) and their use continues to grow (1, 2). Current limitations of the technology prevent more widespread clinical adoption (4). Future innovations in IGSs could overcome these limitations, leading to improved rates of clinical adoption and improved patient care. Several groups have attempted to overcome the limitations of traditional IGSs. However, their implementations have failed to achieve widespread clinical adoption. We performed a comprehensive review to identify weaknesses in modern implementations to better inform the future design and development of a novel image guidance system for use in endoscopic sinus and skull-base procedures.

Methods: We conducted iterative searches of the University of Calgary research library catalogue over September-December 2014 to retrieve articles related to the development of modern image guidance systems. Search terms included “image guidance”, “image-guided surgery”, “endoscopic surgery”, “surgical navigation”, “endoscopy”, “image-guided intervention”, and “virtual endoscopy.” We excluded articles from journals without peer-review and articles published before 2000. We identified weaknesses of experimental state-of-the-art implementations by comparing their reported processing stages against innovations published in technical journals. Based on this review, we propose a novel IGS that includes state-of-the-art processing, including automated anatomic and functional atlas-based segmentation of surgical targets and video-integrated registered volumetric rendering of these targets.

Results: Primary limitations to traditional image guidance systems include 1) the necessity to repeatedly switch between using the tracked probe and other surgical instruments, and 2) the non-intuitive registration of the endoscopic view and preoperative imaging. Modern IGSs (4, 5, 6, 7) have attempted to remove these limitations by tracking the endoscope and integrating the IGS into the endoscopic video. They fail to receive widespread clinical adoption, however, because of ineffective implementation of human-computer interfaces and unsatisfactory user (surgeon) experience (4). Multidisciplinary partnerships between scientific and clinical personnel are essential to overcome user experience limitations (8). Experimental state-of-the-art implementations report statistically significant reduction in user mental demand, effort, and frustration, but show no reduction in temporal and physical demand and no improvement in surgical performance (4).

Conclusions: Modern IGSs continue to implement unsatisfactory interfaces, such as requiring manual contouring of surgical targets in preoperative imaging data, a process that adds on average 60 minutes to each procedure. Many of these limitations can be improved using readily available technical innovations. With the identification of several avenues of innovation in the field, our multidisciplinary team of scientists, engineers, and clinicians will begin to develop a novel IGS with user interaction and surgeon experience as guiding principles.

References: [1] Visvanathan *et al*., J. Laryngol. Otol., 2013. [2] Smith *et al*., Am. J. Rhinol., 2007. [3] Fried *et al*., Laryngoscope, 2008. [4] Dixon *et al*., Laryngoscope, 2014. [5] Rosahl *et al*., Skull Base, 2006. [6] Winne *et al*., Int. J. Comput. Assist. Radiol. Surg., 2011. [7] Shahidi *et al*., IEEE Trans. Med. Imaging, 2002. [8] Cleary *et al.*, Annu. Rev. Biomed. Eng., 2010.

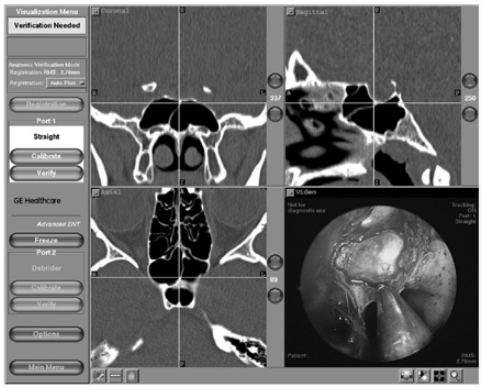

Figure 1. Traditional image guidance system with preoperative CT data (top-left, top-right, bottom-left) and endoscopic video (bottom-right). The crosshair on the image slices indicates the position of the tracked image guidance probe, which can be seen in the endoscopic video. Surgeons must mentally correlate the different perspectives of the views throughout procedures. Source: Fried *et al.*, Laryngoscope, 2008.

Metabolic and functional correlates differentiate between mild and moderate cervical spondylotic myelopathy: A MRS and fMRI study

Izabela Aleksanderek*[1,2], Todd K Stevens[2], Sandy Goncalves[1,2], Robert Bartha[1,2], and Neil Duggal[1,3]
[1]Medical Biophysics, Western University, London, Ontario [2]Robarts Research Institute, London, Ontario
[3]Department of Clinical Neurological Sciences, University Hospital, LHSC, London, Ontario
Medical Imaging Trial Network of Canada Consortium

INTRODUCTION: The ideal timing of surgical intervention for cervical spondylotic myelopathy (CSM) patients, especially with early, mild symptoms, remains particularly controversial since select patients can stabilize clinically without operative intervention. The goal of this study was to compare the recovery of neuronal metabolism and functional reorganization using proton magnetic resonance spectroscopy and functional MRI in the primary motor cortex (M1) between mild and moderate CSM following surgical intervention.

METHODS: Twenty-eight CSM patients had 2 separate imaging sessions on a 3.0 T Siemens Magnetom Tim Trio that included spectroscopy and functional MRI before and 6 months following surgery. The classification of CSM was based on the modified Japanese Orthopaedic Association (mJOA) questionnaire.[1] Mild CSM was defined by a mJOA score of >12 out of 18 (n=15) and moderate CSM by a score of 9–12 (n=13). Ten healthy controls underwent two MRI scans six months apart. Functional MRI scans of a right handed finger-tapping paradigm were acquired using an echo planar imaging sequence (FOV = 256x256mm, 45 slices, 3mm isotropic, TR/TE=2500/30ms, flip angle=90^{o}, iPAT=2). Functional images were analyzed using BrainVoyager QX software where for each contrast, a volume of activation (VOA), corrected *p*-value, and Brodmann area were produced. A 20mm isotropic spectroscopy voxel was placed on the hand area[2] of the M1 contralateral to the greater deficit side in the CSM group and on both sides in the controls. Spectroscopic data were localized using PRESS (TR/TE=2000/135ms, 192 averages, voxel size=8cm^3). The ratio of *N*-Acetylaspartate (NAA) to creatine (Cr) was measured.[3,4]

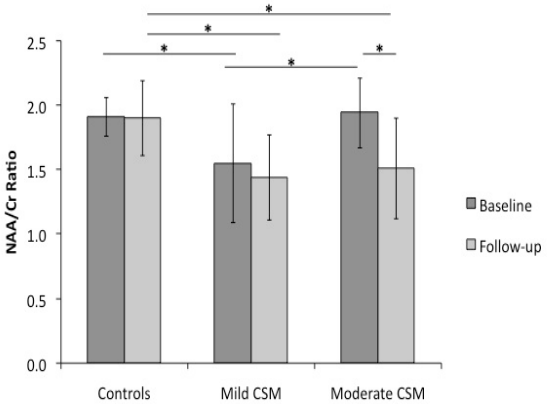

Figure 1: Average NAA/Cr metabolite concentrations at baseline and 6-month follow-up in the controls, and at pre- and post-operative time points in the mild CSM, and moderate CSM groups (error bars represent the SD; * represents significance p<0.05).

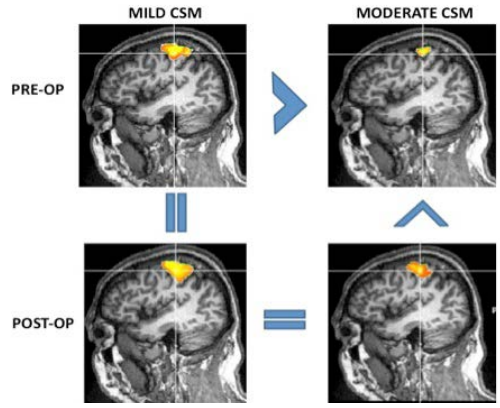

Figure 2: The volume of activation for the mild CSM (left) and the moderate CSM (right) patient groups are shown. The pre-op activation is displayed in the top row showing mild CSM had significantly larger activation near the primary motor cortex compared to moderate CSM. Following surgery, both groups had equal activation volume shifted towards BA 3, the primary somatosensory cortex.

RESULTS: At baseline, mild CSM patients had a lower NAA/Cr ratio in the hand area of M1 compared to healthy controls (p<0.05) and moderate CSM (p<0.05) suggesting neuronal loss or mitochondrial dysfunction (Fig 1). Following successful surgery and clinical improvement, NAA/Cr levels did not recover in mild CSM (p=0.50; Fig 1). The moderate CSM patients, who had significantly worse pre-operative mJOA scores and the largest functional improvement, demonstrated a *decline* in NAA/Cr levels (p<0.05; Fig 1). Pre-operatively, mild CSM had a larger functional VOA than moderate CSM (p=0.05; BA 5; Fig 2). Following surgery, the VOAs were comparable between mild and moderate CSM groups and had shifted towards the primary sensory cortex (p<0.001; BA 3; Fig 2).

CONCLUSIONS: NAA/Cr levels and the size of the VOA in the motor cortex can be used to discriminate between mild and moderate CSM. Following surgery, the metabolic profile of the M1 did not recover in either group, despite significant clinical improvement. We propose that metabolic impairment in M1 may trigger recruitment of adjacent healthy cortex to achieve functional recovery. Further work is needed to determine whether these distinct patterns of remote injury in the sensorimotor cortex in mild and moderate CSM patients could be used to determine the timing and need for intervention.

REFERENCES: [1] Revanappa *et al*. *Eur Spine J* 20:1545-51, 2011. [2] Youstry *et al*. *Brain* 120:141-57, 1997. [3] Bartha *et al. NMR Biomed* 12:205-16, 1999. [4] Bartha *et al. Magn Reson Med* 44:185-92, 2000.

Ventilation Defect Clusters: MRI Measurements of Regional Ventilation Heterogeneity

DPI Capaldi[1,2], K Sheikh[1,2], S Svenningsen[1,2], D Pike[1,2], DG McCormack[3] and G Parraga[1,2]
[1]Imaging Research Laboratories, Robarts Research Institute; [2]Department of Medical Biophysics; [3]Division of Respirology, Department of Medicine, The University of Western Ontario, London, Canada.

Purpose: Gas distribution abnormalities, or ventilation heterogeneity can be regionally quantified using hyperpolarized noble gas MRI. In particular, the ventilation defect percent (VDP)[1] can be generated using semi-automated algorithms. However, as shown in Figure 1, cases can be identified whereby the VDP for two subjects is the same, but the ventilation patterns are different, suggesting that there are measureable differences in ventilation heterogeneity that are not reflected by VDP. As shown in Figure 1, in the COPD subject, ventilation defects were mainly located in the upper right lobe, but in the bronchiectasis subject, such ventilation defects were sparsely distributed. Hence, the objective of this proof-of-concept study was to develop an automated algorithm that quantifies the ventilation heterogeneity using pulmonary functional MRI.

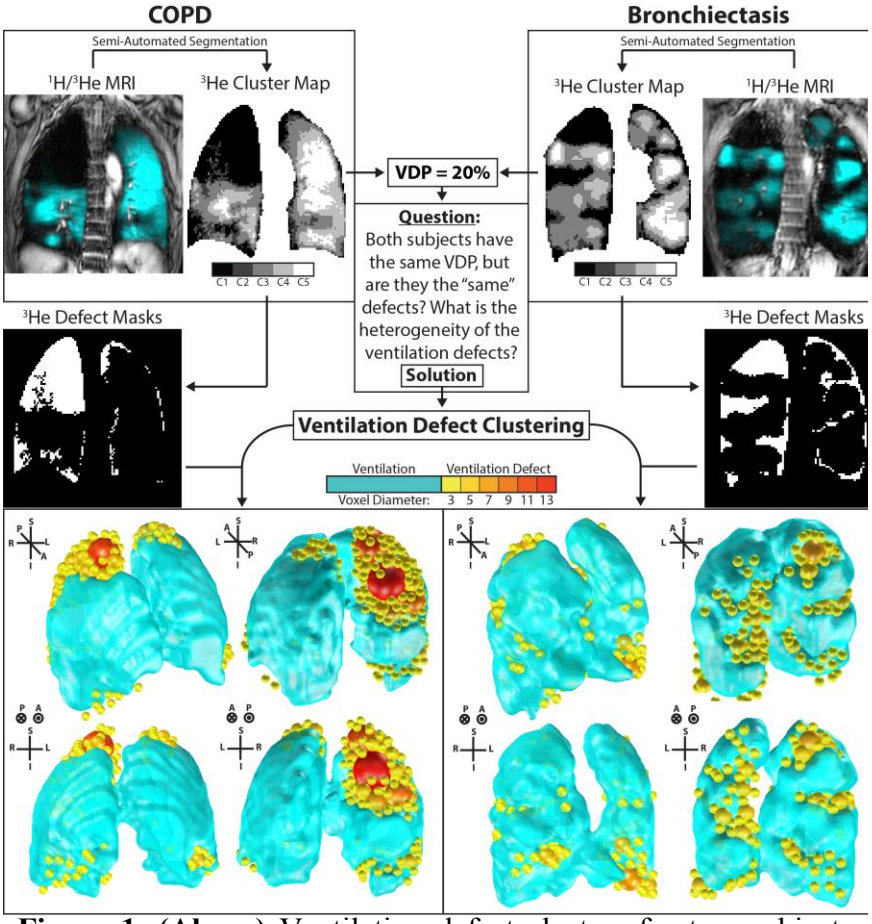

Figure 1. (Above) Ventilation defect clusters for two subjects (COPD and bronchiectasis) with the same VDP – the ventilation defect volume normalizing by the thoracic cavity.

Methods: Thirty-two subjects with COPD or bronchiectasis provided written informed consent to an approved study protocol and were evaluated using MRI, pulmonary function tests, and thoracic CT. Hyperpolarized ^{3}He MRI static ventilation images were acquired at 3T MRI as previously described.[2] Semi-automated segmentation was used to generate ^{3}He MRI VDP[1] and 3D clusters were generated using a proposed ventilation defect clustering algorithm developed in Matlab R2014a. Briefly, the proposed algorithm iteratively traced the ventilation defect volume until the maximum sphere (or multiple spheres of the same size) that can fill within the defect volume is found. Once the largest sphere (or multiple spheres of the same size) was identified, this volume(s) was removed from the ventilation defect mask. This was iteratively repeated until the ventilation defect volume was replaced by spheres. Thus, the algorithm determined the minimum number of unequal size spheres required to fill the defects volume.

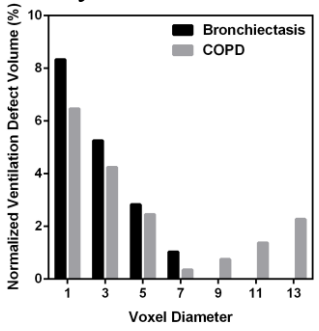

Figure 2. (Right) Ventilation defect volume normalized to the total thoracic volume by sphere size for COPD (gray) and bronchiectasis (black) subjects.

Results: Figure 1 shows the output from the proposed algorithm with ventilation shown in blue and ventilation defects shown as spheres with different volumes shown in colour (red = 13 voxels diameter to yellow = 3 voxels diameter). Two representative subjects (COPD and bronchiectasis) with the same VDP are shown. For the COPD subject, a large upper lobe ventilation defect was reflected by larger sphere sizes that corresponded to 25% of the total defect volume. Alternatively in the bronchiectasis subject, the ventilation defect volume consisted of mostly smaller defects. To better demonstrate this, a cumulative volume sum for each sphere was normalized to the total lung volume and this is shown in Figure 2. When ventilation cluster voxel diameter is plotted in relation to normalized ventilation defect volume, there are numerous smaller ventilation defect spheres, and no regions of large homogeneous ventilation defects for the bronchiectasis subject. Alternatively for the COPD subject, there is a mixture of small and large ventilation defects spheres.

Conclusions: In this proof-of-concept demonstration, we developed a ventilation defect cluster algorithm that may be used to regionally identify and measure ventilation heterogeneity. The algorithm was demonstrated in two subjects with similar VDP and different LCI and showed the relationship of algorithm results with LCI.

References: 1) Kirby, M. *et al. Academic Radiology* (2012); 2) Parraga, G. *et al*. *Investigative Radiology* (2007).

Carotid plaque texture: toward a biological meaning of mathematical algorithms in 3D carotid ultrasound

Lucy Chung, Robert Hammond, Grace Parraga, Aaron Fenster, J. David Spence. Stroke Prevention & Atherosclerosis Research Centre, Robarts Research Institute, Western University, London, Ontario

Background and Purpose: For some time, echolucency (gray scale median) of carotid ultrasound has been used as an indicator of vulnerable plaque. However, much more information is available from radiofrequency signals in carotid ultrasound. We have previously shown that change in carotid plaque texture predicts response to therapy and cardiovascular events. In this study we sought to correlate mathematical algorithms used to assess plaque texture in 3D ultrasound images obtained preoperatively, with histological features of carotid endarterectomy specimens.

Methods: 3D histology of carotid endarterectomy specimens was registered with preoperative 3D ultrasound images of the carotid arteries. Histological features of carotid plaques thought to be important in plaque vulnerability were evaluated by serially assessing each of 54 mathematical algorithms in portions of 3D ultrasound images matched with plaque features seen in 3D histology, in predicting these features of vulnerable plaque.

Results: Two of the algorithms, texture energy features Laws Level/Ripple (LLR) and Laws Edge/Edge (LEE) were clearly better at discriminating features of vulnerable plaque: calcification, fibrous wall, necrotic core, and intraplaque hemorrhage (see figure).

Conclusion: Carotid plaque texture can be used to identify features of vulnerable plaque.

8

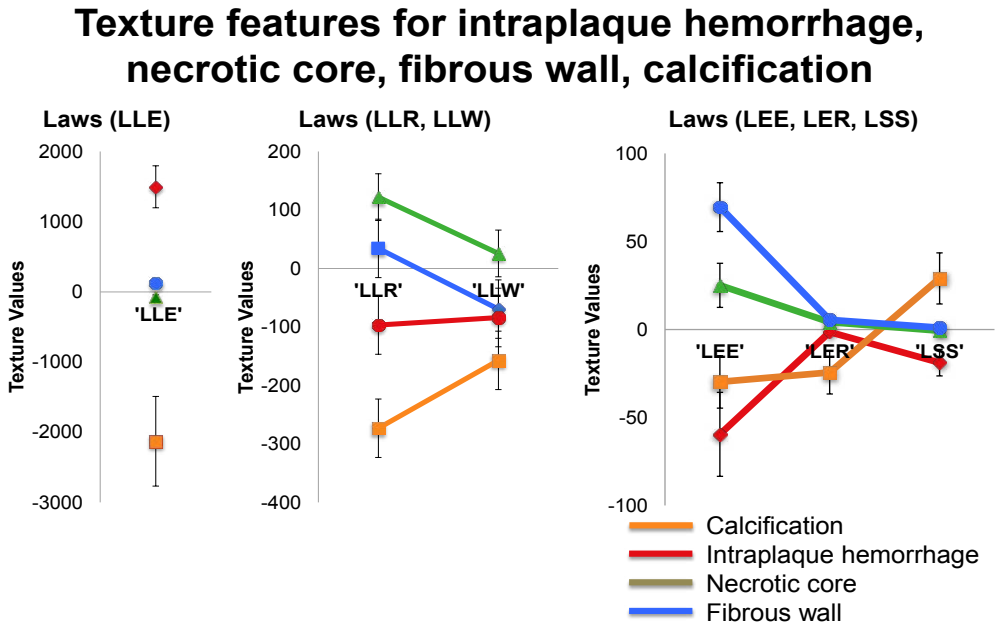

Multi-phase CTA: A New Tool for the Imaging Triage of Patients with Acute Ischemic Stroke

Christopher D. d'Esterre, PhD[1,2,5] ; Bijoy K. Menon, MD[1-5] ; Emmad M. Qazi, BSc[1]; Mohammed Almekhlafi, MD[1,2,6]; Andrew M. Demchuk, MD[1,2,4,5]; Richard Frayne[2,4,5] ; Mayank Goyal, MD[1,2,4,5]

[1] Calgary Stroke Program, Department of Clinical Neurosciences, University of Calgary.
[2] Department of Radiology, University of Calgary.
[3] Department of Community Health Sciences, University of Calgary.
[4] Hotchkiss Brain Institute.
[5] Seaman Family MR Centre
[6] Department of Internal Medicine, King Abdulaziz University

Consortium affiliation: CAIN/MITNEC

Research supervisor: Drs. Richard Frayne and Bijoy Menon

Introduction: Stroke is the leading cause of morbidity in developed countries. As 'time is brain' in the acute stroke setting, an ideal imaging selection tool should detect salvageable brain quickly, reliably and be widely available. Here, we describe a new imaging selection tool i.e. multi-phase CTA (mCTA) in patients with acute ischemic stroke and to demonstrate its reliability, concurrent validity and predictive ability in determining clinical outcome when compared to non-contrast CT (NCCT) and perfusion CT (PCT).

Methods: Data is from the pilot phase of PRove-IT, an ongoing prospective observational study that seeks to understand the utility of multi-modal imaging in the triage of patients with acute ischemic stroke. All patients had NCCT brain, single-phase CTA head and neck, mCTA and PCT at baseline. Pial arterial filling on mCTA is scored using a 6-point ordinal scale. We demonstrate a) inter-rater reliability b) concurrent and c) predictive validity (both measures of criterion validity) of this mCTA based scale. Primary clinical outcome in these analyses is 50% or more drop in NIHSS over 24 hours.

Results: A total of 147 patients were included in the present study. When compared to mCTA, single phase CTA (sCTA) consistently underestimates pial arterial filling. Inter-rater reliability for mCTA is excellent (n=30, kappa=0.81, $p<0.001$). When compared to NCCT and PCT, use of mCTA results in least uncertainty (concurrent validity) when making clinical decisions. ROC analysis, Akaike's Information Criterion and Bayesian Information Criterion demonstrate better predictive validity for mCTA in determining clinical outcome.

Conclusion: mCTA is a quick, easy to use, reliable and valid tool for imaging selection in patients with acute ischemic stroke.

Turbulence in the Carotid Bifurcation Measured Using Particle Image Velocimetry

Amanda DiCarlo*[1], Onaizah Onaizah[2], and Tamie Poepping[1,2]
Department of Physics and Astronomy, Department of Medical Biophysics, University of Western Ontario, London, Ontario, Canada

Introduction: Atherosclerosis in the carotid artery is one of the main risk factors for stroke. Arterial compliance, a measure of the elasticity of blood vessels, is a common indicator of vascular disease and is known to decrease in association with other stroke risk factors, including age, diabetes, and hypertension. Decreased local compliance leads to changes in the flow and pressure waveforms and corresponding changes in the velocity field. Resulting hemodynamic parameters, such as shear stress and turbulence, play a primary role in the process of plaque and clot formation. While it is difficult to accurately extract complex in vivo blood flow structures using clinical techniques, in vitro experimental models can be used to simulate in vivo carotid artery flow. Particle image velocimetry (PIV) is an established in vitro optical technique for measuring velocity fields with high temporal and spatial resolution that can be applied to study specific aspects of the flow system when used in controlled test models.

Methods: Experiments were performed using two versions of optically transparent polydimethylsiloxane (PDMS) phantoms, a thin-walled model with a 1-mm thick vessel wall and a low-compliance block model with a hollow flow channel inside a block of PDMS. The phantoms were constructed with identical vessel geometry, a 50% eccentric volume stenosis of the internal carotid artery as shown in figure 1. Phantoms were perfused with a custom refractive index-matched blood mimicking fluid using a computer controlled pump to generate a physiologically realistic pulsatile flow rate waveform.[1] Downstream flow resistors imposed a physiological flow division at the bifurcation and mimic the effect of downstream vasculature. PIV data were collected using a commercial stereoscopic, time resolved, PIV system (LaVision, Inc), previously described.[2] Thirty cardiac cycles were obtained, synchronized using an external trigger pulse generated by the pump. Double frame exposure PIV images were collected at a recording rate of 100 Hz and velocity vectors were derived using a standard fast fourier transform multi pass algorithm (DaVis, LaVision, Inc.) resulting in a final in plane velocity vector resolution of approximately 0.3 mm. A Reynold's decomposition method was used to separate phase averaged velocity from velocity fluctuations, which were then used to derive turbulence intensity (TI) values.

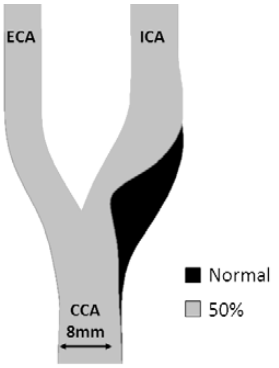

Fig. 1: 50% eccentric stenosis geometry used, compared to disease free normal model

Results: Slightly higher maximum and overall velocities were observed in the block model compared to the thin-walled model however differences in flow pattern were not significant, with both phantoms exhibiting the same velocity jet pattern in the ICA. A phase delay in the time point of maximum velocity in the CCA and ICA is observed in the thin walled model due to the compliance. A stiffer vessel wall resulted in increased ICA turbulence intensity as shown in figure 2. When averaged over the downstream region of interest where the maximum occurred, TI values were 0.48±0.03 m/s in the block model compared to 0.41±0.02 m/s in thin walled model. The rigid model's region of maximum turbulence also occurred more proximal to the bifurcation apex, and higher TI values were sustained over much of the cardiac cycle, indicating a higher cumulative exposure to disturbed flow.

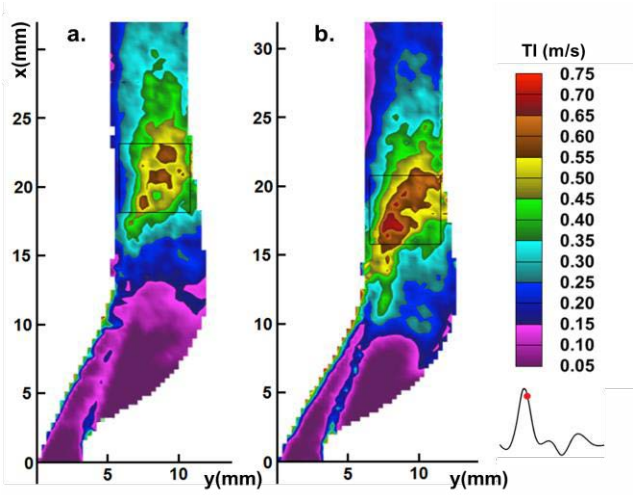

Fig. 2: Turbulence intensity maps for a. thin walled phantom model and b. block phantom model, shown at time point of maximum turbulence for each case.

Conclusion: Particle image velocimetry was used to study the effect of compliance on local hemodynamics. It was observed that decreased compliance leads to higher levels of flow disturbances, suggesting potentially increased stroke risk.

References:

[1] Holdsworth et al. (1999) Physiol Meas 20:219-240
[2] Kefayati et al. (2013) Med Eng Phys 35:898-909

Reproducibility of Quantitative Susceptibility Mapping in Healthy Brains

A Eilaghi[1,2], A Rahmani[1,2], DA McLean[3], CR McCreary[1,2], DG Gobbi[3], ML Lauzon[1,2], M Salluzzi[3], R Frayne[1,2]

[1]Radiology and Clinical Neurosciences, Hotchkiss Brain Institute, University of Calgary, Calgary, Alberta, Canada [2]Seaman Family MR Centre, Foothills Medical Centre, Calgary, Alberta, Canada, [3]Calgary Image Processing and Analysis Centre (CIPAC), Foothills Medical Centre, Calgary, Alberta, Canada.

Introduction: Quantitative susceptibility mapping (QSM) is a novel MR contrast mechanism for measuring regional magnetic susceptibility changes due to iron accumulation in neurodegenerative diseases, such as Alzheimer's disease.[1] We investigated the repeatability of the QSM measurements in cognitively normal, healthy subjects across imaging sessions. We aim to quantify short-term repeatability of QSM measurements in selected regions of brain that are known to have differences in susceptibility with neurodegenerative disease.
Methods: Four healthy individuals (3 male; age: 36 yr ± 12 yr, mean ± standard deviation) were imaged on a 3-T MR scanner (Discovery MR750; General Electric Healthcare, Waukesha, WI). Each individual was scanned three times within two weeks. QSM images were generated using a custom program (Cerebra-QSM; Calgary Image Processing and Analysis Centre, Calgary, AB, www.calgaryimageanalysis.ca). Image processing for QSM included: skull stripping,[2] 3D phase unwrapping,[3] RESHARP background field removal,[4] and regularized deconvolution. Cerebrospinal fluid was used as the background susceptibility reference.[5] The external and internal globus pallidus (eGP and iGP), putamen (P) and caudate nucleus (CN) were identified on the International Consortium of Brain Mapping (ICBM) brain atlas. Regional masks of these four structures were registered to susceptibility maps using symmetric diffeomorphic image registration.[6] Normality of data was tested using a Kolmogorov-Smirnov test and reliability coefficients [7] were calculated for three repeated measurements in P, iGP, eGP and CN.
Results: Regional susceptibility measurements were normally distributed in the P, iGP, eGP and CN ($p > 0.20$). Test-retest reliability showed significant inter-class correlation for all regions of interest ($p < 0.01$). No significant difference was found between multiple measurements in the same subject in P ($p = 0.19$), iGP ($p = 0.24$), eGP ($p = 0.54$), CN ($p = 0.91$). However as anticipated, significant differences existed between subjects in P ($p = 0.01$), iGP ($p < 0.01$), eGP ($p < 0.01$), CN ($p = 0.02$), after controlling for repeated measurements. QSM reliability coefficients for P, iGP, eGP and CN were 0.98, 0.95, 0.91 and 0.92, respectively.
Conclusion: QSM provided reproducible measurements of susceptibility in multiple important brain regions. Such reproducible tool, may improve understanding of Alzheimer's disease without needing radioactive tracers. QSM for iron imaging in neurodegeneration is being piloted at three sites as part of Project C6 of the Medical Imaging Trial Network of Canada (MITNEC).

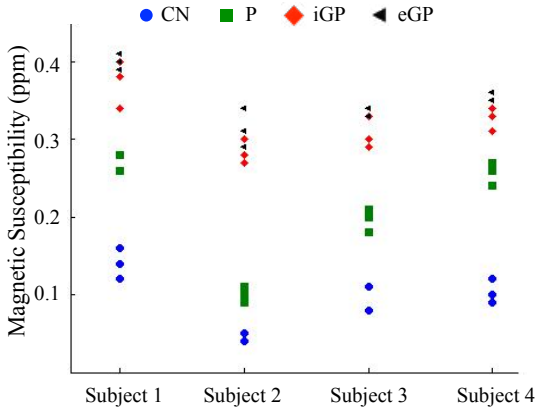

Figure 1. Regional susceptibility variations across subjects. Repeated measurements in each individual ($n = 3$) for each region are shown with same marker.

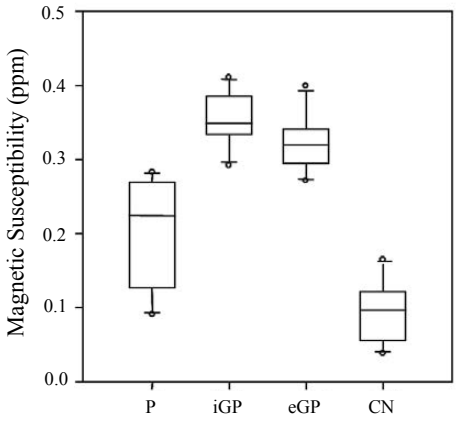

Figure 2. Variation in regional susceptibility measurements across all experiments. Box plot shows median (line), 25%-75% range (box), and 10% and 90% range (error bars).

References: [1] Wang Y, *et al*. *MRM* 2014; 73:82. **[2]** Smith SM, *HBM* 2002; 17:143. **[3]** Jenkinson M, *MRM* 2003; 49: 193. **[4]** Sun H, *et al*. *MRM* 2013; 71: 1151. **[5]** Schweser F, *et al*. *NeuroImage* 2011; 54: 1169. **[6]** Avants BB, *et al*. *NeuroImage* 2011; 54: 2033. **[7]** Eliasziw M, et al. *Physical Therapy* 1994; 74: 777.

Statistical Shape Modeling for the Analysis of Knee Joint Morphology

Jaques S. Milner[1], Sangwoo Leem[1], Todor G. Ivanov[1] and David W. Holdsworth[1,2]
[1]Imaging Research Laboratories, Robarts Research Institute, Western University, London, ON
[2]Departments of Medical Biophysics and Surgery, Western University, London, ON

Introduction. Studies have shown that morphological changes in the knee joint can be linked to degenerative physiological processes occurring both locally in the immediate knee joint area, and also in regions further away, as a result of other bone and joint conditions [1,2]. Statistical shape modeling (SSM) can be applied to 3-D shape reconstructions in order to objectively compare complex morphology without idealizing the underlying geometry [3]. A major challenge to overcome in this process is the difficulty in producing objective and consistent computations of corresponding points on 3-D anatomical surfaces; manually selecting landmark points can be burdensome while still not yielding sufficiently dense correspondence maps, and likewise, automated techniques may rely on specific surface parameterizations, which, in turn, reduce their general applicability to freeform anatomical shapes. ShapeWorks [4] is a promising software tool for automated statistical shape analysis that does not rely on specific surface parameterization and requires little in terms of pre-processing and parameter tuning. The objective of this study is therefore to assess the performance of ShapeWorks in the context of using it prospectively to process and evaluate larger numbers of in vivo human knee joints reconstructed from conventional CT image data.

Methods. A cohort of eight subjects was selected from a pool of 50 early knee OA patients (Kellgren–Lawrence score ≤ 2) previously scanned using CT prior to undergoing arthroscopic surgery. Subvolumes (0.55 mm isotropic voxel size) of each bone were segmented to produce 3-D triangulated surface models of the: femur, patella, tibia, and fibula of each subject. The geometric surface models were converted to binary segmentation images using an isotropic voxel spacing of 0.5 mm. 2048 points were specified for the analysis and automatically placed on the surface each bone - represented implicitly in the binary image by the interface of foreground and background voxels - using a hierarchical splitting regime. Point locations were optimized using a gradient decent energy function that simultaneously minimized point-to-point distances and entropy. General Procrustes registration was applied at regular intervals during the optimization in order to align shapes with respect to rotation and translation and to normalize with respect to scale. Principal component analysis (PCA) was used to examine the major modes of variation among the different bones and determine the contribution to the largest statistical variation.

Results. The first three PCA modes captured 90% of the cumulative variation in each bone (femur: 90.6%, patella: 90.6%, tibia: 89.1%, fibula: 89.2%). Specifically, primary mode accounted for 55.6%, 69.9%, 50.2%, and 53.9% of variation within intra-bone groups (femur, patella, tibia, and fibula respectfully); secondary mode accounted for 29.0%, 13.6%, 29.3%, and 23.2% of variation (femur, patella, tibia, and fibula respectfully); tertiary mode accounted for 5.9%, 7.0%, 9.6%, and 12.1% of variation (femur, patella, tibia, and fibula respectfully). Computational time and overhead remained reasonable yet scaled with cohort sample size and binary segmentation image dimensions and resolution. Local minima related to surface roughness and binary image aliasing had some effect on correspondence point location optimization but was mitigated with proper geometric and image pre-processing.

Conclusions. SSM was used in to evaluate a cohort of human knee joints reconstructed from in vivo CT imaging. Mean shapes models, deviations, and PCA modes of variation were computed in a reasonable amount of time and provide useful quantitative and qualitative information on knee morphology. Based on these findings we believe that rapid, high-throughput SSM of larger cohorts is achievable and of extensive utility.

References. [1] Li *et al*., Knee. 2014 Dec;21(6):1072-6. [2] Wechter *et al*. Knee Surg Sports Traumatol Arthrosc. 2014 Sep 25. [3] Cates *et al*., Inf Process Med Imaging. 2007;20:333-45. [4] http://www.sci.utah.edu/software/shapeworks.html

Lumped Parameter Model of Flow through the Carotid Bifurcation

Onaizah Onaizah*[1], Tamie L. Poepping[1,2], Mair Zamir[1,3]
Canadian Atherosclerosis Imaging Network
[1]Department of Medical Biophysics, [2]Department of Physics and Astronomy, [3]Department of Applied Mathematics, University of Western Ontario, London, Ontario, Canada

Introduction: Stroke remains one of the leading causes of death in North America and about half of all strokes are a direct result of carotid artery disease (obstructive and sclerotic disorders). Obstructive disorders are the result of plaque development and sclerotic disorders are due to the hardening of the artery. Both of these disorders cause changes in local blood flow patterns that have been widely studied using imaging techniques and computational fluid dynamics. In this study, changes in impedance and in blood supply to the brain were examined. The common carotid artery (CCA) branches up from the aorta and bifurcates into the internal carotid artery (ICA) and external carotid artery (ECA). Since the ICA is a major supply route of blood to the brain, changes in blood supply can be studied by measurements made here.

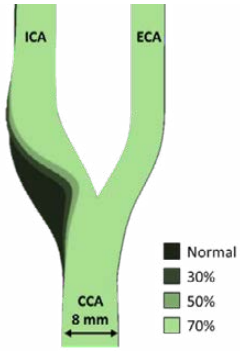

Fig. 1: Family of carotid geometries.

Methods: An experimental in vitro flow loop - incorporating a family of carotid artery phantoms, a programmable positive-displacement pump (CompuFlow 1000, Shelley Medical Imaging) that can generate an idealized pulsatile CCA waveform and downstream compliant and resistive components - is used to mimic realistic blood flow through the carotid artery. Phantoms with varying stenosis severity and compliance are implemented to simulate obstructive and sclerotic disorders. A lumped parameter (LP) model – an electrical analogue to the fluid mechanical system - is designed to match the experimental flow loop. The LP model can be used to quantify the resistance and compliance associated with the different phantoms as well as different segments of the flow loop. Pressure and volumetric flow-rate measurements are made proximal to the carotid bifurcation using a pressure catheter (SPR 350S, Millar Inc.) and in-line electromagnetic flowmeters (EP620/625, Caroline Medical Inc.). The pressure waveform is used as an input to the LP model, its Fourier components are divided by a frequency dependent impedance and recombined to obtain a theoretical flow-rate waveform that is matched to the experimental one by varying the impedance parameters. Mean ICA flow-rates are also calculated from the measured flow-rate waveforms.

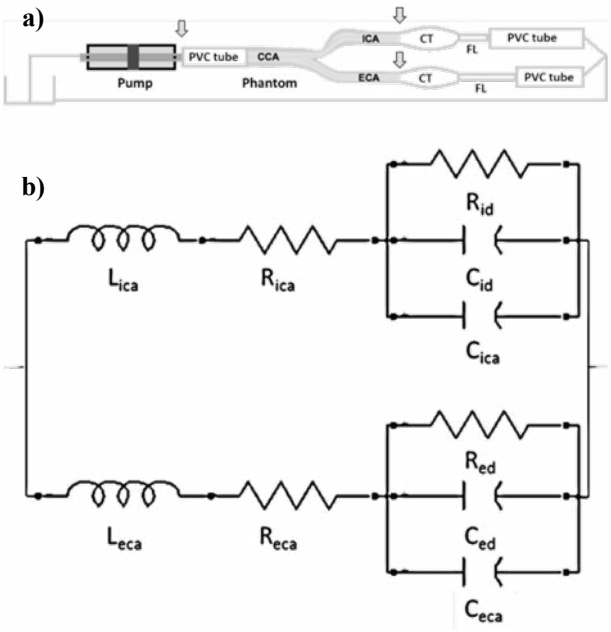

Fig. 2: a) Experimental in vitro carotid artery flow loop and b) matching lumped parameter model.

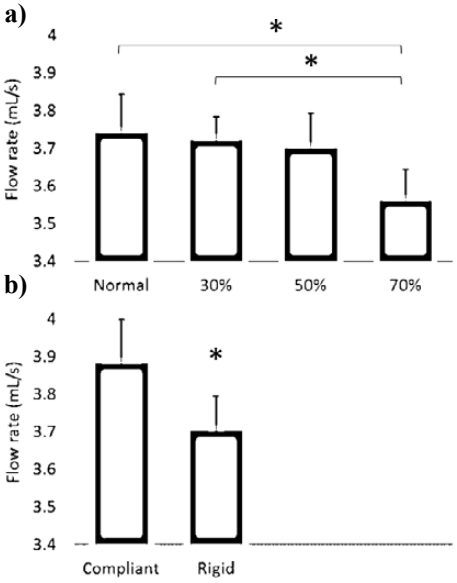

Fig. 3: Changes in flow-rate with a) increasing stenosis and, b) decreasing compliance.

Results: Increasing stenosis severity (defined as per the NASCET criteria) resulted in minimal changes in mean ICA flow-rates until a severe stenosis threshold of 70% was achieved ($p<0.05$). With decreasing compliance (by a factor of 3 – as observed in vivo with aging), changes in mean ICA flow-rates were significant ($p<0.05$). These changes were reflected in the resulting resistance and compliance values from the LP model.

Conclusions: An LP model was successfully designed, validated and used to characterize the impedance of the system. In terms of blood supply to the brain, our observations suggest compliance plays as large of a role as severe stenosis. Often changes in blood supply from one source are compensated for by the other arteries, which is not accounted for in the flow loop or the resulting LP model.

CAROTID ATHEROSCLEROSIS AND CEREBRAL SMALL VESSEL DISEASE.

Ramirez, J., Singh, N., Black, S.E., & Moody, A.R. on behalf of the Canadian Atherosclerosis Imaging Network (CAIN) Project 1

Introduction: Combining *in vivo* imaging of vessel wall disease with imaging of occult end-organ disease, and the acquisition of clinical-pathological end points, CAIN's central goal is to move innovations in clinical evaluation and therapeutic interventions aimed at cardiac and neurological diseases.[1,2] Given the increasing burden of vascular diseases in Canada, the CAIN Project 1 is a unique pan-Canadian brain and carotid imaging project focused on understanding the natural history of carotid disease and effect on cerebrovascular outcomes. The goal of Project 1 is to recruit and serially image approx. n=450 subjects with non-surgical carotid disease (stenosis between 30 and 95%). We describe results from a preliminary analysis performed on a subsample (n=93) of recently acquired baseline data.

Methods: Structural brain MRI (3T) was analyzed using the SABRE-Lesion Explorer pipeline to obtain basic brain tissue measures and small vessel disease volumetric biomarkers: grey matter (GM), white matter (WM), sulcal and ventricular cerebrospinal fluid (CSF), deep white and periventricular subcortical hyperintensities (SH), and lacunes.[3,4] Baseline carotid stenosis was assessed using routine clinical imaging and confirmed with MRI. After head-size correction and normalization of skewed data, brain atrophy and small vessel disease burden was compared between bilateral and unilateral stenosis (>50%) groups controlling for sex and age.

Results: The bilateral stenosis group had significantly greater SH volumes ($p<0.05$), attributed primarily to deep white SH ($p<0.01$) rather than periventricular SH (n.s.). Similarly, the left only stenosis group had significantly more left hemisphere deep white SH volumes than the non-left stenosis group. No significant between group differences were demonstrated for brain tissue atrophy measures. Demographics, medical history and volumetric summaries are shown on Table 1 (below).

Conclusions: These preliminary cross-sectional results suggest a potential relationship between carotid atherosclerosis and end-organ cerebral small vessel disease. In addition to MRI-derived measures for brain volume and distribution of ischemic cerebral white matter disease, future progression analyses will include predictive modelling of end-organ and clinical outcomes using 3D carotid MRI features of vessel disease and other vascular risk factors.

References: [1.] www.canadianimagingnetwork.org; [2.] Tardif et al. (2013); [3.] Dade et al. (2004) [4.] Ramirez et al. (2014)

	Stenosis (bilateral)		
Demographics	**Yes (n=40)**	**No (n=53)**	
Age, years	74.5 (9.0)	74.2 (9.0)	
Sex, n (%) male	24 (60.0)	30 (56.6)	
Medical History			
Hypertension, n (%)	34 (89.5)[a]	48 (92.3)[c]	
Diabetes Mellitus, n (%)	12 (30.8)[b]	12 (22.6)	
Hyperlipidemia, n (%)	37 (92.5)	47 (90.4)[c]	
Coronary Artery Disease, n (%)	14 (35.0)	13 (25.0)[c]	
Mitral Insufficiency, n (%)	2 (5.0)	-	
Peripheral Vascular Disease, n (%)	5 (12.5)	17 (32.7)[c]	
Atrial Fibrillation, n (%)	4 (10.0)	3 (5.7)[c]	
Cardiac Valve Disease, n (%)	2 (5.0)	2 (3.8)	
Hepatic, n (%)	-	2 (3.5)[c]	
Renal, n (%)	4 (10.0)	1 (1.9)	
Amaurosis Fugax, n (%)	3 (7.5)	-	
Hyperhomocysteinemia, n (%)	2 (5.0)	-	
Volumetric Analysis	**Stenosis (bilateral)**		
Whole brain	**Yes (n=40)**	**No (n=53)**	**P**
TIC	1258.7 (113.3)	1225.2 (113.6)	n.s.
BPF%	78.7 (4.7)	78.4 (3.7)	n.s.
Grey matter (GM)	557.3 (44.7)	544.0 (50.0)	n.s.
White matter (WM)	424.0 (62.3)	411.0 (55.6)	n.s.
Ventricular cerebrospinal fluid (vCSF)	37.5 (17.5)	37.2 (16.9)	n.s.
Subcortical hyperintensities (SH)	8.3 (12.4)	4.9 (8.8)	p=0.036
Deep white (dwSH)	1.3 (1.9)	0.5 (0.9)	p=0.007
Periventricular (pvSH)	7.0 (11.3)	4.4 (8.5)	p=0.083
Lacunes, mm^3	270.5 (571.3)	140.0 (299.8)	n.s.

	Stenosis (left only)		
Left hemisphere	**Yes (n=62)**	**No (n=31)**	**P**
Grey matter (GM)	276.4 (21.3)	270.2 (25.5)	n.s.
White matter (WM)	211.3 (31.0)	204.7 (28.0)	n.s.
Ventricular cerebrospinal fluid (vCSF)	19.2 (9.3)	18.7 (9.0)	n.s.
Subcortical hyperintensities (SH)	4.2 (6.3)	2.4 (4.4)	p=0.066
Deep white (dwSH)	0.7 (1.0)	0.3 (0.5)	p=0.007
Periventricular (pvSH)	3.6 (5.7)	2.1 (4.3)	n.s.
Lacunes, mm^3	126.3 (273.1)	59.4 (151.7)	n.s.
	Stenosis (right only)		
Right hemisphere	**Yes (n=53)**	**No (n=40)**	**P**
Grey matter (GM)	280.9 (23.7)	273.8 (24.7)	n.s.
White matter (WM)	212.7 (31.4)	206.3 (27.8)	n.s.
Ventricular cerebrospinal fluid (vCSF)	18.3 (8.8)	18.5 (8.6)	n.s.
Subcortical hyperintensities (SH)	4.1 (6.1)	2.5 (4.5)	n.s.
Deep white (dwSH)	0.6 (0.9)	0.3 (0.4)	n.s.
Periventricular (pvSH)	3.5 (5.7)	2.2 (4.3)	n.s.
Lacunes, mm^3	144.3 (309.9)	80.6 (160.7)	n.s.

Data are presented as Mean (SD) unless otherwise stated. Raw volumes are presented for transparency, statistical analyses were performed on normalized (log transformed), head size corrected data. Volumetrics are reported in cubic centimetres (cc) unless otherwise stated.

[a] Data available for 38/40 subjects
[b] Data available for 39/40 subjects
[c] Data available for 52/53 subjects
Abbreviations: TIC=total intracranial capacity, BPF=brain parenchymal fraction

Site qualification standards for Tc-99m-SPECT perfusion imaging in a multi-centre study of MITNEC (Medical Imaging Trials Network of Canada)

Jennifer M Renaud[1], Manuja Premaratne[1], Marie-Claude Villeneuve[2], Vincent Finnerty[2], Francois Harel[2], Therese Heinonen[2], Jean-Claude Tardif[2], Terrence D Ruddy[1], Robert A deKemp[1]
[1]University of Ottawa Heart Institute, Ottawa ON, Canada
[2]Montreal Heart Institute, Montreal QC, Canada

Introduction: Accuracy of Tc-99m SPECT is being compared to non-nuclear imaging modalities to identify flow-limiting coronary artery disease in patients with symptoms of myocardial ischemia. Phantom qualifying studies established accuracy of SPECT cameras at 6 participating centres for detection of mild ischemia.
Methods: Standardized rest-stress ECG-gated Tc-99m scans were acquired on 21 cameras using a torso phantom with left ventricle (LV) cardiac insert. Stress-induced ischemia was simulated with a 3 cc transmural block in the inferior wall (~3%LV mass). Defects were scored in 17 segments using: 1) automated QGS+QPS ischemic Total Perfusion Deficit (iTPD) and 2) visual interpretation of sum difference scores (SDS). In each vascular territory SDS ≥ 2 and iTPD ≥ 2% were considered positive for ischemia. Visual assessment of inferior-wall ischemia in the right coronary artery (RCA) was the qualifying standard. Sensitivity and specificity were determined for automated scores across all vascular territories. Normal variability of stress – rest LVEF, cavity volume (TID) and perfusion defect (Ischemia) values was assessed as mean ± SD.
Results: All cameras passed the qualifying scan; unblinded visual scoring confirmed expected true-positive ischemia in the RCA and no false-positive ischemia in other regions (Figure 1). Automated scoring sensitivity and specificity were 67% and 81% with 76% accuracy, improving to 90% and 73% with 79% accuracy using an optimized threshold of iTPD ≥ 1.4%. Variability of other diagnostic measures was: LVEF = –0.2 ± 3%, TID = 1.0 ± 0.05, Ischemia = 6 ± 2 %LV across all cameras.
Conclusion: Mild stress-induced ischemia was detected accurately on all SPECT systems using visual interpretation, the primary analysis method for this MITNEC study. Sensitivity of automated scoring was improved slightly using an optimized ischemic threshold. Normal variability in diagnostic measures of LVEF, TID and Ischemia should be considered when interpreting patient scans.

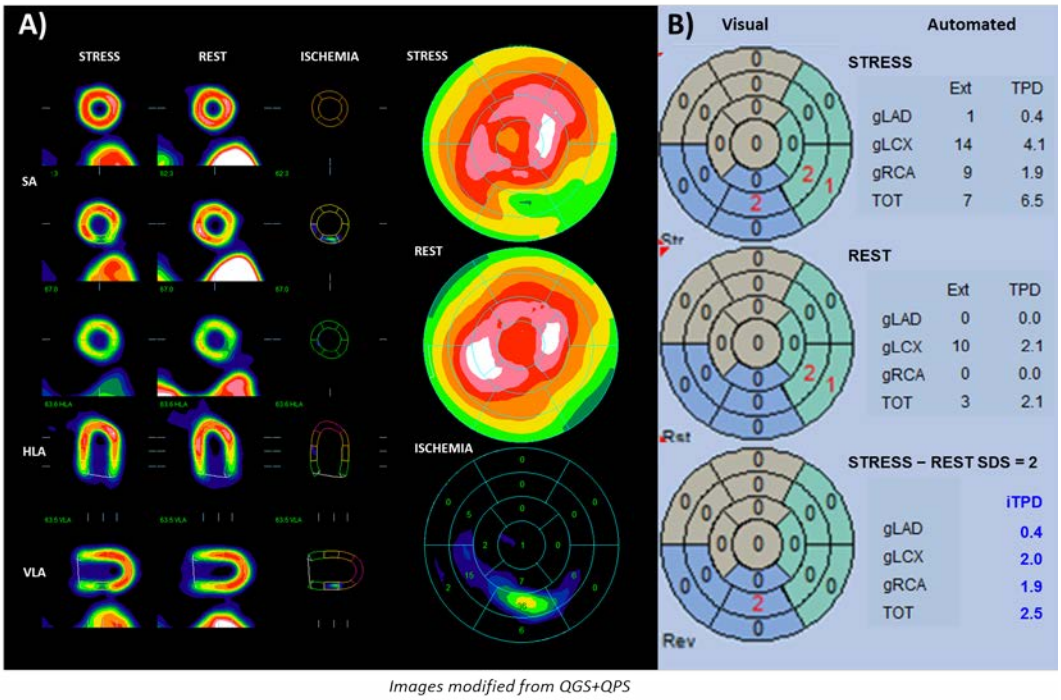

Figure 1. Stress and rest images and polar-maps (QGS+QPS) from cardiac phantom images acquired at one site, demonstrating stress-induced ischemia in the inferior wall (SDS ≥ 2). Rest scan activity distribution is homogeneous throughout the LV myocardium, whereas the stress scan has a 3 cc transmural plastic defect centered in the inferior wall, representing ~3% of the total LV mass.

Visualizing Ipsilateral Activation in Patients with Cervical Myelopathy using Functional Magnetic Resonance Imaging

Kayla Ryan MSc[1,2], Sandy Goncalves MSc[1,2], Izabela Aleksanderek PhD [1,2], Robert Bartha, PhD[1,2], Neil Duggal, MD, MSc, FRCS(C)[3]

[1]Department of Medical Biophysics, The University of Western Ontario, London, Ontario, Canada

[2]Centre for Functional and Metabolic Mapping, Robarts Research Institute, The University of Western Ontario, London, Ontario, Canada

[3]Department of Clinical Neurological Sciences, University Hospital, London Health Sciences Centre, London, Ontario, Canada

Introduction

Cervical spondylotic myelopathy (CSM) is a common neurodegenerative disease caused by compression of the spinal cord, which leads to motor and sensory impairment. Ipsilateral motor activation has been shown to be important in the rehabilitation process in patients recovering from stroke[1]. The purpose of the current study was to contrast the patterns of ipsilateral cortical activation between patients with CSM before and after decompression surgery. We hypothesized that prior to surgery, patients with CSM would have a decreased ipsilateral response to a motor activity in comparison to healthy controls. Secondly, patients with CSM would show a preferential recruitment of ipsilateral supplementary motor area (SMA) and premotor cortex (PMC) after decompression surgery, compared to pre surgery. Lastly, patients with evidence of increased activation of the ipsilateral SMA and PMC would demonstrate greater functionality as measured by clinical scores.

Methods

A 3 Tesla Siemens MRI was used to acquire functional images in 24 patients and 11 healthy individuals. During the functional task, blood oxygenation level dependent (BOLD) images were acquired continuously using an interleaved echo planar imaging pulse sequence (ipat = 2, 80 x 80) acquisition matrix, 45 slices/volume, 3 mm isotropic resolution, repetition time/echo time = 2500/ 30 ms, flip angle = 90º). Participants were instructed to perform finger to thumb opposition ('duck-quack') using a button box with the right hand. To control the frequency at which participants performed the button tapping, visual cues instructed the participant to tap every 3 seconds during a 30 second interval, followed by a 30 second rest period. Healthy individuals performed the task on two different occasions, 6 months apart from each other, while patients participated before surgery and 6 months post decompression surgery. Clinical functional outcomes were assessed before surgery, as well as 6 months after surgery with the modified Japanese Orthopaedic Association scale (mJOA). Correlations between cortical activation and clinical measures were assessed using the Pearson Product Moment Correlation Coefficient.

Results

Healthy controls demonstrated an increase in ipsilateral activation at baseline compared to CSM patients at baseline. In healthy individuals we found a decrease in both the strength and volume of activation in ipsilateral PMC and SMA at 6 months compared to baseline. Additionally, patients with CSM had an increase in the strength and volume of activation of the ipsilateral SMA 6 months after decompression surgery (B) compared to baseline (A) (Figure 1). Cortical activation of ipsilateral SMA and PMC were moderately correlated ($r= 0.60$, $p < 0.01$ and $r=0.41$, $p < 0.05$ respectively) at baseline with the mJOA.

Conclusion

The lack of cortical activation in CSM patients at baseline may indicate that compression of the spinal cord limits information from travelling up and down the spinal cord. However six months after decompression surgery, the integrity of the spinal cord is re-established and information travelling from muscle to brain allows for appropriate recruitment of cortical areas, such as PMC and SMA[2]. The ipsilateral non primary motor areas play an important role in motor learning and may be integral to the rehabilitation of patients with CSM.

References

[1]Calautti *et al.* Stroke. 2003, 34, 1553-1566 [2] Wolpert, *et al.* Trends in Cog. Sci. 2001, 5, 487-494

Ischemia-time dependent absolute CBF threshold for infarction determined in a porcine model of acute stroke

EA Wright*[1,2,3], CD D'Esterre[6], L Morrison[2], N Cockburn[2], M Kovacs[2,3,4], and TY Lee[1,2,3,4,5]
[1]Robarts Research Institute, Western University, London, Ontario, Canada
[2]Lawson Imaging, Lawson Health Research Institute, London, Ontario, Canada
[3]Department of Medical Biophysics, Western University, London, Ontario, Canada
[4]Department of Medical Imaging, Western University, London, Ontario, Canada
[5]Department of Ocology, Western University, London, Ontario, Canada
[6]Department of Radiology, Foothill Medical Center, University of Calgary, Calgary, Alberta, Canada
Research Supervisor: Ting-Yim Lee

Introduction: CT Perfusion (CTP) derived cerebral blood flow (CBF) has been proposed as the optimal parameter for delineating the infarct core prior to reperfusion (1), however lack of ischemia-time dependent CBF thresholds for infarction has been problematic. Previous CTP-CBF threshold derivation studies have been limited by uncertainties caused by infarct expansion, and DWI lesion reversibility (2). This study proposes a porcine model for determining ischemia-time dependent CBF thresholds for infarction using contemporaneous CTP and 18F-fluroethylflumazenil (FFMZ) PET imaging, with the objective of deriving a CBF threshold for infarction after 3h of ischemia.

Methods: Cerebral ischemia was induced in the left hemisphere of 11 pigs by injecting endothelin-1 (ET-1) into the cortex through a burr hole in the skull. CTP scans were completed at baseline, 10, 30 then every 30min until 180min post ET-1 injection. If the CBF map at any time point showed reperfusion of the ischemic tissue then a second dose of ET-1 was administered. F-18 FFMZ was injected 2.5h after the first ET-1 injection and a 25min PET acquisition was started 25min post F-18 FFMZ injection. CBF maps from each CTP imaging time point were co-registered and a median CBF map was produced by taking the median value of each pixel. The median CBF maps, the PET images, average images from the baseline CTP study, and blood volume (BV) maps from the 10min post ET-1 CTP study were co-registered. ROIs were drawn over the cortex on the affected and contralateral side and superimposed onto all maps and images. Infarct pixels were identified on PET images as having signal less than the average minus 2 standard deviations from the contralateral ROI. Average images were used to segment out white matter within the affected side ROI by removing pixels with CT number less than 40HU. Blood vessel pixels were excluded if they had a BV greater than the average plus 2 standard deviations from the affected side ROI or if they had median CBF over $100mL100g^{-1}min^{-1}$. The remaining infarct and non-infarct grey matter ROIs were superimposed onto the median CBF map and pixel values were imported into Matlab for logistic regression and ROC analysis. This process was repeated for each animal that developed infarction.

Results: 6 of the 11 animals developed infarction with an average infarct volume of $1.41\pm0.38cm^3$. The optimal operating points of the ROC curves corresponded to CBF values of 14.2, 11.8, 18.9, 13.4, 13.9, and $19mL100g^{-1}min^{-1}$. The average of these 6 values was calculated to find a 3h ischemia-time CBF threshold for infarction of $15.2\pm1.2mL100g^{-1}min^{-1}$.

Conclusions: The 3h ischemia-time infarction CBF threshold of $15.2mL100g^{-1}min^{-1}$ agrees well with the threshold of $12mL100g^{-1}min^{-1}$ derived in a previous study (3). The ET-1 stroke model has the potential to derive CBF thresholds for infarction at other ischemia times by varying the time between the ET-1 injection and the start of PET imaging.

References: 1) Kamalian et al. Stroke, 2011; 42:1923-1928. 2) Labeyrie et al. Stroke, 2012; 43:2986-2991. 3) Jones et al. J Neurosurg, 1981; 54:773-782.

Principal Component Analysis of the CT Density Histogram to Generate Parametric Response Maps of COPD

N Zha[1], DPI Capaldi[1,2], D Pike[1,2], DG McCormack[3], IA Cunningham[1,2,4,5], G Parraga[1,2,4,5*],
[1]Imaging Research Laboratories, Robarts Research Institute; [2]Department of Medical Biophysics; [3]Department of Medicine; [4]Graduate Program in Biomedical Engineering; [5]Department of Medical Imaging;
Western University, London, Ontario, Canada

Introduction: Pulmonary x-ray computed tomography (CT) is used to characterize emphysema and airways disease in chronic obstructive pulmonary disease (COPD) patients. One such method that utilizes registered inspiratory and expiratory CT image volumes and CT density histogram thresholds was developed in conjunction with parametric response mapping (PRM). There is no definitive consensus regarding the single CT-density-histogram thresholds used to classify the contributions of emphysema and gas trapping, both of which are the backbone of PRM method. Alternatively, principal component analysis of thoracic CT was previously developed to quantifying emphysema using data-driven CT density histogram thresholds. Thus, the objective of this proof of concept demonstration was to develop a way to generate thoracic CT PRM using principal-component-analysis (PCA) of the CT-density-histogram.

Methods: Structural ^{1}H and functional ^{3}He MR images were acquired in 15 COPD subjects (GOLD I: n=5; GOLD II: n=5; GOLD III: n=5) and 5 ex-smokers at inspiration breath-hold. Thoracic CT images were also acquired at full inspiration and full expiration. Images were segmented and an optimized 3D modality-independent-neighbourhood-descriptor algorithm was used to register inspiration-expiration images. A set of principal components were generated for the CT density histograms using the leave-one-out-method. From the resultant principal components, the components with the highest eigenvalues greater than one were summed. Since the values of the principal component curve correlate directly with the variability in the sample, the maximum and minimum points on the curve were used as threshold values for the PCA-adjusted PRM technique.

Results: A significant correlation was determined between conventional and PCA-adjusted PRM with ^{3}He MRI apparent diffusion coefficient ($r = 0.69$, $p < 0.001$ and $r = 0.70$, $p < 0001$, respectively). Conventional and PCA-adjusted PRM was also correlated with CT RA_{950} ($r = 0.99$, $p < 0.0001$ and $r = 0.99$, $p < 0.0001$, respectively). In addition, conventional and PCA-adjusted PRM also correlated with ^{3}He MRI ventilation defect percent, a measurement of both small airways disease ($r = 0.44$, $p < 0.05$ and $r = 0.43$, $p > 0.05$, respectively) and emphysema ($r = 0.53$, $p < 0.05$ and $r = 0.53$, $p < 0.05$, respectively).

Conclusions: Parametric response maps generated using principal component analysis thresholds of the CT density histogram showed significant correlations with CT and ^{3}He MRI measurements of emphysema, but not airways disease.

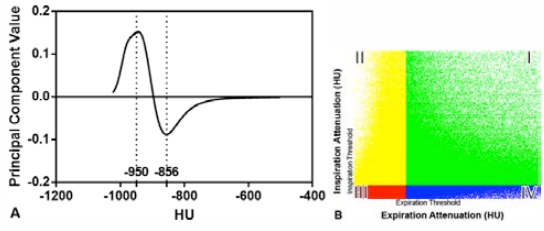

Figure 1. Principal Component Parametric Response Mapping for a single representative subject. **A**) Principal component values for -1024 to -500 HU. **B**) Four categories of voxels generated by setting PRM thresholds on inspiration and expiration CT. Each point denotes a set of expiration and inspiration values for a representative subject.

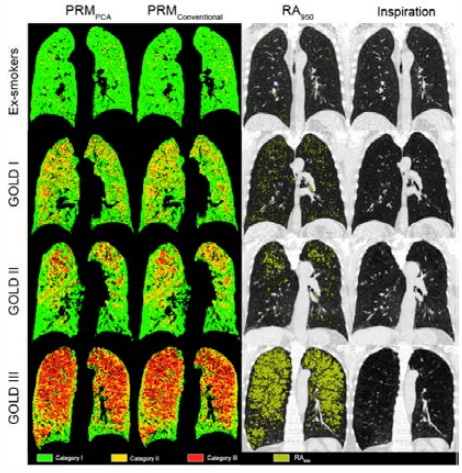

Figure 2. Four representative ex-smokers showing PCA-adjusted, conventional PRM, RA_{950} maps, and inspiration CT

Cancer Imaging Network of Ontario,

Cancer Care Ontario

CINO

Oral Presentation and Poster Abstracts

An open-source design for secure management of medical training data

Authors: Nisrin Abou-Seido*, Tamas Ungi, Andras Lasso, Robert McGraw, Gabor Fichtinger

Affiliation: Queen's University, Kingston, Ontario, Canada

Introduction: Simulation-based medical training and skill assessment software has received steadily growing attention over the past decade. These systems typically compute and record a variety of performance metrics in order to assess trainee skill and competency [1]. Usually, however, training data is manually entered into basic spreadsheets - a time-consuming and error-prone practice. The lack of study data management tools also prevents rolling out simulation-based training methods into institution-wide medical curricula. Throughout our investigations, we have not been able to find open-source tools for managing data associated with simulation-based education programs. Thus, the objective of this project was to develop a practical data management workflow and architecture for simulation-based image-guided intervention training. We will subsequently implement this as a freely available open-source resource for researchers and commercial entities alike.

Methods: We designed the data management workflow to be compatible with the Perk Tutor (www.perktutor.org) free, open-source, medical simulation platform, developed primarily for image-guided intervention training [2] and conveniently available through the 3D Slicer extension manager (www.slicer.org). We consulted medical training experts who routinely use the Perk Tutor for trainee evaluation and documented the current workflow in order to identify its limitations and determine key requirements. A data flow diagram was used to represent the workflow. In the analysis phase of the project, an objective comparison of storage options was conducted by ranking each of the options on a scale of 1 to 5 in terms of how well each one satisfies the given criteria. The options considered were: XML-based storage, CSV files, Moodle (an e-learning platform) and two database tools (SQLite and MySQL). The primary outcome of this project is the design and implementation of a software extension for Perk Tutor simulation training.

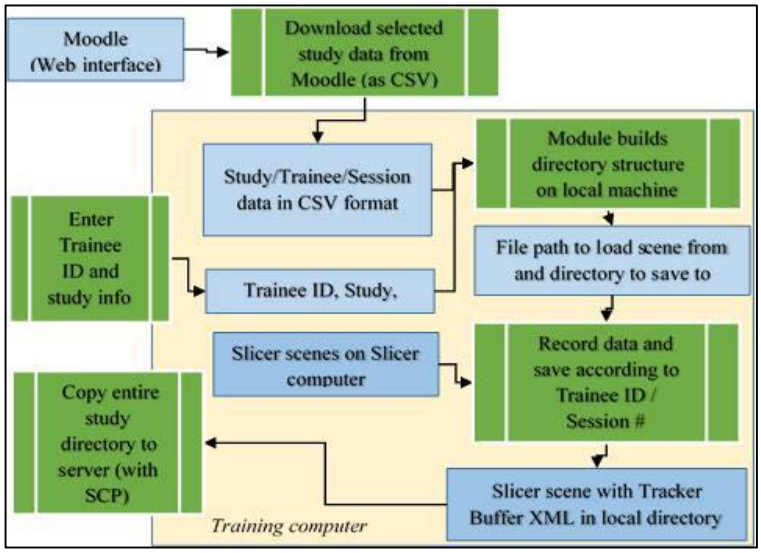

Results: An open-source learning management system, Moodle, (www.moodle.org), used widely by universities for managing courses, was found to be the optimal storage solution based on its built-in authentication system and secure web interface for viewing and editing data. The included figure captures the data flow diagram and outlines in detail the resulting workflow design. The Perk Tutor module downloads and parses trainee data in CSV format from Moodle. Simulation data is recorded and automatically saved to the correct directory based on session metadata. Saved files and metadata are uploaded to a password-protected file server and may later be downloaded for analysis. The result is a software extension to Perk Tutor, for acquiring relevant metadata and ensuring that the simulation results are securely stored and accessible for analysis.

Conclusion: The new workflow design is now allowing us to implement a software module within the open-source Perk Tutor image-guided intervention training platform. Following full testing currently underway, the complete system will be released as open-source through the Perk Tutor distribution site (www.perktutor.org). Future work also includes surveying users to evaluate the usefulness and performance of our data management solution. (This work was funded by Cancer Care Ontario and NSERC Collaborative Health Research Projects.)

References [1] E. R. Petrusa and R. J. Scalese, "A critical review of simulation-based medical education research : 2003 – 2009," *Med. Educ.*, no. 44, pp. 50–63, 2010.

[2] Ungi T, Sargent D, Moult E, Lasso A, Pinter C, McGraw RC, Fichtinger G, "Perk Tutor: an open-source training platform for ultrasound-guided needle insertions", *IEEE Trans Biomed Eng*. 2012 Dec;59(12):3475-81.

Panitumumab modified with metal chelating polymers (MCPs) for dual labeling with ^{111}In and ^{177}Lu as a potential theranostic for pancreatic cancer

Sadaf Aghevlian[1], Yijie Lu[2], Conrad Chan[1], Mitchell A. Winnik [2], Raymond M. Reilly[1, 3, 4]

[1]Department of Pharmaceutical Sciences, University of Toronto; [2]Department of Chemistry, University of Toronto, [3]Department of Medical Imaging, University of Toronto, [4]Toronto General Research Institute, University Health Network, Toronto, ON, Canada

Abstract

Background and Objective: There is a need to develop new therapies for pancreatic cancer (PC) and diagnostic biomarkers for selecting patients for these treatments. Our objective was to develop a novel "theranostic" agent that combines SPECT imaging of PC with radioimmunotherapy (RIT) using the same agent. Panitumumab (PmAb), a fully human anti-EGFR monoclonal antibody was selected to construct the theranostic agents because EGFR is overexpressed on >90% of PC. Panitumumab was modified with novel hydrazino nicotinamide metal chelating polymers (HyNic-MCP) that harbor 9 DOTA chelators per polymer for high specific activity (SA) labeling with ^{111}In and ^{177}Lu and 8 polyethyleneglycol (PEG) pendant groups to impart stealth properties to minimize liver and spleen uptake. ^{111}In is a γ-emitter [$t_{1/2}$ = 2.8 days; $E\gamma_1$=171 keV (90%), $E\gamma_2$=245 keV (94%)] useful for SPECT and also emits subcellular range Auger electrons for RIT of single cells or micrometastatic disease. ^{177}Lu is a β-emitter [Eβ(max)=498 keV (78.6%), Eβ(max)=385 keV (9.1%) and Eβ(max)=176 keV (12.2%)] useful for RIT of millimeter-sized tumours, but also emits low abundence γ-photons [$E\gamma_1$=113 keV (6.4%),$E\gamma_2$=208 keV (11%)] for imaging.

Methods: PmAb was reacted with *N*-succinimidyl-*4*-formylbenzamide (S-4FB) to install functional aldehyde groups for derivatization with HyNic-MCP which forms a UV-measureable bis-arylhydrazone bond with absorbance at 354 nm. The reaction was monitored by UV-VIS spectroscopy and stopped when an average number of two MCPs were conjugated to PmAb. SDS-PAGE analysis was performed to confirm conjugation of PmAb to HyNic-MCP and to assess the purity of the immunoconjugates. PmAb-HyNic-MCP was radiolabeled with $^{111}InCl_3$ or/and $^{177}LuCl_3$ in 0.1M HEPES pH 5.5. For comparison, PmAb was directly modified with N-hdroxysuccinimide-DOTA (NHS-DOTA) at a substitution level of 2 chelators/antibody and labeled with ^{111}In and ^{177}Lu. Labeling efficiency with ^{111}In or ^{177}Lu was measured by ITLC-SG in 0.1 M sodium citrate pH 5.0. EGFR binding affinity of PmAb-HyNic-MCP was assessed in a saturation radioligand binding assay using MDA-MB-468 cells (10^6 receptors/cell).

Results: The purity of PmAb-HyNic-MCP was >95% and SDS-PAGE showed the expected increase in MW for polymer modification of panitumumab. Labeling yields with ^{111}In were 93.1±0.3% and with ^{177}Lu were 93.4±0.1% for PmAb-HyNic-MCP. Labeling yields for PmAb-NHS-DOTA with ^{111}In and ^{177}Lu were 60.3±1.6% and 94.0±0.2%, respectively. PmAb-HyNic-MCP and PmAb-NHS-DOTA conjugates were also labeled simultaneously with ^{111}In and ^{177}Lu in high yield (>94% and >69%). After post-labeling purification, the radiochemical purity was >99%. Polymer immunoconjugates were labeled with ^{111}In and ^{177}Lu to higher SA than PmAb-NHS-DOTA: 5.6±0.2 and 9.5±0.09 MBq/μg, respectively vs. 0.65±0.14 and 3.86±0.09 MBq/μg, respectively. EGFR binding assays revealed a dissociation constant (K_d) of 2.18 ± 0.6 nM and B_{max} of 0.56 ± 0.67 x 10^6 receptors/cell) for ^{177}Lu-PmAb-HyNic-MCP.

Conclusions: PmAb was successfully linked to a novel polymer (HyNic-MCP) that presents 9 DOTA chelators for complexing ^{111}In and/or ^{177}Lu in high labeling yield and at high SA. ^{177}Lu-PmAb-HyNic-MCP exhibited preserved EGFR binding affinity. Studies are planned to evaluate the tumour and normal tissue localization and imaging properties of these dual-labeled theranostic agents.

Research Support: This study was supported by a grant from the Cancer Research Society.

Presenting author contact information: *Sadaf.aghevlian@mail.utoronto.ca*

Cloud computing of anatomical similarity

Jennifer Andrea, Csaba Pinter, Gabor Fichtinger
Laboratory for Percutaneous Surgery, School of Computing, Queen's University, Kingston, ON, Canada

PURPOSE: In image-guided interventions, anatomical structures are typically derived from medical images by means of segmentation. In applications, such as radiation therapy, finding the previously computed treatment plan which shares the most similar anatomy with the current patient helps to determine the optimal treatment plan parameters. This, however, requires a performance-heavy and typically lengthy computation. We propose to use the cloud to find the most similar anatomical structure set, in order to decrease computation time by performing the similarity analyses in parallel.

METHODS: The similarity analysis computation was performed on Amazon Web Services (AWS) Elastic Cloud Compute instances, using 3D Slicer and SlicerRT. 3D Slicer (www.slicer.org) is an open source platform for medical image analysis and visualization and SlicerRT (www.SlicerRT.org) is a radiation therapy research extension for 3D Slicer [1]. The AWS Simple Storage Service and Simple Queue Service were also used, for storage of the previously created studies and messaging between the local computer and the instances, respectively. The anatomical data used in this work were CT scans and structure sets from radiation treatment studies. To find the study in the database most similar to the study under comparison, the CT from the comparison study was registered to the CTs from each study in the database, and the resulting transformation was applied to the structure set from the comparison study. The Dice coefficient was computed for pairs of matching contoured structures from each study.

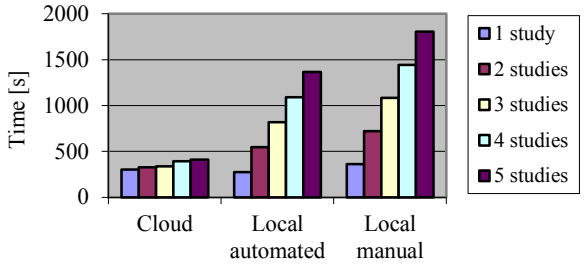

Figure 1. Length of time for treatment plan selection on different setup configurations. Local automated is the local computer using the automated workflow, and local manual is the local computer using the manual workflow.

RESULTS AND DISCUSSION: The system was tested on five simulated datasets. A patient CT with pre-contoured structure set was transformed by random known parameters, to create five different but similar patient studies. Each study was presented to the system as the study under comparison and in each case the system returned the correct result. The computation time was measured for three different setup configurations, for one to five studies (Fig. 1). The different setups were using the cloud, using the local computer with an automated workflow for computing the similarity, and using the local computer and manually performing the comparison using the SlicerRT graphical user interface. The cloud had the smallest computation time of the three setup configurations for two or more studies to be compared to. The computation time for the cloud grew by 27.5 seconds on average, which would produce an estimated computation time of less than 10 minutes for 10 comparison studies.

CONCLUSION: This system presents a new use of the cloud with a system for finding the structure set with the greatest anatomical similarity to a given set. The decrease in computation time was significant when compared to similarity computations performed solely on the local computer. For this proof-of-concept work, contour comparison was used to determine similarity, however as contouring is a time-consuming process, in the future raw anatomical data in the image intensity domain will be compared. The new study, in all likelihood, will show that using the cloud allows for even much greater reduction rates in computation times.

ACKNOWLEDGEMENTS: This work was in part funded by Cancer Care Ontario through Applied Cancer Research Unit and Research Chair in Cancer Imaging grants.

Consortium member / research supervisor: Gabor Fichtinger (CINO)

REFERENCES: [1] C. Pinter, A. Lasso, A. Wang, D. Jaffray, and G. Fichtinger, "SlicerRT: Radiation therapy research toolkit for 3D Slicer", Med. Phys. 39(10), 6332/7 (2012).

Current sensing for navigated electrosurgery

Kaci Carter[1,2], Andras Lasso[1], Tamas Ungi[1], Evelyn Morin[2], Gabor Fichtinger[1]

[1] Laboratory for Percutaneous Surgery, School of Computing, Queen's University, Kingston, ON, Canada

[2]Department of Electrical and Computer Engineering, Queen's University, Kingston, ON, Canada

Introduction: Tracked power-tools are routinely used in computer-assisted intervention and surgical systems. In order to properly perform temporal and spatial monitoring of the tracked tool with the navigation system, it is important to know when the tool, such as an electrosurgical cauterizer, is being activated during surgery. The objective of this work is to implement a general purpose current sensor that can be augmented to tracked surgical devices in order to inform the surgeon and the navigation system when the tool is activated.

Methods: Since clinically applied power tools are approved by FDA and/or Canada Health, an isolated sensing and feedback system is required that does not interfere with the tool in any manner. The current sensing system must be compatible with electromagnetic tracking and electrically isolated from the surgical device. A Hall Effect current sensor (Allegro ACS712) is integrated with the electrosurgical device in an isolated manner (Figure 1). The sensor measures the magnetic field produced by the cable that supplies the current to the electrosurgical device. The output voltage produced by the sensor is fed into an analog input pin of the microcontroller (Arduino Uno). The microcontroller is programmed to turn on a LED when a specific voltage is received. This LED provides visual confirmation for the surgeons that current is flowing into the electrosurgical device. We integrate the sensor with the SlicerIGT open source (www.SlicerIGT.org) surgical navigation system, in which tool tracking functions are implemented using the PLUS toolkit (www.plustoolkit.org) [1]. The microcontroller communicates the voltage information through a serial USB connection via the PLUS toolkit to SlicerIGT. The current sensor is first being applied in EM-navigated breast-conserving surgery [2] to sense the current of the electrosurgery cauterizer. The systems schematic is shown in Figure 2.The sensor and microcontroller are placed far (approximately 2 m) away from the patient in order to prevent a galvanic connection to the patient, as well as to minimize the effect of the EM tracking on the sensor.

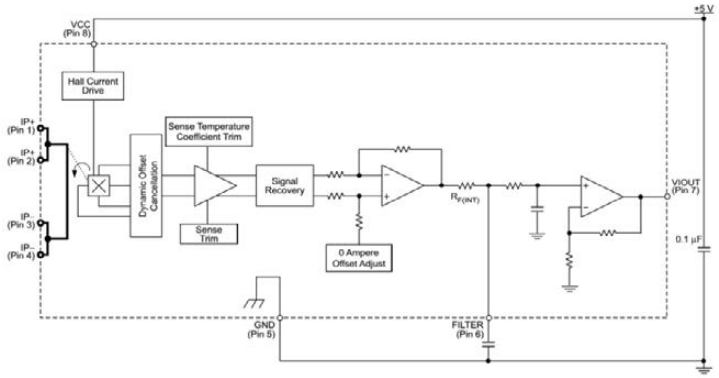

Figure 1: Functional block diagram of Allegro ACS712 Hall Effect current sensor

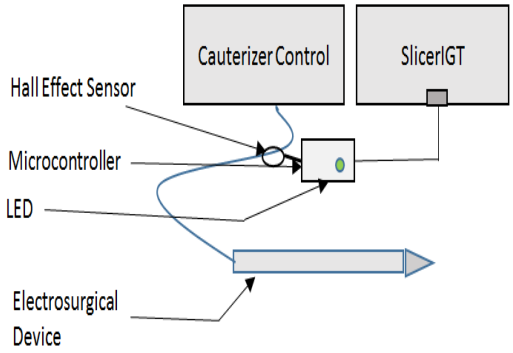

Figure 2: Schematics of the current sensing feedback system

Conclusions: The current sensing device has been designed and is currently being implemented and tested within the context of EM-navigated breast-conserving surgery. The device represents no risk to the patient and thus it can be promptly translated for clinical evaluation within our ongoing patient trial.

Acknowledgments: This work was funded by Cancer Care Ontario through the Applied Cancer Research Unit and the Research Chair in Cancer Imaging grants. Kaci Carter was funded by the National Sciences and Engineering Research Council CGSM.

References: [1] Lasso A, Heffter T, Rankin A, Pinter C, Ungi T, Fichtinger G. "PLUS: open-source toolkit for ultrasound-guided intervention systems." IEEE Trans Biomed Eng. 2014 Oct;61(10):2527-37.

[2] G Gauvin et al., "Real-Time Electromagnetic Navigation for Breast Tumor Resection: Proof of Concept," in The 7th Hamlyn Symposium on Medical Robotics, London, UK, July 13-14 2014, Guang-Zhong Yang and Ara Darzi (Eds.) pp. 39-40, 2014.

Consortium Member: Gabor Fichtinger (CINO)

Visual feedback mounted on surgical tool

Kaci Carter[1,2], Andras Lasso[1], Tamas Ungi[1], Evelyn Morin[2], Gabor Fichtinger[1]
[1] Laboratory for Percutaneous Surgery, School of Computing, Queen's University, Kingston, ON, Canada
[2]Department of Electrical and Computer Engineering, Queen's University, Kingston, ON, Canada

Background: In the operating room, feedback, such as instrument positioning guidance of surgical navigation systems is typically displayed on an external computer monitor (Figure 1). The surgeon's attention is usually focused on the tool and the surgical site, so the display is typically out of the direct line of sight. The objective of this work is to develop a simple visual feedback mechanism mounted on the surgical tool and thus always within direct line of sight, in order to alert the surgeon when it is necessary to look at the monitor for detailed navigation information.

Figure 1: OR layout in EM tracked electrosurgery [1].

Methods: The tool-mounted visual feedback mechanism was designed to be light-weight and compatible with electromagnetic (EM) tracking. Figure 2 shows the schematic of the proposed solution. The feedback device consists of a computer-controlled light source (RGB LED), which is programmed to flash and change color to get the surgeons attention. A variety of colors and flashing frequencies are explored to determine the most effective pattern. The light source is located 1-2m away from the patient and an optical fiber cable is used to transmit the light from this location to the tracked surgical device in order to reduce EM noise and avoid galvanic connection to the patient. A microcontroller (Arduino Uno, http://arduino.cc) communicates with the computer interface through a serial USB connection. We integrate the proposed visual feedback device in the SlicerIGT open source (www.SlicerIGT.org) surgical navigation system, in which tool tracking functions are implemented using the PLUS toolkit (www.plustoolkit.org) [1]. Our visual feedback device also uses the PLUS toolkit to communicate information from SlicerIGT to the microcontroller. The tool-mounted visual feedback device is first being applied in EM-navigated breast-conserving surgery [2] (Figure 1). The optical fiber bundle shares a 3D-printed mounting clamp with the EM tracking sensor, mounted on the distal end of the electrosurgery cauterizer and is placed inside a sterile transparent plastic bag. By varying the colour and flashing frequency of the LED, the surgeon is informed when surgical margins are changing and a severe warning is produced if the resection margin is violated.

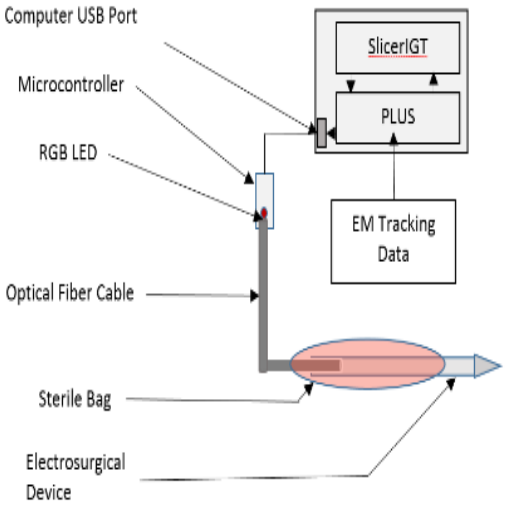

Figure 2: Schematic of Visual Feedback System

Conclusions: The tool-mounted visual feedback device has been designed and is currently being implemented and tested within the context of EM-navigated breast-conserving surgery. The device represents no risk to the patient and it can be promptly translated for clinical evaluation within our ongoing patient trial.

Acknowledgments: This work was funded by Cancer Care Ontario through the Applied Cancer Research Unit and the Research Chair in Cancer Imaging grants. Kaci Carter was funded by the National Sciences and Engineering Research Council CGSM.

References: [1] Lasso A, Heffter T, Rankin A, Pinter C, Ungi T, Fichtinger G. "PLUS: open-source toolkit for ultrasound-guided intervention systems." IEEE Trans Biomed Eng. 2014 Oct;61(10):2527-37.

[2] G Gauvin et al., "Real-Time Electromagnetic Navigation for Breast Tumor Resection: Proof of Concept," in The 7th Hamlyn Symposium on Medical Robotics, London, UK, July 13-14 2014, Guang-Zhong Yang and Ara Darzi (Eds.) pp. 39-40, 2014.

Consortium Member: Gabor Fichtinger (CINO)

Alternative contrast mechanisms in optical coherence tomography: speckle temporal synchronization effects

Valentin Demidov*, I. Alex Vitkin
Ontario Institute for Cancer Research, University of Toronto, Canada

Introduction. Optical coherence tomography (OCT) [1] is an emerging non-invasive imaging modality for visualizing subsurface tissue microstructure *in-vivo* at resolutions approaching histology and blood flow details at the microcirculation level. The obtained OCT images exhibit grainy patterns called speckles [2] which are produced by interference of coherent waves scattered by object features that are smaller than the OCT spatial resolution. While adding to noise, speckle characteristics are also known to contain useful information related to tissue type, cellularity, response to therapy and other quantities of interest that are not directly visible nor spatially resolved on the images. In the current report, we consider an alternative OCT contrast mechanism based on the analysis of speckle temporal synchronization. Synchronization theory has been widely applied to the analysis of various biological signals. The classical concept of synchronization considers the interactive behaviour of two or more coupled oscillators entraining their time scales in terms of their amplitude, frequency or phase [3].

Methods. In this work we suggest a quantitative evaluation of degree of speckle synchronization based on information theory approach [4]. In order to analyse speckle temporal and spatial patterns in OCT images of living tissue, we quantified their information content through the relationship of conditional $H(x_2|x_1)$ and unconditional $H(x_2)$ entropies. These characteristics describe the processes and their interdependence in terms of speckle intensities. Normalizing their difference to unconditional entropy $\mu = [H(x_2) - H(x_2|x_1)]/H(x_2)$, the function μ characterizes the index of temporal synchronization between speckle pixels intensities. When OCT image speckle pixels x_1 and x_2 intensities are connected through a deterministic function, the synchronization is equal to unity. In the case when x_1 and x_2 do not influence each other, their changes in time are unsynchronized (zero synchronization). In other cases the correlation between states of x_1 and x_2 has two components, random and deterministic. In terms of in-vivo OCT imaging contrast, variation from 0 to 1 provides additional differential contrast depending on the mutual image speckle behaviour of different tissues.

Results. Speckle temporal synchronization characterictic μ is able to differentiate between skin, tumor and vessel regions as seen in the Figure 1 (for further details refer to Figure 1 and its caption).

Conclusions. We propose an alternative OCT contrast mechanism based on speckle temporal synchronization. We show that the changes in speckle intensities with time carry information that differentiates tissue types and provide a source of additional contrast for *in-vivo* tissue imaging. The developed technique is initially demonstrated in 1D *in-vivo* study, using the tumour model of mammary carcinoma grown within the mouse dorsal skin-fold window chamber. Generation of 2D and 3D parametric maps is currently under development.

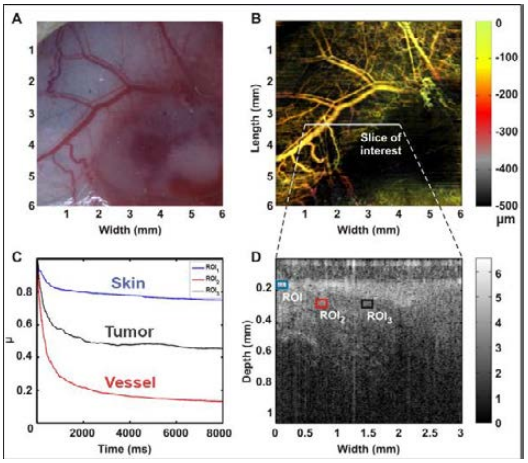

Figure 1. Results obtained *in-vivo* for the mouse dorsal window chamber (WC) model. (A) Photo of the WC; (B) Corresponding en-face depth-encoded view of a 6mm x 6mm (lateral) 0-0.5 mm (depth) region of the detected mouse microvasculature by speckle-variance method; (C) Speckle temporal synchronization for three regions of interest (ROIs) labeled in (D); (D) Cross-section labeled in (B) as a "slice of interest" with three ROIs chosen in regions of skin (ROI_1), vessel (ROI_2) and tumour tissue (ROI_3). A set of 1000 of OCT images of this cross-section was obtained within 8 seconds for speckle temporal synchronization analysis.

References.

[1] Fujimoto JG, Pitris C, Boppart SA, Brezinski ME. Optical coherence tomography: an emerging technology for biomedical imaging and optical biopsy. Neoplasia 2000;2:9–25.

[2] Schmitt JM, Xiang S, and Yung KM. Speckle in optical coherence tomography. J Biomed Opt 1999;4:95-105.

[3] Pikovsky A, Rosenblum M, Kurths J. Synchronization: a universal concept in non-linear sciences. Cambridge Nonlinear Science Series. Cambridge University Press 2003.

[4] Shabunin A, Demidov V, Astakhov V, Anishchenko V. Information theoretic approach to quantify complete and phase synchronization of chaos. Phys Rev E 2002;65:215-9

Speckle formation in Optical Coherence Tomography (OCT): computational study and experiment

Valentin Demidov,*[1] Alexander Doronin,[2] Igor Meglinski[2] and I. Alex Vitkin[1]
[1]Ontario Institute for Cancer Research, University of Toronto, Toronto, Canada
[2]Department of Physics, University of Otago, Dunedin, New Zealand

Introduction. OCT is well established imaging modality capable of acquiring cross-sectional images of turbid media, such as biological tissues, utilizing back scattered low coherent light [1]. The obtained OCT images include repetitive patterns known as speckles. Ultimate understanding of OCT speckle patterns formation, as well as interpretation and quantitative analysis of OCT images requires a development of robust theoretical/computational model describing propagation of low-coherent light in turbid tissue-like scattering media. Due to complexity of structure of many biological tissues the analytical solutions cannot be applied. Therefore, numerical techniques, such as Monte Carlo (MC) method are extensively used for imitation of light propagation in tissue-like turbid media [2]. The early MC models have been applied successfully only to imitate time-domain OCT (e.g. [3]). Multiple scattering is a major limiting factor to the OCT method, and should thus be accounted for in a comprehensive model. In the swept-source OCT (SS-OCT), in spite of quite intense development and implementation of MC modeling, none of the previous models took into account interference of scattering waves that plays a critical role in the formation of SS-OCT speckles. In the current report we propose a new MC based model that solves this problem.

Methods. The developed model is based on the unified MC code for the needs of biomedical optics and biophotonics [2] and takes into account coherence of light, polarization, reflection/refraction at the medium boundaries, mutual interference of the back-scattering waves and their interference with the reference waves. Utilizing the developed model, we consider the mechanism of speckle patterns formation and imitate SS-OCT signals. Two phantom experiments were performed to test this model. Phantoms were established by a) placing two 180 μm thick glass coverslips over one another, b) embedding a scattering medium (mixture of 1% of 0.21 μm diameter polystyrene microspheres (RI = 1.3207 with de-ionized water) between two 180 μm thick glass coverslips. A swept-source OCT system briefly described below was used for data acquisition. A 36 kHz short cavity laser source with a polygon-based tunable filter and wavelength centred at 1310 nm had a sweeping range of 112 nm. The axial resolution (in air) of the system was 10 microns.

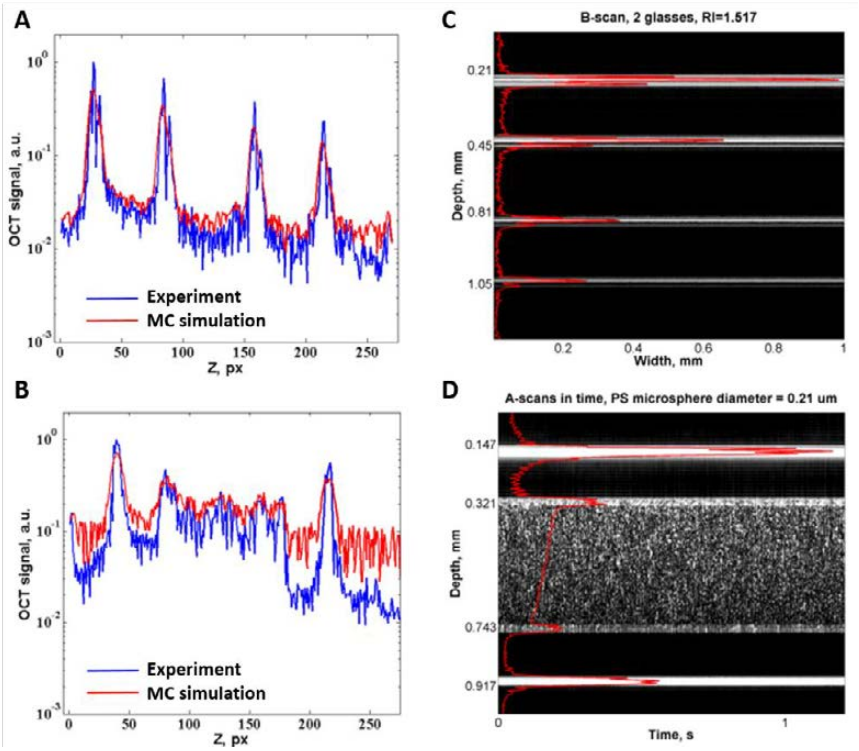

Figure 1. Results of MC simulation compared with experiment for a scattering-free (top row) and turbid (bottom row) medium.

Conclusions. As can be seen in the Figs. 1(A), 1(B) there is a solid agreement between MC-simulated and experimental SS-OCT signals which shows that this newly developed model may prove useful for simulation of the SS-OCT signals and analysis of origins of SS-OCT speckle patterns formation. The developed model is initially demonstrated in 1D and phantom studies. Further work is ongoing in generation of 2D and 3D MC simulated SS-OCT images and their quantitative comparison with the experiment.

References.

[1] Fujimoto J., et al. Neoplasia 2000; 2:9–25.
[2] Doronin A., et al. J Biomed Opt 2014; 19:025005.
[3] Kirillin M., et al. Opt Express 2010; 18:21714–21724.

Positron Detector for Intra-Operative Surgical Margin Evaluation in Breast Cancer

John Dillon[1], Amir Khojaste[1], Alla Reznik[2], Ananth Ravi[1]
Cancer Imaging Network of Ontario, Cancer Care Ontario

1) Sunnybrook Odette Cancer Centre, Toronto, ON, Canada
2) Thunder Bay Regional Research Institute, Thunder Bay, ON, Canada

Introduction

Seventy percent of early stage breast cancer patients are eligible for breast conserving surgery (BCS)[1, 2]. BCS involves excising the gross tumor with a margin of normal tissue surrounding it. Unfortunately, between 15-40% of all BCS procedures result in an inadequate tumor margin upon pathological examination indicating that there is residual disease in the surgical cavity[3-5]. Surgeons typically locate gross disease through palpation and may have pre-operative diagnostic images for guidance. Dense breasts make palpation difficult, and the location and extent of tumors must be estimated entirely by gestalt and pre-operative imaging. High-resolution ultrasound, NIRF, and electromagnetic tissue characterization have all been evaluated as guidance tools. However, these approaches are limited in their ability to robustly identify disease.

A single pixel positron detector was constructed and evaluated as an alternative method to determine the status of the excision margins. This study will evaluate the feasibility of analyzing excised tissue margin involvement intra-operatively, by creating a novel single pixel positron-detector incorporating a second generation silicon photomultiplier (SPM). The SPM has a photon detection efficiency (PDE) almost twice that of conventional photo multiplier tubes (PMT). The work evaluated the 511 keV gamma rejection of the device in order to ensure low background noise, and create a 3D sensitivity map to compare our device to conventional designs.

Methods

The novel device is composed of a CaF_2:Eu scintillation crystal coupled to a SPM with a 9 mm^2 sensitive area. The output is shaped and amplified before being recorded by a multi-channel analyzer. The device was evaluated in a water tank with a 1.00 x 1.00 mm point source of 2-deoxy-2-(^{18}F)fluoro-D-glucose (FDG) that was translated laterally and at depth. This allowed us to create a 3D sensitivity map, point spread functions, and determine the full-width half-maximum of the device.

Results

The device displayed significant gamma rejection, with the 511 keV annihilation photons accounting for 0.3% of the total acquisition. The sensitivity of the prototype has surpassed similar commercial positron detecting devices.

Conclusions

The novel positron detector has an improved sensitivity over conventional devices. The impact of the 511 keV has been minimized resulting in promising outcomes for the translation of this technology to an intra-operative device. Further work will focus on robustly evaluating the design and integration of the detector system.

1) Canadian Cancer Statistics 2011, Statistics Canada; Public Health Agency of Canada; Canadian Cancer Society
2) Tyldesley, S., F *et al.,* "The Appropriate Rate of Breast Conserving Surgery: an Evidence-based Estimate." *Clinical Oncology* 15.3 (2003): 144-55..
3) D. Aziz *et al.*, "The Role of Re-excision for Positive Margins in Optimizing Local Disease Control After Breast Conserving Surgery for Cancer," Breast J. 12 (4), 331-337 (2006).
4) FJ Fleming *et al.*, "Intraoperative margin assessment and re-excision rate in breast conserving surgery," European Journal of Surgical Oncology 30 (3), 233-237 (2004).
5) R. G. Pleijhuis, "Obtaining Adequate Surgical Margins in Breast-Conserving Therapy for Patients with Early-Stage Breast Cancer: Current Modalities and Future Directions," Annals of Surgical Oncology 16 (10), 2717 (2009).
6) Pappo, Itzhak, *et al.,* "Diagnostic Performance of a Novel Device for Real-Time Margin Assessment in Lumpectomy Specimens." Journal of Surgical Research 160.2 (2009): 277-81.

Dosimetric Analysis of Respiratory-Induced Cardiac Intrafraction Motion in Left-sided Breast Cancer Radiotherapy

O El-Sherif*[1,3], E Yu[2,4], S Gaede[1,2,3,4]
Department of Medical Biophysics[1] and Oncology[2], Western University, London Canada, Department of Physics[3] and Radiation Oncology[4], London Regional Cancer Program, London, Ontario Canada

Introduction: Long-term cardiac side effects in left-sided breast cancer patients (BREL) after post-operative radiotherapy has become one of the most debated issues in radiation oncology. Through breathing-adapted radiotherapy, the volume of the heart exposed to radiation can be significantly reduced by delivering the radiation only at the end of inspiration phase of the respiratory cycle. This is referred to as inspiration gating (IG).

The purpose of this study was to quantify the potential reduction in cardiac exposure during IG compared to conventional BREL radiotherapy, and to assess the dosimetric impact of cardiac motion due to natural breathing.

Methods: 24 BREL patients treated with tangential parallel opposed photon beams were included in this study. All patients received a standard fast helical planning computed tomography scan (FH-CT) as well as a 4-dimensional CT scan (4D-CT). Treatment plans were created on the FH-CT, using a clinical treatment planning system. The original treatment plan was then superimposed onto the end of inspiration CT and all 10 phases of the 4D-CT to quantify the dosimetric impact of respiratory motion and IG through 4D dose accumulation.

Results: Through IG, the mean dose to the heart, left ventricle, and left anterior descending artery (LAD) can be reduced in comparison to the clinical standard BREL treatment by as much as 8.39%, 10.11%, and 13.71% respectively ($p < 0.05$).

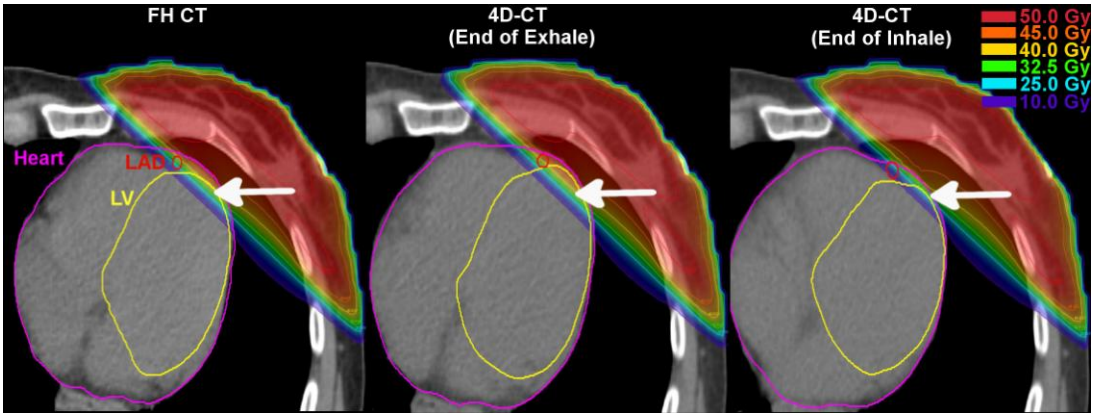

Fig 1. A comparison of the fast helical CT (FH-CT), end of exhalation, and end of inspiration radiation dose distributions for a representative patient. The heart, left ventricle (LV), and left anterior descending artery (LAD) are outlined in magenta, yellow, and red respectively. Differences in the estimated dose deposition to the heart, LV, and LAD is outlined by the white arrows.

Conclusion: Failure to account for respiratory motion can lead to under- or overestimation in the calculated dose volume histogram (DVH) for the heart and sub-structures within it. IG can reduce cardiac exposure especially to the LAD during BREL radiotherapy.

Response Monitoring Using Texton-Based Approach in Locally Advanced Breast Cancer

Mehrdad J. Gangeh[1,2], Hadi Tadayyon[1,2], Lakshmanan Sannachi[1,2], Ali Sadeghi-Naini[1,2], Maureen Trudeau[3], Sonal Gandhi[3], and Gregory J. Czarnota[1,2,4]

(1) Department of Medical Biophysics, University of Toronto, Toronto, Canada
(2) Physical Sciences, Sunnybrook Research Institute, Sunnybrook Health Sciences Centre, Toronto, Canada
(3) Division of Medical and Haematologic Oncology, Department of Medicine, Sunnybrook Health Sciences Centre, Toronto, Canada
(4) Department of Radiation Oncology, Sunnybrook Health Sciences Centre, Toronto, Canada

*Background and Motivation***:** Assessing the efficacy of cancer treatments in preclinical and clinical treatments is presently limited; results may not be available to the clinician for typically months. This can lead to ineffective cancer treatments continued needlessly as no faster feedback mechanisms have yet reached broad biomedical adoption. Quantitative ultrasound (QUS) methods provide a promising alternative framework that can non-invasively, inexpensively and quickly assess tumour response to cancer treatments using standard ultrasound equipment. Due to heterogeneous responses developed in tumours as a result of treatment, texture methods can potentially characterize these responses and assist to quantify the assessment of cancer response monitoring. In this research, texton-based methods as the state-of-the-art technique for texture analysis was used to model locally advanced breast cancer (LABC) responses to chemotherapy.

Methods: Fifty six patients with locally advanced breast cancer (LABC) who received neoadjuvant chemotherapy treatments were imaged before and at 4 times during treatment, i.e., weeks 1, 4, 8 and pre-operatively. Data were acquired using a Sonix RP ultrasound machine at a central frequency of ~7 MHz. Mid-band fit and 0-MHz intercept parametric maps were computed by deploying quantitative ultrasound spectroscopy techniques. The patients were grouped into good and poorly responding based on their ultimate clinical and pathological response to treatment. Codebooks of textons were constructed for each patient by extracting 500 random patches of 11×11 segments from parametric maps and by using *k*-means methods with the *k* value of 30. Subsequently, a histogram of textons was computed for each parametric map using the associated codebook as the model/feature set to represent the pre- and during-treatment images for each patient at a specific time frame after treatment. The distance between these features for each subject was used as a criterion of the effectiveness of the treatment, which was ultimately submitted to a naïve Bayes classifier to classify the patients to responding or non-responding in a leave-one-subject-out manner.

Results: The classification of patients with LABC to responding and non-responding using the proposed texton-based system achieved an accuracy of 83.85 ± 10.06% and 85.00 ± 6.79%, area under curve (AUC) of 80.30 and 83.14, sensitivity of 86.92% and 86.36%, and specificity of 80.77% and 83.64% after 4 and 8 weeks of treatment, respectively.

Conclusion: In this study, texture methods based on texton-based approach was proposed to quantify the assessment of LABC response to neoadjuvant chemotherapy. The proposed system achieves a promising accuracy and sensitivity 4 weeks after treatment initiation. This would permit clinicians to receive feedback and switch to alternate treatments far earlier, in a step towards the goals of *personalized medicine*.

Three-Dimensional Pulmonary ^{1}H MRI Multi-Region Segmentation Using Convex Optimization

F Guo[1,2], S Svenningsen[1,3], A Fenster[1-3] and G Parraga[1-3]
[1]Imaging Research Laboratories, Robarts Research Institute; [2]Graduate Program in Biomedical Engineering;
[3]Department of Medical Biophysics, The University of Western Ontario, London, CANADA

Purpose: Proton (^{1}H) MRI can be optimized for comprehensive and quantitative evaluation of the respiratory system in chronic pulmonary diseases including chronic obstructive pulmonary disease (COPD), asthma and cystic fibrosis. For example, conventional ^{1}H acquisition using Fourier Decomposition techniques and in combination with oxygen-enhanced or inhaled polarized gases MRI provides sensitive and regional functional information of the lungs such as ventilation and perfusion, potentially enabling a better understanding of the biomechanical and physiological abnormalities in subjects with respiratory diseases. To quantitatively evaluate regional physiological lung function, it is necessary to accurately segment the lung cavity. However, pulmonary ^{1}H MRI segmentation is particularly challenging because of low proton density, magnetic susceptibility and motion artifacts[1]. Therefore, the objective of this study was to develop a high performance algorithm for pulmonary ^{1}H MRI lung cavity segmentation.

Methods: Ten COPD subjects (GOLD U, I–IV) were enrolled and provided written informed consent to a study protocol approved by Health Canada. MRI was performed using a whole body 3.0T Discovery MR750 system (General Electric Health Care, Milwaukee, Wisconsin, USA). Subjects were instructed to inhale 1.0L medical grade nitrogen (N_2) from functional residual capacity and coronal ^{1}H MRI was acquired using a whole-body radiofrequency coil and a ^{1}H fast spoiled gradient-recalled echo (FGRE) sequence[2] (16s total acquisition time; repletion time/echo time/flip angle = 4.3ms/1.2ms/20°; field-of-view = 40cm x 40cm; matrix = 256 x 256; number of slices = 14 – 17; slice thickness = 15mm). We proposed a convex optimization based approach[3] to simultaneously segment the left and the right lungs from pulmonary ^{1}H MRI in three-dimensional (3D). We formulated the original multi-region segmentation problem as the *Potts model*[4], and studied the resultant combinatorial optimization problem by means of convex optimization, which provides global optimum to the original binary labelling problem. We further proposed a *continuous max-flow* model and proved its duality to the convex relaxed formulation, for which we derived an efficient *continuous max-flow algorithm* based on the augmented Lagrangian theory[5]. The proposed algorithm explores dual optimization of the original challenging optimization problem and was implemented on a parallel computation platform to achieve high performance in numerics. A single observer (F.G) performed algorithm segmentation five times on five different days separated by at least 12 hours. The performance of the proposed approach was evaluated using Dice Similarity Coefficient (DSC), root-mean-squared-error (RMSE) and absolute percentage volume error ($|\delta V_p|$) as region-, distance- and volume-based similarity metrics[6] by comparing algorithm results to manual outcomes performed by a single expert observer (S.S). The precision of the proposed approach was evaluated by calculating the Coefficient of Variation (CoV) and Intra-class Correlation of Coefficient (ICC) in terms of DSC for each lung as well as for the whole lung. The mean run time was recorded to evaluate computational efficiency of our proposed algorithm.

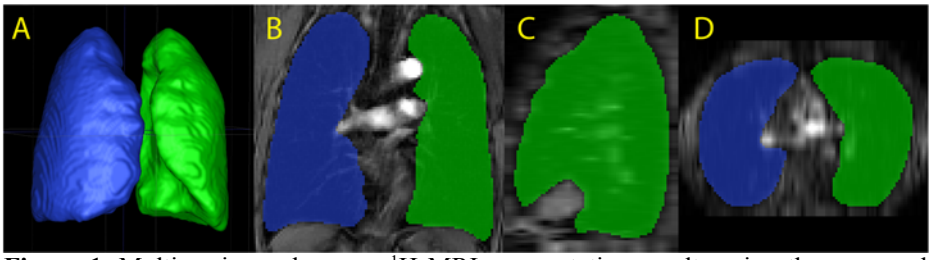

Figure 1. Multi-region pulmonary ^{1}H MRI segmentation results using the proposed algorithm for a representative subject. The right (blue) and left (green) lung have been rendered and are shown in 3D (A), and 2D (B) coronal, (C) sagittal and (D) axial plane.

Results: Figure 1 shows the ^{1}H MRI segmentation result for a representative COPD subject. As shown in Table 1, the proposed algorithm yielded a mean DSC of 89.5 ± 8.9%, 90.4 ± 5.3% and 90.0 ± 6.9% for the right, left and whole lung, respectively. The corresponding RMSEs were 4.4 ± 1.2mm, 4.3 ± 1.1mm and 4.4 ± 1.0mm, and the $|\delta V_p|$s were 12.1 ± 13.8%, 11.2 ± 10.1% and 11.3 ± 11.7%, respectively, as shown in Table 1. The CoVs for the right, left and whole lungs were 2.0%, 1.4% and 1.6%, respectively and the corresponding ICCs for the three sessions were 0.977, 0.947 and 0.967, as shown in Table 2. In addition, the semi-automated algorithm segmentation required ~10s for each subject, whereas manual segmentation required ~15min.

Conclusions: The proposed algorithm demonstrated high computational efficiency, good agreement with manual segmentation, and high reproducibility, suggesting its potential for accurate and reproducible lung cavity segmentation from thoracic ^{1}H MRI with minimal user interaction.

References: 1. Bergin CJ *et al.* J. of thoracic imaging (1998); 2. Kirby M *et al. Radiology (2012);* 3. Yuan J *et al. Computer Vision and Pattern Recognition (CVPR).* (2010); 4. Potts RB. *Math. Proc. of the Cambridge Philosophical Society (1952);* 5. Bertsekas DP. (1999); 6. Ukwatta E *et al. IEEE. Trans. Med. Imaging.* (2013).

Three Dimensional CryoViz™ Cryo-Imaging as a Validation Tool for Medical Imaging Modalities

Amanda M. Hamilton, Paula J. Foster, Terry Peters

Robarts Research Institute, London, ON, Canada

The CryoViz™ instrument is a cryo-imaging system for three dimensional (3D), microscopic imaging of large samples including whole mice or excised organs. Originally developed in collaboration between BioInVison Inc and Case Western Reserve University, the only unit in operation in Canada is housed at the Robarts Research Institute. Cryo-imaging fills the gap between multiple modalities of whole animal *in vivo* imaging and endpoint histology. By alternating between tissue sectioning and imaging, the instrument generates high-resolution, large field-of-view microscopic images that can be rendered into a representative 3D volume. With both brightfield and fluorescence imaging capabilities, the CryoViz™ can simultaneous collect images of true-colour anatomy and fluorescent entitites, thereby enabling both the imaging of anatomic anomalies and the precise localization of fluorescent protein reporters or imaging agents.

Tissue preparation: Whole mice or excised organs are frozen embedded in optimal cutting temperature (OCT) medium by liquid nitrogen freezing. Samples can either be fixed and cryoprotected in increasing concentrations of sucrose (10-30%) or fresh flash frozen. Samples as large as 25 x 11 x 5 cm^3 can be imaged in an individual session.

Cryo-imaging: The CryoViz™ system consists of a modified brightfield/fluorescence microscope, a robotic imaging positioner and a motorized cryostat. The microscope is capable of in plane resolutions between 2.4-17.5 μm and cryosectioning can be performed at thicknesses ranging between 5-40 μm. Sectioning and imaging is programmable such that images can be collected for every tissue section or at programmed increments.

Image processing: The CryoViz™ preprocessor software stiches together images corresponding to individual sections to generate large meshed tiff files. Meshed tiff files can be used for registration with 2D images from other image modalities. In addition, the CryoViz™ preprocessor software also aligns the meshed tiffs to generate lda files that can be used to manipulate 3D volumes in two BioInVision-developed, Amira-based software programs.

To date the CryoViz™ instrument at Robarts has been used in the evaluation of animal models, novel imaging techniques and treatment strategies in multiple disease states including cardiovascular disease, obesity and cancer.

Example: Validation of MRI using CryoViz™ imaging: Human Jint1-BR3-eGFP+ breast carcinoma brain metastases in mouse brain

Green fluorescent protein (GFP)-positive Jint1-BR3 (human breast carcinoma) cells were injected into the left ventricle of a female nude mouse to enable direct cell delivery to the brain. At approximated one-month post cell injection the mouse was imaged by magnetic resonance imaging at 3 Tesla field strength using a balance steady state free precession sequence. The mouse was sacrificed post-imaging and the excised brain was fresh flash frozen in OCT. The brain was sectioned and imaged every 20 μm with an in plane resolution image of 6.5 x 6.5 μm^2. Brightfield and fluorescent images were generated.

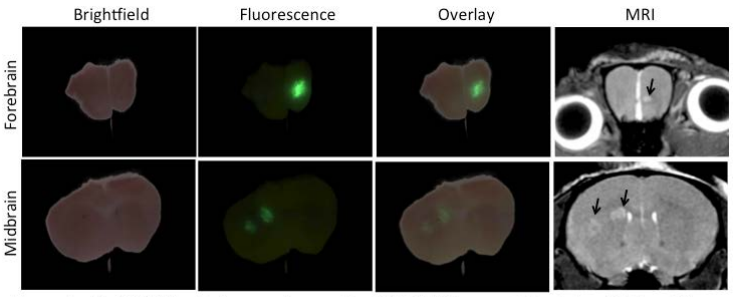

Figure 1: Jint1-BR3 brain tumors imaged by bSSFP MRI were detected as GFP positive growths in CryoViz™ images.

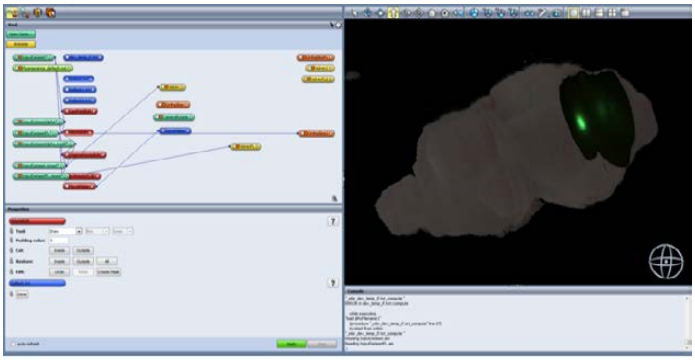

Figure 2: 3D volume datasets can be viewed and manipulated in BioInVision amira-based software programs

In *in vivo* bSSFP MR images, tumours were evident as hyperintense regions within the mouse brain parenchyma (Figure 1, black arrows). When the excised mouse brain was sectioned and imaged by the CryoViz™, Jint1-BR3 tumours were seen as GFP positive regions in fluorescence images (examples in figure 1). Based on the brain morphology evident in brightfield images, GFP positive regions corresponded well to the hyperintense regions seen in bSSFP MR images, thereby validating the MRI technique.

Low-cost USB ultrasound in scoliosis measurement

Maggie Hess[1], Daniel P. Borschneck[2], Gabor Fichtinger[1], Tamas Ungi[1]
[1] Laboratory for Percutaneous Surgery, School of Computing, Queen's University, Kingston, Canada
[2] Department of Surgery, School of Medicine, Queen's University, Kingston, Ontario, Canada

Introduction. Idiopathic scoliosis is the most frequent spinal deformation presenting as a spatial deviation from the medial vertebral line. It is diagnosed in early adolescence and monitored until adulthood when surgical correction may happen. Patients are monitored by X-ray imaging every 3-6 months, exposing them to aggregating ionizing radiation, which increases the risk of cancer. Tracked three-dimensional ultrasound imaging allows for risk-free and accurate measurement of spinal curvature (Ungi *et al*., Ultrasound Med Biol, 2014). We compared the utility of inexpensive portable ultrasound with more expensive stationary ultrasound in spinal curvature measurement for scoliosis assessment.

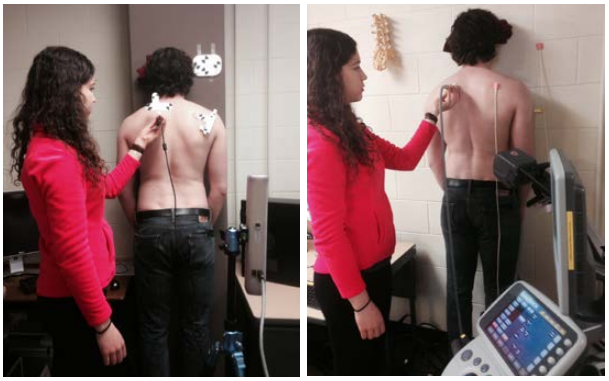

Figure 1. Interson (left) and Ultrasonix (right) setup

Methods. An open-source tracked ultrasound-based scoliosis measurement platform (Ungi et al. Ultrasound Med Biol, 2014) was utilised. This system is based on the SlicerIGT (www.SlcierIGT.org) open source environment that allows for seamless swapping among tracking devices and ultrasound scanners without requiring any programming or engineering development. Two configurations (Figs.1 and 2) of this system were compared: Interson USB ultrasound (Interson Corp, Pleasanton, CA, USA) with optical MicronTracker Hx60 (Claron Technology Inc., Toronto, ON, Canada); and Sonix Touch (Ultrasonix, Richmond, BC, Canada) with electromagnetic Ascension M180 (Ascension, Milton, VT, USA). In both configurations, a reference marker was attached to the patient and to the wall to compensate for gross body motion during ultrasound scanning. The intrinsic accuracy of SlicerIGT with both optically and electro-magnetically tracked ultrasound was previously analyzed (Lasso *et al*., IEEE TBME, 2014). This work focused on ultrasound image utility. Three human volunteers were scanned from the 7th cervical vertebra along the thoracic and lumbar regions. Two physicians experienced in musculoskeletal ultrasound imaging evaluated the visibility and clarity of the tip of transverse process, the requisite feature for spinal curvature measurement (Fig.3).

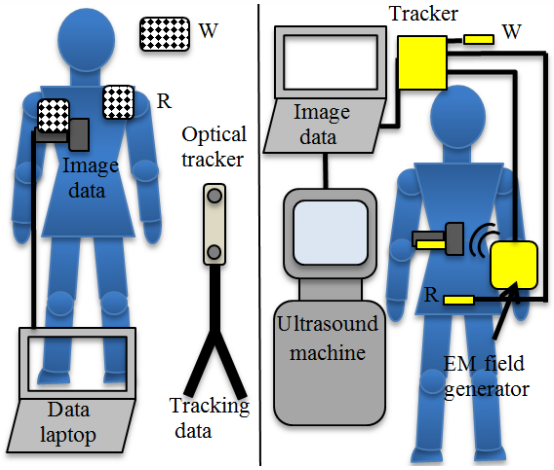

Figure 2. Schematic Interson (left) and Ultrasonix (r) setup (W = wall reference, R = patient

Results. For both physicians, in all patients and in all vertebras, the transverse process tip (N=102) was clearly visible with both Interson and Ultrasonix, without failure.

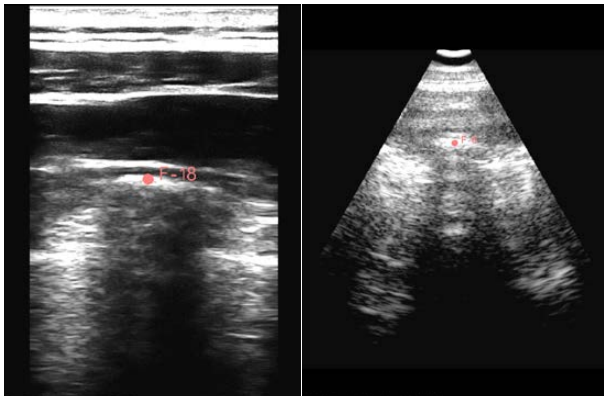

Figure 3. Transverse process identified with Interson (left) and Ultrasonix (right) imaging

Conclusions. In the hands of these two experienced physicians, the Interson and Ultrasonix scanners were functionally identical for the purpose of scoliosis measurement. The Interson scanner costs only $5,000. The optical and electromagnetic trackers cost about the same. The complete system with Interson, Micron tracker and laptop computer easily fits into a backpack. Altogether this configuration offers a highly portable, inexpensive and risk-free solution for ultrasound-based scoliosis measurement and it may open the way for scoliosis screening and may be adopted in chiropractic care.

Consortium Member: Gabor Fichtinger (CINO)

Open source software for intracranial blood clot measurement

Maggie Hess[1,2], Thomas Looi[2], Andras Lasso[1], Gabor Fichtinger[1], James Drake[2]
[1]Laboratory for Percutaneous Surgery, Queen's University, Kingston, Canada
[2]Centre for Image Guided Innovation and Therapeutic Intervention, Hospital for Sick Kids, Toronto, Canada

Purpose. Intraventricular hemorrhage (IVH) affects nearly 15% of preterm infants. It can lead to ventricular dilation and cognitive impairment. MR-guided focused ultrasound surgery (MRgFUS) is investigated as a non-invasive method to ablate clots. This procedure requires accurate, fast and consistent quantification of changes in ventricle and clot volumes, which is lacking in existing manual segmentation (MS) techniques. We propose a semi-autonomous segmentation (SAS) workflow to resolve these issues.

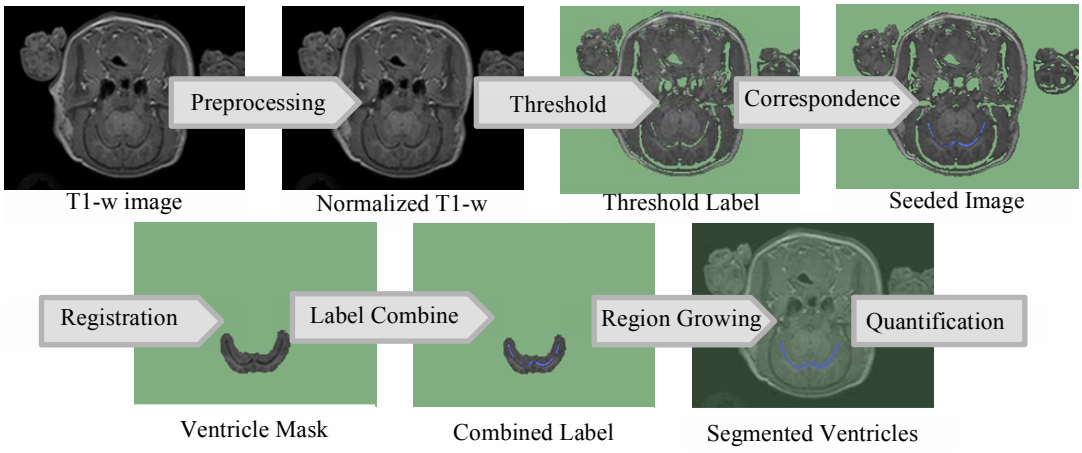

Figure 1. SAS workflow with corresponding ventricle segmentation screen captures.

Methods. We developed a semi-autonomous segmentation (SAS) algorithm for measuring changes in the ventricle and clot volumes. The free open-source image analysis and visualization software, 3D Slicer[5], was chosen to develop a SAS workflow for the MRgFUS experiment. Images are normalized, and then ventricle and clot masks are registered to the images. Voxels of the registered masks and voxels obtained by thresholding the normalized images are used as seed points for competitive region growing, which provides the final segmentation. The threshold values are predetermined, which is possible because of the normalization step. The user selects the areas of interest for correspondence after thresholding and these selections are the final seeds for region growing. This workflow was implemented in Python programming language as a standalone application that is built on 3D Slicer. The application computes nearly all the steps of the workflow automatically, and requires minimal user interaction (loading data, selection of appropriate data, one button to initialize workflow, and selection of structures of interest to create correspondence). This application provides volumetric information and creates a 3D model. It includes a simple graphical user interface, which also allows for visualization of segmentation contours and creation of a 3D model. This workflow SAS was evaluated on an IVH porcine model.

Results. This open source embodiment of SAS is a viable tool open source implementation of SAS was compared to ground truth manual segmentation (MS) for accuracy, efficiency, and consistency. Accuracy was determined by comparing clot and ventricle volumes produced by SAS and MS, and comparing contours using the 95% Hausdorff distance between the two labels. In Two-One-Sided Test, SAS and MS were found to be significantly equivalent ($p < 0.01$). SAS on average was found to be 15 times faster than MS ($p < 0.01$). Consistency was determined by repeated segmentation of the same image by both SAS and manual methods, SAS being significantly more consistent than MS ($p < 0.05$).

Conclusion. SAS is a viable method to quantify the IVH clot and the brain ventricles and it is serving in a large- scale porcine study of MRgFUS treatment of IVH clot lysis.

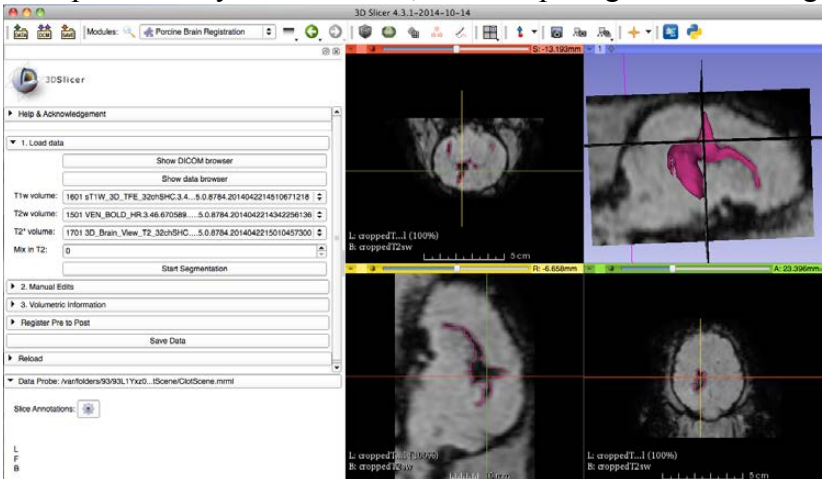

Figure 3. User interface in 3D Slicer showing a segmented blood clot and model.

Consortium Member. Gabor Fichtinger (CINO)

Clinically-Relevant Labs for the DeskCAT™ Educational CT scanner

L. Kaci[1], C. Versnick[1] , K. Dekker[2], J. Dietrich[3], K. Jordan[1, 2], J.Miller[3], J.J. Battista[1, 2]

[1]London Regional Cancer Program, London Health Sciences Centre
[2]Department of Medical Biophysics, Western University
[3]Modus Medical Devices Inc. London Ontario

Introduction. DeskCAT™ is an optical CT scanner that has proven to be student-friendly as a teaching tool for demonstrating the principles of computed tomography (CT) interactively. It is in use at 40 universities with a set of 9 lab modules for experimental imaging of small 'phantom' specimens that help explain quantitative aspects of 3D cone and 2D fan-beam CT image reconstructions. The scanner unit is safe through the use of visible light instead of x-rays, portable, and easy to use by instructors and students in classroom or lab settings. At Western University, we have used DeskCAT for imaging and lab courses at the undergraduate and graduate student levels, as a refresher tool for postgraduate residents in medical imaging, as well as for public education. In this presentation and demonstration, we describe a prototype set of 3 new labs for the DeskCAT™ scanner.

Method. The first two new labs focus on clinically observed issues such as artifacts occurring due to cyclical motion (e.g. respiration) or beam hardening (spectral effects). The 3rd new lab introduces iterative reconstruction methods. CT projection data sets are exported to off-line algorithms, which show noise and artifact suppression in comparison with standard filtered backprojection reconstruction. These topics are timely as most clinical CT scanners now offer iterative reconstruction as a means of dose and artifact reduction for diagnostic CT examinations.

Results.

A. 

B. 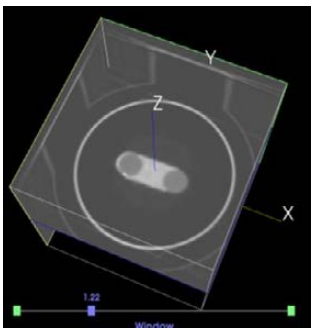

C. 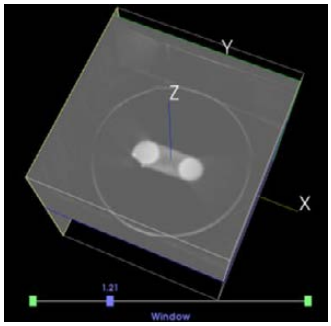

Figure illustrates beam hardening artifact:

(A) Phantom with two "green" absorbers shadowing an in-between "red" absorber
(B) Central CT image obtained with Green light only
(C) Central CT image obtained with Red plus Green Light. The spectral effect is confounded by a photon starvation effect, forming a darker streak region between the two green absorbers.

A comparison of multiple damage models in cancer therapy using radiofrequency ablation

Shefali Kulkarni-Thaker[†], Dionne Aleman[†], Aaron Fenster[††]

[†] Department of Mechanical and Industrial Engineering, University of Toronto

[††] Robarts Research Institute, Western University

Introduction: In radiofrequency ablation (RFA), a localized, minimally invasive treatment modality for small- to medium-sized tumors, single or multiple needles are inserted into the target and high frequency alternating current is passed through it from an RF source. Tissue achieves necrosis when exposed to high temperatures for adequate amount of time. However, incorrect needle placement and insufficient time of heat delivery can cause incomplete target ablation.

Method: We develop treatment plans for single- and clustered-RFA needles in two stages. First, we identify needle position and orientation, referred to as needle orientation optimization (NOO), and then we perform thermal dose optimization (TDO) to determine optimal treatment time for adequate thermal dose deposition. Vendor specifications and experimental simulations indicate an ellipsoidal or spherical shape of the thermal lesion, which we exploit to perform NOO. We solve minimum volume covering ellipse (MVCE) or sphere (MVCS) optimization models to cover all the target voxels with appropriate heat. Penne's bioheat transfer equation is used to obtain temperature distribution using a specific energy absorption rate for each voxel obtained using Laplacian with constant electrical conductivity. Finally, we perform TDO to determine the optimal treatment time. Our model has a quadratic objective, which minimizes the deviation from prescribed dose, with nonlinear constraints defining dose received by a each voxel using its temperature history to compute the dimensionless Arrhenius thermal damage index. We therefore linearly relax our constraints and pre-determine the coefficients given by the mean Arrhenius thermal damage per unit time step.

Results: We perform our computations on an Intel Core i7-3770 CPU with 8 GB RAM using MATLAB R2008b (Mathworks, Inc.) on 3D patient models under two scenarios: 1) all target voxels are considered and 2) only boundary target voxels are considered. We use CVX to solve MVCE and MVCS models. An average computational gain of 71% and 47% is obtained when only boundary voxels are used for MVCE and MVCS, respectively. A target treated with a single RFA needle appears in Figure 1(a) where the red dots indicate the position of the needle obtained using MVCE model; Figure 1(b) shows the rate of thermal damage using different damage models, obtained prior to TDO; and Figure 1(c) is a treatment plan at time $t = 20$ min, showing isodose lines for the threshold temperature and Arrhenius damage index.

Conclusion: Our NOO models provide fast needle placement while TDO computes the true dose for complete target ablation. Our preliminary results show that the rate of thermal damage varies for different thermal damage models. As a result, the treatment plans vary significantly in target coverage when using different thermal damage models and therefore, choice of thermal damage model is crucial for inverse planning.

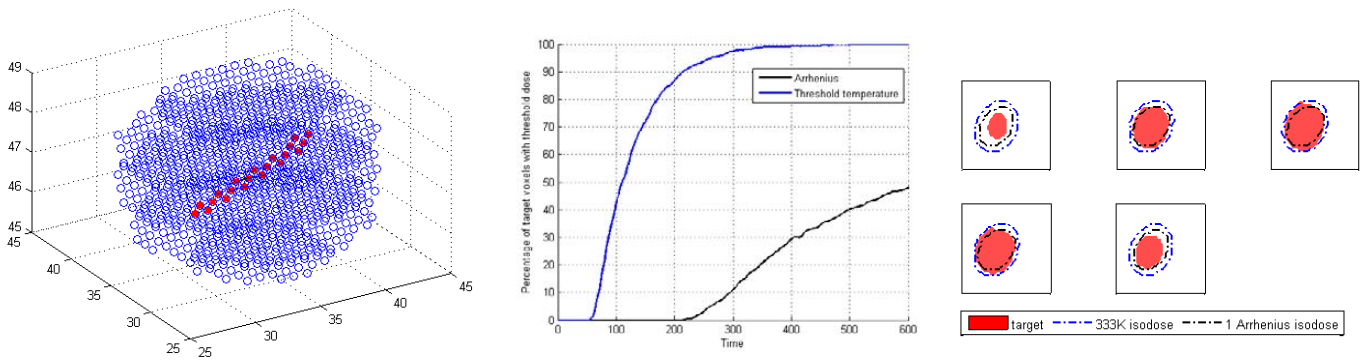

(a) NOO results (b) Rate of thermal damage (c) TDO result

Figure 1: Results for 3D patient model, 898 mm^3 target

Predicting the Impact of Surgery on Quality of Life and Risk Management in Patients Afflicted with Glioblastoma Multiforme

Luca Y. Li, David G. Gobbi, Jacob C. Easaw, Yves P. Starreveld
Departments of Biomedical Engineering, Clinical Neurosciences, Oncology, and Hotchkiss Brain Institute, University of Calgary; Seaman Family Centre, Calgary Image Processing and Analysis Centre (CIPAC), and Tom Baker Cancer Centre, Foothills Medical Centre, Calgary, Alberta

Introduction: Glioblastoma multiforme (GBM) is the most common malignant brain tumor with an average survival time of 3 months if left untreated, 12-18 months with surgery, radiation and chemotherapy (1). Present efforts focus on extending patient survival time following an operation (2). Surgical reduction of tumour volume by 78% or more increases patient life expectancy which can be further extended by adjuvant radio/chemotherapy.[3] Current efforts aim for complete resection, however, more aggressive surgery may harm the patient and its impact on post-operative patient quality-of-life (QOL) is unknown (3,4,5). This study hypothesizes: 1) there is a threshold between 78% and 98% percent resection where the decrease in QOL outweighs the increase in life expectancy, and 2) the utility of a tumour assessment score (TAS) will reliably predict a lower post-operative functional score to optimize treatment options by using tumour location and size to predict if the patient will be healthy enough for adjuvant therapy.

Methods: 90 patients with GBM have non-enhanced and gadolinium enhanced T1 magnetic resonance (MR) images taken pre- and post-surgery. Image pairs are registered and subtracted to highlight active tumour tissue and have their volume measured to calculate the extent of resection (EOR) (Figure 1). Patient QOL is measured with the Karnofsky Performance Scale (KPS) score. A TAS with a value between 1 and 10 is assigned based on: 1) which lobes the tumour infiltrates, 2) which hemisphere the tumour infiltrates, and 3) the volume of tumour within each region (Figure 2). The impact of surgery looks at the relationship between EOR and post-surgical KPS. The predictive ability of TAS is determined by how closely it can estimate post-surgical KPS.

Preliminary Results: Fourteen test patients were run with an EOR of 87.2% ± 5.9% for 6 gross-total resection (GTR – complete removal of tumour) patients, and 63.8% ± 29.5% for 8 sub-total resection (STR – partial removal of tumour) patients. KPS was slightly higher (p = 3.03) in STR (81 ± 8) than GTR (75 ± 14), supporting our first aim.

Conclusion: Preliminary findings indicate that the pipeline can successfully segment the tumour for EOR calculation and volumetric measurement of TAS.

References:

[1] Holland EC. PNAS 2000; 97(12): 6242-44. [2] Dea et al. CJNS 2012; 39: 632-37. [3] Sanai et al. JNS 2011; 115: 3-8. [4] Bloch et al. JNS 2012; 117(6): 1032-38. [5] Lacroix et al. JNS 2001; 95(2): 190-98

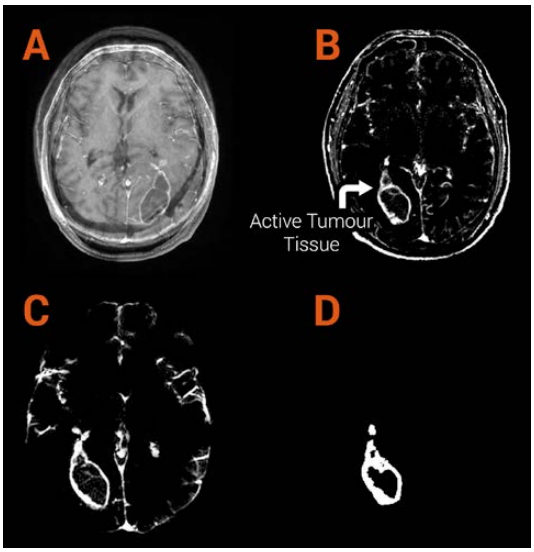

Figure 1: Tumour segmentation pipeline. (A) Registration of gadolinium contrast enhanced and non-enhanced axial T1 images. (B) Subtraction of the two images highlights active tumour tissue. (C) Brain extraction to remove the skull and erosion to remove smaller blood vessels. (D) Tumour is segmented with a connectivity filter and its volume is measured.

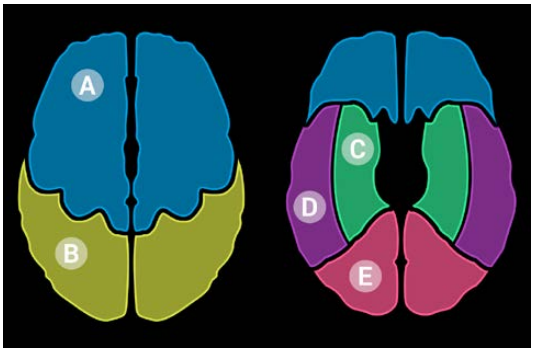

Figure 2: Approximate delineation of the regions used for TAS. The frontal lobe (A), parietal lobe (B), two sections to represent deeper and more superficial temporal lobe (C, D), and the occipital lobe (E). All regions are divided into left and right hemispheres giving a total of ten regions.

Ultrasonic evaluation of antiangiogenic therapy on patient-derived renal cell carcinoma xenograft tumors in the chicken embryo model

Matthew R. Lowerison*, Chantalle J. Willie, Siddika Pardhan, Nicholas E. Power,
Ann F. Chambers, Hon S. Leong, and James C. Lacefield
Cancer Imaging Network of Ontario (CINO)
Robarts Research Institute, Western University, London, Ontario, Canada

Introduction: Assessing patient-specific drug resistance to antiangiogenic agents is a promising application of the patient-derived xenograft model in the chicken embryo. However, conventional methods of monitoring, such as tumor-take rates, light microscopy, and histology either do not provide sufficient vascular detail for in-depth therapy evaluation, or are reserved for end-point analysis.

Ultrasonic monitoring permits non-destructive longitudinal evaluation of tumor growth and progression in the chorioallantoic membrane (CAM) xenograft ex ovo model. Antiangiogenic treatment response will be apparent in perfusion parameters estimated using contrast-enhanced ultrasound imaging.

Methods: A subset of tumor stem cells (RCC243) was isolated from a patient-derived parental renal carcinoma cell line (RCC22). Cells were grown to confluence, pelleted, and combined with an equal volume of Matrigel. On the ninth day of embryonic development (EDD-9), the CAM surface of 8 animals was pierced, and 10 µL of the cell-Matrigel mix was deposited into the opening. Half of the embryos were treated every two days with 10 µL of TAK-441, a Hedgehog inhibitor with hypothesized antiangiogenic effects.

Three-dimensional anatomical (B-mode) and contrast-enhanced images were acquired using a Vevo 2100 ultrasound system (VisualSonics Inc.) equipped with a 20 MHz linear array transducer. On EDD-18, tumor volumes were assessed using the B-mode images. The CAM vasculature was then cannulated with a glass capillary needle, and a 50 µL solution of Vevo MicroMarker™ (VisualSonics Inc.) microbubble contrast agent (2×10^9 microbubbles/mL) was injected. Perfusion imaging was performed using a destruction-reperfusion protocol after the contrast agent had reached a steady-state concentration. Digital radio-frequency contrast images were exported, tumor volumes manually segmented, and the time-kinetics of the contrast agent wash-in was assessed using MATLAB (The MathWorks Inc., Natick, MA) to determine blood perfusion metrics (blood volume, velocity, and flow).

Results: Hedgehog inhibition of RCC243 tumors via TAK-441 therapy produced significant decreases in mean tumor volume (vehicle: 187.68 ± 69.55 mm^3 vs. treatment: 78.94 ± 52.35 mm^3; $p = 0.047$) and blood flow (vehicle: 645.7 ± 261.5 mm^3/min vs. treatment: 190.8 ± 133.4 mm^3/min; $p = 0.049$). There were non-significant trends of reduced blood volume (vehicle: 97.0 ± 64.7 mm^3 vs. treatment: 33.7 ± 23.8 mm^3; $p = 0.12$) and flow velocity (vehicle: 6.34 ± 1.07 mm/s vs. treatment: 5.52 ± 1.18 mm/s; $p = 0.34$) in the treated tumors.

Conclusions: This proof of principal study shows that tumors implanted in an ex ovo chick CAM model can be imaged using high-frequency ultrasound and quantitative measures of tumor volume, blood volume, velocity and flow can be obtained. Responses to antiangiogenic therapy can be quantified. This approach to therapy evaluation is inexpensive and permits observation of tumor-induced angiogenesis over a 9-day timeframe. Since antiangiogenic agents are the primary therapy for RCC, this procedure could be useful for patient-specific drug sensitivity evaluation, enabling selection of individualized treatments prior to initiating systemic therapy.

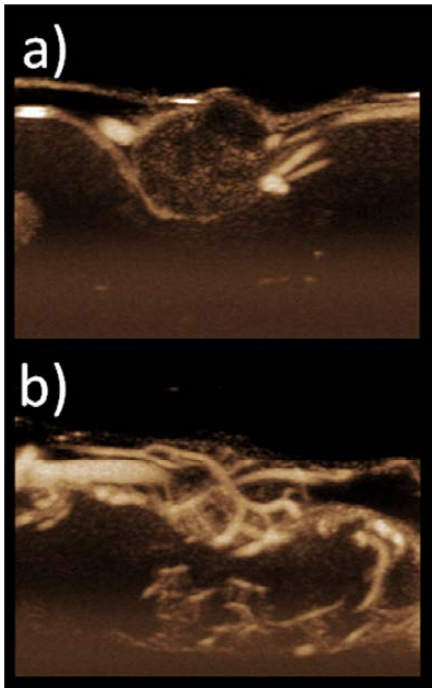

Treatment with a) TAK-441 resulted in a reduction of tumor vascularization in comparison to the b) vehicle control, as demonstrated by contrast-enhanced ultrasound.

Design of a Hypoxia PET Imaging Phantom

Brooks MacLachlan*, Emmanuel Villamejor, Brandon Driscoll, Harald Keller,
David Green, Doug Vines, Ivan Yeung
Cancer Imaging Network of Ontario Consortium (*Research Supervisor: Ivan Yeung)
Department of Radiation Physics, Princess Margaret Cancer Centre, Toronto, Ontario, Canada

Introduction. Dynamic hypoxia PET imaging involves injection of radiotracer (e.g. ^{18}F-fluoroazomycin arabinoside or FAZA) which is preferentially taken up by hypoxic cells. The transport process of tracer uptake can be modeled as i) tracer leaking from the vascular to the extravascular diffusional space, ii) tracer traveling across the diffusional space, and finally iii) tracer being taken up by hypoxic cells. The overall goal of this project is to design a dynamic PET phantom simulating the process of radiotracer traveling across the 3 compartments so that the phantom can be used for validation of compartmental analysis of dynamic hypoxia PET data. As shown in Fig 1, the phantom will consist of a box with a porous tube across the input and output end. Water will be running continuously at a constant speed carrying radiotracer to the box. There is a smaller box with a semipermeable membrane window simulating the hypoxic cell compartment. Resin will be confined in the hypoxic cell compartment such that radiotracer diffused into the compartment will be trapped by the resin. The present work is to examine appropriate materials for the semipermeable membrane to arrive at the phantom design. Simulation time activity curves were also constructed for the hypoxic cell compartment based on measured physical parameters of the chosen membrane.

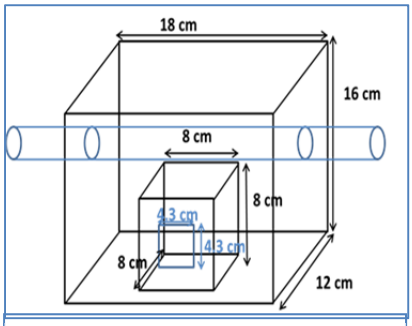

Figure 1 Model of the planned hypoxia PET phantom.

Method. Two compartments were created in an open top box (10cm x 15cm x 20cm) by a partition consisting of a 5cm x 5cm window which can be mounted with a semi-permeable membrane. The two compartments were filled with saline solution (compartment 1) and deionized water (compartment 2) respectively. Ion concentrations (conductance) of these two compartments were measured with an ion probe meter over time. The compartments were under constant stirring and concentration measurement was taken until equilibrium was established between the two compartments. It can be shown based on the Fick's law of diffusion that the concentration of compartment 1 is governed by the following equation:

$$q_1(t) = \frac{T}{V_1}\left(1 - \frac{K}{V_1}t\right) + \frac{1}{V_1}\left(K + \frac{K}{V_1}V_2\right)\int_0^t q_2(u)du$$

where q and V are the concentration and volume respectively with subscript corresponding to the compartment. T is the total amount of ions, t is time and K is the transfer constant (mL/s) of the membrane being tested. For each trial, the data was fitted using the least squares method to the equation for K.

Results. Four types of membranes were tested and the measured K-value estimates are summarized in Table 1. Using the estimated dimension of the planned PET phantom, we have calculated the expected time intensity of the hypoxia cell compartment. We have chosen the acrylic cloth for the phantom in order to have concentration in the hypoxic cell compartment at the expected concentration (300 Bq/cc) in an hour time as shown in Fig 2.

Membrane:	100 kDa membrane	Coffee filter	Acrylic cloth	Cotton cloth
Mean K-value (mL/s)	0.00692	0.0674	0.196	0.175
s.d.	N/A	0.00480	0.0034	0.0140

Table 1. Results of K values of the 4 materials investigated

Conclusions. The acrylic cloth appears to have the appropriate K value for the membrane of the hypoxic cell compartment. We will incorporate the material for construction of the hypoxia PET imaging phantom.

Fig 2. The expected time intensity for the diffusional space is assumed and that in the hypoxic cell compartment was calculated.

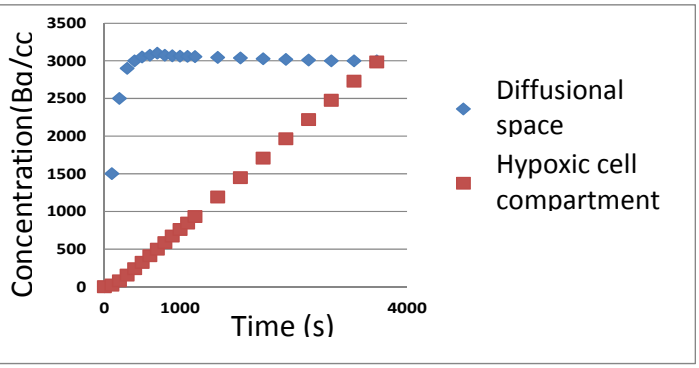

Optimizing MRI-targeted fusion prostate biopsy: the effect of systematic error and anisotropy on tumour sampling

Peter R. Martin[1], Derek W. Cool[2,4], Cesare Romagnoli[2], Aaron Fenster[1,2,4], Aaron D. Ward[1,3]
Departments of [1]Medical Biophysics, [2]Medical Imaging, [3]Oncology; [4]Robarts Research Institute;
The University of Western Ontario
Cancer Imaging Network of Ontario Consortium, Research Supervisor: Aaron D. Ward

Introduction: Magnetic resonance imaging (MRI)-targeted, 3D transrectal ultrasound (TRUS)-guided "fusion" prostate biopsy intends to reduce the ~23% false negative rate [1] of clinical 2D TRUS-guided sextant biopsy. Although it has been reported to double the positive yield [2], MRI-targeted biopsies still yield false negatives. We propose optimization of biopsy planning, according to the clinician's desired probability of sampling each tumour. This optimizes needle target positions within tumours, accounting for guidance system errors, image registration errors, and irregular tumour shapes.

Methods: We obtained multiparametric MRI and 3D TRUS images from 49 patients. A radiologist and radiology resident assessed these MR images, and contoured 81 suspicious regions, yielding tumour surfaces that were registered to the 3D TRUS images using an iterative closest point prostate surface-based method (Fig. 1A). The probability of obtaining a sample of tumour tissue in one biopsy attempt was calculated by integrating a 3D Gaussian distribution over each tumour domain, where the standard deviation σ was used to model the overall needle delivery error. We first modeled an isotropic needle delivery error with no systematic components, and investigated its effect on the probability of obtaining a cancer positive biopsy sample, with core involvement of 50% or greater. Next we investigated the effect of error anisotropy by varying the components of the error such that the resulting Gaussian distribution was anisotropic. We measured the effect of each error component on sampling probability. Finally, we ran an exhaustive simulation to investigate the relative effects of systematic and random needle delivery errors on tumour sampling probabilities. Fig. 1B, 1C and 1D illustrate examples of isotropic, anistropic, and systematic error respectively.

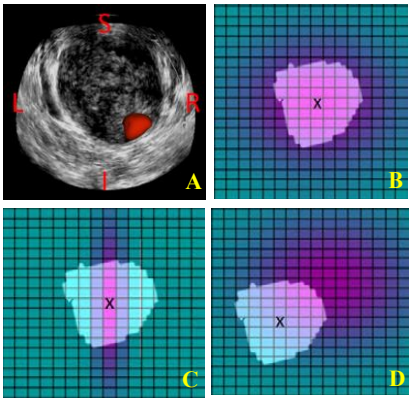

Fig. 1: (A) A red suspicious region contoured on MRI, registered to 3D TRUS. **(B)** An isotropic Gaussian distribution centered onto the biopsy target point of a prostate tumor projection. Note a 2D tumor projection and 2D distribution are used for clarity of illustration; our calculations used 3D tumor volumes and 3D distributions. **(C)** An anisotropic Gaussian distribution centered onto the biopsy target point. **(D)** A Gaussian distribution with non-zero systematic error, hence it has been shifted off-centre from the biopsy target point.

Results: Our experiments indicated that a biopsy system's lateral and elevational errors have a much greater effect on sampling probabilities, relative to axial error. Systematic errors with magnitude < 2 mm have a relatively small incremental effect on sampling probabilities. For a fusion biopsy system with a typical needle delivery error of 3.5 mm [3], only 13% of tumours of volume ≥ 0.5 cm^3 may be sampled with 95% probability of obtaining a core involvement $\geq 50\%$. We have inferred from these results that tumours of volume ≤ 1.9 cm^3 may require more than one biopsy attempt to ensure 95% probability of a sample with 50% core involvement, and tumours ≤ 1.0 cm^3 may require more than two attempts (Fig. 2).

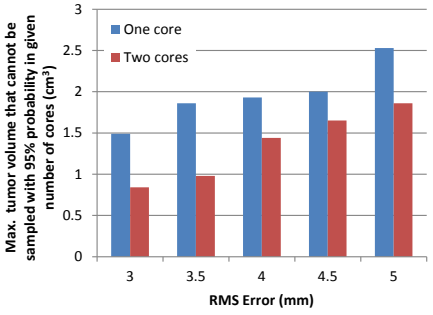

Fig. 2: The upper bound of tumour volume such that there is < 95% probability of obtaining a sample with ≥ 50% core involvement, given needle delivery error of the biopsy system.

Conclusions: Motivated by our aim to provide early and accurate diagnosis of prostate cancer via improved positive yield of MRI-targeted, 3D TRUS-guided fusion biopsy, we have determined a rule set for the number of necessary biopsy attempts (one, two, or more) to obtain a 50% core involvement from patients who should accordingly be provided with immediate treatment, as a function of overall needle delivery error of the biopsy system (Fig. 2). Optimized planning of within-tumour targets for fusion biopsy could support earlier diagnosis of prostate cancer while it remains localized to the gland and curable, reducing the need for repeat biopsies.

[1] Rabbani, F., J Urol 159(4), 1998 [2] Cool, D., LNCS 6963, 2011 [3] Martin, P., Med Phys 41(7), 2014

An inverse planning treatments interface using MATLAB and 3D Slicer

Yago Oliveira[1], Kimia Ghobadi[2], Kevin Wang[2], Dionne M. Aleman[1], David A. Jaffray[2]
Cancer Care Ontario Consortium
1. University of Toronto 2. Princess Margaret Cancer Centre

Introduction. We developed a module, Gamma Knife Inverse Planning (GK-InversePlan), for Leksell Gamma Knife® Perfexion™ (PFX) using 3D Slicer to provide a user-friendly interface to help analyze and design inverse treatment plans. Slicer is an open-source software used to visualize and analyze images with image-guided therapy, and allows developers to improve its available interfaces by creating new modules that better fit specific treatments, such as radiotherapy. PFX is a Cobalt-60 radiosurgical robot primarily used to non-invasivelly treat brain lesions. Our module, GK-InversePlan is developed using Python and MATLAB® and provides a platform for the user to create, evaluate, and refine PFX plans using different parameters.
Methods. The module workflow starts with importing patient images and organs of interest (including target volume), which can be provided in any data format accepted by Slicer, e.g., DICOM. Once the primary data is imported, target volumes, their prescription doses, and an area around each target for accelerated dose-gradient fall-off can be selected by the user (Figure 1, a). The module creates the dose fall-off volume using SlicerRT extension functionalities. The next step uses Slicer's MATLAB bridge to run an inverse treatment plan algorithm in MATLAB (Figure 1, b). The GK-InversePlan module allows the user to employ any inverse treatment plan that has a MATLAB interface. Once the algorithm has run in MATLAB, it returns a dose-volume matrix to GK-InversePlan. Other outputs including shot location and the dose delivery path can be returned to GK-InversePlan as well (Figure 1, c), and their visualizationd can be adjusted by the user. The final step is the evaluation of the obtained plan based on the returned dose-volume matrix. The user can inspect isodose lines and/or dose-volume histograms. The isodose lines are generated based on the user's preferred levels and color scheme (Figure 1 ,d). The dose-volume histograms are generated using SlicerRT functionalities that are available in the GK-InversePlan (Figure 1, e).
Results. The GK-InversePlan module is illustrated using Slicer sample CT image and a continuous dose delivery inverse treatment planning algorithm for PFX (Figure 1, f). GK-InversePlan provides a platform to easily import data, interface it with MATLAB-written inverse treatment planning algorithms, and illustrate the quality of the obtained plan using isodose lines and volumes and dose-volume histograms.
Conclusion. The Gamma Knife Inverse Treatment Planning module provides an intuitive and well-designed workflow to help visualize and generate inverse treatment plans for PFX. GK-InversePlan has the ability to interface with any inverse treatment plan that is written in MATLAB. The module employs powerful functions of Slicer to provide a better perspective of the clinical impact of the treatment plan. This module can be used as a template for inverse planning for other modalities, including IMRT and brachytherapy.

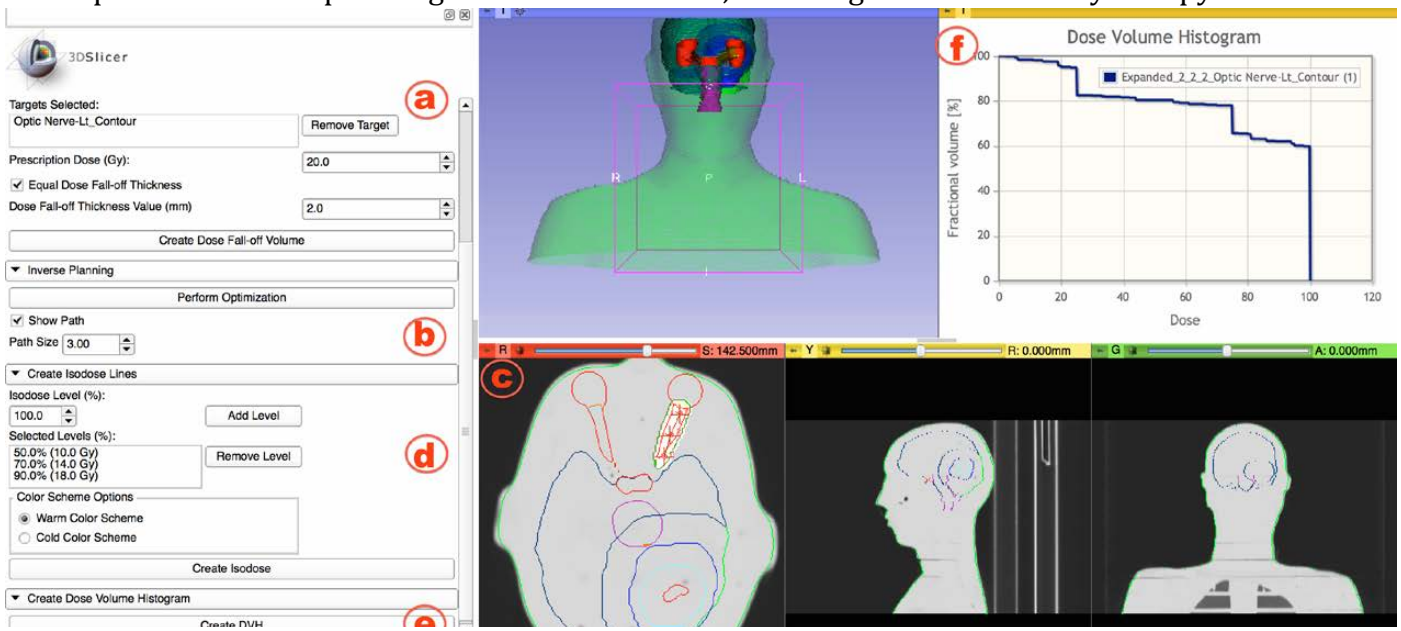

Tumour Motion Phantom for PET/MRI/CT

J.C. Patrick[1, 2, 3], M.A. Tavallaei[4, 5], F.S. Prato[2, 3], R.T. Thompson[2, 3], M. Drangova[2, 4], S. Gaede[1, 2, 3] *(Supervisor)*
Cancer Imaging Network of Ontario
[1]Physics and Engineering, London Regional Cancer Program, London/Canada,
[2]Medical Biophysics, Western University Canada, London, ON/Canada,
[3]Imaging, Lawson Health Research Institute, London, ON/Canada,
[4]Imaging Research Laboratories, Robarts Research Institute, London, ON/Canada,
[5]Biomedical Engineering Graduate Program, Western University Canada, London, ON/Canada

Introduction: Siemens' hybrid PET/MRI acquires both modalities simultaneously, eliminating the impact of respiratory motion due to sequential scanning. This could have a major impact on respiratory-gated lung cancer radiotherapy. Before implementing PET/MRI for lung cancer radiotherapy clinically, the benefits of this novel imaging technique should be validated in an appropriate phantom. The goal of this work is to demonstrate a PET/MR/CT compatible respiratory motion phantom that can be used to understand and validate the impact of tumour motion on hybrid PET/MRI.

Materials and Methods: The phantom's torso compartment has internal dimensions of 274.5mm long with an oval profile of 292mm by 240.5mm. The lung compartments have oval profiles with internal dimensions of 89mm by 125.5mm, by 274.5mm long. The spine compartment has an oval profile with internal dimensions of 32.3mm by 23.6m, by 274.5mm long. The superior-end cap has two fill holes; one to fill the spine compartment and one to fill the torso compartment. The inferior-end cap has two through holes to match the profiles of the lung compartments, which allow a spherical tumour compartment with stem to be mounted to an MRI-compatible motion stage. This motion stage from Vital Biomedical Technologies can provide user-defined motion profiles to move the tumour (Figure 1A). The 3.5cm diameter spherical tumour compartment was filled with saline and 17kBq/mL of F18 to mimic tumour uptake of FDG. The torso compartment was filled with saline and 4.27kBq/mL of F18 to mimic normal back ground uptake in a patient body. The motion stage was programmed to produce a repeating 4 second sinusoidal cycle of linear motion that was 2cm long in the superior/inferior direction. PET/MR images were acquired on a Siemens Biograph mMR via T1-VIBE sequence with simultaneous list-mode PET acquisition.

Results: The PET/MR/CT-compatible Tumour Motion Phantom can be used to generate accurate images of known geometries and reproducibly simulate respiration motion or user-defined motion profiles of a tumour. Figure 1B shows that the co-registration of the PET and MRI was achieved with no post-processing, despite the presence of motion.

Conclusions: The PET/MRI/CT compatible phantom we have developed can be used to generate images in all 3 modalities. It is compatible with Vital Biomedical Technologies MR-compatible motion stage, which can provide user-defined motion profiles to move the tumour compartment. Future work will involve the use of this phantom to investigate the utility of PET/MR imaging of tumour motion in the context of radiotherapy planning and making comparisons with currently available PET/CT techniques.

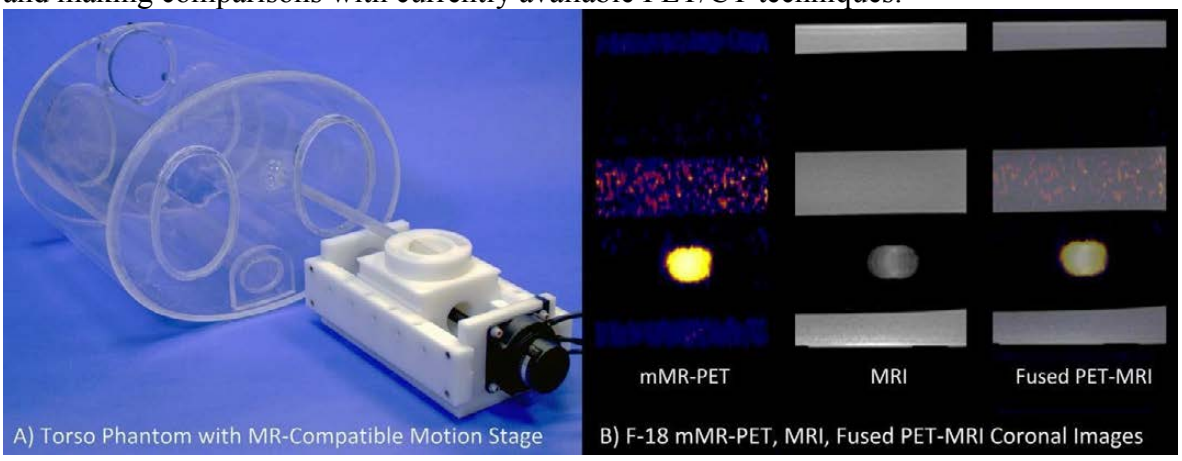

Figure 1. A) Completed Phantom with B) Non-gated images in mMR-PET, T1-VIBE MRI, and Fused PET-MRI of moving phantom filled with saline and F-18.

Quantitative ultrasound monitoring of tumour cell death responses

Lakshmanan Sannachi[1,2], Azza Al-Mahrouki[1,2], William Tyler Tran[1,2], and Gregory J. Czarnota[1,2,3]

(1) Department of Medical Biophysics, University of Toronto, Toronto, Canada
(2) Physical Sciences, Sunnybrook Research Institute, Sunnybrook Health Sciences Centre, Toronto, Canada
(3) Department of Radiation Oncology, Sunnybrook Health Sciences Centre, Toronto, Canada

Introduction: Quantitative ultrasound techniques have been shown to be capable of detecting cell death through studies conducted on in vitro and in vivo models. Recently, hybrid models have been developed based on quantitative ultrasound parameters (QUS) to quantify cell death percentage from treated mice tumour and to distinguish treatment responders and non-responders from locally advanced breast cancer patient (LABC) populations early on during chemotherapy. QUS parameters estimations using radio frequency echoes acquired with clinical ultrasound systems must be independent of the data acquisition setup. This study was performed to compare this QUS method in monitoring tumour cell death response from animal and human using two different clinical array systems.

Methods: Radio frequency data were acquired from xenografted human breast cell line tumours (MDA-MB231) before and after injection (4, 8, 12 and 24 hours) of paclitaxel chemotherapy agent, using low frequency linear array transducers L14-5/36 and 9L with frequency range 4 – 9 MHz with Ultrasonix and GE-LOGIQ clinical systems, respectively. Similarly, RF data were acquired from LABC patients before and during treatments (week 1, 2, 4 and 8) using the same clinical scanners. QUS parameters, including midband fit (MBF), spectral slope (SS), and 0-MHz intercept (SI) were estimated from tumour regions.

Results: In both mice tumour and LABC treatment monitoring studies, the trends observed in the changes of QUS parameters after treatment using GE and Ultrasonix systems were similar. The mean squared (RMS) errors between clinical scanners were highly variable. For example, in mouse tumours, the average RMS errors calculated for the MBF parameter before treatment was 1.5 dB. Tumour sampling differences yielded up to 28.5 dB RMS error after treatment. In LABC patients, the RMS errors calculated for this QUS parameter before and after treatment were 2.7 dB and 2.3 dB respectively, with similar volumes sampled.

Conclusions: The histological analysis showed increases in MDA mice tumour heterogeneity after treatment. This increase in heterogeneity within the tumour accounted for QUS parameter varations from slice to slice. This results in variations between scanners due to limitations in acquiring identical planes. The discrepancy in the RMS error for changes in QUS parameters after treatment between MDA mice tumour and LABC is likely due to the difference in transducers characteristics used in this study. This technical advance shows the potential for QUS technology to function with difference imaging platforms.

Improving the Image Quality of Cone-Beam Computed Tomography (CBCT) Scans

Raghav Singal[*,1], Dionne Aleman[1,2,3], Douglas Moseley[4,5]
[1] *Department of Mechanical and Industrial Engineering, University of Toronto*
[2] *Institute for Health Policy, Management and Evaluation, University of Toronto*
[3] *Techna Institute, University Health Network*
[4] *Department of Radiation Oncology, University of Toronto*
[5] *Princess Margaret Cancer Centre*

Introduction: A highly accurate CT image captured at the onset of a radiotherapy treatment is used to plan the dose to deliver the patient. As the patient is exposed to the radiation, his/her anatomy changes. In the status quo, the treatment plan, which is spread out over 25-30 days (called fractions), is not updated to account for these internal changes, i.e., the treatment is not adaptive/dynamic. Daily CTs would allow clinicians to observe and correct for the anatomical changes, but CTs cannot be taken each fraction since the amount of radiation delivered by a CT is significant. Cone-beam CT (CBCT) images are taken simultaneously during treatment without delivering additional radiation, but CBCT images are not used to dynamically plan treatments because of their relatively poor image quality. We apply image transformation methods to restore correct density values to CBCTs based on the original CT scan and show improvements over existing transformation methods.

Methods: We consider four image correction models: (1) modified shading correction (MSC), (2) selective regression (SR), (3) polynomial correction using linear programming (PCLP), and (4) polynomial correction using quadratic programming (PCQP). The MSC is a modification of the shading correction (SC) algorithm [1], whereas the other three models are novel contributions. The SR model performs a robust regression between the selected pixels of the CBCT and CT images and corrects the CBCT scans accordingly. The PCLP and PCQP involve a constrained linear optimization model and an unconstrained quadratic optimization model, respectively. Both these mathematical programs calculate a polynomial that minimizes the pixel value differences between the CT and the CBCT scans. The resulting polynomial is added to the CBCT as a correction factor.

Results: In our experiments on eight treatment sites, we observe that the performance of correction algorithms depends on the intensity variation (contrast) of the treatment site. The SC algorithm outputs good results for the prostate nodes, which is in agreement with previous SC findings [1]. However, it produces significant artifacts for bilatglottis (Figure 1), lungs, and larynx. Interestingly, the MSC algorithm dominates the SC algorithm for all the eight sites we tested. PCLP and PCQP methods show promising results for low-contrast sites whereas the MSC methods perform well for medium- and high- contrast sites.

Conclusions: In addition to suggesting new algorithms for improving the CBCT image quality, we propose that the CBCT image correction should be done based on the pixel intensity variation.

[1] T. E. Marchant, C. J. Moore, C. G. Rowbottom, R. I. MacKay, and P. C. Williams. Shading correction algorithm for improvement of cone-beam CT images in radiotherapy. Phys Med Biol, 53(20):5719-33, 2008.

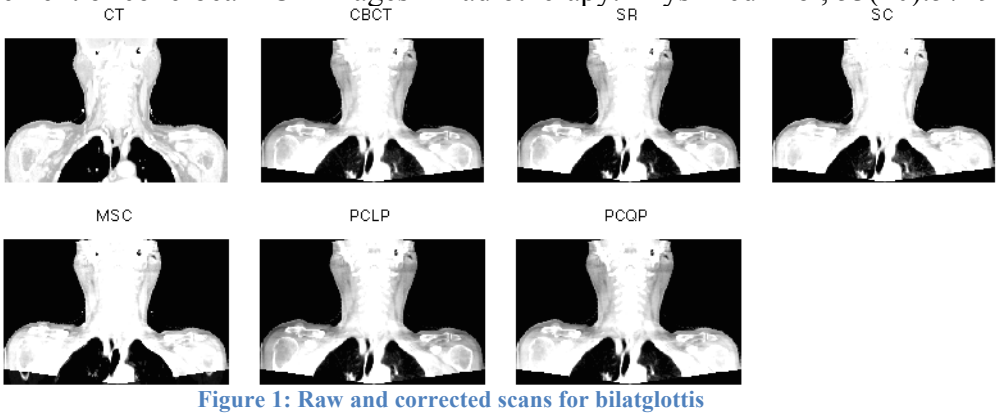

Figure 1: Raw and corrected scans for bilatglottis

Development of Bipyridine-Containing Peptide Imaging Probes for SPECT Imaging

William L. Turnbull[1], Jinqiang Hou[2], André H. St. Amant[2], and Leonard G. Luyt*[1,2]
[1] *Department of Chemistry, University of Western Ontario, London, Ontario, Canada*
[2] *London Regional Cancer Program, London, Ontario, Canada*

Introduction. C-X-C chemokine receptor type 4 (CXCR4) is involved in chemotaxis of many cell types, especially lymphocytes and stem cells. However, CXCR4 is overexpressed in more than 23 types of cancer and has been shown to promote metastasis, angiogenesis and tumour growth. Targeting this receptor with a ^{99m}Tc imaging probe could allow for the visualization of metastatic cancer by single photon emission computed tomography (SPECT). CVX15 is a small, 16 amino acid macrocyclic peptide antagonist of the CXCR4 receptor and is known to exist in a β-hairpin conformation. The X-ray crystal structure of the peptide bound to CXCR4 indicates that the turn region is outside of the binding pocket[1], and that modification of this turn region doesn't significantly impact the peptide's affinity for the receptor[2]. A suitable ^{99m}Tc chelator could replace this turn region to make an imaging probe with high affinity toward the CXCR4 receptor. Peptides containing bipyridine residues have been shown to nucleate β-hairpin formation when coordinated to a metal[3]. A model peptide has been developed to ensure that a bipyridine-containing peptide will form a β-hairpin when coordinated to a Re or ^{99m}Tc core, with Re being used as a surrogate (non-radioactive) metal for characterization purposes. The bipyridine residue can be incorporated into a peptide as an unnatural amino acid by standard solid phase peptide synthesis techniques. The goal is to then incorporate this bipyridine residue into the turn region of CVX15 and coordinate the peptide with ^{99m}Tc to form an imaging probe for the CXCR4 receptor.

Methods. The bipyridine amino acid was synthesized by Ullmann coupling of 3-nitro-2-chloropyridine, followed by reduction to the diamine, addition of a succinic group to one of the amines, followed by protection of the free amine with an Fmoc group. Peptides were synthesized using Fmoc solid-phase peptide chemistry, and purified using reverse-phase high performance liquid chromatography (RP-HPLC) and analyzed by ESI-MS, 2D NMR, and CD spectroscopy. Peptides were coordinated with $Re(CO)_3^+$ and the resulting complexes purified by RP-HPLC and analyzed by ESI-MS and CD spectroscopy. Peptides were also radiolabelled with $^{99m}Tc(CO)_3^+$, analyzed by HPLC and the retention time compared to the Re standard.

Results. The bipyridine amino acid was synthesized in 4 steps with >95% purity. Bipyridine peptides were synthesized in >95% purity and characterized by ESI-MS. Further characterization by CD spectroscopy and 2D NMR suggests the presence of β-sheet-like secondary structure. Coordination of the peptide to $Re(CO)_3^+$ was performed in water using $[Re(H_2O)_3(CO)_3]OTf$, followed by the addition of a third ligand to form a [2+1] complex and the coordination confirmed by ESI-MS. Characterization by CD spectroscopy suggests retention of the secondary structure upon complexation to Re. Coordination to $^{99m}Tc(CO)_3^+$ was performed by reduction of $^{99m}TcO_4^-$ to $[^{99m}Tc(H_2O)_3(CO)_3]^+$ and then following similar coordination conditions as for $Re(CO)_3^+$. HPLC analysis confirmed the presence of the radiolabelled product, through comparison to the Re standard.

Conclusion. Peptides containing a bipyridine residue are able to mimic β-sheet secondary structure and retain this secondary structure upon coordination to $Re(CO)_3^+$. This novel method of forming a β-sheet mimic may have future value for the development of receptor targeted $^{99m}Tc(CO)_3^+$ imaging probes.

References.

(1) Wu, B.; Chien, E. Y. T.; Mol, C. D.; Fenalti, G.; Liu, W.; Katritch, V.; Abagyan, R.; Brooun, A.; Wells, P.; Bi, F. C.; Hamel, D. J.; Kuhn, P.; Handel, T. M.; Cherezov, V.; Stevens, R. C. *Science.* **2010**, *330*, 1066–1071.

(2) Liu, T.; Liu, Y.; Wang, Y.; Hull, M.; Schultz, P. G.; Wang, F. *J. Am. Chem. Soc.* **2014**, *136*, 10557–10560.

(3) Schneider, J. P.; Kelly, J. W. *J. Am. Chem. Soc.* **1995**, *117*, 2533–2546.

Automated segmentation of whole-slide histology for vessel morphology comparison

Yiwen Xu[1], J. Geoffrey Pickering*[1, 2], Zengxuan Nong[2], Aaron Ward*[1, 3]
Cancer Imaging Network of Ontario * Supervisors
1. Dept. of Medical Biophysics, 2. Robarts Research Institute, 3. Dept. of Oncology, Western University

Introduction: Microvasculature characteristics can be revealed by immunohistochemical staining, but manual quantification of these characteristics on whole slides containing potentially hundreds of vessels is tedious and subject to operator variability. Conventionally, manual quantification is performed for selected regions of the whole tissue sections, which may not be fully representative of the pathology. Our objective was to develop and validate a fully automated segmentation of the vascular smooth muscle layer on whole-section histology of normal and regenerated post-ischemia mouse hind limb microvasculature, stained for smooth muscle using 3,3'-diaminobenzidine (DAB) immunostain.

Materials and Methods: The experiments were conducted on the tibialis anterior, hind limb muscle bundle of normal (n=2, 10 and 9 sections) and regenerated vasculature two weeks post ischemia (n=1, 12 sections) of the wild type C57BL/J6 mouse. Our approach accounts for irregularity of vessel wall staining using colour deconvolution to isolate the DAB stain, and joining the morphological skeletons of the vessel wall fragments disjointed by inconsistent staining. Artefactual fragments were removed based on incoherence of neighbouring tissue in an accurate 3D histology reconstruction (Y Xu, SPIE Medical Imaging 2014). The vessel wall thickness, vessel density, area, and perimeter were quantified.

Results: For segmentation validation, vessels were manually delineated and compared to the automated segmentation approach on a normal mouse with measures shown in Table 1. Descriptive statistics on vessel density and count are shown in Table 2. There was a significant difference in median density and count between all three samples ($p < .05$). The morphological measures on the automated segmentation are shown in Table 3 (non-normal, $p < .05$). Bonferroni correction was performed, using a significance level of $\alpha=0.05/12=0.004$. A difference in area was found for all sample comparisons ($p < .002$), and in perimeter between normal and regenerated tissues ($p < .001$). There were significant differences for all thickness measures ($p < .001$).

Table 1: Segmentation validation measures

	Median	IQR
MAD	0.44 µm	0.21 µm
Dice overlap	0.84	0.09
Recall	0.80	0.14
Precision	0.95	0.09

Table 2: Descriptive statistics of vessel count and density

	Sample 1 (n = 10)		Sample 2 (n = 9)		Sample 3 (n = 12)	
	Median	IQR	Median	IQR	Median	IQR
Vessels/Section	228.50	32.00	292.00	59.75	324.00	28.00
Vessel Area/Section Area $\left(\frac{\mu m^2}{\mu m^2}\right)$	0.0044	0.0003	0.0037	0.0003	0.0082	0.0013

Conclusions: The automatic vessel segmentation detected, delineated, and measured a total of 8565 vessels on the 31 whole-slide images used in this study. Manual delineation and quantification of vasculature on this scale is clearly impractical, and this technique paves the way for high-throughput, fully automatic vasculature quantification. Concordance with manual measurements was found with a few outlier segmentations, typically from unusually faintly stained vessels (Fig. 1). With refinement and validation of this method on a larger data set, we aim to provide a valuable tool for scientists requiring high-throughput vascular segmentations and morphological measures for the analysis of vasculature for disease state comparisons.

Table 3: Automatic vessel smooth muscle morphological measures

	Area (µm²)		Perimeter (µm)		Thickness (µm)					
					5th Percentile		50th Percentile		95th Percentile	
	Median	IQR	Median	IQR	Median	IQR	Median	IQR	Median	IQR
Sample 1 (n = 2189)	27.78	69.29	19.67	22.03	0.56	0.75	1.41	1.56	2.66	2.69
Sample 2 (n = 2568)	23.14	58.78	20.76	21.11	0.51	0.55	1.25	1.40	2.50	2.35
Sample 3 (n = 3808)	31.14	82.75	19.06	24.61	0.71	0.75	1.64	1.58	2.80	2.73

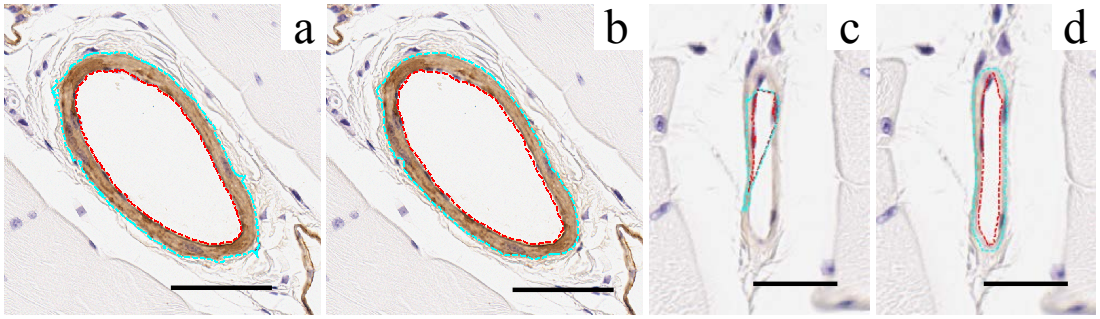

Fig. 1: Contours of automatically segmented (a,c) and manually delineated (b,c) vessel walls in the wild type mouse hind limb stained with DAB for α-actin smooth muscle. Cyan depicts the outer vessel wall contour and red depicts the inner lumen wall contour. Scale bar (a,b) 50 µm, (c,d) 25 µm.

Ontario Consortium in Imaging for Cardiovascular Therapeutics

OCICT

Oral Presentation and Poster Abstracts

A Novel Nasopharyngeal Method for Rapid Selective Brain Cooling in a Rabbit Model

Mohammad Fazel Bakhsheshi, PhD[1, 2], Laura Morrison, RVT[1], Lynn Keenliside[1], Ting-Yim Lee, PhD, FCCPM[1,2,3]

[1]Imaging Program, Lawson Health Research Institute, London, Ontario, Canada, [2]Imaging Research Laboratories, Robarts Research Institute, London, Ontario, Canada. [3]Department of Medical Imaging and Biophysics, Western University, London, Ontario, Canada,

BACKGROUND & PURPOSE: Mild hypothermia (HT33°C) can be neuroprotective to reduce brain injury and decrease death and disability in patients with cardiopulmonary arrest.[1] Selective brain cooling (SBC) could minimize systemic complications associated with systemic hypothermia but maximize neuroprotection.[2] Recently, we developed a novel method of SBC and demonstrated its safety and efficacy in a piglet model. The method was based on spraying room temperature or cold air into the nostrils at different flow rates.[3] Pigs possess a carotid rete (a set of small parallel arteries) which is surrounded by the cavernous sinus; together these serve as an effective heat exchange mechanism for the brain. However, in mammals in which carotid rete is missing such as rabbits, some have suggested that there is no effective heat exchange in the cavernous sinus and, consequently, SBC is not possible. The primary focus of the current study was to evaluate the effectiveness of this approach on rabbits and compare it with our previous finding on newborn piglets.

METHODS and MATERIALS: Experiments were conducted on six rabbits (n=6). A tracheotomy was performed and the animal was ventilated with a volume-controlled mechanical ventilator to deliver oxygen/medical air mixture (2:1). Rabbits were induced and maintained with isofluorane gas anaesthesia at 4% and 2.5% concentration, respectively. Two successive experiments were performed on each animal. In the first series of measurements, brain nasopharyngeal cooling was initiated with blowing room temperature air, delivered from hospital medical air outlet, at a flow rate of 14-15 min as measured by a flowmeter into both nostrils for 60 min (Group I). The temperature of the brain then gradually increased to reach to the baseline temperature. Following rewarming, the second series of measurements and brain cooling was performed in the same manner as the first one but blowing cold air (-7°C) at the same flow rate (Group II). Altogether, 12 cooling experiments were performed on rabbits (n =6 in each group). Rectal temperature was recorded from a rectal probe inserted to 1-3 cm from the anal margin. Deep brain temperature was also measured continuously and invasively with a thermocouple probe. A 5-mm burr hole was made in the skull with a Dremel tool. The needle thermocouple probe was inserted laterally through the skull into the brain to a depth of 2 cm vertical from the brain surface and 1.5 cm posterior to the bregma.

RESULTS: Changes in rectal and brain temperatures were continuously monitored and are shown in Figure 1. One hour post cooling with room temperature air at a flow rate of 14-15 L/min, the brain temperature was 34.1°C ± 1.2°C which resulted in mean brain cooling rates of 3.7 ± 0.9°C/h, as displayed in Figure 1(a). Figure 1(b) shows greater cooling rate by using -7°C air at the same flow rate. Brain and rectal temperature could be reduced more rapidly at mean rates of 5.2 ± 1.9°C/h and 1.6 ± 0.4°C/h, respectively. Figure 2 displays the average cooling rates as monitored in the brain obtained in the nasopharyngeal cooling approach using either room temperature or cold air at a flow rate of 14-15 L/min for rabbits and newborn piglets. Mean brain cooling rate was significantly greater with -7°C as compared with room temperature air in both species.

CONCLUSIONS: Comparing results between piglets and rabbits demonstrate clearly that lack of a carotid rete does not prevent the existence of SBC. This study was the first step in developing a reliable, safe and efficient cooling device for future clinical trials on the neuroprotective effects of mild hypothermia and will be of benefit to different patient populations.

BIBLIOGRAPHY:

1 Busch, H.J., et al., Resuscitation, 2010. 81(8): p. 943-9.

2. Sarkar, S. and J.D. Barks, Semin Fetal Neonatal Med, 2010. **15**(5): p. 270-5.

3. Bakhsheshi, M.F., PhD Thesis, Department Medical Biophysics, Western University: London. (2014), Western University.

Figure1:

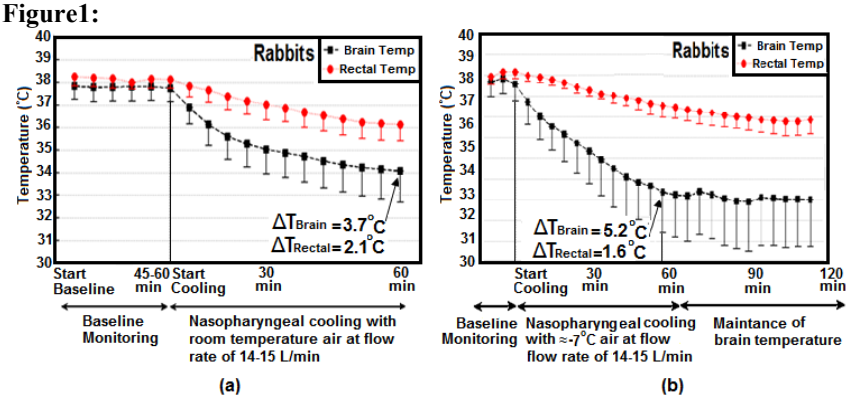

Figure 1. Brain and rectal temperature over time for nasopharyngeal cooling method with (a) room temperature air and (b) cold air at a flow rate of 14-15 L/min in rabbits (N=6).

Figure 2:

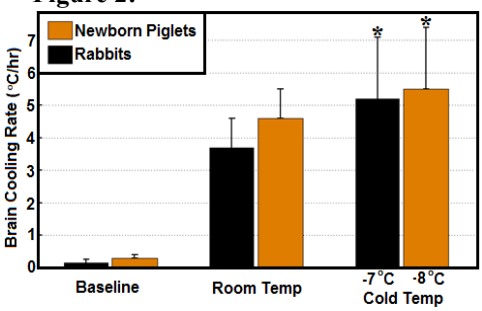

Figure 2. Mean brain cooling rate with different on rabbits and newborn piglets (N=6). * signifies a statistically significant (P<0.05) difference between cold temp versus room temp.

Roemer-Optimal Reconstruction of Hyperpolarized ^{13}C Cardiac Images with an 8 Channel Coil

William Dominguez-Viqueira[1], Justin Lau[1,2], Ben Geragh[1,2], Albert P. Chen[3] and Charles H. Cunningham[1,2]
[1] Imaging Research, Sunnybrook Health Sciences Centre, Toronto, ON, Canada
[2] Medical Biophysics, University of Toronto, Toronto, ON, Canada
[3] GE Healthcare, Toronto, ON, Canada

Introduction: Extended coverage of the heart was demonstrated using rapid multislice imaging of hyperpolarized ^{13}C pyruvate[1] using a single shot spiral pulse sequence and with a 5-channel receiver[2]. Roemer-optimal coil combination using a numerical model of the sensitivity maps[3,4] has been used to avoid wasting the limited polarization available for map measurements. The objective of this work was to extend this numerical estimation method to the 8-channel receiver array that will be used in human studies. Pyruvate images of the heart were acquired *in vivo* and reconstructed using Roemer-optimal channel combinations using the simulated sensitivity maps and compared to a simple sum of squares.

Methods: A commercially available ^{13}C eight-channel 2-paddle receive-array was used in conjunction with a clamshell transmit coil (USA Instrument, Inc., Aurora, OH) on a GE MR750 3T MR scanner. Gated ^{13}C images of the heart were acquired in short and long axis (6 slices, single-shot 16384 samples, Tread = 64 ms, BW = 250 kHz, FA = 90◦, 10 mm / 1 mm slice/gap, FOV = 24cm. Two slices were acquired each cardiac cycle in a 160 ms diastolic window[1].

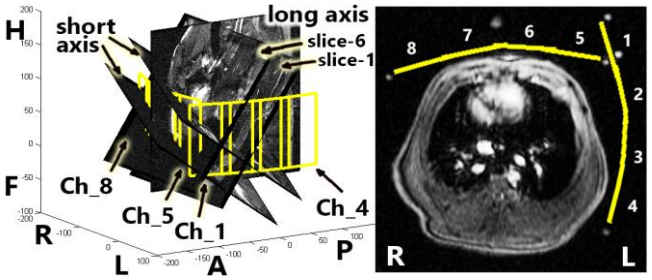

Fig. 1: Numerical space and coil position. **Right**: Axial slice showing fiducial markers (white dots) and coil positions. **Left:** 3d position of all coils for maps calculation and slice positions for long axis and short axis slices of the heart.

The channels were combined using the Roemer optimal combination. Coil coefficients were computed in Matlab (The MathWorks Inc., Massachusetts, USA) using a Biot-Savart model of the coils. Fiducial markers placed on the ^{13}C receiver coils were used to estimate coil positions in the proton images (Fig 1) and calculate 3D sensitivity maps of all eight receiver coils. Maps were used for reconstruction using Roemer-optimal and compared to Sum of Squares of all channels (Fig. 2).

Results and Discussion: Figure 1 shows the receiver coils position defined by the yellow lines (only for visualization proposes); white dots in Fig 1. right are the signal from fiducial markers on the coils. Figure 2 shows the images of *in-vivo* hyperpolarized ^{13}C pyruvate in the pig heart. As shown in Fig. 1 left, slice 1 is at the back of the heart, distal to the coils, while slice 6 is closer to the chest wall and coils. As expected, the signal intensity is very similar for both methods for slices close to the coils (i.e slice 5 and 6), while for slices farther from the coils (slices 1, 2 and 3) the Roemer-optimal combining using the estimated maps gives higher signal in these distal areas comparing to Sum of Squares (see white arrows slice 3). The best results were obtained with the estimated Biot-Savart sensitivity maps, giving signal intensity that was more homogeneous throughout all slices and with up to 100% increase in SNR measured in distal areas of the heart (slices 1, 2 and 3).

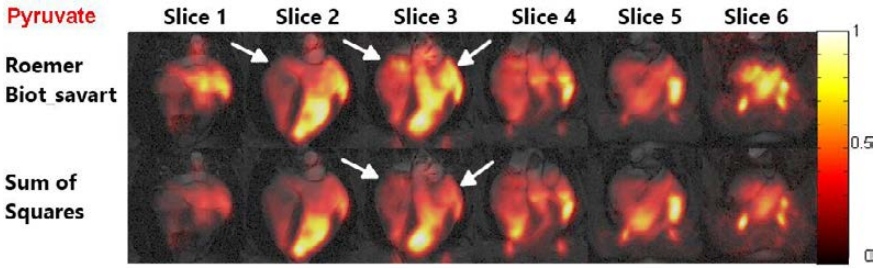

Fig. 2: *In-vivo* hyperpolarized ^{13}C pyruvate images of the pig heart (long axis) for all three reconstruction methods. All ^{13}C images were overlaid onto the corresponding anatomical images (Slices 1 through 6 from right to left). SNR improvement and signal homogeneity are noticeable in the Roemer method using estimated Biot-Savart coefficients (top row).

Conclusions: Roemer optimal reconstruction using numerically estimated coefficients using Biot-Savart resulted in better image quality than using Sum of squares of the acquired images. SNR improvements of up to a 100 % in areas closer to the base of the heart were demonstrated by using the Roemer reconstruction, as compared with sum-of-squares. This coil array and image reconstruction scheme may be suitable for human cardiac ^{13}C studies in the near future.

References: **1-** Lau et al. Rapid multislice imaging of hyperpolarized ^{13}C pyruvate in the heart. MRM (64) 2010. **2-** Dominguez-Viqueira et al. A five channel receive array for cardiac imaging using Hyperpolarized ^{13}C at 3T. ISMRM (4496) 2013. **3-** Dominguez-Viqueira et al. Optimal Reconstruction Using Receive Arrays for Hyperpolarized 13C Cardiac Imaging at 3T. ISMRM (4409) 2014. **4-** Roemer, P.B., et al., The NMR phased array. MRM, 1990. 16(2): p. 192- 225.

VURTIGO: Visual Understanding of Real-Time Image Guided Operations

Sebastian Ferguson[1], Labonny Biswas[1], Robert Xu[1,2], Philippa Krahn[1,2] Roey Flor[1], Samuel O. Oduneye[1,2], Mihaela Pop[1,2], and Graham A. Wright[1,2]
Ontario Consortium in Imaging for Cardiovascular Therapeutics
[1]*Physical Sciences, Sunnybrook Research Institute,* [2]*Medical Biophysics, University of Toronto*

Introduction. In recent years, many image-based methods and tools have been developed to improve the effectiveness of minimally invasive diagnostic and therapeutic procedures for the treatment of cardiac heart diseases. Fluoroscopy is still used routinely in clinical procedures, while MRI provides excellent tissue contrast and 3D information regarding subtle characteristics such as the 'gray zone' where the substrate of potentially lethal arrhythmia resides [1]. Our research efforts are focused on developing, testing and implementing a unique visualization platform named Vurtigo [2] for integration in preclinical and clinical frameworks relevant to X-ray guided and MR-guided interventions.

Methods. Vurtigo is designed to aggregate and display many sources of information in real-time. In particular, prior volumes, real-time scan planes, catheter coordinates, segmented ventricle models, and electro-anatomical maps can be visualized together to provide the experimenter with a much better picture of their procedure in progress. Vurtigo also contains advanced data analysis capabilities in order to streamline and enrich post-procedure analysis. It is capable of segmenting volumes manually or semi-automatically to produce meshes. Interactive landmark registration can be applied to images. Vurtigo is written in C++ and built upon several open-source, cross-platform projects: Qt [3], Visualization Toolkit (VTK) [4], Insight Segmentation and Registration Toolkit (ITK) [5], and Common Toolkit (CTK) [6], It uses Qt's plugin framework to enable the rapid and modular development of new features.

Results. Vurtigo has played an important role in several experiments:

- Visualization of actively tracked catheters; Vision-MR conditional catheters (Imricor Medical Systems, Burnsville, MN) were visualized in real-time [7].
- Electrophysiological (EP) mapping; Catheter guidance as well as post-processing done using Vurtigo to obtain left-ventricle electroanatomic voltage and isochronal maps [7], fusion of MR-derived meshes and isochronal maps (from X-ray guided CARTO systems) for validation of simulation studies [8].
- DE-MRI Tissue Characterization; Semi-automatic tissue classification of myocardium into 'healthy', 'infarct', and 'gray zone' [9].

Conclusion. We have successfully developed Vurtigo, a cross-platform, extensible visualization platform capable of advanced visualizations for image-guided interventions, which has a vital role in supporting our image-guided, in-vivo experiments. Ongoing work using Vurtigo includes guidance of catheters to ablation targets in the heart, and navigation of guidewires across chronic total occlusions.

References. [1] Pop. M, et al. IEEE Trans. Biomed. Eng. 2014;61(12):2930-38 [2] http://www.vurtigo.ca/ [3] http://qt-project.org/ [4] http://www.vtk.org/ [5] http://www.itk.org/ [6] http://www.commontk.org/ [7] Oduneye SO, et al. IEEE Trans. Biomed. Eng. 2013;60(9):2442–2449 [8] Pop M, et al. LNCS 2012;7746:364-74 [9] Lu Y, et al. Quant Imaging Med Surg. 2012;2(2):81–6.

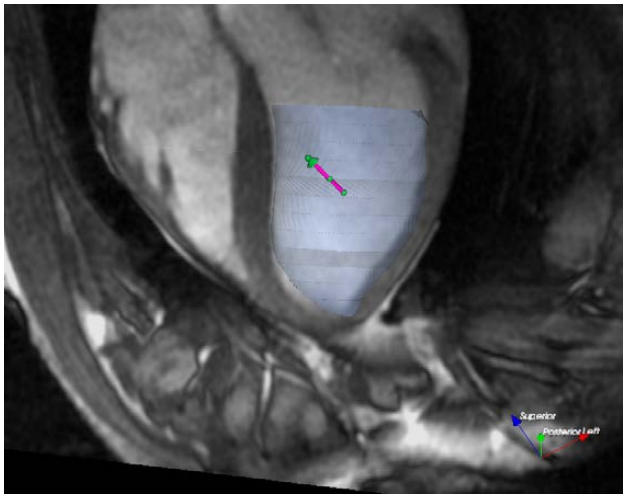

Figure 1: Segmented left ventricle, roadmap image, and catheter tip tracked in real-time.

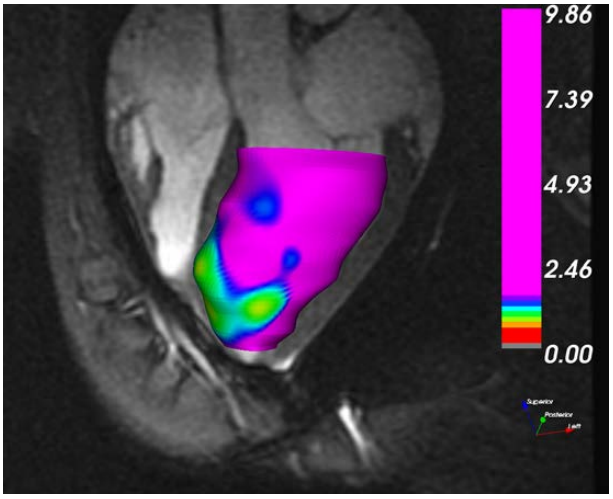

Figure 2: A segmented left ventricle mesh painted with an electroanatomical voltage mapping.

An Instinctive 3-Degree-of-Freedom Master-Side Input Device to a Robotic Catheter Navigation System

D. Gelman,[1] M. K. Lavdas,[1] M. Drangova[1,2]

[1]Robarts Research Institute, Biomedical Engineering Graduate Program; [2]Department of Medical Biophysics, Schulich School of Medicine & Dentistry, Western University, Canada

Introduction. Commercial robotic catheter navigation systems (RCNS), used for many types of cardiac ablation therapy, enable the interventionalist to remotely manipulate a catheter's position. Typically, the interventionalist operates the robotic systems unnaturally with a provided user interface that is not instinctive, often including a joystick-based controller. Specialized training is required to operate these systems, which may lead to future dependence on this technology. An intuitive solution was previously developed to facilitate translation form conventional to robotic intervention [1]. This device detects axial and rotational changes of a master-side catheter and although inherent to the interventionalist, its use in contemporary RCNSs is limited because modern interventional catheters are steerable, permitting catheter tip deflection. To address this, we have developed a master-side input device that detects motion changes in all three positional degrees-of-freedom.

Methods. The input device (Figure 1) enables direct manipulation of an ergonomic master-side catheter handle. A shell of a recycled steerable catheter handle is rigidly attached to 3D-printed concentric inserts. Incremental optical rotary encoders are coupled to extended shafts from these inserts in order to detect motion changes in the rotational and deflection degrees-of-freedom. The catheter handle assembly is then mounted on a custom linear motion stage whereby a rack and pinion mechanism coupled to another encoder detects axial motion. A dedicated embedded electronic system with a powerful microcontroller provides quadrature encoding and robotic motion scaling to enable high levels of precision. A wireless module enables streaming of position information to a slave robot. The design of the input device provides a calculated axial resolution of 13 μm and both rotational and deflection resolution of 0.18°. The accuracy of the input device was evaluated using an optical tracking system. Five 20-second motion profiles were manually imposed on each degree-of-freedom. Position data provided by the embedded electronic and tracking systems were then compared and the overall mean error was calculated.

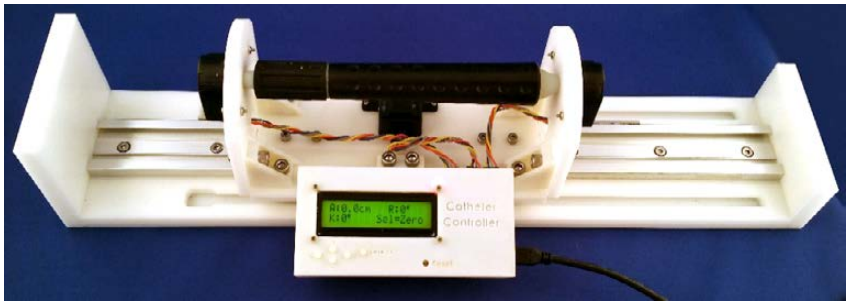

Figure 1. Master input device is shown. Encoders detect imposed motion from manual manipulation of the black handle. Position information is processed in real-time and then streamed to a slave robot.

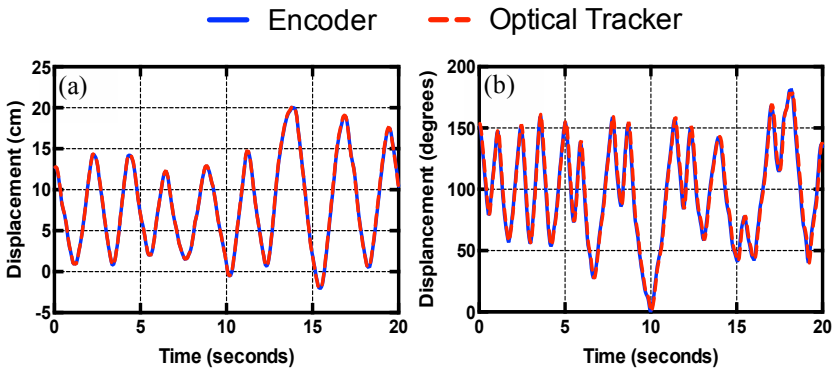

Figure 2. Examples of manual motion profiles of the input device and the corresponding tracked data with respect to time. Samples of axial and rotational motion, a) and b), are shown respectively.

Results and Conclusion. The input device shown to have an absolute mean error in the axial direction to be 0.44 ± 0.33 mm, rotary direction to be 0.41 ± 0.15°, and deflection direction to be 0.54 ± 0.43°. Indicative of a reliable master input device to an RCNS, the position data provided by the embedded electronic and tracking systems consistently overlapped (Figure 2). The on-board embedded system enables a user interface, real-time encoder processing, selectable motion scaling, and high-speed data transmission for optimal master-slave robotic control. We have developed and evaluated an instinctive master-side input device that can be used with an RCNS to fully manipulate a slave-side steerable interventional catheter with high precision and dexterity.

References. [1] Y. Thakur *et al.*, *SPIE*, vol. 6509, 2007.

Generation of high-contrast single-slice susceptibility weighted images in the brain at 7T

Z. Hosseini[1], J. Liu[2], and M. Drangova[2,3] (Supervisor)
[1]Biomedical Engineering Graduate Program, [2]Imaging Lab, Robarts Research Institute,
[3]Department of Medical Biophysics, University of Western Ontario, London, Ontario, Canada
Consortium affiliation: Ontario Consortium in Imaging for Cardiovascular Therapeutics

Introduction: Susceptibility weighted imaging (SWI) is an established magnetic resonance imaging (MRI) technique for visualization of veins in the brain. It utilizes information in the phase component of MRI to generate contrast between veins and the surrounding structures. Parallel imaging has become a commonly used tool to allow for faster image acquisition. However, a robust channel combination algorithm is required to ensure that the integrity of phase image is preserved.[1] Inter-echo variance (IEV) channel combination technique was shown to generate very accurate field maps from multi-echo data.[2] An accurate phase image can be generated from this channel combined field map. We hypothesize that high-contrast single-slice susceptibility weighted images can be generated from phase image obtained from IEV technique provided an optimal filter parameter is used in the pipeline.

Methods: Five healthy volunteers were scanned at 7T using a 16-channel head coil. Each image data were unwrapped[3] and filtered using a Gaussian filter constructed with several different kernel sizes. The output of each filtering operation was saved separately. The inter-echo variance was calculated for each of the images and used as a weighting factor for channel combination. A phase mask was generated from this channel-combined data. The fourth power[4] of this mask was then applied to the magnitude image to generate SWI slices. For quantitative analysis, single-slice SWI as well as minimum intensity projection (mIP) images through three, five, and seven slices of the SWI were investigated. Contrast analysis was performed as follows: five lines were drawn across individual veins and each line profile was used to isolate the vein intensity (minimum on the line profile – Fig. 1) and the intensity of white matter (mean of the pixel values on the line, outside the vein). The absolute difference of the two was taken as the contrast. Similarly, contrast in magnitude images were calculated and used to normalize the SWI contrast. The resulting contrast calculated from each line drawn across the vein was then averaged.

Results: Single slice SWI was found to have the highest normalized contrast, followed by three-slice, five-slice, and seven-slice mIP's (See Figures 1 and 2). Smallest vein detected had a diameter of 0.57 mm and observed on single-slice SWI processed with kernel size of 7 pixels.

Discussion & Conclusions: Normalized contrast calculated for the single slice SWI (not shown in Fig. 1b) was particularly high compared to the mIP images. Additionally, the smaller the volume of the tissue, through which the mIP was taken, the greater the contrast calculated was. This can be due to increased clutter of veins in the mIP images, as they reflect the structures in a volume. High contrast observed in the single slice images is important as it allows accurate localization of veins. Furthermore, it enables accurate registration with images acquired with other sequences or modalities.

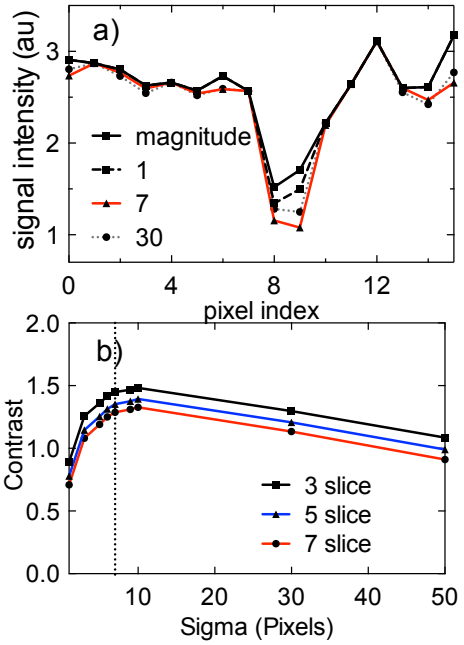

Fig. 1 a) Representative signal intensity profiles though a vein at varying σ. b) Normalized contrast plots as a function of increasing σ, demonstrating peak contrast near 7 pixels. Normalized contrast could not be calculated for the single slice case, since veins were not visible in the single-slice magnitude image.

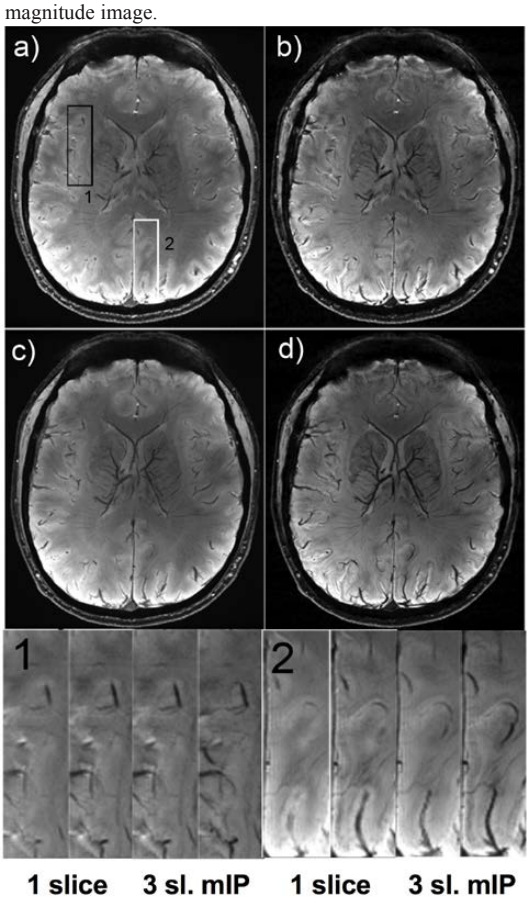

Fig. 2 Single slice (SS) (a) magnitude image and (b) IEV-SWI. 3-slice mIPs through (c) magnitude and (d) IEV- SWI. Magnified images of regions 1 and 2, shown in a), demonstrate the increased vessel conspicuity using IEV-SWI.

References: (1) Schweser *et al*., MRM 2013, 69:1581-1593. (2) Liu *et al.,* MRM 2014. (3) Liu and Drangova, MRM 2012, 68:1303-1316. (4) Haacke *et al.,* MRM, 2004, 52:612-618.

Enhancing CT visualization for left atrial wall thickness measurement

J. Inoue,[1] A. C. Skanes,[2] and M. Drangova[1]
[1]Robarts Research Institute, [2]Department of Medicine, The University of Western Ontario, London, Ontario, Canada
Consortium: OCICT, Supervisor: M. Drangova

Introduction. Left atrial wall thickness (LAWT) is a possible cause of radiofrequency catheter ablation (RFCA) failure in the left atrium.[1] The suspected mechanism is under-ablation of unexpectedly thicker tissue, leading to incomplete ablation,[2] but dosing cannot be arbitrarily increased due to the possible complications of over-ablation such as often-fatal atrioesophageal fistulae.[3] With contrast-enhanced cardiac CT, the endocardial boundary of the left atrial wall (LAW) is easily distinguished, but the epicardial boundary is not. A typical method is to identify hypo-intense pixels beyond the atrial wall that indicates a fat layer,[4] but visually separating layers of tissue in the region is difficult, even for experts.[5] Our goal is to investigate if enhancing the image visualization can improve the reliability of measuring LAWT.

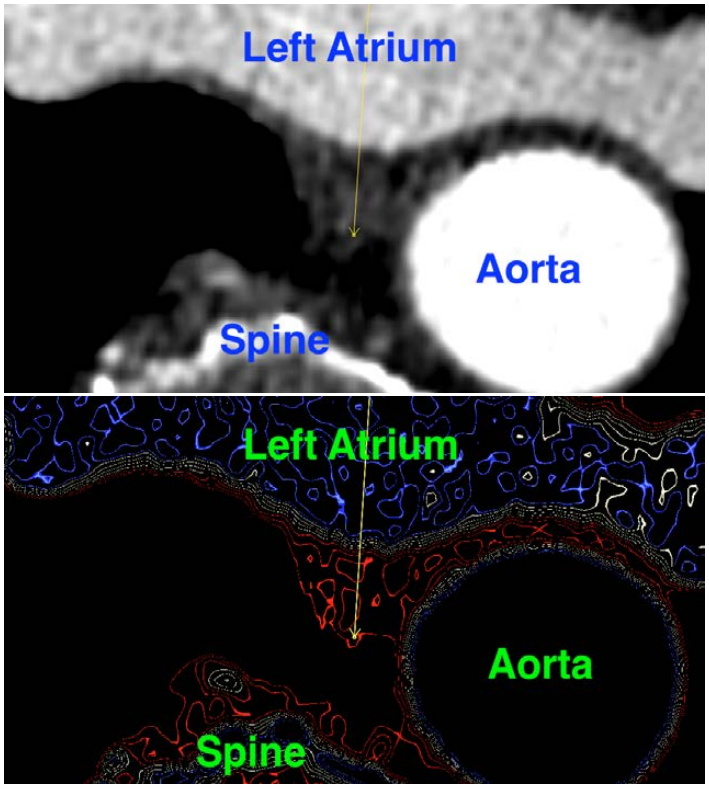

Figure 1: Cardiac CT with arrow marking measurement location/direction. (Above) *Traditional* method: intensity image. (Below) *Enhanced visualization* method: iso-Hounsfield unit contours.

Methods. LAWT measurements were made using two visualization methods (figure 1) at identical locations and compared for intraobserver and interobserver variability.

Measurements: Both methods used single axial slices of contrast-enhanced CT images with a preselected measurement location and direction. For the *traditional* method, the image was displayed as an intensity image with a linear transfer function based on Hounsfield units. The observer adjusted the contrast to emphasize the LAW, then drew a line segment across the thickness of the wall with a mouse. For the *enhanced visualization* method, software was developed that displayed sets of coloured iso-Hounsfield contour lines. The observer adjusted the iso-Hounsfield contours to bound the atrial wall by relatively smooth contours, then further smoothed the contours by adjusting a blurring parameter before marking the LAW.

Experiment: Twenty contrast-enhanced cardiac 3D CT images were each measured at three preselected locations: (1) the posterior LAW adjacent to the lungs, (2) the posterior LAW adjacent to the esophagus, and (3) the left lateral ridge (just inside the left superior pulmonary vein). Each location was measured by an observer once by each method per experiment in a randomized order. One observer (A: postdoctoral fellow experienced with cardiac CT) performed the experiment twice (different randomizations) to establish intraobserver reliability. A second observer (B: clinical cardiac electrophysiologist) performed the experiment once to establish interobserver reliability.

Results. Intraobserver reliability, measured by interclass correlation coefficient (ICC), favored the *enhanced visualization* method over the *traditional* method overall (0.54 vs. 0.29, $p = 0.01$) and at locations (2) (0.64 vs. 0.34, $p = 0.04$) and (3) (0.55 vs. 0.21, $p = 0.04$). Interobserver ICC favored the *traditional* method (0.29 vs. 0.05, $p = 0.03$) overall, and specifically at location (2) (0.19 vs. -0.24, $p = 0.03$). All other regional ICC differences were non-significant. Blurring use varied between observers: observer (A) increased the smoothing parameter 5.4 and 5.5 times per measurement compared to 0.7 times per measurement for observer (B).

Conclusions. Intraobserver reliability was improved due to the *enhanced visualization* but this did not generalize to the interobserver case. This may be due to differences in observers' use of the blurring parameter – a new source of variation that should be accounted for.

References. [1] Suenari *et al.* Heart Vessels. 2012;28:360-368. [2] Callans *et al.* J Cardiovasc Electrophysiol. 2004;15:1050-1055. [3] Somnez *et al.* Ann Thorac Surg. 2003;76:281-283. [4] Beinart *et al*. J Cardiovasc Electrophysiol. 2011;22:123201236. [5] Koppert *et al.* Proc. IEEE ISBI. 2010;480-483.

Three dimensional retrospective motion correction in MRI using spherical navigator echoes (SNAV)

P. Johnson,[1] J. Liu,[1] T. Wade[1] and M. Drangova[1,]
Consortium: Ontario Consortium in Imaging for Cardiovascular Therapeutics
[1] Imaging Laboratories, Robarts Research Institute, Western University, London, Ontario, Canada

INTRODUCTION: Patient motion during magnetic resonance imaging (MRI) can corrupt image data and severely degrade image quality. Three dimensional motion is a significant problem that remains unsolved; it is a limiting factor in many MRI applications. If the motion of the subject is known, the raw image data can be adjusted to compensate for the motion. Image space navigators, navigator echoes, optical tracking and autocorrect methods are all techniques that measure subject motion. Navigator echoes, acquired in the Fourier domain of the image (k-space), can be acquired more quickly than image space navigators[1] and unlike optical tracking, do not require additional external hardware. They can measure a larger range of motion than autofocus methods and are less computationally demanding[2]. Spherical Navigator Echoes (SNAV) can measure motion in all 6 degrees of freedom simultaneously[3,4]. The objective of this work is to develop a navigated fast gradient echo sequence (EFGRE-SNAV) and retrospectively correct phantom images to improve image quality.

METHODS: ***SNAV-interleaved imaging sequence.*** The navigated image sequence developed in this study is a modified fast gradient echo sequence (EFGRE-SNAV). This sequence acquires two Cartesian lines of k-space data for the image and then acquires a SNAV; this is repeated until all the image data is acquired. The built-in SNAV has a radius of $0.40cm^{-1}$ and 2508 sample points.

Data acquisition. Two motion trials were performed. In each trial a pineapple was scanned using the EFGRE-SNAV sequence following a required 4s baseline prescan. The imaging parameters were TR/TE = 25/7.6 ms, flip angle =10°, bandwidth = 125 kHz, FOV = 16×16×24cm^3 and scan time = 6.5 mins. The pineapple was manually rotated and translated several times during the acquisition. An additional reference image was acquired of the stationary pineapple after both motion trials. These no-motion images serve as a gold standard.

Motion Correction. All 6 rigid-body motion parameters were extracted from 3712 interleaved navigators. Using Matlab, motion compensation was performed on the raw data of the severely motion corrupted images based on the measured motion. The resulting images were compared to the no-motion reference images qualitatively and quantitatively using the Signal to Artifact Ratio metric (S2AR)[5].

RESULTS: For both motion trials, the image acquired during phantom motion has motion artifacts. The corrected images are of visibly better quality. Motion artifacts are reduced and several features obscured in the corrupted images are recovered in the corrected images. The S2AR was calculated for the uncorrected and corrected images. S2AR increased from 4.0 to 15.4 for trial 1 and 5.8 to 19.7 for trial 2. The results for trial 2 are shown in the figure.

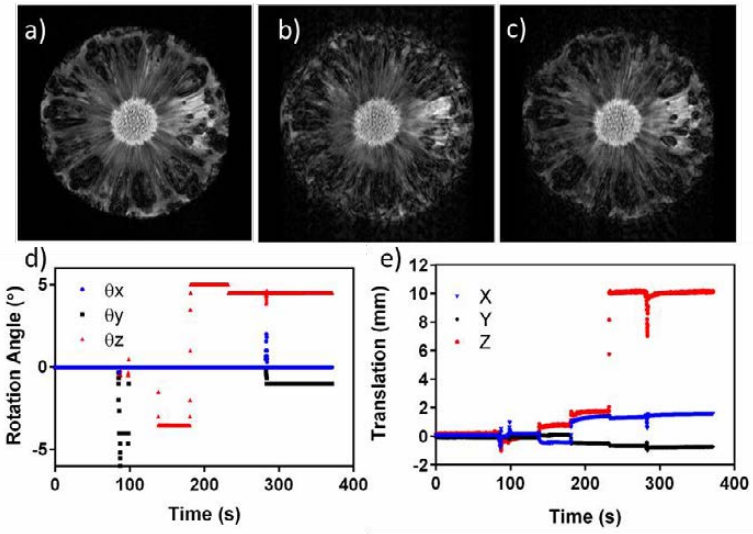

Single axial slice of the 3D (a) reference image (b) uncorrected motion image (S2AR=5.8) (c) motion corrected image (S2AR=19.7). The measured rotations are shown in (d) and the translations in (e).

DISCUSSION & CONCLUSIONS

EFGRE-SNAV, was able to track the rigid motion of a phantom during image acquisition. The SNAV data was successfully used to improve image quality. SNAV measurement and processing times are very short (<30ms), making this technique feasible for a prospective motion correction in the future. For the first time, we have demonstrated that spherical navigators can be used for intra-image motion correction. Our results provide initial validation that a SNAV technique may be useful for real time motion correction in brain and cardiac MRI.

REFERENCES (1)Maclaren, et al., MRM 69:621-36, 2013 (2)Loktyushin, et al., MRM 70:1608-18, 2013 (3) Welch, et al., MRM 47:32-41, 2002. (4)Liu et al., MRM 65:506-14, 2010. (5)Maclaren et al., MRM 63:162-70, 2010.

Taking advantage of artifacts: Coherent half field of view replication passive tracking technique for controllable susceptibility devices for magnetic resonance imaging in the presence of motion

Justin Y.C. Lau[1,2], Jennifer Barry[2], and William Dominguez-Viqueira[2]
Ontario Consortium in Imaging for Cardiovascular Therapeutics
[1]Medical Biophysics, University of Toronto, [2]Physical Sciences, Sunnybrook Research Institute, Toronto ON

Introduction: We previously demonstrated the passive tracking of a controllable device where the susceptibility effect can be mechanically turned ON and OFF.[1] The mechanism of device location exploited the creation of a coherent replication of the susceptibility artifact that is precisely shifted half a field of view (FOV) in the phase-encode direction, achieved by toggling the susceptibility effect every repetition time (TR) to create a modulation of k-space. In this study, the device is toggled only once in between the sequential acquisition of odd and even phase-encodes, which improves temporal resolution.

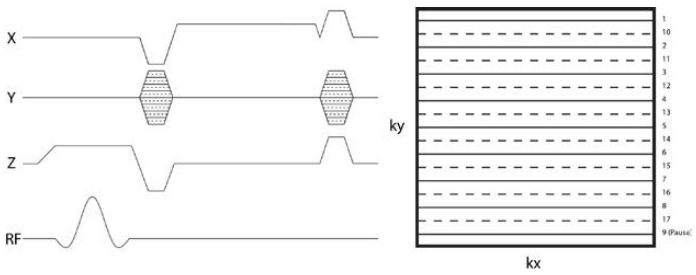

Figure 1: 2D FSPGR sequence with modified phase-encoding scheme (right) to sample odd k-space lines in stage 1, pause to allow manual device toggling, then sample even k-space lines in stage 2.

Methods: Experiments were performed on a 3 T scanner using a modified 2D FSPGR sequence with an acquisition scheme (Fig 1) sampling in two stages separated by a pause. A modulation of k-space is achieved by running the first stage with the device ON and the second stage with the device OFF, toggling the device during the pause. *In vivo*, a 6F sheath was placed in the femoral artery of a healthy Yorkshire pig and the catheter was advanced toward the common iliac artery via a guidewire under X-ray fluoroscopy.

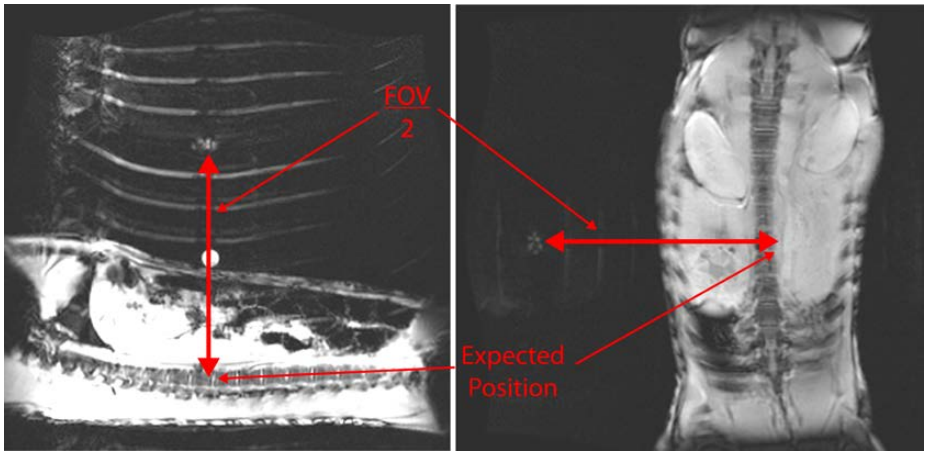

Figure 2: Sagittal (left) and coronal (right) images of pig abdomen showing FOV/2 artifacts of the controllable susceptibility device in the common iliac artery. TR/TE = 100/6.6 ms, FA = 20°, 48 cm FOV, 1 cm slice thickness, acquisition time 28.8 s, total scan time 40 s.

Results: In the iliac artery of the pig, the region of dephasing around the device attached to the catheter tip appears bright in the phase-encode direction displaced by exactly FOV/2 in the sagittal and coronal views (Fig 2). In addition to the artifact from the device, other artifacts resulting from a combination of motion and flow of the femoral artery are especially apparent in the sagittal image. These images were acquired without respiratory gating or breath hold to examine the full impact of motion on the feasibility of locating the device. Despite the severity of the motion artifacts, the FOV/2 ghost of the device was distinct and the device was located unambiguously *in vivo*. This technique also works with a 9 mm balloon catheter (Fig 3).

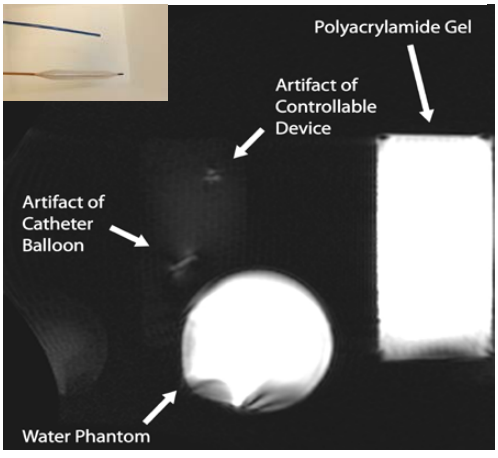

Figure 3: Projection of gel phantom showing the FOV/2 artifacts of the controllable device and a 9 mm catheter balloon (imaging time 2 s).

Conclusions: A method for passive tracking using our susceptibility device and a clinical balloon catheter was demonstrated *in vitro* and *in vivo* without respiratory gating. This new method reduces imaging time from several minutes to less than 45 s. This tracking method may be extended to other tools or devices for interventional MR procedures.

Acknowledgements: Funding support from NSERC and OICR

References: [1] W. Dominguez-Viqueira *et al*. (2014) *Proc ISMRM* 22: 3705. [2] W. Dominguez-Viqueira *et al*. (2014) *MRM* 72(1): 269.

Influence of MagA Expression on MRI Relaxation Rates in Different Cell Types

Liu, L; Sengupta, A; McGirr, R; Thompson, RT; Prato, FS; Hoffman, L; Gelman, N and Goldhawk, DE
Ontario Consortium in Imaging for Cardiovascular Therapeutics
Imaging Program, Lawson Health Research Institute, London, ON, Canada
Medical Biophysics, Western University, London, ON, Canada

Introduction: In all mammalian cells analyzed to date, MagA expression leads to increases in iron contrast [1]. However, iron handling activities do vary among cell types and may influence detection of magnetosome-like structures by MRI. We compared MDA-MB-435 melanoma cells with P19, a model for cardiac differentiation.
Methods: Cells were cultured in the presence or absence of iron supplementation: 250 µM ferric nitrate / medium. Total cellular iron was measured by inductively-coupled plasma mass spectrometry (ICP-MS). MRI relaxation rates (R2*; R2; R2' = R2* - R2) were obtained at 3T using cells mounted in gelatin phantoms [2].
Results: Figure 1 indicates the specificity of R2' for detection of cellular iron in human MDA-MB-435. Table 1 shows that both untransfected (P19) and MagA-expressing (MagA) P19 cells exhibit similar iron uptake when cultured 1 week in the presence of iron supplementation (+Fe 0h). However, approx. 24 hours after the removal of iron supplement from P19 culture (+Fe 18h), active iron export is apparent. Importantly, MagA-expressing cells retain their intracellular stores of iron (+Fe 24h) and R2' contrast (Fig. 2) while parental cells do not.
Conclusions: The iron handling activities of P19 cells are quite different than those of MDA-MB-435 [2]. Nevertheless, MagA expression is positively correlated with R2' in both cell types in response to iron uptake.

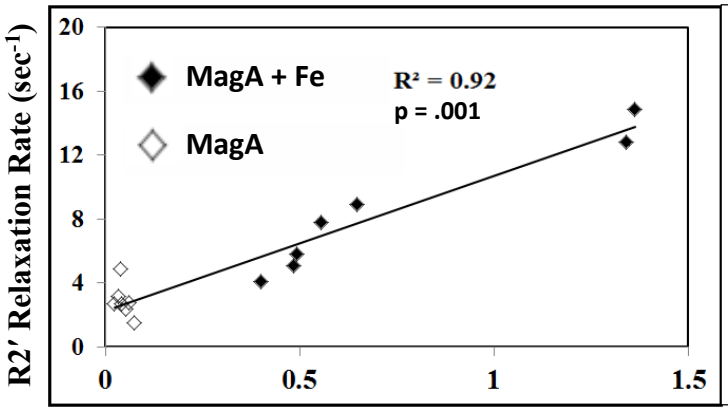

Figure 1. R2′ Relaxation Rate Reflects Total Iron Content in MagA-expressing Cells. An increase in the R2' component of transverse relaxation rate is related to increasing iron content in MagA-expressing MDA-MB-435 tumour cells, cultured in the presence (filled diamonds) or absence (empty diamonds) of iron supplementation. A significant correlation ($p < 0.005$) was observed between R2′ and total cellular iron content. Similar analysis in P19 cells gives $R^2 = 0.96$ ($p < 0.001$).

Table 1. MagA Expression Overrides the Iron Export Activity of P19 Cells

Sample	Cellular Fe*	Cellular Zn*	Ratio Fe/Zn
P19	0.035	0.252	0.14
P19 + Fe 0h	1.805	0.240	3.76
P19 + Fe 1h	0.625	0.262	2.39
P19 + Fe 2h	0.386	0.264	1.46
P19 + Fe 18h	0.258	0.284	0.91
MagA	0.051	0.264	0.26
MagA + Fe 0h	2.055	0.235	4.37
MagA + Fe 1h	0.907	0.178	3.40
MagA + Fe 2h	0.970	0.241	4.02
MagA + Fe 24h	0.939	0.284	3.31

* Elemental analysis was obtained by ICP-MS and reported as µg Fe or Zn / mg protein.

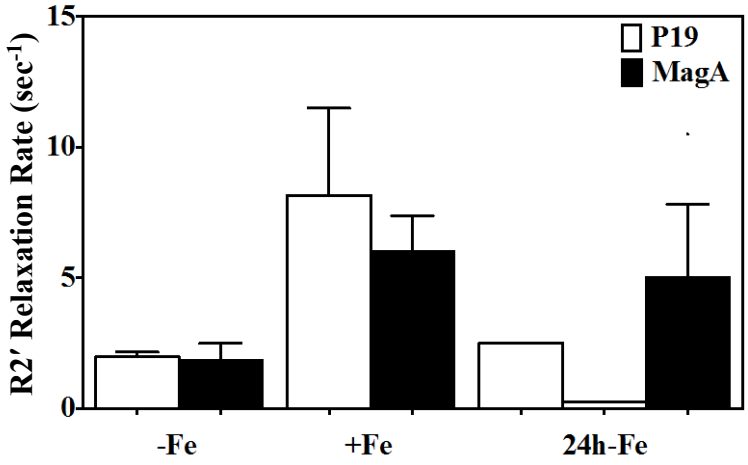

Figure 2. Influence of Iron Supplementation on Transverse Relaxation Rates in MagA-expressing P19 Cells. After 1 week of culture +/- iron-supplemented medium, cells were harvested either immediately (±Fe) or after a further 24 hours of culture in non-supplemented medium (24h-Fe). 3T MRI was performed as previously described [2]. Averaged data are +/- SEM; n = 3-7.

References: **[1]** Goldhawk et al (2012) Nanomed Nanobiotechnol **4**, 378-88; **[2]** Sengupta et al (2014) Frontiers in Microbiol **5**, article 29.

Design, Development and *in vivo* Evaluation of a Remote Catheter Navigation System with 3-Degrees-of-Freedom

M. A. Tavallaei,[1] D. Gelman,[1] M. K. Lavdas,[1] A. Skanes, [2] D. L. Jones[2,3] and M. Drangova[1,4]
[1]Robarts Research Institute, Biomedical Engineering Graduate Program; [2]Division of Cardiology, Department of Medicine, Schulich School of Medicine & Dentistry; [3]Department of Physiology and Pharmacology, Schulich School of Medicine & Dentistry; [4]Department of Medical Biophysics, Schulich School of Medicine & Dentistry, Western University, Canada

INTRODUCTION

Cardiac catheterization has become an essential tool in the management of cardiac and vascular diseases, in general, and the treatment of cardiac arrhythmias in particular. The conventional approach to percutaneous transluminal catheter procedures relies on fluoroscopic x-ray imaging for guiding the catheterization procedure. However, fluoroscopic imaging is a source of irradiation that exposes the interventionalists and staff to scattered radiation on a daily basis. This necessitates the use of heavy lead aprons for partial protection [1,2] that are known to cause chronic neck and back pain with prolonged use [1]. To overcome this limitation, we have proposed a robotic system that allows for remote navigation of a conventional steerable catheter with 3-degrees-of-freedom. The proposed design is an attempt to overcome the limitations of our group's earlier work [3] and other robotic solutions [4].

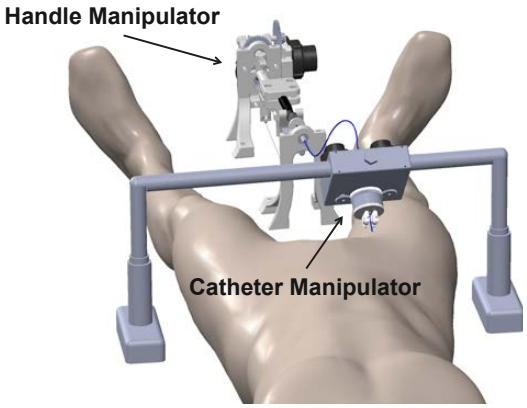

Fig. 1. The slave robot is shown. In the example setup, the catheter manipulator is positioned arbitrarily on top the patient and the handle manipulator between the patient legs.

METHODS

The master-slave robotic system measures the motions imparted by the user on a conventional catheter handle in a master unit [3] and relays them to a slave robot (Fig. 1), replicating this motion on a patient catheter. The slave is comprised of a catheter manipulator (CM) and a handle manipulator (HM). A versatile mount allows the CM to be positioned and orientated arbitrarily at the catheter point of entry. The CM incorporates a differential gear mechanism and a set of rollers that grip the patient catheter. This mechanism enables radial and axial catheter manipulation while the actuators remain fixed. Components of the CM that come in contact with the catheter can be easily disconnected for replacement/sterilization. The HM is comprised of a rotating gantry that holds the catheter handle and uses a winch/spring combination to push/pull the catheter knob/plunger to flex the catheter. Two actuators are used in the HM – one pulls the string (actuates winch) and another rotates the gantry in synchrony with catheter rotation to prevent catheter twisting. The presented robot was evaluated *in vivo* by an interventionalist, using 3 male swine. To evaluate the efficacy of navigation, 4 leads were placed at: the right atrial appendage (RAA); the right ventricle lateral wall (RV-LW); the right atrium lower septum (RA-LS), and the right ventricle outflow track (RV-OT). For each target, 4 navigation attempts were made with each of the manually operated catheter (MOC) and the robotically operated catheter (ROC) guided with fluoroscopy. Navigation time of each mode to each target was recorded. To evaluate the feasibility of remote ablation, using the ROC, 50-watts (60 s) was delivered at 5 anatomical targets: high lateral right atrium (HL-RA); RAA; RV-LW; coronary sinus (CS), and right atrial septum (RAS).

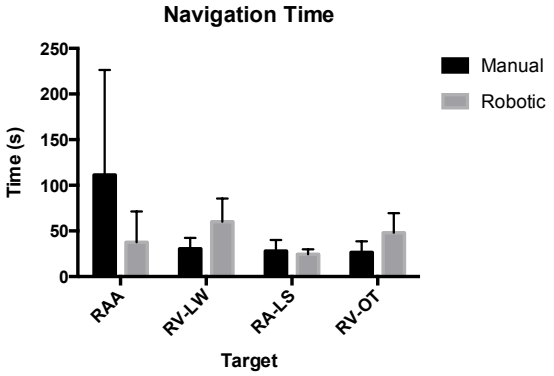

Fig. 2. Navigation time to four targets using both the manual and robotic method are shown.

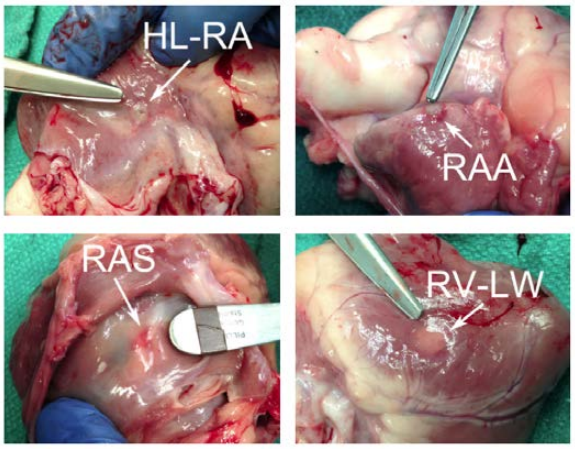

Fig. 3. Visual confirmation of the created ablation lesions on the: HL-RA, RAA, RAS, and RV-LW.

RESULTS AND DISCUSSION

All 4 lead targets were successfully reached with both the MOC and the ROC in all trials. A successful navigation was confirmed based on orthogonal fluoroscopic images, that both showed the catheter tip in contact with the target lead. Figure 2 shows the navigation time of each method to each of the four targets. Statistical evaluations (2-way ANOVA) showed that the method of navigation had no significant effect on navigation time (p=0.705). Large ablation lesions were clearly visible directly after excising the heart. The lesion placed at the CS was not clearly visible. Figure 3 provides visual confirmation of the created ablation lesions. This study demonstrated, *in vivo,* the feasibility and safety of the presented robotic system for remote navigation and ablation using conventional catheters.

REFERENCES

[1] L. W. Klein *et al., Catheter Cardiovasc Interv,* vol. 73, 2009. [2] A. Roguin *et al*., *Amc Journal of Cardiology,* vol. 111, 2013. [3] Y. Thakur *et al.*, *IEEE Trans Biomed Eng,* vol. 56, 2009.[4] H. Rafii-Tari *et al., Ann Biomed Eng,* vol. 42, 2014.

Image-based Personalized Analysis and Modeling of Cardiac Structure and Function: A Robust Method for Automatic Left-Ventricular Infarct Segmentation

Eranga Ukwatta,[1,3] Katherine Wu,[2] Natalia A. Trayanova,[3] and Fijoy Vadakkumpadan[3]

[1]Sunnybrook Research Institute, University of Toronto, ON, Canada
[2]Division of Cardiology, Department of Medicine,
Johns Hopkins Medical Institutions, Baltimore, MD, USA
[3]Department of Biomedical Engineering, Johns Hopkins University, Baltimore, MD, USA

Introduction: Segmentation of myocardial infarct from late-gadolinium enhanced magnetic resonance (LGE-MR) images is paramount to quantification of infarct mass and patient-specific cardiac modeling aimed at guiding the treatment of arrhythmias under ischemic cardiomyopathy. Existing approaches to this segmentation are either labor-intensive or inaccurate under image noise and intensity variation.

Methods: Short-axis LGE-MR images were acquired from 61 post-infarct patients. Left ventricular (LV) infarct was segmented from the image slices using a convex max-flow (CMF)–based optimization algorithm, where the objective function incorporated spatial regularization. Three-dimensional (3D) infarct geometries were reconstructed from the segmentations using a novel shape-based interpolation method. The methodology was evaluated, in comparison with the widely used signal-threshold to reference mean (STRM) and full-width at half maximum (FWHM) methods, using geometry-based metrics and outcomes of electrophysiological simulations of sinus rhythm and ventricular tachycardia (VT) to those of manual segmentations.

Results: The CMF method was significantly more accurate than the alternatives as per Dice similarity coefficient (Panels A-C). The activation maps observed in electrophysiological simulations conducted with models incorporating segmentations by CMF and manual methods matched closely (Panel D).

Conclusion: Our novel method to segment LV infarct from LGE-MR images has outperformed alternatives. The developed method is an important step toward automatic and robust segmentation of infarcts for image-based, personalized analysis and modeling of cardiac structure and (dys)function.

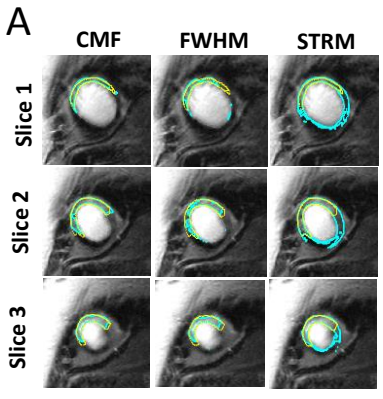

Infarct segmentations computed by different methods (cyan), and manual delineations (yellow), for three example LGE CMR image slices.

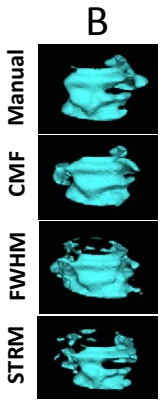

Surfaces of 3D infarct reconstructions obtained from segmentations by different methods, for an example patient heart.

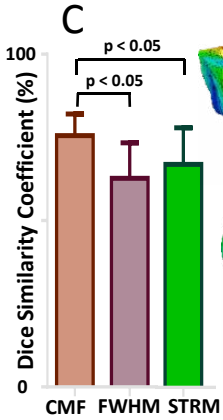

Accuracies of infarct segmentations by different methods, according to the Dice similarity coefficient.

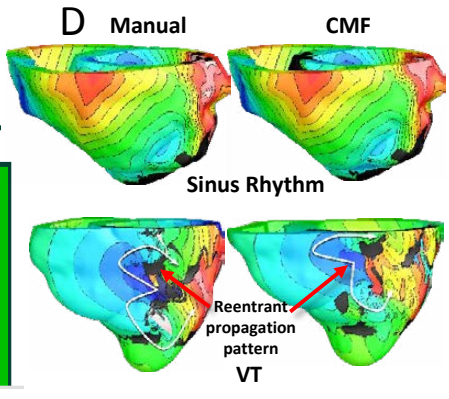

Activation maps of one beat of sinus rhythm, and one cycle of ventricular tachycardia simulated with models that incorporate manual and CMF infarct segmentations.

Respiratory motion model based correction for MRI-guided intracardiac electrophysiology procedures

Robert Xu[1,2], Prashant Athavale[3], Philippa Krahn[1,2], Kevan Anderson[1,2], Jennifer Barry[1], Labonny Biswas[1], Venkat Ramanan[1], Nicolas Yak[1], Mihaela Pop[1,2], Graham Wright[1,2]

1. Physical Sciences Platform, Sunnybrook Research Institute, Toronto, ON, Canada. 2. Medical Biophysics, University of Toronto , Toronto, ON, Canada. 3. Mathematics, University of Toronto , Toronto, ON, Canada.

Background: Recently, there is an increased interest in using MRI to guide electrophysiology (EP) procedures as an alternative to X-ray fluoroscopy guidance, due to its excellent soft tissue contrast and lack of radiation. However, there exist tradeoffs between different MRI guidance schemes. In this work, we explore the feasibility of deriving a motion model from complementary prior and realtime datasets, and evaluate its potential for improving the targeting accuracy of MRI-guided EP procedures.

Methods: Motion imaging studies were performed for 6 healthy pigs, and 9 MRI-guided catheter ablations were successfully applied. Initially, a multi-slice 3D roadmap volume was acquired using a GE FIESTA imaging sequence, while the animal was mechanically ventilated and breath-held at end expiration. During the same experiment, a fast 2D balanced-SSFP spiral sequence (HeartVista) was also used to acquire free-breathing images of the heart, along with synchronized physiology data representing cardiac and respiratory phase. Under 3D prior roadmap guidance, an MR compatible and actively tracked catheter (Imricor Medical Systems) was then placed into the left ventricle (LV), while the distal tip of the catheter was continuously tracked in realtime [1], along with the corresponding physiology data. Subsequently, the catheter was maneuvered to a location along the LV wall, where an RF ablation was performed. The anatomical location of the lesion was confirmed in a post-ablation contrast enhanced IR-SSFP image. We retrospectively computed the distance between the tracked catheter ablation positions and the observed lesion center. A respiratory motion model based on multiscale registration of the ECG gated 3D prior image to 2D realtime free-breathing images was also generated [2]. The individual motion parameters were extracted and fitted as a function of the respiratory physiology data (Fig. 1). The specific motion model was then used to correct the erroneous catheter tracked positions relative to the heart wall based on their physiology data, and the distances between the motion corrected positions and the lesions were computed.

Results: The mean distance between the uncorrected catheter tracked positions and the lesion locations was 5.44±1.70 mm. After the motion correction was applied from the derived model, the mean distance between the corrected catheter positions and the lesions was 3.97±1.67 mm. An example of motion correction is shown in Fig. 2.

Conclusions: We successfully demonstrated the feasibility to produce a data-driven model to retrospectively correct for the respiratory motion of the heart. Future work will focus on exploring the potential of the model to prospectively correct for motion and improve the targeting accuracy during interventional MR-EP procedures.

References: 1. C. Dumoulin *et al.: MRM* 1993, **29**: 411-415. 2.R. Xu *et al.: IEEE TBME* 2014, **61**: 2621 - 2632

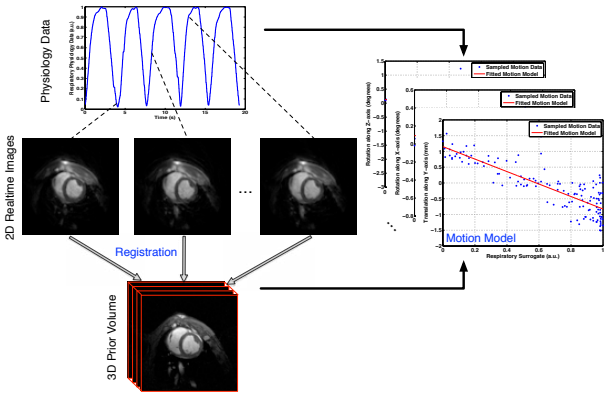

Fig. 1 Schematic diagram of the motion model. Realtime 2D free breathing images of each pig are registered to a corresponding end expiration 3D prior volume. All images are cardiac gated and acquired along with synchronized respiratory physiology data. Image registration was used to extract motion parameters consisting of rotations and translations along the x,y,z imaging axes. Each parameter is then fitted as a linear function of the physiology data to produce a subject-specific respiratory motion model.

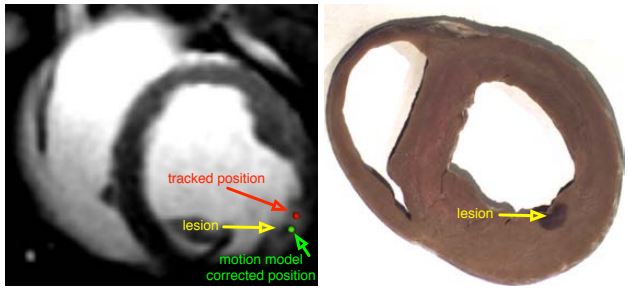

Fig. 2 Ablation position correction. (a) Contrast enhanced IR-SSFP image showing the created lesion. Red arrow points to the location of an erroneous realtime tracked catheter tip position during RF ablation. Yellow arrow points to the actual anatomical location of the created lesion. A green arrow points to the corrected catheter position after motion model was applied to the erroneously tracked position. (b) The same lesion is shown in gross pathology at the approximate short axis slice location, after the animal was sacrificed.

OICR Imaging Translation Program

OICR ITP

Oral Presentation and Poster Abstracts

Energy-subtraction angiography for dynamic vascular imaging: Comparison of image quality with conventional methods

Christiane Sarah Burton and Ian A Cunningham

Imaging Research Laboratories, Robarts Research Institute, 100 Perth Drive, London Ontario, N6A 5K8, Canada
Department of Medical Biophysics, The University of Western Ontario, London, Ontario N6A5C1, Canada

Introduction:
Cardiovascular disease (CVD), as of 2008, is currently the leading cause of mortality worldwide.[1] It is estimated that 17.3 million people died of CVD in 2008, representing 30% of all global deaths, and of these an estimated 7.3 million were due to coronary artery disease.[2] Vascular imaging is widely used for the assessing the location and severity of arterial narrowings. Digital subtraction angiography (DSA) is widely used for vascular imaging that removes anatomic structures by subtracting a pre-injection image (mask) and post-injection images (contrast). However, any motion that occurs during the time gap of several seconds between a mask and contrast image results in improper subtraction that obscures important details of iodinated vessels making DSA unsuccessful particularly for imaging the heart. We are investigating energy subtraction angiography (ESA) of two contrast images acquired at low and high energies in rapid succession (~10 ms) thereby making the method insensitive to motion artifacts. This method was suggested in the 1970's, however, it was concluded at the time that image quality for ESA could not compete with that of DSA and the approach was essentially abandoned.[3] We think that reduced SNR for ESA was limited by technology at the time which is why we are investigating the potential of ESA with modern technology and evaluating technological requirements to make ESA successful today. In this study we will look at comparing the fundamental signal-to-noise ratio (SNR) between ESA and DSA for similar patient exposures.

Methods:
A custom hardware and software interface was developed to synchronize fast ESA acquisition. Iodine signal and noise was measured experimentally by constructing a vascular phantom consisting of an iodinated step-wedge submerged in 20 cm of water. In a horizontal beam set-up, ESA and DSA images of the phantom were acquired. For ESA low and high applied tube voltages of 50 and 120 kV (2.5 mm of copper), respectively, and for DSA it was 80 kV. Iodine SNR per root entrance exposure was calculated for each iodine concentration.

Results:
It is shown both theoretically and experimentally that ESA can provide angiographic images with comparable SNR to DSA for iodine low mass loadings of 0-0.1 g cm^{-2} for lower patient entrance exposures. This requires very low noise detectors to ensure images are acquired above the quantum noise limit. We show that our iodine SNR measurements are in excellent agreement with theory and therefore validate our theoretical calculations of iodine SNR. We demonstrate that we can obtain iodine-specific images of ESA and how it compares to DSA.

Significance of results:
With current medical equipment it is possible to obtain angiographic iodine-specific images using ESA with image quality similar to DSA for the same patient entrance exposure. ESA can to produce vascular images with background suppression, similar to DSA, without the need for a mask image. For the same patient entrance exposure, iodine signal-to-noise ratio is comparable between ESA and DSA indicating that the total patient exposure does not need to be increased. ESA shows removal of non-uniform background which indicates that it can be used in applications where there is a varying soft-tissue background.

Current work:
Demonstrate real-time ESA by implementing both a fast kV-switching generator and fast high quality sensor leading to a demonstration system. We will also compare real-time ESA SNR per root exposure with coronary angiography, and show other ways of optimizing parameters for ESA and compare to DSA. We have introduced gadolinium as a contrast agent to reduce the quantum noise and remove soft-tissue contrast and bone from the image.

Reference:
1. "Statistics Canada, CANSIM Table 102-0529: Deaths, by cause, Chapter IX: Diseases of the circulatory system (I00 to I99), age group and sex, Canada, 2000 to 2006," 2010.
2. Dejan Loncar Colin D Mathers. Projections of global mortality and burden of disease from 2002 to 2030. PLoS Medicine, 3(11):442, 2006.
3. C. A. Mistretta, M. G. Ort, F. Kelcz, J. R. Cameron, M. P. Siedband, and A. B. Crummy. Absorption edge fluoroscopy using quasi-monoenergetic x-ray beams. Invest Radiol, 6:402–412, 1973.

Multi-Frequency Intravascular Imaging Probe for Ultrasound and Frequency Domain Photoacoustic Imaging

Robin F. Castelino*[1,2], Hyunggyun Lee[1] and F. Stuart Foster[1,2]
[1]Imaging Research, Sunnybrook Research Institute, Toronto, Canada
[2]Medical Biophysics, University of Toronto, Toronto, Canada

Introduction: Photoacoustic (PA) imaging is a hybrid imaging modality based on the photoacoustic effect – the generation of acoustic waves by the absorption of electromagnetic radiation [1]. By illuminating biological tissue using light, the delivered energy will be absorbed and converted into heat which leads to a transient thermo-elastic expansion creating ultrasonic emissions. PA imaging is most commonly performed using pulsed lasers [1]. More recently, it has also been shown that continuous wave (CW) lasers can be used to generate PA signals, and this technique has been denoted as frequency domain photoacoustic (FDPA) imaging [2]. Although, the efficiency of generating FDPA signals is lower when compared to the pulsed technique, it is possible attain good SNR using signal processing methods such as cross-correlation [2]. Intravascular ultrasound (IVUS) imaging is an established technology for diagnostic and guidance protocols in interventional procedures. Although routinely used, it is reported to have low sensitivity in the detection of thrombus and lipid-rich lesions due to the limited acoustic contrast of soft tissues [3]. Intravascular photoacoustic (IVPA) imaging has potential to characterize lipid-rich structures based instead on the optical absorption contrast of these tissues and has been previously reported using the pulsed PA technique [3-4]. We demonstrate IVPA imaging using a CW laser diode and the FDPA method.

Method: A challenge in FDPA imaging, especially in intravascular applications, is to amplitude modulate light at high frequencies sensitive to the bandwidth (BW) of the detector. In this study, we also develop a novel multi-frequency intravascular imaging prototype capable of simultaneous IVUS and FD-IVPA imaging. The probe consists of two back-to-back transducers viewing outward at 180 degrees with independent signal electrodes, sharing a common backing layer. The IVUS transducer has an active area of 0.5mm by 0.5mm and centered at 40MHz (35% BW). The active area of the FD-IVPA transducer is 1mm by 1mm, centered at 22MHz (60% BW) and co-aligned with a 600μm fiber delivering 1.5W over an amplitude modulated linear chirp from 16-25MHz.

Results: This technique is initially demonstrated in agar vessel phantoms with lipid targets showing a 14dB increase in PA signal when compared to the surrounding at 1210nm. Next, atherosclerotic *ex-vivo* rabbit aortas were excised and imaged simultaneously with both ultrasound and FD-IVPA at 1210nm. It can be shown, that the FD-IVPA images can detect fatty deposits within the vessel with better efficacy as compared with the IVUS images alone. A healthy section of the aorta was used as a control to demonstrate the viability of this imaging technique.

References: [1] C. Li *et al.* Phys. Med. Biol. 54, R59–R97 (2009) [2] S. Telenkov *et al.* SPIE BiOS (2011) [3] S. Sethuraman *et al.* Opt. Express 16, 3362–7 (2008) [4] K. Jansen *et al.* Opt. Lett. 36, 597–9 (2011) .

Optical CT scanning for skeletal imaging in an optically cleared mouse

Kurtis H. Dekker[1]*, Tom S. Villani[3], Michael Johnson[3], Nick Crider[3], Jerry J. Battista[1,2], Kevin J. Jordan[1,2]
[1]Department of Medical Biophysics, Western University, London, Ontario, Canada
[2]London Regional Cancer Program, London Health Sciences Centre, London, Ontario, Canada
[3]Phytosys LLC, New Brunswick, New Jersey, USA

Introduction: Optical clearing[1] is a process by which biological specimens can be rendered transparent. This is used in optical microscopy and optical projection tomography (OPT). OPT systems are used for a variety of small samples such as mouse embryos or excised organs[2]. However, in some applications, adult whole animals must be imaged with a larger field of view, necessitating the use of micro-CT (x-ray) or MRI. For accessibility, it would be beneficial if a less expensive imaging modality could be used instead. Here, we examine the use of optical CT to image the skeleton and surrounding muscles of an optically cleared mouse, and present images obtained using a commercially available optical cone beam scanner.

Methods: Visikol™ (Phytosys LLC, New Brunswick, USA) is an optical clearing agent with a refractive index similar to that of many biological components. Therefore light rays passing through a sample do not deviate significantly from straight line paths[3], making optical CT possible. Visikol was used to perform optical clearing on a mouse (*Mus musculus*) which had its skin and internal organs removed, leaving only the skeleton and surrounding muscles. The skeleton was stained using alizarin red. The sample (Figure 1) was immersed in glycerol inside a Pyrex glass vial. Optical CT scanning was performed on a modified Vista10™ optical cone beam CT system (Modus Medical Devices Inc., London, Canada). The sample was imaged within a glycerol-filled aquarium for refractive index matching, and a vial filled with only glycerol was used as the reference condition for the CT scan. The camera was positioned 16cm from the scanner's rotation axis, resulting in a field of view of about 3.5cm x 3cm. 512 projections of 640x480 pixels each, spanning 360° of rotation, were acquired using a 635nm wavelength LED collimated by a Fresnel lens as the light source. Reconstruction was performed on a 512^3 grid of 62.5 micron voxels, using filtered backprojection with a ramp filter.

Figure 1: Optically cleared mouse specimen in vial. Note that muscles surrounding the skeleton are still present.

Results: Figure 2a shows a reconstruction slice through the spine of the mouse. The hind limb of the mouse can be seen in Figure 2b. Although transmission through the bones is low, the CT reconstruction clearly shows their exterior shape. Good contrast is seen in the fine details of surrounding muscle. Artifacts are present due to mechanical misalignments in scans and bubbles trapped in the highly viscous glycerol.

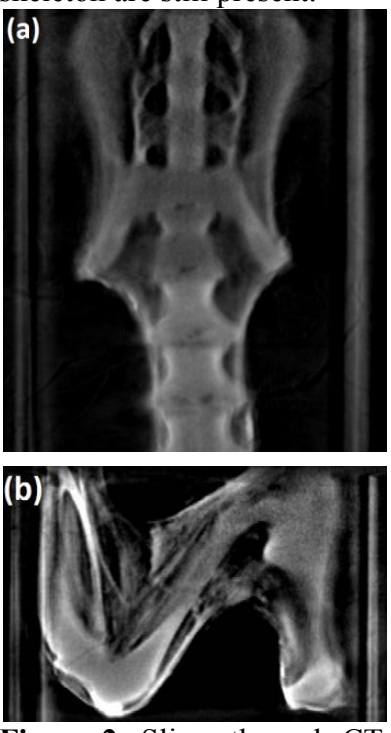

Figure 2: Slices through CT reconstruction, showing (a) spine and (b) hind limb of optically cleared mouse.

Conclusions: Preliminary imaging of an optically cleared mouse sample with cone beam optical CT shows promise for scanning the 3D structure of the mouse skeleton and surrounding muscle tissue. Future work will involve scanning optically cleared samples with organs intact. Multiple-wavelength scans should allow more information to be extracted. Different scan types (e.g. back-scatter or side-scatter imaging) could also provide information which may improve image reconstructions. Comparisons between optical and x-ray micro-CT will be made to evaluate the performance of this method.

References:

[1] V. V. Tuchin, *J. Phys. Appl. Phys.*, vol. 38, no. 15, p. 2497, Aug. 2005.
[2] Wong *et. al.*, *PLoS ONE*, vol. 8, no. 9, p. e73491, Sep. 2013.
[3] Zhu *et. al. Laser Photonics Rev.*, vol. 7, no. 5, pp. 732–757, 2013.

Development of a Quantitative PET QA Procedure for Multi-Center Clinical Trials

B. Driscoll[1,2], I. Yeung[1,3], D. Vines[1], H. Keller[1,3]

(1) Radiation Medicine Program, Princess Margaret Cancer Center, Toronto, Canada
(2) Techna Institute, University Health Network, Toronto, Canada
(3) Dept Radiation Oncology, University of Toronto, Toronto

Purpose: To develop an inter-institutional PET QA procedure especially tailored to the increasing requirement for quantitative (as opposed to qualitative) image analysis. Such a QA procedure should allow for harmonization of image acquisition and reconstruction such that images can be pooled across institutions.

Methods: The PET QA procedure utilizes the NEMA IEC Body Phantom which contains a set of 6 spheres and a torso shaped background reservoir. The phantom is filled at two background levels (2:1 and 4:1) and imaged three times at each level. Well counter readings from the signal and background compartments are collected for absolute quantification. The sites were each asked to select the protocol they would utilize for a full body PET scan with a time per bed position of 5 minutes.
At this stage, 7 different scanners have been tested across 4 institutions. For each scanner a number of quantitative measures were analyzed such as dose calibrator to well counter cross-calibration, absolute agreement with well counter, recovery ratios, and background noise levels.

Results: The protocols utilized by individual sites varied considerably in terms of reconstruction and image acquisition parameters. Two PET scanners had Time-of-Flight acquisition capability contributing to the variability.
The relative average background noise at 6000 Bq/cc activity level was 9.6% with a substantial variation between the scanners (7.6-18.9%).
Variations of the recovery ratio were equally severe especially for the smaller spheres. The average recovery ratio for the 13mm sphere was 0.51 with relative standard deviation of 26%.

Conclusions: There is a large variation in noise and sensitivity of the PET images across the different institutions. Some PET metrics such as tumour hypoxic fraction rely on local quantification of image noise and are therefore especially prone to variations. Reliability of such metrics for multi-center clinical trials requires harmonization of PET image acquisition and reconstruction.

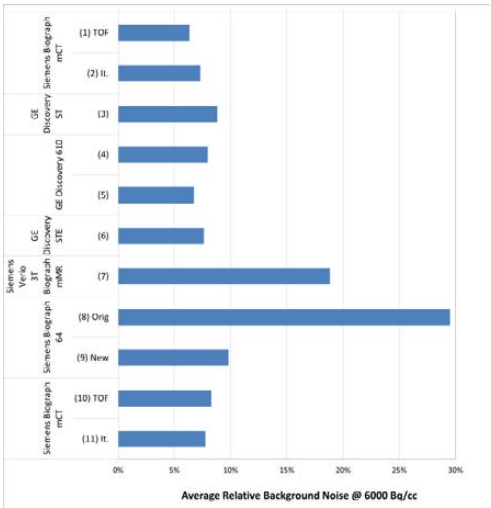

Figure 1: There is a substantial variation in image noise across scanners. Relative average background noise was 9.6%, however substantial variation exits (7.6 to 18.9%) even between optimized protocols.

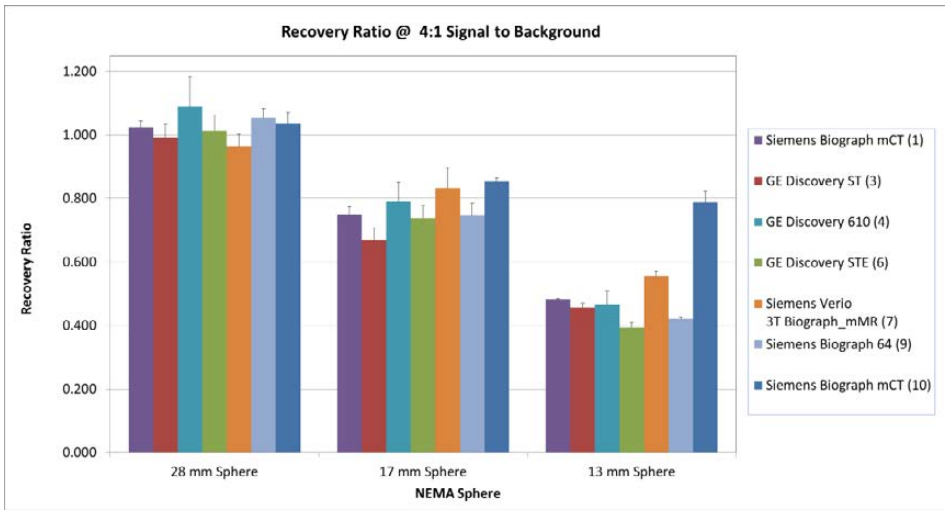

Figure 2 : Variations in the Recovery Ratio (RR) can be significant for small spheres. The RR of the 28 mm and the 17 mm spheres are not significantly different. There is greater variability in RR for the smaller spheres. The recovery ratio for the 13 mm sphere was 0.51 +/- 0.26.

Development of a Multi-Center Clinical Trial Data Archiving and Analysis Platform

B. Driscoll[1,3], I. Yeung[1,2], C. Coolens[1,2,3], H Keller [1,2],G. Disney[1], I. Svistoun[1] & D. Jaffray[1,2,3]

(1) Radiation Medicine Program, Princess Margaret Cancer Center, Toronto, Canada
(2) Dept Radiation Oncology, University of Toronto, Toronto,
(3) Techna Institute, University Health Network, Toronto, Canada

Introduction: Quality results from multi-center clinical trials require consistent and robust trial protocols capable of quantifying or eliminating differences across participating institutions. The vision of the Quantitative Imaging for Personalized Cancer Medicine (QIPCM) program is to provide end to end testing and analysis support for clinical trials to achieve improved consistency and reliability in clinical trial data.

Methods: The QIPCM clinical trial data archiving and analysis platform consists of a customizable image anonymizer and secure transport pipeline (RSNAs Clinical Trial Processor, CTP), a dedicated remote analysis platform, and a dedicated server for the archival and storage of medical images.

The anonymized images received from the remote sites are held in a secure drop box where there are subjected to a quality assurance check. This check ensures both that no patient health information remains and that the image set is complete before it is then subsequently forwarded to the clinical trial PACS at which point trial based permission controls are enforced. The images can then be analyzed either by QIPCMs dedicated team of imaging experts or remotely by the trial investigators.

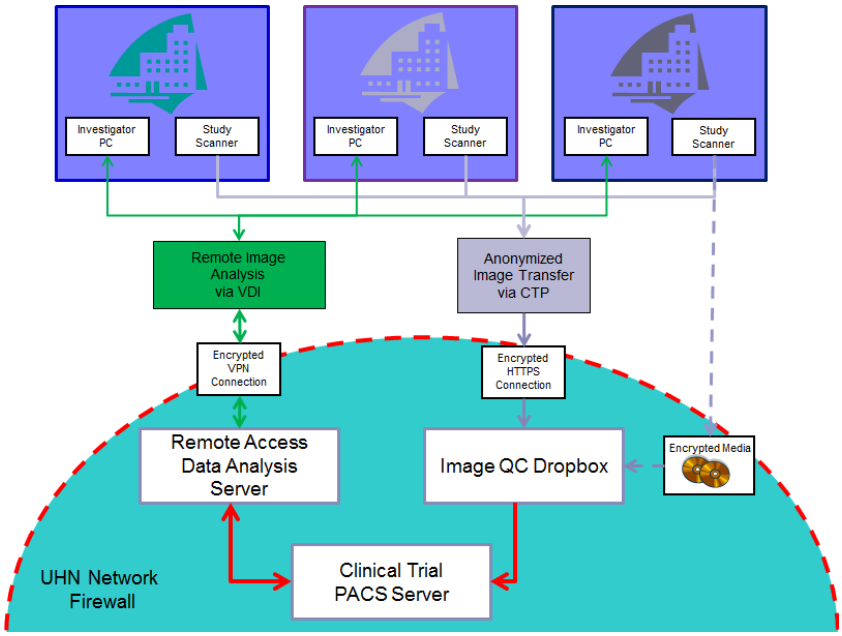

Figure 1 : Graphical representation of multicenter clinical trial data management and analysis setup

In addition to the platform infrastructure, a set of customized image analysis tools has been developed which are available for use on the remote analysis workstations. These tools range from quantitative functional imaging tools for 4D kinetic modeling of dynamic contrast enhanced-CT and MR and hypoxic fraction analysis in PET; to simple 1D RECIST. Alternatively remote users can choose to utilize their own custom applications on the virtual environment while still making use of the central data storage and powerful remote analysis servers.

Results: The QIPCM team has established infrastructure and support services to sustain an ever growing number of multi-centre clinical trials. The platform currently serves 15 internal and 6 multi-center clinical trials spanning 9 hospitals and imaging centers in Canada and the United States, with more trials to be added over the upcoming months. The image store currently holds in excess 1.8 million individual tomographic slices comprising more than 510 individual imaging studies from over 145 patients. The QIPCM team has also provided PET QA services for 3 different multi-center trials at 10 different sites across North America.

Conclusions: The current QIPCM platform is a fully functional commercial system with robust backup, storage and processing capacity. Within the next two months a further 50 TB of storage and 2 more high powered computational servers will further enhance performance.

Mechatronic Image Guided Needle Manipulation System for Small Animals in 9.4T Bore

Matthew Gravett*[1,2,3] Jeremy Cepek[1,2] and Aaron Fenster[1,2,3,4]

1. Robarts Research Institute, The University of Western Ontario, London, Ontario

2. Schulich School of Medicine and Dentistry, The University of Western Ontario, London, Ontario

3. Department of Biomedical Engineering, The University of Western Ontario, London, Ontario

4. Department of Medical Biophysics, The University of Western Ontario, London, Ontario

Introduction: Many pre-clinical research techniques require accurate injections of cells or contrast agent into specific sites in small animals, such as mice. Currently, these injections are performed outside of the MRI bore, by hand and with no reference, which can result in inaccurate placement of the needle due to human error. An MR image guided minimally invasive in-bore, MR compatible, robotic manipulation system used to place the needle into the target would serve to resolve this issue and ensure that the targeting of the needle to its intended site is accurate and repeatable.

Methods: Once the system and MR coordinates are registered using 3D fiducials as reference, MR images of the brain will be used to locate the desired target and trajectory of the needle. The target location from the MR images will then be processed and the mouse bed stage, as seen in Fig. 1a, will move the mouse to the position in space where the desired target in the mouse brain coincides with the remote center of motion of the spherical linkage. The spherical linkage, as seen in Fig. 1b, will then position the hydraulic needle driver to the desired trajectory so the needle can pass through the pre drilled skull hole, through the brain tissue and to the target at the remote center of motion when actuated. The desired accuracy of the needle tip with respect to the target is less than 400 µm, which is the minimum voxel size in the images that are normally acquired for mice brains in the 9.4T Varian MR system, and a trajectory error less than one degree.

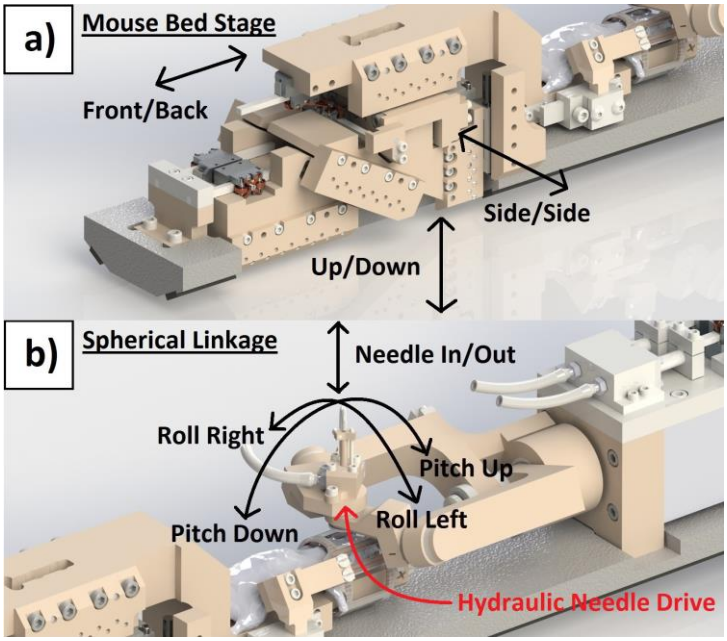

Figure 1: a) Three linear degrees-of-freedom mouse bed stage used to position the mouse so that the desired target is at the remote center of motion (the point in space about which the needle pivots). b) Spherical linkage arms used to manipulate the trajectory of the hydraulic actuated needle driver by pitch and roll. The hydraulic needle driver uses a hard stop for positioning.

Current and Future Work: The system has been built and each degree of freedom is completely functional in the MRI. The control system has been redesigned in order to control all five degrees of freedom simultaneously, and once that is assembled, the system will be calibrated and the total accuracy and repeatability of the system will be tested.

Conclusions: Once this system is complete, it will be tested to demonstrate that it will be successful in performing accurate injections in small animal brains, as indicated by the hardware and software tests that have been conducted on the various components of the system. Developing a consistently functional image-guided system for needle manipulation in the MRI bore will redefine small animal injection imaging in high strength magnetic field MR systems.

A pilot study of BOLD MRI and FLT PET in patients with locally advanced breast cancer undergoing neoadjuvant chemotherapy (IMPACT)

KY Gulenchyn[1], MN Levine[2], K Hahn[3], D Vergidis[4], K Pritchard[5], M Noseworthy[6], A Singnurkar[1], J Valliant[7], C Singh[8], A Bane[8], S Mukherjee[2], GR Pond[2]

Departments of Nuclear Medicine[1], Oncology[2], Electrical and Computer Engineering[6], Centre for Probe Development and Commercialization[7], Pathology[8], McMaster University, Medical Oncology, London Health Sciences Centre[3], Medical Oncology, Thunder Bay Regional Health Sciences Centre[4], Department of Medicine, Sunnybrook Odette Cancer Centre[5]

Introduction: Locally advanced breast cancer (LABC) account for 10-20% of all breast cancers and is usually treated with a combined modality approach, involving pre-operative neoadjuvant (NA) chemotherapy (CT) for 4-6 months followed by surgery and radiation therapy. The goals of this approach are to increase the chances of successful tumour resectability and to improve clinical outcomes by eradicating micrometastatic disease. Patients with LABC who receive NA CT are usually evaluated with physical examination at the beginning of each CT cycle to determine whether or not there has been a clinical tumour response; a more precise method of assessing tumour response to CT could assist the clinician in making treatment decisions. Blood Oxygen Level Dependent (BOLD) MRI is performed using echo planar imaging sequences; the change in BOLD signal results from changes in metabolism, blood flow, blood volume or any combination of the three. FLT, a radiolabelled analog of thymidine, is a PET imaging agent developed as a noninvasive probe for the *in vivo* assessment of cellular proliferation. Uncontrolled cellular proliferation is a key feature of malignant tumours and FLT uptake has been shown to correlate with proliferation in a number of cancer types, suggesting it may have promise as a diagnostic tool to provide an early signal of the effectiveness of anti-cancer drug treatments.

Methods: 32 patients with histologically confirmed breast cancer, a clinical diagnosis of LABC and able to undergo NA CT were recruited at 4 Ontario Cancer Centres. Patients followed the protocol outlined in Figure 1. FLT PET studies were reviewed by 2 Nuclear Medicine physicians and primary and metastatic lesions identified. SUV_{max} corrected for lean body mass was calculated for the primary lesion. Post Cycle 1 images were reviewed in the same manner with access to the initial set of images. Discrepancies were resolved by consensus. BOLD MRI was performed following each of the FLT PET studies.

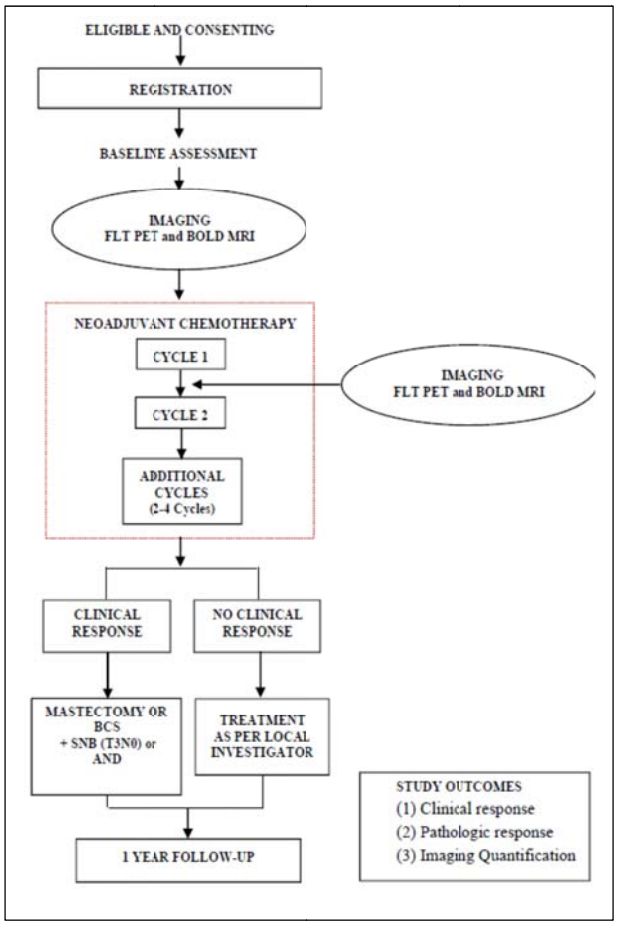

Results: 29 patients underwent baseline FLT PET and the primary tumour demonstrated uptake of FLT in 28 with a mean SUV of 4.24 (std dev=2.37, median=3.9, range=1.3 to 11.7). 28/29 patients underwent FLT PET post Cycle 1 at Day 8; the % change in maximum SUV across all breast sites (n=26) was a mean of -36.0% (std dev=25.7%). 7 of 28 (25.0%) patients had no tumour found on pathology at surgery (pCR). Neither baseline SUVmax (p=0.69) nor the % change from baseline to day 8 across breast sites (odds ratio=0.99, 95% CI=0.96 to 1.03 / percent change, p-value=0.69) was a prognostic factor for pCR. Results are similar if clinical complete response was used as the outcome.

Conclusions: We were unable to confirm the prognostic utility of a change in SUV as determined by FLT PET imaging to predict pathological or clinical complete response. BOLD MRI analysis is ongoing.

Translation of Medical Image Analysis Tools to a Clinical Trial-Ready Platform

Carol A. Johnson[1], Sarah A. Mattonen[2], Timothy Pok Chi Yeung[1,2], Aaron D. Ward[1-3*]

OICR Imaging Translation Program

[1]London Regional Cancer Program, London Health Sciences Centre, London, Canada; Department of [2]Medical Biophysics, [3]Oncology, The University of Western Ontario, London, Canada, [*]Research Supervisor

Introduction: As part of the OICR's strategy to translate current imaging and image analysis research to clinical trial, we are motivated to integrate cutting edge software tools developed in the laboratory into a robust, clinician-friendly, interactive platform accessible for use in clinical trials anywhere in the world.

Methods: Software techniques for image analysis, such as image registration and the extraction and analysis of quantitative "radiomic" image features, are frequently used by researchers in our lab with in-house developed applications running on research platforms such as MATLAB. We are incorporating these image processing functions by developing software plugins in ClearCanvas Workstation, an open-source PACS viewer.

Results: The image registration tool is an interactive system where the user can register two image studies, adjusting parameters such as the optimization algorithms, image similarity metrics, and transformation parameters to achieve the desired results (Figure 1). The radiomic feature extraction tool, currently at a prototype stage and under continuing development, allows for quantitative evaluation of image features throughout the entire image or within regions of interest. Advanced machine learning techniques are then used to correlate radiomics signatures with clinical outcomes.

Conclusions: Development of the image registration and feature extraction tools into ClearCanvas Workstation provides a user-friendly interface to perform advanced image analysis techniques. These plugin tools may assist the clinician in designing personalized treatment plans and evaluating the effectiveness of these treatments. Further development will provide machine learning tools for predicting clinical outcome. All of these developed tools will be deployed for widespread use in clinical trials via the Quantitative Imaging for Personalized Cancer Medicine initiative within the OICR Imaging Translation Program.

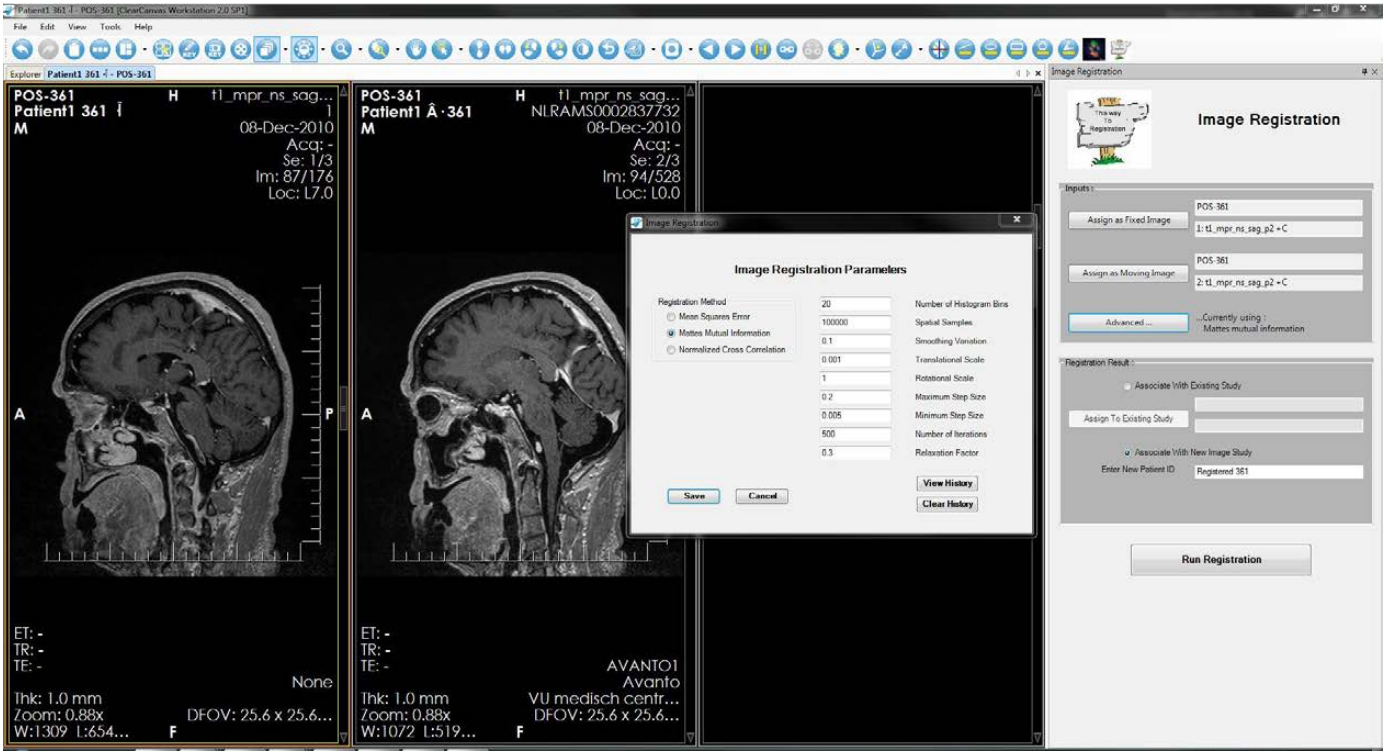

Figure 1. A screen shot of the Image Registration plugin tool for ClearCanvas Workstation.

Characterizing human diaphragm motion hysteresis for biomechanics based lung tumor motion prediction during EBRT

Elham Karami[1,2],Stewart Gaede[1,3,4], Ting-Yim Lee[1,2,5,6], Abbas Samani[1,2,7,8]

[1]Department of Medical Biophysics, Western University, London, Ontario; [2]Imaging Research Laboratories, Robarts Research Institute, London, Ontario;[3]Department of Physics and Engineering, London Regional Cancer Program, London, Ontario; [4]Department of Oncology, Western University, London, Ontario;[5]Imaging Program, Lawson Health Research Institute, London, Ontario; [6]Department of Medical Imaging, Western University, London, Ontario; [7]Department of Electrical and Computer Engineering, Western University, London, Ontario; [8]Graduate Program in Biomedical Engineering, Western University, London, Ontario, Canada

Lung cancer isfrequently treated with radiation therapy, which is often combined with chemotherapy, surgery or both.However, External Beam Radiation Therapy (EBRT) may lack desirable dosimetric accuracy because of respiration induced tumor motion. This motion can be predicted using biomechanical modeling of the respiratory system which requires accurate data pertaining to lung geometry, thoracic pressure variation, diaphragm position and tissue biomechanical properties. However, given the pleural pressure nonuniformity on the lung's surface and contact between the lung, diaphragm and heart, modeling the lung loading is cumbersome. A simple approach frequently used in lung models appliesuniform negative pressure on the lung's surfaceat the end exhalation phase to simulate the inhalation phase.

To our knowledge, none of the existing lung biomechanical models account for respiratory cycle hysteresis which results from surfactant action and tissue recoiling. In this paper, we present preliminary results obtained from lung 4D CT image processing which indicate that the human diaphragm motion's hysteretic nature.This hysteresis furthercontributes to the lung hysteresis. To track the diaphragm motion, 22 points located on its surface were tracked in a 4D CT image using Free Form Deformable registration. The displacements in the superior-inferior direction were normalized between 0 and 1 for all the points. The average curve depicted in Figure 1 indicates that the diaphragm motion has similar pattern to the lung compliance curve. These results suggest that, to achieve desirable accuracywith lung biomechanical modeling, this strongdiaphragm motion hysteresis should be considered. This was done bymodifying the model we presented recently,leading to significant improvement in tumor motion prediction.

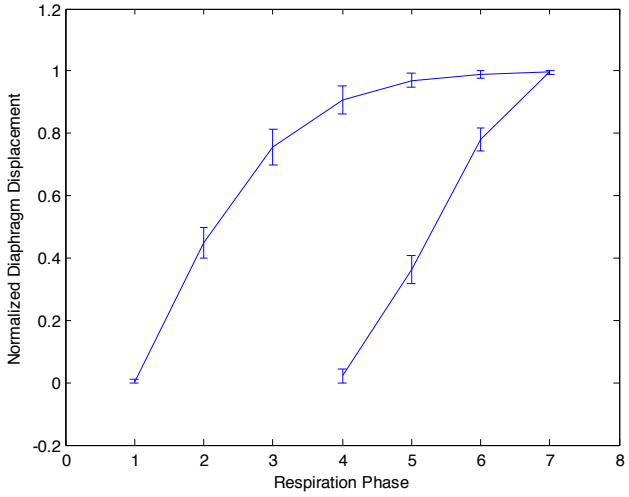

Figure 1 : Normalized Diaphragm displacement versus respiratory phase

Development of an image based classification method for the interventional treatment of preterm neonates with intraventricular hemorrhage using 3D ultrasound

Kishimoto, J[1,2], Fenster, A[1,2], Lee, D.S.C.[3], de Ribaupierre, S[4]

[1]Department of Medical Biophysics, University of Western Ontario; [2]Robarts Imaging, University, Western Ontario; [3]Department of Neonatology, University of Western Ontario, London Health Sciences Centre; [4]Department of Clinical Neurological Sciences, University of Western Ontario, London Health Sciences Centre: London, Ontario, Canada

Consortia: Centre for Imaging Technology Commercialization

Research Supervisors: Sandrine de Ribaupierre and Keith St. Lawrence

Introduction Following a bleed in cerebral ventricles (intraventricular hemorrhage, IVH), preterm babies are at risk of ventricle dilation (VD), which has been linked to brain injury and morbidities such as poor motor coordination and cerebral palsy.[1] VD is currently monitored with 2D cranial ultrasound (US), though no consensus has been determined for when interventional surgical therapy is required. Patients with rapid VD will require interventions known as 'taps' to remove excess cerebral spinal fluid from the ventricles to prevent further brain injury through excess intracranial pressure. Ventricle volumes (VV) derived from 3D US will be able to distinguish neonates with rapidly increasing VV (Figure 1) versus those with stable ventricles.

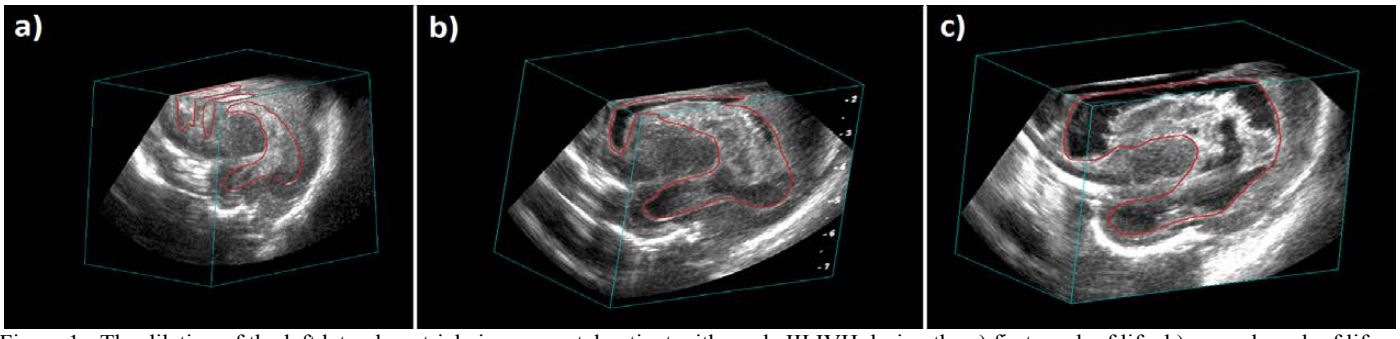

Figure 1 - The dilation of the left lateral ventricle in a neonatal patient with grade III IVH during the a) first week of life, b) second week of life, and c) third week of life (taken immediately prior to the first interventional ventricle tap). Manual contours shown on each image.

Methods Neonates with IVH were enrolled into the study after informed parental consent following a protocol approved by the REB. Clinical 3D US images were acquired 1-2 times per week throughout the patient's stay in the Neonatal Intensive Care Unit (usually 2-4 months) and analyzed offline. Ventricle volume (VV) was measured from 3D US images by a trained observer and reviewed by a collaborating clinician. Changes in the measurements between subsequent image sets were recorded for each patient. Comparisons were performed through two-sample t-tests using a Bonferroni correction and a $\alpha < 0.05$. Prior to the t-tests, a Shapiro-Wilk normality test was performed, and if the normality test was not passed, the nonparametric Mann-Whitney test was performed.

Results We report that there are significant differences in ventricle volume ($p<0.001$) between the patients requiring therapy and those who have eventual resolution of ventricle dilation even in the first week of life (Fig. 2a). The differences between patients groups as characterized through VV increases dramatically over time (Fig. 2b-e).

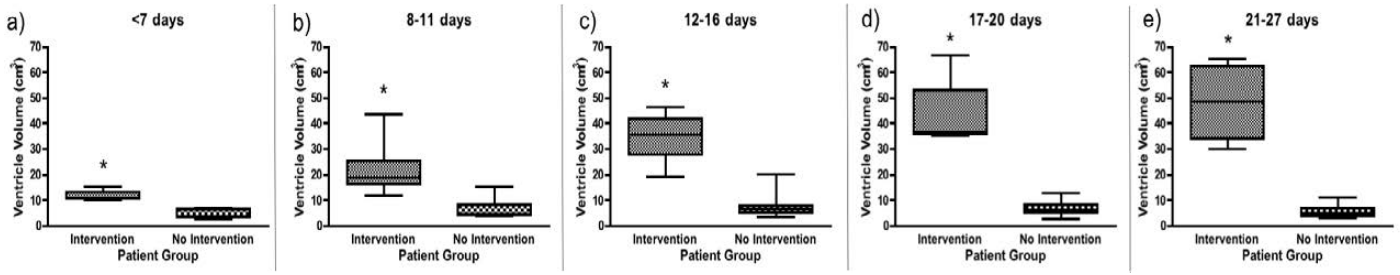

Figure 2 – Ventricle volumes post-hemorrhage for 18 IVH patients (6 required interventions) **a)** <7 days; **b)** 8-11 days; **c)** 12-16 days; **d)** 17-20 days; **e)** 21-27 days.

Conclusions Quantified ventricle volume measurements show promise to be able to characterize IVH patients into those who require interventional therapies and which ones do not. This characterization would allow patients with higher risks could to be monitored more actively allowing for more timely interventions, and hopefully, a better neurological prognosis later in life.

[1]Miranda, P., "Intraventricular hemorrhage and posthemorrhagic hydrocephalus in the preterm infant," Minerva Pediatr, 62(1), 79-89 (2010).

Hand Gesture Control System for Manipulation of Images during Three-Dimensional Ultrasound Guidance

Eric Knull[1,2], Nirmal Kakani[1,3], and Aaron Fenster[1,2]
OICR Imaging Translation Program
[1]Robarts Research Institute, London, Ontario, Canada
[2]Biomedical Engineering, The University of Western Ontario, London, Ontario, Canada
[3]Department of Medical Imaging, London Health Sciences Centre, University Hospital, London, Ontario, Canada

Introduction: Liver tumour ablation therapy offers a minimally invasive alternative to transplantation or resection of the liver for treatment of hepatocellular carcinoma. However, ablation therapy suffers from higher local recurrence rates due mainly to inaccurate placement of the ablation needles or insufficient heating of the malignant tissues. Needle placement is guided by three-dimensional (3D) ultrasound images. Currently available methods for manipulating these images use mechanical devices such as a mouse and keyboard or touchscreen. These devices are limited because they are two-dimensional, they are difficult to sterilize, and the presence of bodily fluids could interfere with their use. It is believed that a contact-free approach could reduce overall surgery times by avoiding these limitations, provided reasonable accuracy can be obtained.
Methods: Computer vision software is being developed using the Microsoft Kinect depth camera to implement a hand-gesture control system for interacting with 3D images. The first stage of the software fits a 26 DOF model of the user's hand to a cloud of points generated by the depth camera. The joints in the hand model were constrained to a natural range of motion, and their position determined using forward kinematics. A cost function aligned the model with the point cloud, and was minimized using a combination of gradient-descent and particle swarm optimization.

The optimization was evaluated with and without Kalman filtering performed on the results. Kalman filtering was used to attempt to remove bad frames where the model temporarily jumps to an incorrect pose. Evaluation was performed on a set of 400 sequential depth images of a moving hand. The average error in the position of the model's finger and thumb tips with respect to the ground truth positions was measured.
Results: Without Kalman filtering, the algorithm achieved an average error in Euclidean distance of 18.43 mm per finger/thumb tip. After Kalman filtering, the average error increased to 23.74 mm. A strong correlation was found between error in the initialization model and error in the model after optimization. On average, optimization reduced the average error in the finger/thumb tip locations by about 10 mm.
Conclusion: An algorithm was implemented to estimate the pose of the human hand in 3D based on images from a depth camera. Kalman filtering failed to improve the results, but improvement may be found by tuning the filter or by improving the initialization of the hand model before optimization. The software will be integrated into a system which allows physicians to interact with 3D ultrasound images contact-free during liver tumour ablation procedures.

Next-generation MRI of the human spinal cord: Translating measures of microarchitecture and function to clinical utilization

Allan R. Martin*[1], Izabela Aleksanderek[1], Julien Cohen-Adad[2], David W. Cadotte[1], Sukhvinder Kalsi-Ryan[1], Natalia Nugaeva[1], David J. Mikulis[1], Adrian Crawley[1], Howard Ginsberg[1], Michael G. Fehlings[1]
Consortium: OICR Imaging Translation Program
[1]Toronto Western Research Institute, University of Toronto, Toronto, Ontario, Canada
[2]Polytechnique Montreal, Montreal, Quebec, Canada

INTRODUCTION: Novel spinal cord MRI techniques that reflect microstructure and function have become technically feasible: diffusion tensor imaging (DTI) relates to axonal integrity, magnetization transfer (MT) corresponds with myelin content, T2*-weighted imaging (T2*-WI) demonstrates gray/white contrast, and functional MRI (fMRI) displays activity and connectivity. Existing studies using these methods are largely preliminary in nature, employing a wide range of acquisition techniques, often requiring custom coils, and lacking detailed assessments of the clinical status of patients, resulting in conclusions that lack external validity. Robust translational studies focused on specific patient populations are needed to prove the value of these novel imaging techniques to drive their adoption into medical practice.

METHODS: We have developed reliable methods for spinal cord DTI, MT, and T2*-WI, and brainstem fMRI using commercial coils and a GE Signa 3.0T scanner. Our protocols include: 1) DTI: single-shot EPI, 25 directions, 12 axial slices (C1-C7), 1.25x1.25x5mm voxels, acquisition time (AT): 6 min; 2) MT: 2D SPGR, 1x1x5mm voxels, +/- MT pre-pulse for MT ratio (MTR), AT: 7 min; 3) T2*-WI: multi-echo (MERGE), 0.6x0.6x4mm voxels, AT: 4 min; 4) fMRI: BOLD T2*-WI, 11 coronal slices, 3x3x3mm voxels, electrical ulnar stimulation in 1 min blocks, AT: 7 min. The total acquisition time (including T1 brain and T2 spine) is 35 minutes. Post-processing is completed using the Spinal Cord Toolbox [1] to co-register images, automatically segment spinal cord, warp to anatomical atlas, and extract quantitative metrics for the entire cord, white matter, grey matter, and specific tracts. fMRI data is processed using FSL [2]. Quantitative values are compared with a battery of clinical measures and somatosensory evoked potentials (SSEPs).

RESULTS: Several translational studies have been initiated to demonstrate reliability and generate normative values in healthy controls, and to study patients with acute spinal cord injury (SCI), chronic SCI, and degenerative cervical myelopathy (DCM). Data collection to date includes 15 healthy controls and 15 DCM patients. Group results are pending a complete analysis, but representative images are displayed in figures 1-5.

CONCLUSIONS: Reliable acquisition of DTI, MT, T2*-WI, and fMRI images is possible. We have begun 3 translational studies to determine the suitability of these methods for clinical uses in acute and chronic SCI, and DCM populations.

REFERENCES: [1] http://sourceforge.net/projects/spinalcordtoolbox/
[2] http://fsl.fmrib.ox.ac.uk/fsl/fslwiki/

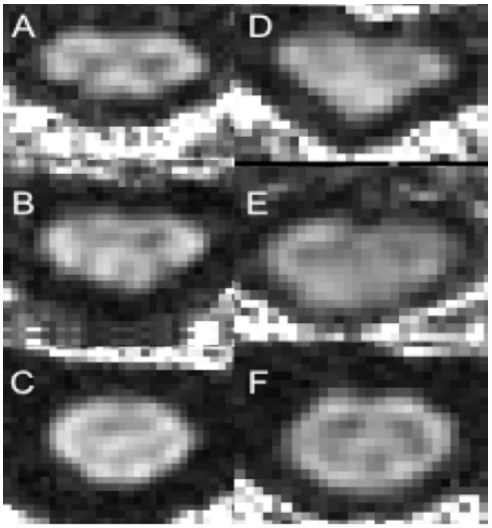

Figure 1: DTI fractional anisotropy maps through C4, C3, and C2 in a healthy control (A-C) and DCM patient (D-F).

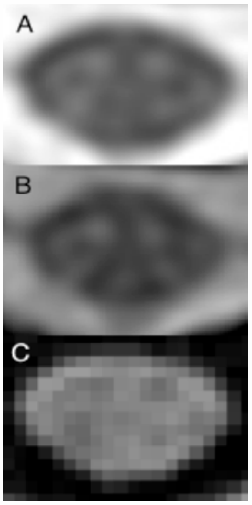

Figure 2: MT images A) with pre-pulse, B) without, C) MTR

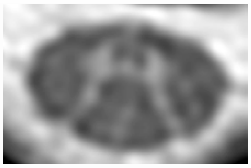
Figure 3: T2*-WI in a healthy control

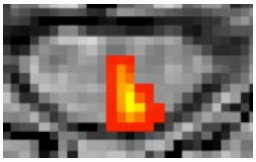
Figure 4: MTR image with atlas-based left dorsal columns

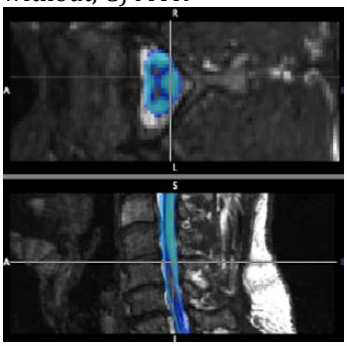
Figure 5: Axial (upper) and sagittal (lower) segmented cord with atlas-based white matter

Early prediction of lung cancer recurrence after stereotactic radiotherapy using texture analysis of automatic graph cuts segmentations

Sarah A. Mattonen[1], David A. Palma[1,2], Cornelis J. A. Haasbeek[3], Suresh Senan[3] and Aaron D. Ward[1]
[1] *Department of Medical Biophysics, Western University, London, Ontario, Canada*
[2] *Division of Radiation Oncology, London Regional Cancer Program, London, Ontario, Canada*
[3] *Department of Radiation Oncology, VU University Medical Center, Amsterdam, Netherlands*
OICR Imaging Translation Program; Research Supervisors: Aaron D. Ward & David A. Palma

Purpose: Stereotactic ablative radiotherapy (SABR) is becoming a standard treatment option for patients with early-stage lung cancer, and can achieve local control rates comparable to surgery. However, following SABR benign radiation-induced lung injury (RILI) causes radiographic changes on computed tomography (CT) imaging. These changes can be tumour-mimicking, making it difficult to distinguish recurrence from benign RILI. Current approaches do not reliably detect recurrence within a year post-SABR. Our previous work has shown the utility of CT texture features calculated within manually delineated regions of interest for recurrence prediction post-SABR. The purpose of this study was to evaluate the accuracy CT texture features extracted within automatically derived regions of interest for prediction of eventual tumour recurrence.
Methods: We analyzed 22 patients with 24 lesions (11 recurrence, 13 RILI). Two regions of common post-SABR changes were manually delineated: consolidative and ground-glass opacity (GGO), shown in red and green respectively in Figure 1. The consolidative regions were also automatically delineated using a *OneCut* graph cuts algorithm with the only operator input being the single line segment measuring tumour diameter, normally taken during the clinical workflow. Surrogate GGO regions were approximated by automatic expansion of the consolidative regions. Within the GGO regions, second-order texture features from grey-level co-occurrence matrices were calculated. Classification was performed using a linear Bayes normal classifier and evaluated using cross-validation (CV). Delineation times for the manual and automatic approach were also measured on a subset of 46 images taken at 2–5 and 5–8 months post-SABR.
Results: Leave-one-out CV on images taken 2–5 months post-SABR showed robustness of the entropy texture measure, with classification error of 26% and area under the receiver operating characteristic curve (AUC) of 0.77 using the automatic segmentation; results using a fully manual segmentation were 19% and 0.80 respectively. Using our fully automated approach, AUCs for this feature increased to 0.82 and 0.93 at 8–14 months and 14–20 months post SABR, respectively, suggesting even better performance nearer to clinical diagnosis of recurrence. The average time (± SD) to manually delineate the solid and GGO on each image was 266±314 and 292±187 seconds respectively, versus 15±15 and 5±2 seconds using our automatic approach.
Conclusions: Texture features calculated within GGO delineated from a fully automated algorithm using only an input diameter measurement have shown the potential to predict recurrence in individual patients within 6 months of SABR, eliminating the need for any manual delineations. Based on our ongoing validation on a larger sample, we aim to develop a computer-aided diagnosis system which can be integrated into a physician's workstation to improve their assessment of response post-SABR. This could allow for earlier salvage for patients with recurrence, and result in fewer investigations of benign RILI.

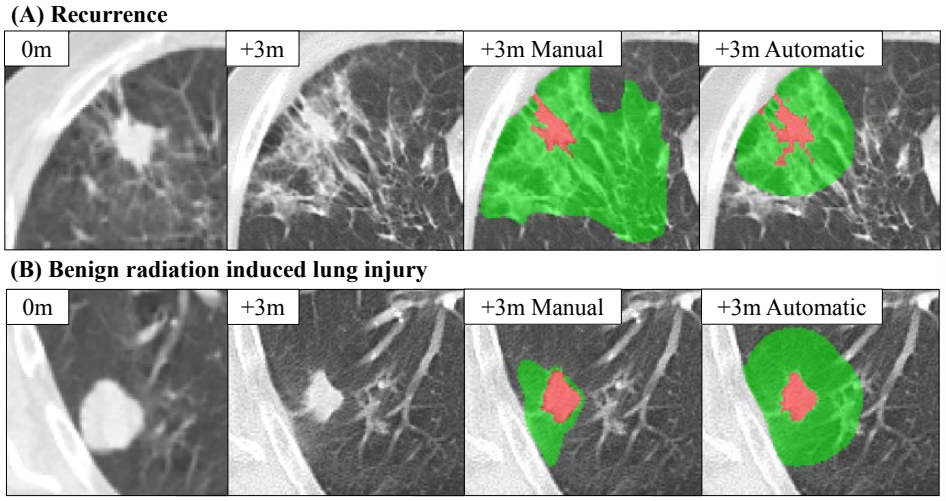

Figure 1: Manual and automatic delineations of post-SABR consolidative (red) and ground-glass opacity (green) findings at 3 months follow-up for a patient with recurrence (A) and radiation-induced lung injury (B). The zero-month (0m) time point indicates the pre-treatment lesion.

Non-uniform object counting method in large-format pyramid images applied to CD31 vessel counting in whole-mount digital pathology sections

Mayan Murray[1], Melissa L. Hill[1], Kela Liu[1], James G. Mainprize[1], and Martin J. Yaffe[1,2]
[1]Sunnybrook Research Institute, Toronto, Canada
[2]Department of Medical Biophysics, University of Toronto, Toronto, Canada

Introduction: The pyramid tagged image file format (TIFF) contains multi-resolution representations of the complete image and may be tiled (i.e. the image is subdivided into smaller sub-images). These are useful for large-slide high-resolution digital pathology. Vessel counting in digital pathology is a time consuming task that requires automation. There are two primary obstacles associated with detecting and counting specified non-uniform objects in large (>4 GB) pyramid images: managing large amounts of data with limited computer memory and reducing the effect of double-counting along block seams. Block-processing [1] is a common method for handling such large images. This process breaks up the largest image in the pyramid TIFF into smaller blocks, and runs the image analysis protocol on every block. This approach is very useful for certain tasks, such as calculating area density of a histology stain. However, it is ill-equipped for object counting in which many partial objects lie along the seams of the blocks, and are therefore counted multiple times. This issue is intensified as the block size decreases, and for semi-discontinuous objects; such as blood vessels multiply crossing a single plane. An image handling method was devised to account for these issues, and the results can be used to produce an object-density map of the entire image.

Method: VX2 tumours in New Zealand white rabbit leg muscle were used in this study. The tumours were sectioned and immunostained for CD31, and the whole-mount sections were then digitized using a Leica SCN400 (Leica Microsystems) scanner [2]. A pathologist-verified colour filter was designed to isolate the objects of interest by a colour threshold. This was applied in two distinct rounds of block-processing. The first used a standard grid and only counted objects which did not touch the borders of the block. The second round used a grid shifted half a block-width vertically and horizontally to ensure that all subsequent blocks encircle the seam-intersection. This round only counted objects that touched a centre-cross applied to the location of the seam from the first round of block processing. This is represented in Fig. 1.

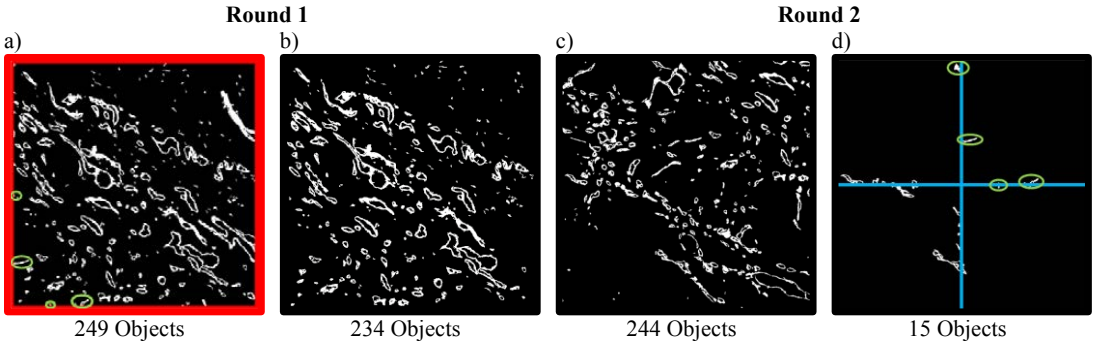

Figure 1: Examples of the two rounds of block-processing. a) Original filter generated block from the first round. Border of the block is highlighted in red, b) Border objects are removed, c) Original filter generated block from the second round of block processing; d) Only objects touching the centre-cross (represented in blue). Objects circled in green correspond to objects circled in green in subfigure a).

Results: An example of an object-density map produced by the two-round approach is shown in Fig. 2. High correlation was observed between the high vessel-dense regions computed through the method outlined (Fig. 2b), and the tumour region outlined by the pathologist (Fig. 2a).

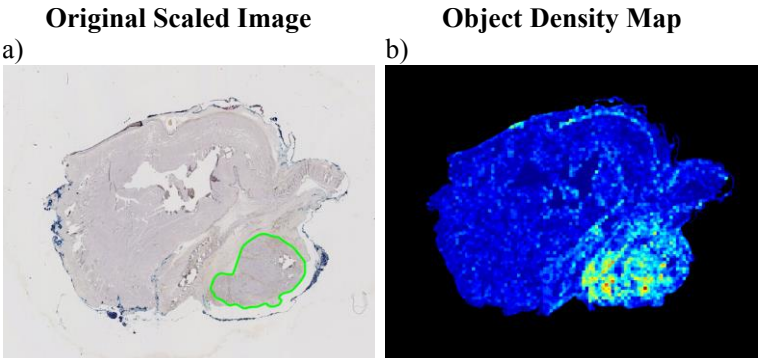

Figure2: a) Original colour image of CD31 whole-mount VX2 tumour is highlighted in green by a pathologist. b) Final vessel-density map, taken with an 800 pixel block-width. Lighter pixels represent higher density regions.

Discussion: This method is highly adaptable to different block-sizes, without a large increase in oversampling. It also produces a higher sampling object-density map than conventional block-processing. Future work involves validation against human reader vessel counting at multiple block-resolutions.

References: [1] Wang et al., IEEE VLSI, 6(2), 1998; [2] Hill et al, Springer, 2012;

Differences in Pulmonary Ventilation in Ex-smokers With and Without COPD after Three years: Longitudinal Results of the TINCan Cohort

Damien Pike[1,2], Miranda Kirby[3], Dante Capaldi[1,2], Nanxi Zha[1,2], David G McCormack[4], Harvey O Coxson[3] and Grace Parraga[1,2]

[1]Robarts Research Institute; [2]Department of Medical Biophysics, The University of Western Ontario, London, Canada; [3]Department of Radiology and James Hogg Research Centre, University of British Columbia, Vancouver Canada; [4]Division of Respirology, Department of Medicine; The University of Western Ontario, London, CANADA. OICR Imaging Translation Program

INTRODUCTION: Previous work showed that ^{3}He MRI ventilation measurements are reproducible (1), reflect response to therapy (2) and predict exacerbations (3) of COPD. The Thoracic Imaging Network of Canada (TINCan) is a three-year ^{3}He magnetic resonance imaging (MRI) study in ex-smokers with and without airflow limitation. Here we report the preliminary findings and summarize the changes in ^{3}He ventilation observed after three-years. We hypothesized that ^{3}He MRI ventilation measurements would show an accelerated decline in ex-smokers, inconsistent with spirometry and plethysmography measurements and predictions (4) of lung function decline.

METHODS: Ex-smokers (pack year≥10yr) underwent ^{3}He MRI, CT, spirometry and plethysmography at baseline and follow-up (mean follow-up=29 ±5 months). The ^{3}He MRI ventilation defect percent (VDP) (5) was generated and this reflects the percent of the lung not participating in ventilation. The difference for VDP at follow-up (ΔVDP) was VDP at follow-up minus VDP at baseline and the difference in spirometry (forced expiratory volume in one second, FEV_1) (ΔFEV_1) was FEV_1 at follow-up minus baseline FEV_1. Paired t-tests were used to compare baseline and follow-up VDP and FEV_1 and unpaired t-tests were used to compare ΔVDP and ΔFEV_1 between subgroups.

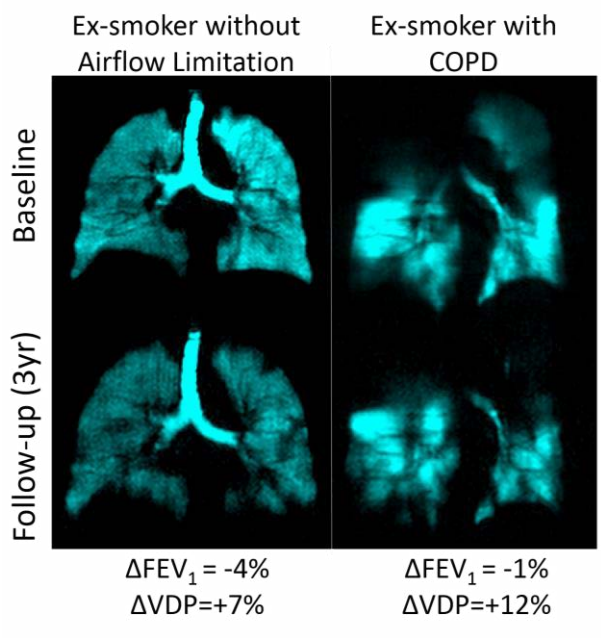

Figure 1: ^{3}He Static-ventilation MR images at baseline and follow-up in an ex-smoker without airflow limitation and a COPD ex-smoker

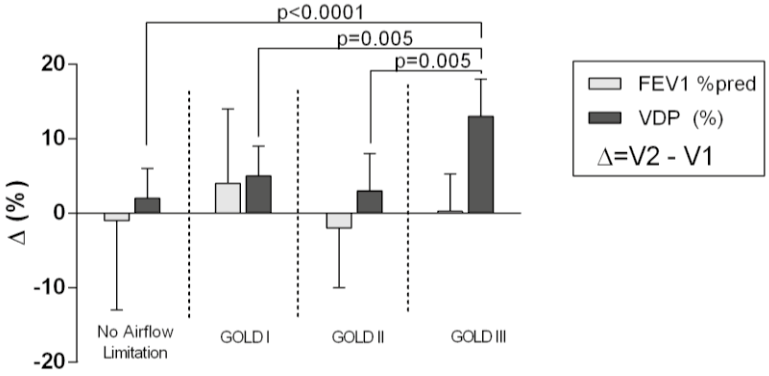

Figure 2: Longitudinal change in FEV_1 (ΔFEV_1) and VDP (ΔVDP) for ex-smokers without airflow limitation and Grade I, II and III COPD ex-smokers

RESULTS: Forty-four ex-smokers completed ^{3}He MRI at baseline and follow-up (29±5months). FEV_1 was not significantly different between baseline and follow-up for all subjects (88±25% vs. 88±27%, p=0.93), COPD subjects (77±23% vs. 78±27%, p=0.84) or ex-smokers without airflow limitation (105±15% vs. 104±19%, p=0.86). Figure 1 shows baseline and follow-up ^{3}He MR images of representative subjects with and without COPD. Mean VDP at follow-up was significantly greater (worse) (15±11% FU; 10±8% BL, p<0.0001) in all subjects and for COPD ex-smokers (21±13% FU; 14±10% BL, p<0.0001). As shown in Figure 2, ΔVDP in grade III COPD subjects (13±5%) was significantly greater than in ex-smokers without airflow limitation (2±4%, p<0.0001) as well as in grade I (5±4%, p=0.005) and grade II COPD subjects (3±5%, p=0.005).

CONCLUSIONS: These preliminary results indicate significant worsening of pulmonary ventilation in COPD ex-smokers after 3 years, in the absence of changes in FEV_1.

REFERENCES. **1**. Mathew L, *et al.,* Academic Radiology 2008. **2**. Kirby M, *et al.* Radiology 2011. **3**. Kirby M, *et al.,* Radiology 2014. **4**. Fletcher C and Peto R BMJ 1977. **5**. Kirby M *et al*. Academic Radiology 2012.

Phase-matched 4DCT for AC in 4D gated PET

Julia Publicover[1*], Douglass C. Vines[2], Tina Shek[1,2], Brandon Driscoll[1,2],
Stephen L. Breen[2], David A. Jaffray [1,2]
OICR Imaging Translation Program
(1)Techna Institute, UHN, Toronto, ON, Canada
(2)Princess Margaret Cancer Centre, UHN, Toronto, ON, Canada

Introduction: Gating PET data for respiratory motion has been shown to reduce the effects of both blurring and improve the accuracy of quantitation. Although artifacts and quantitation errors can be partly corrected by using a gated (4D) acquisition, a mismatch between the CT used for attenuation correction (AC) and the PET phase has been shown to introduce further quantitation errors. The purpose of this study is to investigate the quantitative accuracy of phase-matched (PM) 4DCT versus helical CT (hCT) for AC in 4D gated PET.

Methods: We have built an insert compatible with a commercially available respiratory motion phantom. This phantom simulates breathing patterns using a moveable cylinder inside of a body-shaped oval. The custom-built insert contains a removable target of inner diameter of 20, 30 or 40 mm. The cylinder and target can be filled separately. In this study three scenarios were created by filling the cylinder with one of the following: air; polystyrene beads in water simulating lung density; or polystyrene beads in ^{18}F and water. In each the target is filled with ^{18}F and water.

The phantom was imaged both without motion and with a speed of 4 s per breath and target motion of 1, 2 or 4 cm. The phantom was imaged using hCT, 4DCT (6 bin), static PET and gated PET (6 bin).

Data for each of the 6 PET bins was reconstructed using the hCT for AC and the matching phase of the 4DCT for AC. The reported radioactivity in the target was measured for each phase of motion for both reconstructions.

The figure below shows reconstructed images for (1) ungated PET with hCT for AC (2) 4D gated PET with hCT for AC and (3) 4D gated PET with the matching phase of the 4DCT for AC.

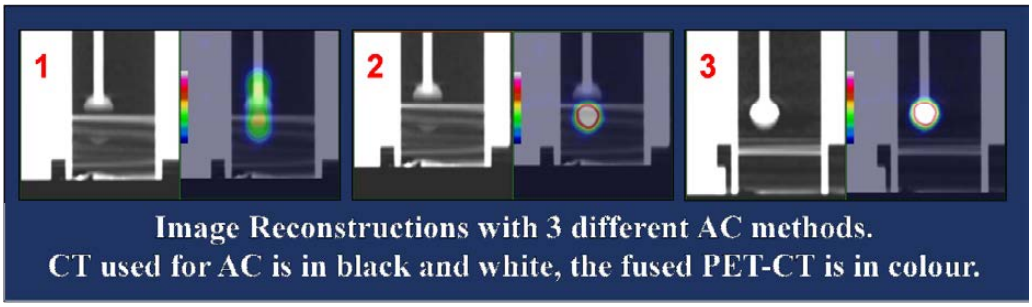

Image Reconstructions with 3 different AC methods.
CT used for AC is in black and white, the fused PET-CT is in colour.

Results: PM 4DCT for AC was compared to hCT for AC for the various experimental setups. In 19 of 24 cases PM 4DCT AC resulted in reported radioactivity concentrations closer to those seen in the corresponding static scan.
There is an element of unpredictability due to target position dependency. Since the tumor position during hCT is unknown during clinical acquisition there is uncertainty in the AC which can lead to errors in quantification.

Conclusions: For these reasons we suggest the use of PM 4DCT for AC instead of hCT for improved quantitation.

Development of Polymer Substrates for Waveguide Evanescent Field Fluorescence Microscopy

[1]**Rony Sharon and** [2]**Silvia Mittler**
[1]Program of Biomedical Engineering, [2]Department of Physics and Astronomy
The University of Western Ontario, London, ON, Canada
rsharon2@uwo.ca

Introduction. Waveguide Evanescent Field Fluorescence (WEFF) Microscopy was developed recently to image ultra-thin films and to investigate adhesion of cells to substrates and to produce quantitative distance maps of the plasma membrane to the substrate. A key component is the glass device containing a planar waveguide and a coupling grating.

Previous work has shown a better growth of cells on polymer substrates. Therefore, the objective of this study is the development and fabrication of polymer based substrates with similar characteristics to existing glass substrates.

Methods. Polymethymethacrylate (PMMA) substrates were fabricated by hot embossing a coupling grating from a master silicon mold, and subsequent spin coating of OrmoCore, a photoresist, or alternatively polystyrene serving as waveguides. The master mold was fabricated by spin coating Shipley 1805 photoresist on a silicon wafer followed by laser interference lithography implementing the grating pattern. Photoresist gratings were developed and oxygen plasma cleaned before preforming reactive ion etching to embed the structure within the silicon.

The correlation between the embossed substrate and the silicon mold grating constant was examined with scanning electron microscopy: taking the variations of temperature, the time and process pressure into consideration.

Results. Determined a set of parameters for PMMA substrate fabrication, and demonstrated that the same quality of coupling gratings can be achieved as seen in existing glass substrates. The next step is the fabrication of optical quality polymer waveguides on top of the PMMA substrate to start imaging fixed and living cells.

Discussion. WEFF microscopy could have many applications, especially in the field of tissue engineering, cellular biology and implant development. Paving the rode for mass production of WEFF substrates and to foster WEFF microscopy, spreading it among optical microscopy users which will be able to upgrade their existing microscopes to a surface sensitive tool and extend research capabilities without major modifications, is the driving force and importance of this work.

How do Exercise Responses Relate to ^{3}He Magnetic Resonance Imaging Apparent Diffusion Coefficients in Older Never-Smokers?

Khadija Sheikh[1,2], Gregory A Paulin[1,2], Sarah Svenningsen[1,2], David G McCormack[3], J Alberto Neder[4], and Grace Parraga[1,2]

[1]Imaging Research Laboratories, Robarts Research Institute; [2]Department of Medical Biophysics; [3]Division of Respirology, Department of Medicine, The University of Western Ontario, London, Canada. [4]Laboratory of Clinical Exercise Physiology, Queen's University, Kingston, Canada.

Primary Author: Khadija Sheikh
Research Supervisor: Grace Parraga

INTRODUCTION: Cardiopulmonary exercise testing (CPET) measurements correlate more strongly with health status than do resting lung function measurements [1]. ^{3}He magnetic resonance imaging (MRI) apparent diffusion coefficients (ADC) provide a surrogate measure of lung acinar duct and alveolar microstructure [2] that is reflective of emphysema in COPD patients. Although the relationship between ^{3}He MRI ADC and age was previously ascertained [3], the functional impact of ^{3}He MRI ADC in older never-smokers is not well-understood. Here we explored the potential consequences of elevated ^{3}He MRI ADC in older never-smokers and hypothesized that MRI measurements of emphysema would be related to CPET measurements.

METHODS: Volunteers, 60-90 years of age with ≤0.5 pack-year smoking history and no current acute or chronic respiratory disease provided written informed consent. All subjects were evaluated using hyperpolarized ^{3}He MRI, spirometry, plethysmography and CPET. The slope of the minute ventilation change as a function of pulmonary CO_2 output ($\Delta V_E/\Delta VCO_2$) was determined—where an increased slope was previously shown to be reflective of hyperventilation [4]. The y-intercept of the V_E-VCO_2 (i.e. the ventilation in the absence of pulmonary gas exchange) and the ventilatory equivalent for CO_2 (V_E/VCO_2) at nadir and VO_2max were also determined. The end-tidal partial pressures of O_2 and CO_2 ($P_{ET}O_2$, $P_{ET}CO_2$) were determined as measurements of pulmonary gas exchange. ^{3}He MRI ADC values were determined as previously described [5]. Univariate Pearson correlations and multivariate models for exercise capacity were generated using the forward, step-wise method using SPSS 20.0 software (IBM, Armonk, NY).

RESULTS: In 52 subjects (71±6yrs, 21M/31F), mean ADC was correlated with VO_2max ($r=0.28$, $p=0.002$), V_E/VCO_2max ($r=0.38$, $p=0.006$), $V_E$max ($r=0.48$, $p=0.0002$), and $P_{ET}CO_2$max ($r=-0.36$, $p=0.009$), and not age, DLCO, $\Delta V_E/\Delta VCO_2$ or V_E-VCO_2 intercept. In a forward, step-wise multivariate regression model with $V_E$max as the dependent variable, ^{3}He ADC and RV/TLC, but not FEV_1 or DL_{CO}, significantly added to the regression model ($R^2=0.31$, $p<0.001$), with ^{3}He ADC providing the greatest contribution (24%, $\beta=0.46$, $p<0.001$). In a multivariate model with VO_2max as the dependent variable, only ^{3}He ADC significantly added to the regression model ($R^2=0.08$, $p=0.046$) as was the case for V_E/VCO_2max as the dependent variable ($R^2=0.15$, $p=0.006$).

CONCLUSIONS: ^{3}He MRI measurements of emphysema was the strongest predictor of exercise capacity in older never-smokers. These results suggest that in older never-smokers, emphysema was associated with greater maximal exercise tolerance.

REFERENCES:

1. *ATS/ACCP Statement on cardiopulmonary exercise testing.* Am J Respir Crit Care Med, 2003. **167**(2): p. 211-77.
2. Yablonskiy, D.A., et al., *Quantitative in vivo assessment of lung microstructure at the alveolar level with hyperpolarized 3He diffusion MRI.* Proc Natl Acad Sci U S A, 2002. **99**(5): p. 3111-6.
3. Fain, S.B., et al., *Detection of age-dependent changes in healthy adult lungs with diffusion-weighted 3He MRI.* Acad Radiol, 2005. **12**(11): p. 1385-93.
4. O'Donnell, D. and K. Webb, *Breathlessness in patients with severe chronic airflow limitation. Physiologic correlations.* CHEST Journal, 1992. **102**(3): p. 824-831.
5. Parraga, G., et al., *Hyperpolarized 3He ventilation defects and apparent diffusion coefficients in chronic obstructive pulmonary disease: preliminary results at 3.0 Tesla.* Invest Radiol, 2007. **42**(6): p. 384-91.

Functional MRI Ventilation Discriminates Well-controlled Asthmatic and Healthy Subjects: Sensitivity, Specificity and Comparison with FEV_1

S Svenningsen[1,2], B Driehuys[3], DG McCormack[4] and G Parraga[1-2]

[1]Imaging Research Laboratories, Robarts Research Institute; [2]Department of Medical Biophysics, The University of Western Ontario, London, Canada. [3]Department of Radiology, Duke University, Durham, NC, USA. [4]Division of Respirology, Department of Medicine, The University of Western Ontario, London, Canada.

OICR Imaging Translation Program

Introduction: Asthma is commonly diagnosed and monitored using the spirometry measurement of the forced expiratory volume in one second (FEV_1) - a global measurement of lung function that is relatively insensitive to changes in the small airways.[1] Accordingly, there is an urgent need for alternative methods to evaluate asthma progression and treatment response. Previous work using hyperpolarized ^{3}He MRI provide a strong foundation for the use of MRI in asthma clinical care. However, to accelerate clinical translation and regulatory approval, the etiology of MRI ventilation must be determined and validated against clinically-acceptable measurements, such as FEV_1. Therefore, our objective was to evaluate the performance of hyperpolarized ^{3}He MRI ventilation heterogeneity measurements to discriminate asthmatic patients from healthy volunteers. We hypothesized that MRI ventilation measurements would provide sensitivity and specificity that was not different than FEV_1.

Methods: Well-controlled asthmatic patients and healthy volunteers provided written informed consent to the study protocol approved by the local research ethics board and Health Canada. At a single visit, subjects performed spirometry and MRI. Imaging was performed on a 3.0 T Discovery MR750 system (General Electric Health Care, WI, USA). For hyperpolarized ^{3}He MRI, subjects inhaled a $^3He/N_2$ gas mixture from functional residual capacity and image acquisition was performed under breath-hold. ^{3}He MRI ventilation segmentation was performed to generate the ventilation defect percent (VDP)[2] and the ventilation coefficient of variation (VenCOV).[3] Receiver operating characteristic (ROC) analysis was used to characterize the performance of FEV_1, ^{3}He MRI VDP and VenCOV as predictors of asthma using clinical diagnosis (Asthma/No Asthma) as the diagnostic threshold. The optimum cut-off point was determined according to the maximum Youden's index value and the corresponding sensitivity, specificity, positive and negative likelihood ratios were calculated.

Results: Subject measurements are provided in Table 1 for 26 asthmatics and 9 healthy volunteers. ROC curves for each of the diagnostic measurements (FEV_1, ^{3}He MRI VDP and VenCOV) are shown in Figure 1. Similar to $FEV_1\%_{pred}$ (AUC=0.82; p=0.006), ^{3}He MRI VDP (AUC=0.79; p=0.01) and VenCOV (AUC=0.76; p=0.02) discriminated asthmatics from healthy controls. For each diagnostic measurement, the established cut-off point and the corresponding performance characteristics (sensitivity, specificity, positive and negative likelihood ratios) were: $FEV_1\%_{pred}$: <92%, 68, 89, 6.1, and 0.4; VDP: >1.5% 80, 89, 7.2, and 0.2; and VenCOV: >0.20, 52, 100, ND, and 0.5. Comparison of the diagnostic measurements using their performance characteristics showed that the largest positive likelihood ratio (7.2) and smallest negative likelihood ratio (0.2) at the established cut-off was associated with ^{3}He MRI VDP. Figure 2 shows ^{3}He MRI ventilation images for a true positive asthmatic and false negative asthmatic diagnosed using the established cut-off point for VDP.

Table 1. Subject measurements.

Parameter (±SD)	Healthy (n=9)	Asthma (n=26)
Age yrs	34 (11)	35 (11)
Male Sex	5	11
$FEV_1\%_{pred}$	101 (9)	84 (15)
VDP %	1.4 (0.4)	3.3 (3.1)
VenCOV	0.19 (0.01)	0.20 (0.02)

SD=Standard Deviation, FEV_1=forced expiratory volume in 1 second; VDP, ventilation defect percent; VenCOV, ventilation coefficient of variation.

Conclusions: ^{3}He MRI measurements of ventilation significantly discriminated asthmatic patients from healthy controls and this is a necessary step towards clinical translation and regulatory approval. Because it is well-understood that ^{129}Xe MRI is more sensitive to ventilation abnormalities in asthma than is ^{3}He MRI,[4] next steps include validation of ^{129}Xe MRI in asthmatics.

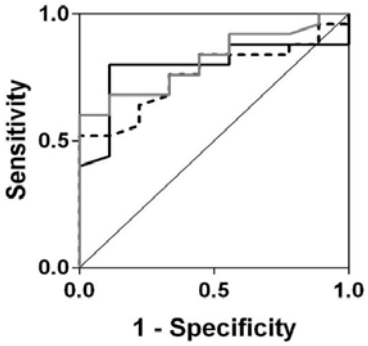

Figure 1. Receiver operating characteristic curve for the diagnosis of asthma using FEV_1 (grey solid line), ^{3}He MRI VDP (black solid line) and VenCOV (black dashed line).

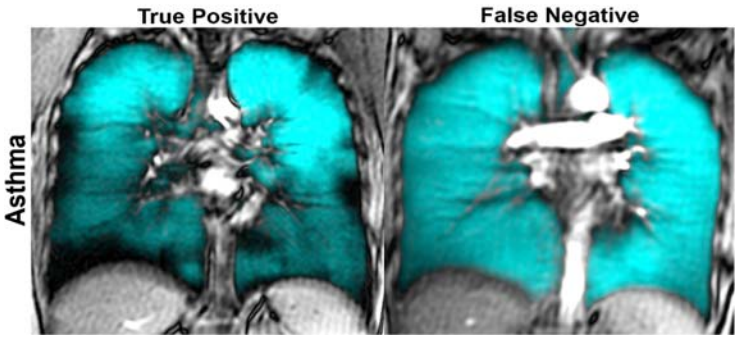

Figure 2. ^{3}He MRI ventilation for two well-controlled asthmatics. The true positive is a 36 yr old F, $FEV_1=66\%_{pred}$, VDP=7.8% and the false negative is a 23 yr old F, $FEV_1=96\%_{pred}$, VDP=0.9%.

References: 1) Burgel P. Eur Respir Rev. 2011. 2) Kirby M et al. Acad Radiol. 2012. 3) Sheikh K et al. J Appl Physiol. 2014. 4) Svenningsen S et al. J Magn Reson Imaging. 2013.

Deep Neural Network Based Segmentation of Lesions in Breast DCE-MRI

Hongbo Wu[1,*], Cristina Gallego[1], Anne Martel[1,2]
OICR Imaging Translation Program
[1]Medical Biophysics, University of Toronto; [2]Physical Sciences, Sunnybrook Research Institute

Introduction. Dynamic Contrast Enhanced Magnetic Resonance Imaging (DCE-MRI) is widely used as a diagnostic tool in breast cancer screening for "high-risk" women. However, this type of screening method suffers from poor specificity which results in many unnecessary biopsies. Recent studies have suggested that a Computer Aided Detection and Diagnosis (CAD) system can improve overall diagnostic accuracy of radiologists and thereby reduce the number of patients sent for biopsies. Most CAD systems use morphological and kinetic features to differentiate between benign and malignant lesions. In order to compute these features, robust outlines of these lesions must be first provided. However, outlining lesions by trained experts is prohibitively expensive and time-consuming. We therefore propose a robust method to automatically segment breast lesions in DCE-MRI in the context of an automated CAD pipeline.

Methods. Figure 1 outlines our proposed segmentation framework. Our approach uses a trained Deep Belief Network (DBN) to classify small 5x1x3x3 voxel (time, slice, y, and x) tiles in breast DCE-MRI images as possible lesion or non-lesion tiles. The classified tiles are then binarized using an optimized threshold and contiguously classified lesion tiles are connected to form candidate lesion regions. We reduce the number of false candidate regions by discarding regions that are smaller than 5mm in size which correspond to foci points not characterized by radiologists.

Results. An FROC curve was generated by plotting the detection rate of malignant lesions against the number of detected regions in normal breasts. By varying the decision threshold of the image binarization and choosing the best compromise between sensitivity and false candidate region, our method achieves 94.7% sensitivity and an average of 12 false candidate regions per normal breast (figure 2).

Conclusions. We proposed a robust completely automated segmentation method to outline lesions in breast DCE-MRI. Our method essentially captures the temporal signal intensity information of 8-neighbourhood connected voxels to achieve lesion segmentation. Figure 3 shows a lesion segmented using our algorithm. Our results suggest that there is sufficient information in raw intensity values to detect lesions in breast DCE-MRI.

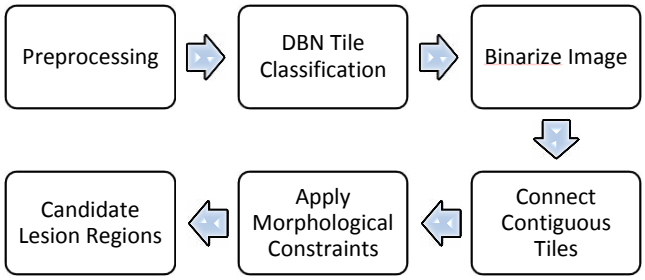

Figure 1. Outline of the segmentation method.

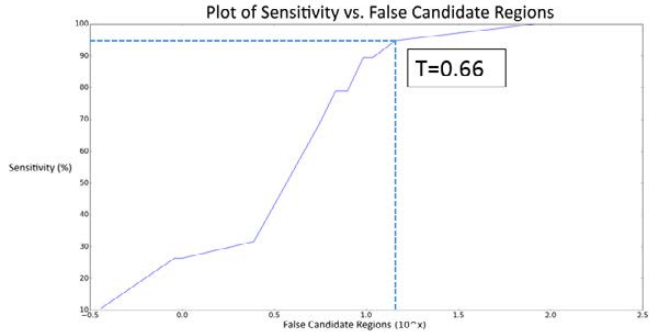

Figure 2. The threshold of 0.66 provides the best compromise between sensitivity and false candidate regions.

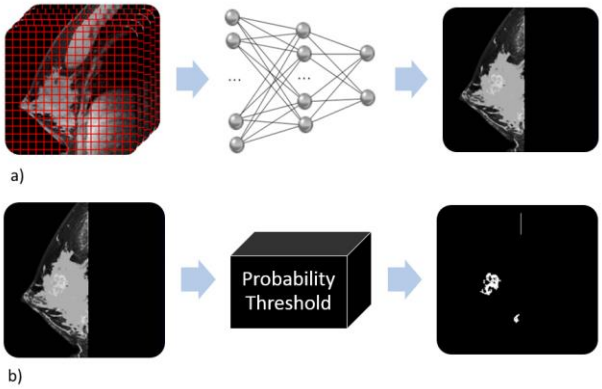

Figure 3. Example of segmentation process. a) 5x1x3x3 image tile classification. b) Image binarization and candidate region selection.

Personalized Treatment Selection for Brain Metastases Using MRI Radiomics

Timothy Pok Chi Yeung[a,c], George Rodrigues[b,c], Sarah Mattonen[a,c], Andrew Warner[c], Carol Johnson[c], Frank Lagerwaard[d], Miguel Palacios[d], Omar Bohoudi[d], Aaron D. Ward[a-c]

Department of [a]Medical Biophysics, [b]Oncology, The University of Western Ontario, London, Canada; [c]London Regional Cancer Program, London Health Sciences Centre, London, Canada; [d]Department of Radiation Oncology, VU University Medical Center, Amsterdam, The Netherlands

Introduction: For patients with brain metastases, early and accurate treatment selection is critical to maximizing quality of life and potentially extension to life. Prediction of response to stereotactic radiosurgery (SRS) informs personalized treatment selection. The classification of brain metastases as "homogeneous", "heterogeneous", and "ring-enhancing" has been shown to be predictive of overall survival (OS) after SRS [1], but is subject to inter-observer variability. Our objective was to improve OS prediction by developing and testing a radiomics software platform for quantitative assessment of brain metastases appearance.

Methods. Thirty-one brain metastasis patients (44 lesions) underwent routine gadolinium-enhanced T1 weighted magnetic resonance (MR) imaging prior to SRS. Each lesion was manually contoured and classified as "homogeneous", "heterogeneous", or "ring-enhancing" [1]. Image intensities were normalized using the brain ventricles as a statistical reference. Image features including the first-order image statistics, size and shape-based features, and gray-level co-occurrence (GLCM) textures averaged over 13 three-dimensional offsets were measured. Image features between the three contrast-enhancement groups were measured using the Kruskal-Wallis test followed by the Mann-Whitney *U* test. Correlations between image features and OS were evaluated using the Spearman correlation.

Results. The median time to compute 335 image features was 0.6 minutes/patient (range: 0.3 – 4.6) using a non-parallel and unoptimized MATLAB implementation. The three contrast-enhancement patterns showed significantly different first-order statistics ($P < 0.0025$) (Figure 1). Size and shape-based features and GLCM-based textures were not significantly different amongst the contrast-enhancement groups. Using the largest lesion in each patient as the index lesion, first-order energy showed a significant correlation with OS (rho = -0.61, P < 0.001). Range, 90th percentile, 99th percentile, surface area, normalized radial length entropy, correlation, and cluster prominence showed marginal correlations with OS ($P < 0.05$).

Conclusions. First-order image statistics calculated by our radiomics platform correlated with expert qualitative classification of contrast-enhancement patterns, and first-order energy correlated with OS. Future work includes optimizing the calculation of GLCM-based textures and determining a combination of image features that can accurately predict OS for individual patients.

Reference. [1] Goodman KA, et al. *Int J Radiat Oncol Biol Phys*. 2001;50:139-46.

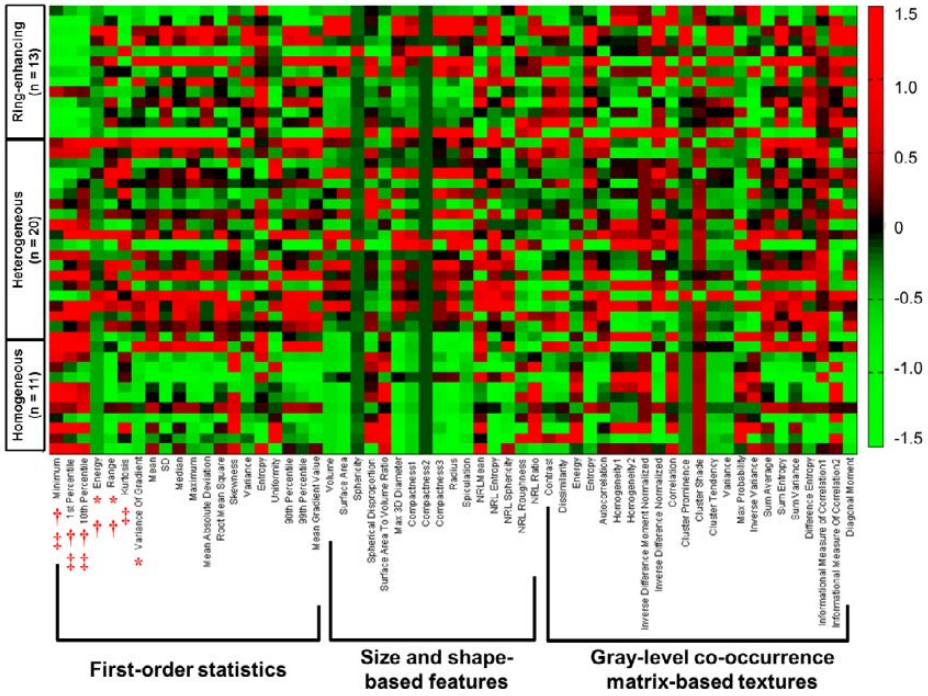

Figure 1. A heat map showing image features (columns) for each lesion (rows). Red and green indicate higher and lower standardized scores, respectively. (*), (†), and (‡) represent significant differences between homogeneous vs. heterogeneous lesions, homogeneous vs. ring-enhancing lesions, and heterogeneous vs. ring-enhancing lesions, respectively. A Bonferroni-corrected P < 0.0025 was considered significant.

Simultaneous Measurement of Perfusion and Hypoxia in Pancreatic Cancers

I. Yeung[a], C. Metran-Nascente[b], D. Vines[a], U. Metser[c], N. Dhani[b], D. Green[a], M. Milosevic[a], D.Hedley[b], D.Jaffray[a]
OICR Imaging Translation Program
[a]Radiation Medicine Program, Princess Margaret Cancer Centre, [b]Medical Oncology, Princess Margaret Cancer Centre, [c]Medical Imaging, Princess Margaret Cancer Centre, Toronto, Ontario

Background: Pancreatic cancers are believed to be poorly perfused and hypoxic, and these characteristics have been suggested to explain in part their aggressive biology and poor response to standard treatment. Quantification of perfusion and hypoxia may enable development of novel agent to improve clinical outcome.

Method: We have developed a method to quantify perfusion and hypoxia in pancreatic cancers with dynamic PET imaging post injection of ^{18}F-fluoroazomycin arabinoside (FAZA). A cohort of 19 patients with pancreatic cancers was scanned with a protocol of dynamic PET acquisition in the first 60 min followed by a single static scan at 2 hr. The dynamic data were binned for image reconstruction with intervals starting from 10s up to 5 min whereas the static scan was scanned with 2 bed positions of 15 min each. The images were viewed and tumor contoured by a radiologist. To quantify the perfusion component of the tracer kinetics of FAZA, the dynamic data (of 19 patients) were analyzed with a two-compartment model with which, 'Ktran' was calculated as a surrogate of perfusion. The analysis was performed on data over 1.5, 5.5 and 15 min respectively to investigate the length of data required to estimate Ktran. The static images at 2hr were analyzed with the 'Mortensen's method' [1] for hypoxic fraction. The method determines, for each patient, the tumor to mean muscle (skeletal muscle) uptake ratio for each voxel in the tumor; those tumor voxels with uptake ratio higher than unity plus 3 times the standard deviation of the population normalized muscle uptake will be classified as 'hypoxic'. The percentage of 'hypoxic' voxel within the whole tumor will give 'hypoxic fraction'.

Results: Fig 1 shows an example of the patients with low and high uptake of FAZA in the pancreatic tumors. Ktran estimates of 1.5 min data are found to be poorly correlated (r=0.60, 0.62) based on the Pearson correlation test with those of 5.5 min and 15 min respectively, whereas ktran estimates of the latter two times are found to be highly correlated (r=0.98). The mean Ktran of 5.5 min data is 0.384±0.108 ml/min/g and the hypoxic fraction ranges from 0.0 to 57.6% with median hypoxic fraction of 2.2%. Fig 2 is a plot of tumor perfusion vs hypoxic fraction; the Pearson correlation between Ktran values and hypoxic fractions gives a negligible slope of -0.001 and r= 0.0016 as shown in the figure.

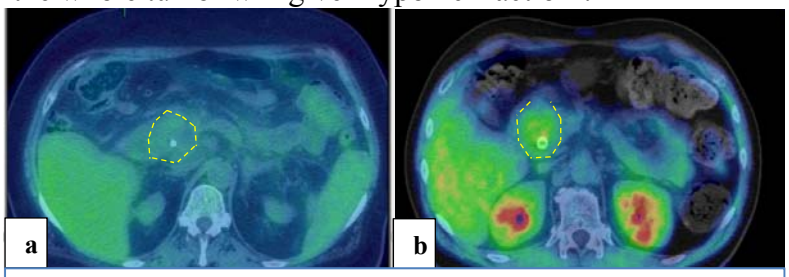

Figure 1: (a) and (b) are examples of low and high uptake of FAZA in pancreatic tumors respectively in our cohort.

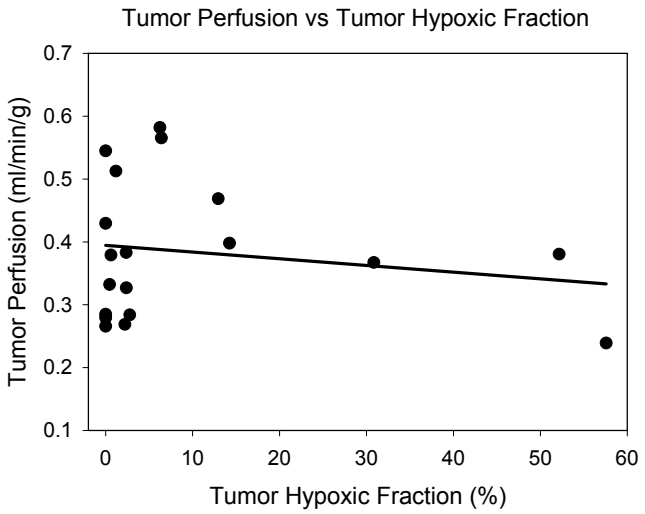

Figure 2: Tumor perfusion plotted against hypoxic fraction in the cohort of 19 patients. No significant correlation is observed.

Conclusions: The preliminary results suggested that (i) dynamic PET data of 5.5 min are sufficient to provide robust estimates of Ktran - a surrogate of perfusion, (ii) The preliminary results do not support the notion that pancreatic cancers are highly hypoxic, and (iii) there is no significant correlation between perfusion and hypoxia in our cohort of patients.

Reference:[1]Mortensen LS et al. Radiother Oncol. 2012 Oct;105(1):14-20

Development of ^{18}F-Labeled Peptides for Imaging EGFL7 in Prostate Cancer

Lihai Yu[a], John D. Lewis[b], Michael S. Kovacs[c], Leonard G. Luyt[a,d]

[a]London Regional Cancer Program, 790 Commissioners Road East, London, Ontario N6A 4L6; [b] Department of Oncology, University of Alberta, Edmonton, Alberta T6G 2E1; [c]Lawson Health Research Institute, London, Ontario, N6A 4V; [d]Departments of Oncology, Chemistry, Medical Imaging, The University of Western Ontario, 1151 Richmond Street, London, Ontario N6A 5B7.

Introduction: Angiogenesis plays a critical role in the expansion and metastasis of tumors. EGFL7 protein, specifically secreted by endothelium cells, is upregulated during vascular remodeling and is a promising target for imaging angiogenesis. Using one-bead one-compound (OBOC) methodology, we previously discovered a peptide (LCE72) that binds to EGFL7 with strong affinity (K_d = 13.2 nM), as determined by surface plasmon resonance (SPR). Here, we report on the radiosynthesis of ^{18}F-labelled LCE72 and the corresponding biological evaluation in vitro and in vivo.

Method: We modified the structure of LCE72 allowing for radiolabelling with cyclotron produced F-18 by azide-alkyne click chemistry, resulting in [^{18}F]LCE72 (Figure 1A). [^{18}F]LCE72 was evaluated in a series of biological studies in vitro and in vivo to determine it's potential for imaging angiogenesis. Cell uptake studies were performed in EGFL7 transfected HT1080 cells and control HT1080 cells. PET image data was obtained in four xenograft murine models, EGFL7-HT1080, control HT1080, LNCaP and PC3.

Results: [^{18}F]LCE72 was synthesized using click chemistry in high specific activity and radiochemical purity, as determined by HPLC analysis. In vitro analysis demonstrated retained affinity to EGFL7 protein as indicated by higher uptake in EGFL7-HT1080 cells than in control HT1080 cells. The tumors in all four types of cell line implanted mice are clearly identified in the PET images(Figure 1B). As seen in the SUV curves taken from the PET images(Figure 1C), [^{18}F]LCE72 keeps higher uptake in EGFL7-HT1080 tumor after 30 min post injection and decreases slower than in control HT1080, LNCaP and PC3 tumors.

Conclusion: [^{18}F]LCE72 was successfully radiolabelled and it was demonstrated to be a promising radiotracer for imaging prostate cancer. Further preclinical evaluation will be performed prior to advancing to clinical trials.

Figure 1.

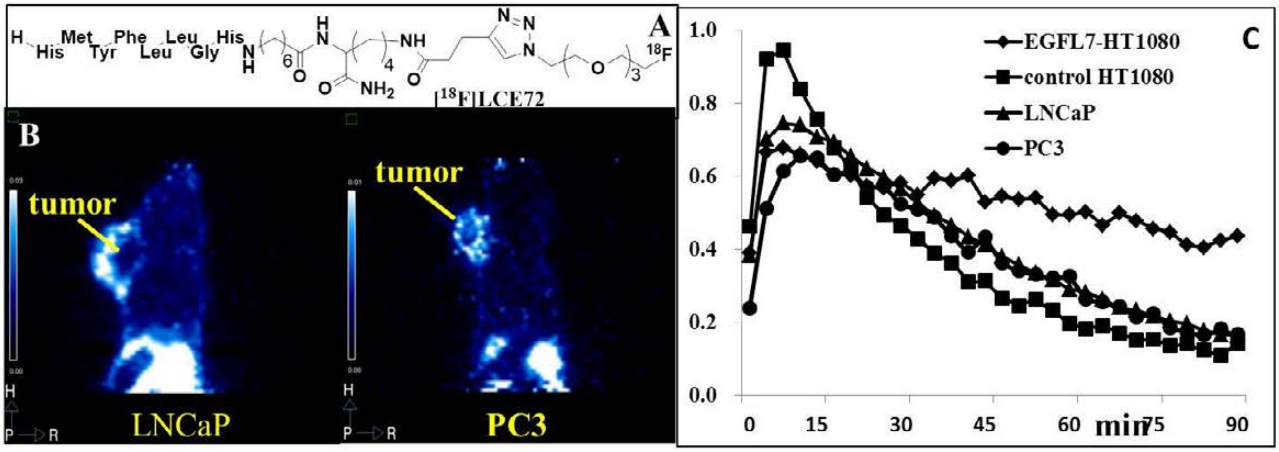

OICR Smarter Imaging Program

OICR SIP

Oral Presentation and Poster Abstracts

In Vivo Whole-Body Spin-Lattice Relaxation Dispersion at 1.5 Tesla using Delta Relaxation Magnetic Resonance (dreMR) Imaging

Yonathan Araya[1,2], Francisco Martínez-Santiesteban[2], Chad Harris[3], William Handler[3], Paula Foster[1,2], Blaine Chronik[1,2,3], and Timothy Scholl[1,2,4]

[1]*Department of Medical Biophysics,* [2]*Imaging Research Laboratories, Robarts Research Institute,* [3]*Department of Physics and Astronomy, Western University, London, ON Canada,* [4]*Ontario Institute for Cancer Research*

PURPOSE The ability to exploit spin-lattice relaxation rates (R_1) and their associated dispersion over a range of magnetic field shifts (ΔB_0) at clinical field strengths, using field-cycling magnetic resonance imaging (MRI) imaging, is a potential tool to differentiate between normal and atypical tissues. [1,2,3,4] Using delta relaxation enhanced magnetic resonance (dreMR) imaging, molecular interactions can be probed with the administration of targetable contrast agents, from which only tissues from the bound portion of the contrast agent demonstrates significant R_1 magnetic field dependence, thereby increasing the specificity and sensitivity of the targetable contrast agent.[3]

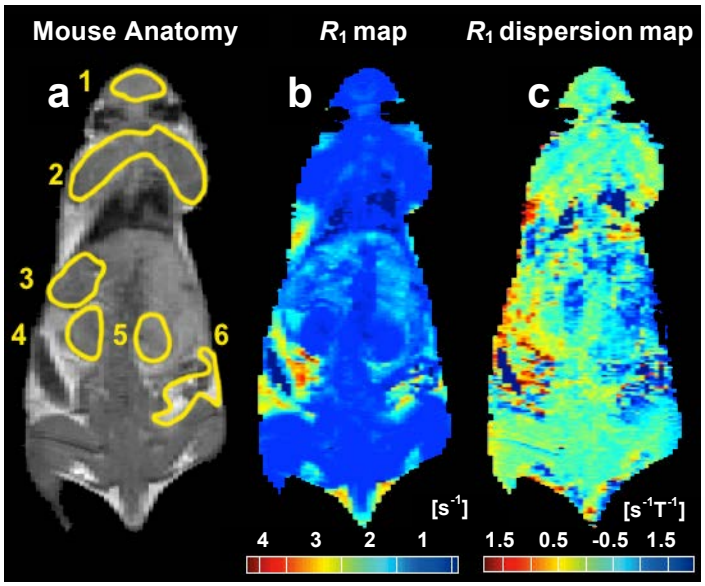

Figure 1. **[a]** Anatomical T_1-weighted MRI highlighting ROIs of selected tissues. **[b]** R_1 [s^{-1}] map at 1.5T in false colour. **[c]** R_1 dispersion dreMR map, $\Delta R_1/\Delta B_0$, [s^{-1}T^{-1}] at 1.5T.

METHODS Imaging was performed on a 1.5T GE CVMR system outfitted with a dreMR field-cycling coil to dynamically control B_0 prior to imaging.[3] Three dreMR images, T_{1+} (+0.11T), T_{1-} (-0.11T), and T_1 (0.0T), were acquired using a field-cycling T_1-weighted fast spin-echo inversion recovery pulse sequence, where ΔB_0 was modulated for a duration of relaxation times prior to imaging (50, 75, 100, 125, 150, 200, 400, 750, 1000, 1500, 2000, 3000, 5000, 8000 ms). Prior to each magnetic field shift, the sample was allowed to polarize for 2000 ms at 1.5T followed by an 180° inversion radiofrequency (RF) pulse, after which the magnetic field shift was applied (ramp time=10 ms, 6 ms delay before imaging). The remaining sequence parameters were as described (TE=14.2 ms, NEX=2, matrix=320x128, FOV=12.0x4.8 mm^2, slice thickness 2.0 mm, 4 echoes). The repetition time was maintained as the sum of the polarization, relaxation and imaging times over the course of imaging. A healthy female NU/NU mouse (26g) anesthetized with 2% isofluorane was placed on a custom water heated (37°C) bed in a Tx/Rx birdcage RF coil within the dreMR coil for imaging.

Tissue Type	$\Delta R_1/\Delta B_0$ ± SD
1 Brain	-0.21 ± 0.09
2 Muscle	-0.13 ± 0.02
3 Liver	-0.57 ± 0.28
4&5 Kidneys	-0.24 ± 0.79
6 Fat	-0.045 ± 0.77

Table 1. ROI analysis of selected tissues for R_1 dispersion. The dispersion slope ($\Delta R_1/\Delta B_0$) ± one standard deviation [s^{-1}T^{-1}] was determined by linear regression.

RESULTS *In vivo* whole-body spin-lattice relaxation rates (R_1) and dispersion maps of protons at 37°C for a healthy mouse have been quantified for a dreMR magnetic field of shift of ±0.11T about 1.5T. On the T_1-weighted MRI, regions of interest (ROI) were drawn for the brain, liver, kidneys, mammary fat, and limb muscle (Fig. 1.a). R_1 maps were produced 1.61T, 1.5T (Fig. 1.b), and 1.39T using a 3-parameter non-linear fit for spin-lattice relaxation (R1, amplitude & offset parameters) on a pixel-by-pixel basis. ROI analysis of the tissues showed little dispersion, $\Delta R_1/\Delta B_0$ (Fig. 1.c & Table 1), across a dreMR field shift of ±0.11T about 1.5T.

CONCLUSION These findings emphasize the R_1 magnetic field dependence of tissues at the clinical field strength of 1.5T over a range of ±0.11T, presenting a basis for investigations of cancerous and atypical tissues with magnetic field cycling (dreMR) after administration of targetable contrast agents.

REFERENCES **[1]** Lurie D.J., *et al.*, C. R. Physique (2010);11:136-148. **[2]** Hoelscher, U.C., *et al.*, Magn Reson Mater Phy (2012);23:223-231. **[3]** Alford, J.K., *et al.*, MRM (2009);61:796-802. **[4]** Koenig, S.H., *et al.*, Invest Radiol (1984);19:76-81.

ACKNOWLEDGEMENTS We are thankful for research funding from the Ontario Institute for Cancer Research, Smarter Imaging Program, and the Natural Sciences and Engineering Research Council of Canada.

Quantitative Functional Imaging of Prostate Cancer with Improved Kinetics Modeling of Hybrid ^{18}F-Fluorocholine PET-CT Imaging

Adam Richard Blais[1,2], Mark Dekaban[1,2], Eli Gibson[3], Jennifer Hadway[1], Ting-Yim Lee[1,2]
[1] Lawson Health Research Institute, London, ON, Canada
[2] Department of Medical Biophysics, Western University, London, ON, Canada
[3] Department of Biomedical Engineering, Western University, London, ON, Canada

Introduction: ^{18}F-Fluorocholine (FCH) PET imaging is of interest for the localization of prostate cancer (PCa) and has the potential to allow for more accurate targeting of both biopsy and intra-prostatic radiation dose escalation. However, studies using the standardized uptake value (SUV) have been unable to differentiate PCa from benign prostatic hyperplasia, despite the fact that PCa exhibits overexpression of choline kinase as well as higher phosphocholine levels compared to benign tissue. This may be due to the confounding effects of blood flow and blood volume in the local vasculature, which cannot be discriminated using the SUV. Quantitative kinetic analysis of FCH PET can account for this confounding effect by estimating the k_3 parameter, which represents the enzymatic activity of choline kinase. However, it is difficult to obtain a robust estimate of k_3 because of high covariance between kinetics model parameters.

Methods: A linearized solution was developed for the compartment model of FCH uptake in tissue. Hybrid DCE-CT/PET imaging allowed the blood flow, blood volume and permeability DCE-CT functional maps to be used as *a priori* knowledge in the PET model to reduce the parameter covariance in the curve fitting, resulting in more robust parameter estimates. Furthermore, the linearized solution can be fitted to the measured uptake curve using a non-negative least squares algorithm, which is computationally efficient and converges to a unique and optimal set of model parameters. Using computer simulation, this work compared the accuracy of k_3 estimates from the linearized solution of the compartmental model to that from the non-linear solution with and without DCE-CT priors using the Levenberg-Marquardt algorithm. For proof of concept, a PC-3 human prostate cancer mouse model and a human prostate cancer study were analyzed with this technique.

Results: Simulations showed the linear solution had a k_3 bias of 51.3% with precision of 44.6%, which improved to 9.5% and 23.5%, respectively, when DCE-CT priors were incorporated into the model (1,000 runs, signal-to-noise ratio = 10). Preliminary results from a PC-3 mouse model (Figure 1) and a human prostate cancer study show that k_3 functional maps exhibit significantly higher tumor-to-background ratios compared to SUV maps and distribution volume maps calculated via graphical Logan Plot analysis.

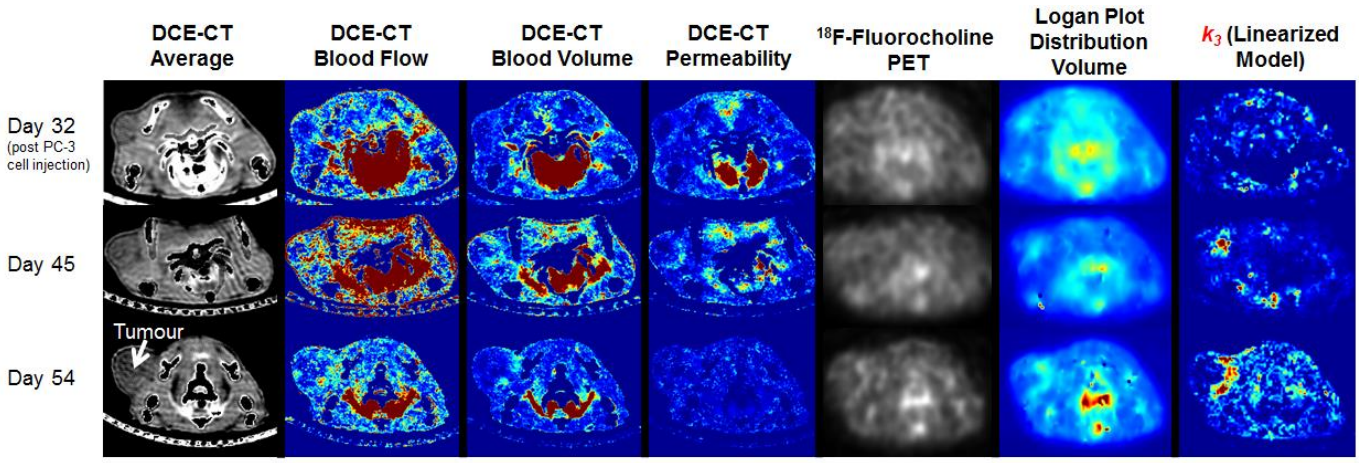

Figure 1: DCE-CT functional maps and PET SUV, graphical analysis, and k_3 parametric maps of a PC-3 human prostate cancer mouse model. The tumor was implanted in the left flank. The k_3 parametric map exhibited higher tumor-to-tissue contrast compared to SUV and graphical analysis maps.

Conclusions: In summary, we have developed a computationally efficient technique for accurate estimation of the k_3 parameter that may be capable of differentiating prostate cancer foci from benign tissue. This technique has the potential to allow for more accurate biopsy sampling as well as more accurate targeting for intra-prostatic radiation dose escalation, which would reduce patient discomfort and potentially improve patient outcomes.

Evaluation of [^{68}Ga]-DOTA Ghrelin (1-19) in LNCaP Prostate Carcinoma

Charlton, Carlie L.[1,2]; Dhanvantari, Savita,[1]; Luyt, Leonard G. [1,2]
1 The University of Western Ontario, London, Ontario, Canada; 2 London Regional Cancer Program, London, Ontario, Canada.

Introduction. Ghrelin is a 28-amino acid peptide found to be the endogenous ligand for the growth hormone secretagogue receptor-1a (GHSR-1a). GHSR-1a is a G-protein couple receptor known to be differentially expressed in various human cancers, including prostate cancer. In a previous study, ghrelin was shown to be capable of distinguishing between healthy, benign and cancerous *ex vivo* prostate tissue using optical imaging. We have now developed a [^{68}Ga]-DOTA-ghrelin(1-19) analogue capable of imaging the GHSR-1a using positron emission tomography (PET).

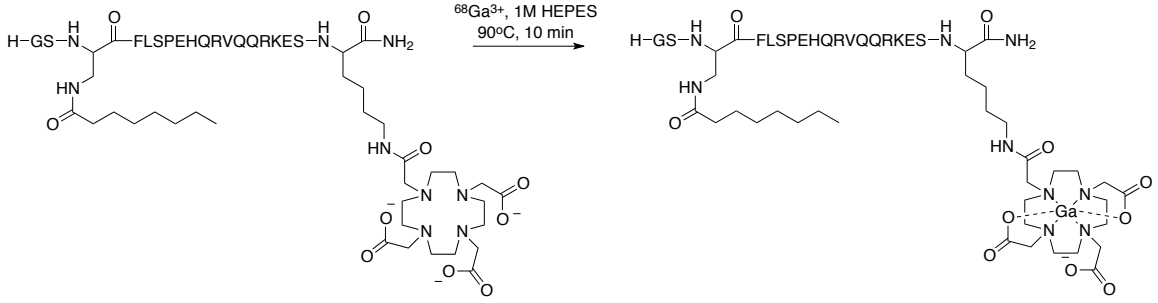

Figure 1: Synthetic scheme for the radiolabelling of DOTA-ghrelin(1-19) using $^{68}Ga^{3+}$.

Methods. Ghrelin(1-19) analogues were synthesized by solid phase Fmoc-based peptide synthesis. Using orthogonal protecting groups at diaminopropanoic acid-3 and lysine-19, the analogue was functionalized with octanoic acid and DOTA respectively. A non-radioactive gallium standard was prepared by complexing [$^{69/71}$Ga] with HPLC purified DOTA-ghrelin (1-19). IC_{50} values were obtained using competitive binding assays with ^{125}I-ghrelin(1-28) (PerkinElmer) in HEK293 cells stably transfected with GHSR-1a. Radiochemistry was performed with generator produced [$^{68}Ga^{3+}$] incubated at 90°C with DOTA-ghrelin(1-19) in 1M HEPES buffer (Figure 1). Purified [^{68}Ga]-DOTA ghrelin(1-19) was used for *in vitro* and *in vivo* evaluation.

Results. The IC_{50} of [$^{69/71}$Ga]DOTA ghrelin(1-19) was 9.1 nM compared to 8.1 nM for native ghrelin (1-28). Optimized radiolabeling of DOTA-ghrelin(1-19) yielded specific activities >22 GBq/μmol and radiochemical purity of >95%. *In vitro* studies using HEK293/GHSR-1a cells showed specific uptake of ^{68}Ga-DOTA ghrelin(1-19) that was decreased in the presence of GHSR-1a blocking agent, hexarelin (IC_{50} = 6.4 nM). A one hour dynamic μPET scan showed tumour localization of ^{68}Ga-DOTA ghrelin(1-19) as early as 10 minutes post-injection in NOD/SCID mice bearing LNCaP xenografts, although washout was observed within one hour suggesting low *in vivo* stability. Administering hexarelin significantly reduced tumour uptake visualized at 10 minutes.

Conclusions. A ^{68}Ga-DOTA ghrelin(1-19) analogue has been successfully synthesized and radiolabelled in respectable yields. This analogue is capable of visualizing LNCaP tumours as early as 10 minutes using PET.

[1] Rosita, D., *et al., J. Med. Chem.*, **2009**, 52, 2196-2203.
[2] Chen, L., *et al*., *The Prostate*, **2012**, 72, 825-833.

Comparison of Functional Lung Imaging using Inert Fluorinated Gas and Hyperpolarized ^{3}He MRI

Marcus J. Couch[1,2*], Iain K. Ball[3], Tao Li[2], Matthew S. Fox[4], Birubi Biman[5,6], and Mitchell S. Albert[1,2].

(1) Lakehead University, Thunder Bay, Ontario, Canada. (2) Thunder Bay Regional Research Institute, Thunder Bay, Ontario, Canada. (4) Robarts Research Institute, Western University, London, Ontario, Canada. (5) Thunder Bay Regional Health Sciences Centre, Thunder Bay, Ontario, Canada. (6) Northern Ontario School of Medicine, Thunder Bay, Ontario, Canada.

Introduction: Pulmonary fluorine-19 (^{19}F) magnetic resonance imaging (MRI) using inhaled inert fluorinated gases provides functional lung images similar to hyperpolarized (HP) noble gas MRI. Inert fluorinated gas MRI is possible without the expensive polarizer and scarce isotopes that are required for HP gas MRI, and the gases are nontoxic, abundant, and inexpensive. Inert fluorinated gas MRI of the lungs has been recently demonstrated in healthy volunteers (1) and patients with lung diseases (2). This preliminary study demonstrates for the first time, a direct comparison between inert fluorinated gas and HP ^{3}He MR lung imaging in the same subjects.

Methods: This study was performed using a 3T Philips Achieva scanner and two flexible wrap-around quadrature transmit/receive coils tuned to either the ^{3}He or ^{19}F resonant frequencies (Clinical MR Solutions). Five healthy female volunteers (mean age = 23±3 years) were enrolled in this study with no previous history of lung disease. Conventional ^{1}H MR images were initially acquired using a 1 L breath-hold of room air for localization. ^{3}He 2D multi-slice gradient echo images were acquired during a 15 s breath-hold following inhalation of a 330 mL ^{3}He dose balanced to 1 L with N_2. ^{19}F 3D ultrashort echo time (UTE) or 3D gradient echo (GE) images were obtained during a 25 s breath-hold of a mixture of 79% perfluoropropane (PFP) and 21% O_2. The signal-to-noise ratio (SNR), ventilated volume (VV), and ventilation defect percent (VDP) were measured and compared between ^{3}He and ^{19}F acquisitions (3).

Results: Figure 1 shows a comparison of 4 central coronal slices that were obtained in a representative volunteer using a ^{1}H localizer, HP ^{3}He gradient echo, ^{19}F gradient echo, and ^{19}F UTE. Compared to HP ^{3}He images, the ^{19}F images have a lower SNR, poorer resolution, more poorly defined edges, and T_2^*-induced blurring is apparent in the UTE images. As expected the HP ^{3}He SNR was significantly greater than the SNR from inert fluorinated gas imaging ($p = 0.01$ from a two-tailed paired t-test). For three subjects that all had a consistent slice thickness, the VV, VDV, and VDP measurements from HP ^{3}He and inert fluorinated gas imaging were statistically indistinguishable ($p > 0.05$).

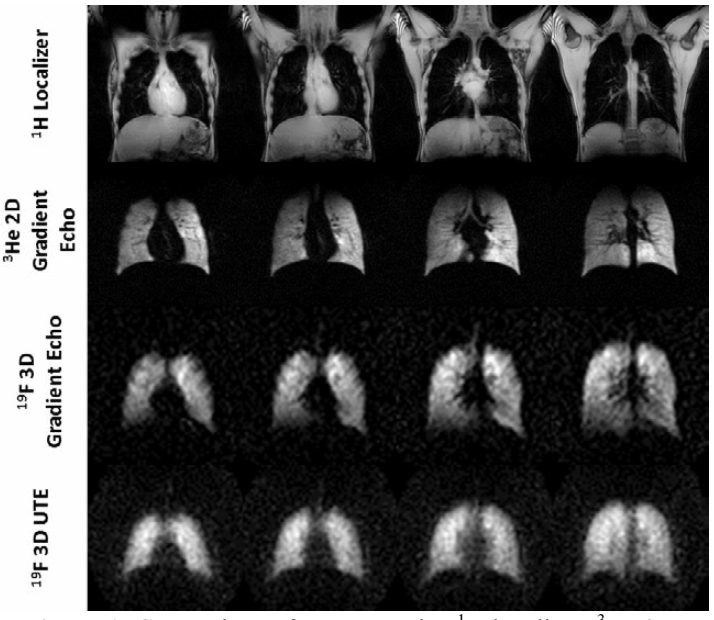

Figure 1: Comparison of representative ^{1}H localizer, ^{3}He 2D gradient echo, ^{19}F 3D gradient echo, and ^{19}F 3D UTE images acquired in the same healthy volunteer.

Conclusions: Overall, the SNR from ^{19}F MR lung imaging was less than HP ^{3}He imaging; however, the quantitative lung volume measurements in this preliminary study were statistically indistinguishable between the two techniques. Although more subjects will be required in order to fully validate inert fluorinated gas MRI, this technique has the potential to yield meaningful functional information that is similar to HP ^{3}He MRI and this technique may become a viable clinical imaging modality that can aid in diagnostic decision making.

References: [1] Couch et al. (2013) *Radiology* 269:903-909. [2] Halaweish et al. (2013) *Chest* 144:1300-1310. [3] Kirby et al. (2012) *Acad Radiol* 19:141-152.

^{19}Fluorine (^{19}F) cellular magnetic resonance imaging to monitor *in vivo* therapeutic cell migration

Fink, C[1,2], Gaudet, J[1,3], Foster P[1,3], Dekaban, G[1,2]
OICR Smarter Imaging Program
Molecular Medicine, Robarts Research Institute[1], Departments of Microbiology and Immunology[2] and Medical Biophysics[3], Western University, Canada

Introduction: Cancer immunotherapy is an emerging research area that uses one's own immune system to combat cancer. An example involves the *ex vivo* preparation and loading of antigen presenting cells (APC), in the form of a homogeneous dendritic cell (DC)-based cancer vaccine or heterogeneous APC-based vaccine, with tumor-specific antigen (Ag) to create a cancer vaccine. Tumor-Ag presenting DC or mixed APC must track to secondary lymphoid organs post injection to exert their function as adjuvants in cell-based cancer vaccines. Within secondary lymphoid organs like the lymph node, they present Ag to T cells and induce tumor Ag-specific T cell proliferation, forming the basis of cancer immunotherapy. Previous research has demonstrated that the quantity of tumor Ag-loaded DC reaching a lymph node is directly proportional to the magnitude of the ensuing tumor Ag-specific immune response. Thus, we propose that ^{19}F cellular MRI and a ^{19}F perfluorocarbon cell labeling agent, Cell Sense, can non-invasively track and quantify *in vivo* human APC migration and that this novel imaging technique can be used to improve upon APC-based cancer vaccines while also assessing their anatomical fate and longevity.

Materials and Methods: Peripheral blood mononuclear cells (PBMC) were isolated from the blood of male volunteers and cultured with Cell Sense (5.0mg/mL) for 48 hours. Twenty-four hours into culture, granulocyte macrophage colony-stimulating factor (GM-CSF) was added to activate the APC contained within the PBMC mixture. Following culture, Cell Sense-labeled PBMC were injected into the footpads of nude mice. Two days post injection, mice were imaged at 9.4T using ^{19}F cellular MRI to track and quantify migration to the draining popliteal lymph node. Also, PBMC from prostate cancer patients were isolated and labeled with Cell Sense (5.0mg/mL) overnight under Good Manufacturing Practice conditions, and injected subcutaneously into the upper flank of nude mice. ^{19}F cellular MRI was conducted on day 0 and 2 days post injection to observe if migration to secondary lymphoid organs occurred. In each cell culture condition, the phenotype and viability of Cell Sense-labeled PBMC were assessed using flow cytometry and compared to unlabeled controls. Furthermore, a red fluorescent Cell Sense label was used with flow cytometry to observe Cell Sense uptake by each cell lineage. This preclinical data will be used to progress towards imaging autologous Cell Sense-labeled PBMC in prostate cancer patients using ^{19}F cellular MRI.

Results: Thus far, our laboratory has been able to efficiently label human PBMC from both healthy male volunteers and prostate cancer patients with Cell Sense without toxicity being observed. Human APC migration post footpad injection to both the popliteal and inguinal lymph nodes has been detected and quantified in a mouse model using ^{19}F cellular MRI. Work is currently being conducted using PBMC samples from prostate cancer patients while optimization of this novel imaging technique is being performed in order to progress towards imaging autologous Cell Sense-labeled PBMC in humans.

Conclusions: Our laboratory is able to track and quantify the migration of human therapeutic cells in mice to secondary lymphoid organs using ^{19}F cellular MRI and a ^{19}Fluorine-based cell labeling agent, Cell Sense. Future work will focus on correlating therapeutic cell migration with anti-cancer immune response in order to improve upon the immunogenicity of APC-based cancer vaccine efficacy as well as conducting imaging studies in humans. By doing so, we would be the first in Canada to conduct ^{19}F cellular MRI in humans.

Hyperpolarized 129Xe gas production for lung and brain MRI

Avner Fitterman[1,2], Tao Li[2], Marcus Couch[1,2], Gowtham Gajawada[1,2], Mathew Fox[3], Mitchell Albert[1,2]
1.Lakehead University, Thunder Bay, Ontario 2.Thunder Bay regional Research Institution, Thunder Bay, Ontario 3.Robarts Research Institution, London, Ontario.

Introduction. The magnetic resonance imaging (MRI) modality is based on the magnetization that is formed by the influence of a strong polarizing magnetic field on the spin of protons, typically those of water molecules within the body. In Hyperpolarized (HP) gas MRI, a dramatic increase in spin polarization is achieved using spin-exchange optical pumping (SEOP), which allows images to be obtained with high signal-to-noise ratio (SNR). Batch-mode custom-built polarizers can serve to produce the HP gas, however, such custom-built systems, as any other polarizers, require optimization in terms of pressure parameters and temperature. This study is composed of three objectives: i) Gaining understanding regarding the physics of the nuclear polarization process of ^{129}Xe; ii) Understanding the pressure and temperature dependences of the polarization as it may be inferred by the theory and previous studies; iii) Exploiting that knowledge for the benefit of the optimization of the custom-built polarizer in our lab.

Methods. Our polarizer is combined from several components: a glass 245ml cell (Polarean Inc.) that contains 2g of rubidium, sufficient to saturate the cell with rubidium vapour once heated (fig. 2). The rubidium vapour is needed to transfer angular momentum from incoming circularly polarized laser light to the xenon's nuclei. The laser beam is produced by a 2-diode laser tuned to 794nm, and is guided by an optical fiber into a quarter-wave-plate to form circular polarized the light. The xenon gas is inserted into the cell via a pipe system that enables several different gas mixtures: 1% xenon, 10% N_2 and 89% He, or a variable ratio of xenon and N_2. The cell is heated by airflow upon the cell's surface, and is equipped with a temperature controller. Once polarized, the gas is let out of the cell to a Tedlar bag that is transported into an MRI (3T Philips Achieva), where the MR scanning is performed for measuring the xenon's spin polarization, using head coil (clinical MR Solutions).

Results. This gas mixture has an optimal polarization at a temperature of 130C. The pure xenon presented optimal temperature at 100C. Moreover, the dependence on the total cell pressure was examined and similar trends were found in both cases. The main goal of the experiment was measuring the polarization with respect to Xe/N_2 ratio and it presented in Figure 1. The polarization rates are between 0.4% and 0.7% (where in reference 2 the polarization rates are about 80-90%).

Conclusions. Two main results were observed as expected [1]: the higher optimal temperature for the lean xenon with respect to the pure xenon mixture; the inverse relationship between the polarization and the partial xenon pressure. The polarization rates are low in comparison with other groups that worked on polarizer optimization [2]. It is worth mentioning that one of the primary causes is likely the low radiation flux that was measured before it enters the cell (15W in this study, versus 100-200W in reference 2). The contribution of this work is in providing the proper temperature and pressure values for achieving maximal polarization in this specific polarizer, and more generally, it provides the guidelines (with the theory behind) for optimizing any custom-built polarizer.

References. [1] Whiting *et al*. Journal of Magnetic Resonance 2011;208;298-304.[2]. Nikolaou *et al.* Journal of the American Chemical Society 2014;136(4);1636-1642.

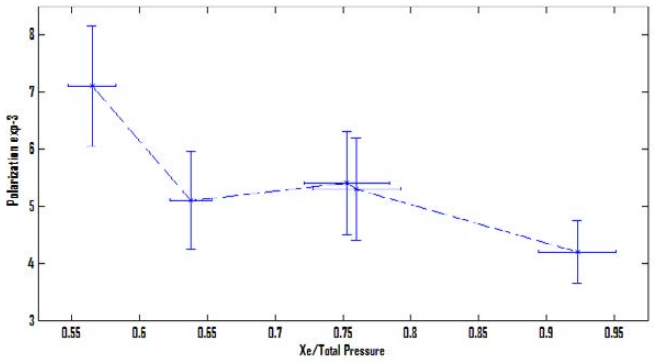

Figure 1. The polarization as a function of the xenon to total cell Pressure ratio

Figure 2. The cell of the custom-built polarizer

Cellular MRI: Monitoring the Fate of Human Stem Cells and the Inflammatory Response

OICR – Smarter Imaging Program
Jeff M Gaudet[1,2], Matthew S Fox[1,2], Amanda M Hamilton[1], and Paula J Foster[1,2]
[1]Imaging Research Laboratories, Robarts Research Institute, London, Ontario, Canada, [2]Medical Biophysics, Western University, London, Ontario, Canada

Background: Regenerative stem cell therapy is anticipated to revolutionize modern medicine. Mesenchymal stem cells (MSC) are a leading candidate for clinical trials due to their multipotent properties and presence in adult tissue. However, before treatment can progress to the clinic there are still many questions that must be answered concerning the immune rejection of transplantations. Cellular MRI offers a tool to non-invasively track the fate of stem cells and improve treatment outcomes. In this study we use dual iron/fluorine MRI to monitor two distinct cell populations: (i) MSC, labeled *in vitro* with ^{19}F prior to implantation and, (ii) phagocytic immune cells, labeled *in situ* through administration of intravenous (IV) iron.

Methods: Immune competent, C57Bl/6 mice were implanted intramuscularly with $1.05x10^6$ human MSC (hMSC) labeled with a red fluorescent perfluorocarbon emulsion. This model was chosen to produce an acute immune response. 7 days after hMSC implantation, mice received an IV tail vein injection of ultra-small iron oxide nanoparticles (USPIO) at a dose of 4μg Fe/g. On day 8, 4 hours prior to imaging, the mice received 10ng of lipopolysaccharide (LPS) IP to stimulate macrophages. Proton (^{1}H) and ^{19}F images were acquired at 9.4T with a dual-tuned ^{1}H/^{19}F mouse body coil using a 3D-balanced steady state free precession (bSSFP) sequence. Total scan time was under 90 minutes. Mice were anaesthetized with isoflurane and imaged four times, up until day 8. NMR was performed using $2x10^6$ ^{19}F-labeled hMSC in order to determine the intracellular loading. Quantification of the ^{19}F-labeled cells was performed by measuring the signal in the region of interest and in a reference of known concentration using Voxel Tracker software. Following imaging, mice were sacrificed and tissues removed for immunohistochemistry (IHC).

Results/Discussion: On the day of implantation (day 0) the ^{19}F-labeled hMSC were visible in all mice and *in vivo* ^{19}F-MRI quantification agreed strongly with the number of implanted cells (Fig 1A). The ^{19}F signal gradually decreased between days 0 and 6 (Fig. 1B). Proton images obtained on day 8, 24 hrs after the IV injection of USPIO, showed a large region of signal void at the transplantation site (Fig 1C). Coincident with this was a significant drop in the ^{19}F signal at the transplant site. The ^{19}F signal on day 8 was decreased by 63% from day 6. The observation of signal loss in proton images after IV USPIO is consistent with the infiltration and accumulation of iron-labeled macrophages at the implant site. Many studies have proven the utility of IV iron for macrophage tracking. In addition, the transplant model we used would be expected to cause an acute cellular inflammatory response; host macrophages migrate into transplants in response to cell death and inflammation. It is noteworthy that the signal loss, generated by what we presume to be iron-positive macrophages, did not quench the entire ^{19}F signal. IHC is underway to confirm and quantify the presence of hMSC and macrophages in tissue. In this study, we have shown that it is possible to non-invasively monitor implanted stem cells with ^{19}F-MRI, while simultaneously monitoring the influx of iron-labeled immune cells.

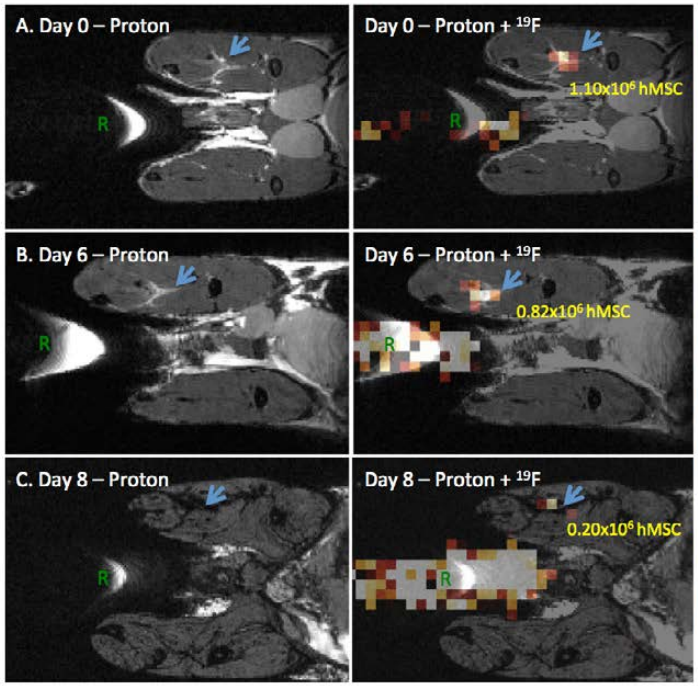

References: 1. Hitchens TK, Liu L, Foley LM, Simplaceanu V, Ahrens ET, Ho C. Combining perfluorocarbon and superparamagentic iron-oxide cell labeling for improved and expanded applications of cellular MRI. *Magnetic Resonance in Medicine*. 2014.

Rational design of Mn^{III}-porphyrin based MRI contrast agents: Insights from the electronic structure theory

Wilfred C. Ho, Xiao-an Zhang, Artur F. Izmaylov
Department of Physical and Environmental Sciences, University of Toronto Scarborough, Toronto, Ontario, Canada

Introduction: Gd^{III} complexes are currently the most common MRI type of contrast agents. Despite is popularity, there are very rare cases where patients experience nephrogenic systemic fibrosis (NFS) from Gd^{III} contrast agents due to existing kidney problems. The relaxivity of Gd^{III} also decreases with the strength of the external magnetic field, making it difficult to obtain high resolution MRI images. In collaboration with other groups[1], we have demonstrated the substantial relaxivity of Mn^{III} porphyrin based compounds at high magnetic fields. Without significant side effects, Mn^{III} porphyrin complexes appear to be promising alternatives to Gd^{III} contrast agents. The goal of this project is to construct a predictive model for the relaxivity of Mn^{III} porphyrin compounds which accounts for their electronic structure. This model can then be used to predict possible chemical modifications which would increase Mn^{III} porphyrin's relaxivity and make them more efficient contrast agents.

Method: Structures with various ligands bonded to porphyrin and coordinated to Mn^{III} were optimized with density functional theory methods[2]. Hyperfine interaction between nuclear spins of hydrogen atoms in coordinated water molecules and electron spins of Mn^{III} porphyrin complexes as well as zero field splitting tensor were calculated and integrated into the conventional relaxivity model[3] to account for the effects of the contrast agent's electronic structure.

Results and Conclusion: The calculations have shown that Mn^{III} porphyrin's high relaxivity is quite sensitive to distribution of electron spin density. MnTCP and MnTPPS have been found to have higher relaxivity compare to that of the unsubstituted Mn^{III} porphyrin compound, where as direct coordination of halogens to Mn^{III} and to the meso position of the porphyrin ring have very little effect. Ring modifications using N-confused porphyrins (MnNCP) have also shown significant improvements to the relaxivity of the pristine Mn^{III} porphyrin compound. These results indicate that extra sources of electron spin density are beneficial in Mn^{III} based contrast agent design.

References: [1]Cheng, W., Zhang, X.et al.; J. Med. Chem. 2014, 57, 516 (2013)
[2]Perdew, J.; Density Functionals for Non-relativistic Coulomb Systems in the New Century. In A Primer in Density Functional Theory, 1st ed.; Springer: 1 (2003)
[3]Schaefle, N.; Sharp, R. J. Phys. Chem. A, 109, 3267 (2005)

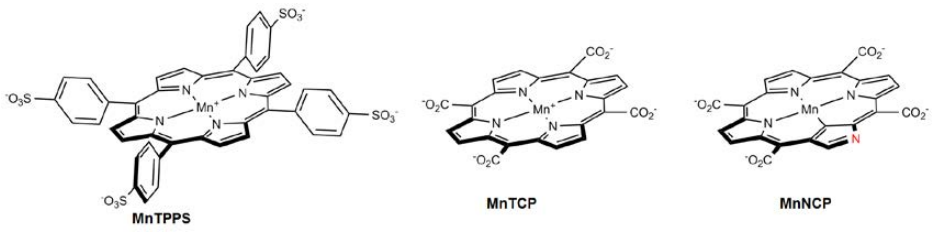

Figure 1: Manganese (III) meso-tetra(4-sulfonatophenyl)porphyrin (MnTPPS), Manganese (III) [5, 10, 15, 20]-tetrakis(carboxyl)porphyrinato (MnTCP), and Manganese(III) meso-tetra(carboxyl)N-confused porphyrin (MnNCP)

Molecular Modeling Studies for Rational Design of GHSR-1a Agonist for Prostate Cancer Diagnosis Using PET

Jinqiang Hou[a], Milan Mrázek Fowkes[b], Leonard G. Luyt[ab]*

[a] London Regional Cancer Program, 790 Commissioners Road East, London, ON, Canada
[b] Depts. Oncology, Chemistry, Medical Imaging, The University of Western Ontario, London, ON, Canada.

Introduction: Prostate cancer is the third most frequent cancer in men worldwide. A non-invasive clinical technique to accurately diagnose, and especially, to effectively distinguish benign and malignant tissue is urgently needed. Our studies have suggested that targeting the growth hormone secretagogue receptor 1a (GHSR-1a), a highly expressed G protein-coupled receptor in prostate cancer, could distinguish benign and malignant tissue in prostate[1]. Therefore, the development of a positron emission tomography (PET) imaging agent for GHSR-1a has great potential for accurate prostate cancer diagnosis. G-7039 is a peptidomimetic agonist that binds GHSR-1a with an IC_{50} of 5.2 nM. Structural modification of G-7039 is required to improve the binding affinity, stability, pharmacokinetics and ease of radiolabelling with ^{18}F.

Methods: To facilitate the structural optimization, a series of computational studies including homology modeling (MODELLER), molecular docking (Z-dock), molecular dynamics simulation (amber) and binding free energy calculation (MM-PBSA) were carried out and a 3D model detailing the interaction between G-7039 and GHSR-1a at an atomic scale is proposed.

Results: The model reveals that G-7039 is directly involved in strong interactions with residues Phe279, Arg283 and Phe312, all of which have been reported to play a crucial role in receptor activation. The result correlates well with the fact of G-7039 being an agonist for this receptor[2-3].

Conclusions: A 3D model detailing the interactions between G-7039 and GHSR-1a at an atomic scale is proposed. The model suggests that the residue phenylalanine and naphthalene on G-7039 are solvent-exposed and not directly involved in the binding (Fig 1). They are the better sites to incorporate the ^{18}F prosthetic group without reducing the binding affinity. Structural modification of these two residues to include fluorine is currently underway. The model will aid in the rational design of G-7039 analogs for the development of PET imaging agents for prostate cancer diagnosis.

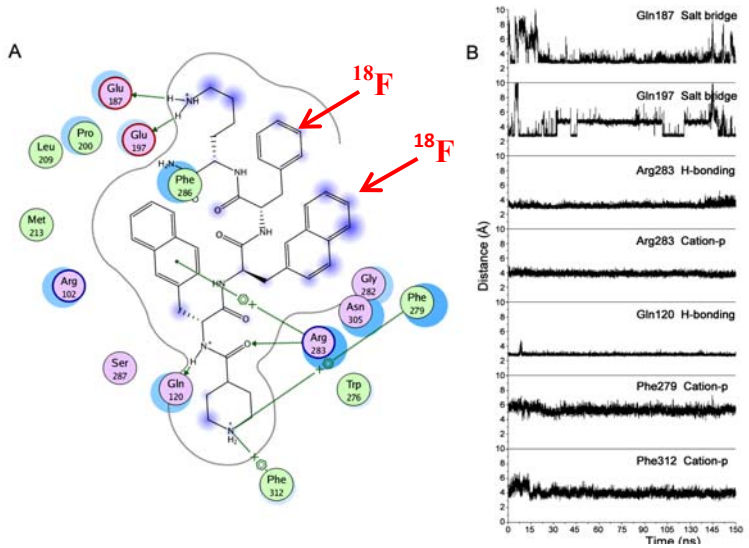

Fig1. (A) The detail interactions between G-7039 and GHSR-1a; (B) Distances of interactions. The arrows indicate the residues which are not directly involved in the binding and are to be incorporated with ^{18}F prosthetic group.

References:

[1] Lu C, et al., Prostate 2012, 72(8):825-833. [2] Holst B, et al., J Biol Chem 2004, 279, 53806-53817. [3] Floquet N, et al., J Mol Biol 2010, 395, 769-784.

Sagittal sinus enlargement in female athletes with mild traumatic brain injury

O. Hough, D. Fraser, L. Fischer, C. Barreira, T. Jevremovic, K. Asem, T. Doherty, A. Brown, G. Dekaban, R. Menon, and R. Bartha
on behalf of the London Sport Concussion Program

Robarts Research Institute, Schulich School of Medicine and Dentistry, Western University, London, Ontario, Canada

Introduction. Mild traumatic brain injury (mTBI) or concussion is the most common form of brain injury in Canada. Though extremely common, knowledge surrounding mTBI is limited and it is largely unknown how mTBI affects the brain structurally and physiologically. In this study, 3Tesla MRI was used to assess structural changes in mTBI patients in the superior sagittal sinus (SSS), a large sinus that runs anterior to posterior in the brain, along the falx cerebri. The SSS allows for the drainage of blood and cerebrospinal fluid in the brain. This study is the first to examine the effects of mTBI on superior sagittal sinus size in humans.

Methods. 3D T1-weighted MPRAGE anatomical MRI scans (1 mm isotropic resolution, Fig 1) were acquired in female undergraduate students on the varsity rugby team at the beginning of the competitive season. Players who sustained a mTBI received MRI scans after the concussion event at the 3 day, 3 month, and 6 month time points. All non-concussed players received an MRI scan at the end of the season. Images were blindly analyzed in the DICOM viewer OsiriX Lite (6.0.2). Regions of interest were outlined around the superior sagittal sinus (SSS, Fig 1 outlined) and the total brain using a freehand tracing tool. In each subject, 6 images were used, each 10 slices apart to calculate the average SSS/brain ratio. Paired t-tests were used to compare SSS/brain ratio between time points.

Results. Non-concussed athletes (n=23) showed a 7% increase in SSS/brain ratio over the course of the season ($p<0.05$). Concussed athletes (n=6) had a 17% greater SSS/brain ratio three days after concussion compared to baseline ($p<0.05$), which appeared to return to baseline levels after 3 months. The SSS/brain ratio increase at three days post concussion was significantly greater than the SSS/brain ratio increase in the non-concussed athletes.

Conclusions. The enlargement of the superior sagittal sinus observed in concussed female rugby players in this preliminary study may be an indicator of cerebrovascular dysregulation, indicating vascular injury. This result is consistent with the common occurrence of headache after mTBI, perhaps due to decreased cerebral blood flow as indicated by this change in vessel size. The return of the superior sagittal sinus back to baseline size after a 3 month period indicates that the superior sagittal sinus enlargement after mTBI is not permanent.

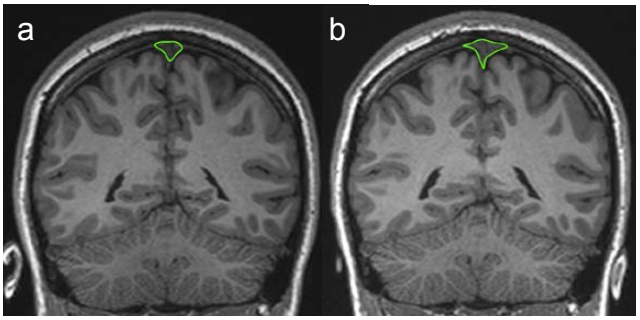

Figure 1. (a) MPRAGE MRI of an athlete pre-concussion and **(b)** post-concussion. Enlargement of the superior sagittal sinus (outlined in green) is visible.

Automatic segmentation of multiple needles in 3D trans-rectal ultrasound images for high-dose-rate prostate brachytherapy treatment planning

W. Thomas Hrinivich[1,2], Douglas Hoover[1,3,4], Kathleen Surry[1,3,4], David D'Souza[3,4], Aaron Fenster[1,2,4,5*], Eugene Wong[1-5*]

1 Dept. of Medical Biophysics, Western University; 2 Robarts Imaging Research Laboratories; 3 London Regional Cancer Program; 4 Dept. of Oncology, Western University; 5 Dept. of Physics and Astronomy, Western University, London ON; Consortium: OICR Smarter Imaging Program; *Trainee Supervisors

Introduction: High-dose-rate brachytherapy (HDR-BT) is a prostate cancer treatment option where 10-18 hollow needles (applicators) are inserted into the gland through the perineum guided by a template. Dose is delivered by indexing a high-activity source to dwell positions within the applicators based on the relative positions of applicator tips, the prostate, and nearby organs. Modern HDR-BT involves applicator insertion, 2D trans-rectal ultrasound (TRUS) imaging, manual segmentation, treatment planning, and delivery while the patient is under general anesthesia constraining procedure time. Automatic trans-perineal needle segmentation techniques only possible with high-resolution 3D TRUS could potentially be applied to HDR-BT applicator imaging and segmentation, reducing procedure time and patient discomfort. The purpose of this study was to investigate the application of an automatic needle segmentation technique to 3D TRUS images of HDR-BT patients containing multiple applicators. **Methods:** 8 prostate cancer patients underwent conventional HDR-BT. Following treatment delivery, a 3D TRUS image was acquired with 12-16 applicators present (120 applicators total). A version of the randomized Hough transform (RHT) based on Robert's line representation (Qui et al. 2013) was implemented in MATLAB 2014b using HDR-BT template insertion coordinates to initialize the algorithm. All applicators were segmented manually on the 3D TRUS images enabling comparison with auto-segmentation results. **Results:** Mean±SD auto-segmentation time was 221±5 ms per applicator. The algorithm identified applicator tips within 5 mm of those identified manually in only 39% of all 120 applicators. The majority of algorithm errors were attributed to misassigning applicators near one-another. Of the applicator tips identified within 5 mm error, mean±SD errors in the right/left, anterior/posterior, superior/inferior direction were -0.8±1.4 mm, 0.0±0.8 mm, and 0.15±1.4 mm respectively. **Conclusions:** 3D TRUS and the RHT with template-based initialization shows promise for reducing HDR-BT procedure time, but is not currently robust when images contain many nearby applicators. We are currently developing regularization techniques to handle nearby applicators in the presence of template uncertainty, and will present updated results.

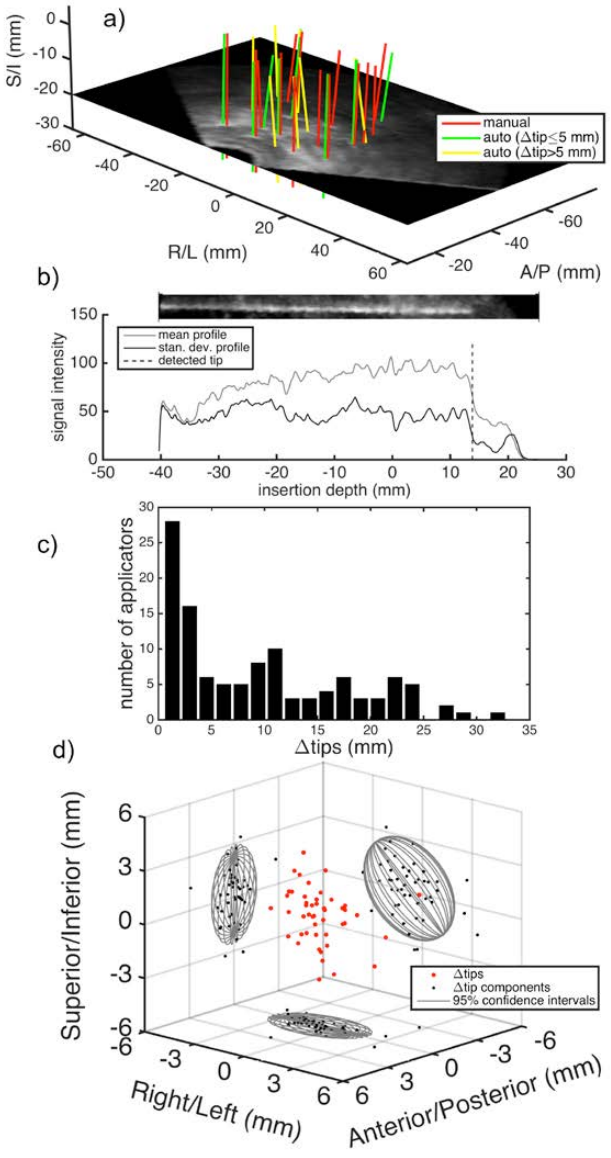

Figure 1a) Example manual and automatic applicator segmentations for a single patient, indicating tips automatically identified within 5 mm error. **b)** Example signal intensity mean and standard deviation profiles used to detect insertion depth. **c)** Histogram of Euclidean distances between manually and automatically segmented applicator tips (Δtips) for all 120 applicators. **d)** 3D differences between manually and automatically segmented tips for the 39% of applicators identified within 5 mm error. 2D difference projections (Δtip components) and 95% confidence interval projections are also shown.

References: Qui et al. Med Phys 40(4); 2013

A novel detector design for increasing detection of early disease by increasing the high-frequency detective quantum efficiency

Elina Ismailova and Ian A Cunningham

Dept. of Medical Biophysics and Robarts Research Inst., Western University, London,

Introduction

Development of new x-ray detectors with substantial performance improvements at high spatial frequencies is necessary for improved detection of fine image details for early detection of disease. This can only be achieved by increasing the high-frequency detective quantum efficiency (DQE) of the detector. We propose a novel design that will eliminate noise aliasing, a primary cause of poor DQE in many detectors. The design requires the use of extremely small detector elements (eg. 25 μm) and an optimal method of synthesizing image pixel values with practical spacings (eg. 100 μm).

Methods

We describe a method of optimizing the design of a linear filter used to synthesis image pixels. Using a cascaded-system analysis (CSA), we describe the imaging system as a serial cascade of elementary physical processes. Two methods are described to maximize the area under the DQE curve expressed as a function of spatial frequency. The first method is based on an "expanding" algorithm as we grow the pass-band and shape of the synthesis method. The second method is based on a "shrinking" algorithm as we reduce the pass-band while maintaining a uniform frequency response.

Results

Both methods showed that the optimal pass-band has a cutoff frequency equal to the sampling cut-off frequency for the size of image pixels used. In addition, while the filter shape influenced the MTF of the resulting detector design, it did not influence the DQE. The design was validated using a CMOS-CsI prototype detector where the DQE was increased by a factor of 2x, from 0.2 to 0.4 at 2.5 cycles/mm.

Conclusions

The proposed detector design increased the DQE by 2x at 2.5 cycles/mm in a prototype. This will double the contrast of fine image details, critical for detection of early disease.

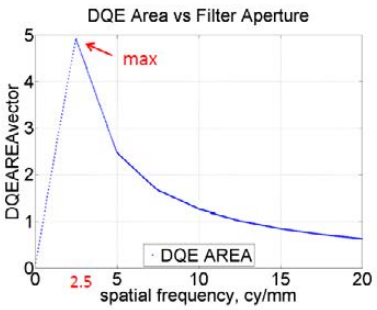

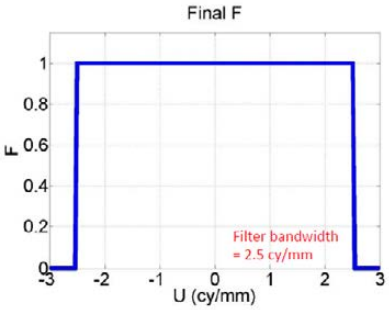

MicroPET/CT Imaging of EGFR and HER2 in Breast Cancer Tumour Xenografts in Mice using Bispecific Radioimmunoconjugates (bsRICs)

Luke (Yongkyu) Kwon[1], Deborah Scollard[2], and Raymond M. Reilly[1]
[1]*Leslie Dan Faculty of Pharmacy, Department of Pharmaceutical Sciences, University of Toronto, Ontario, Canada*
[2]*STTARR Innovation Centre, University Health Network, Toronto, Ontario, Canada*

Background: HER2-EGFR heterodimerization is critical step in activation of cellular signaling pathways for growth of breast cancer (BC). Molecular imaging employs probes to detect biomarkers and could be a valuable tool in identifying and treating BC patients with high levels of HER2 and/or EGFR. The purpose of this study was to examine the imaging properties of bispecific radioimmunoconjugates (bsRICs) intended for imaging both EGFR and HER2 in human BC xenografts in mice using microPET/CT.

Methods: BsRICs (^{64}Cu-NOTA-Fab-PEG$_{24}$-EGF) were constructed by reacting maleimide derivatized trastuzumab Fab fragments which bind HER2 with thiolated Epidermal Growth Factor (EGF) through a 24-mer polyethylene glycol (PEG$_{24}$) spacer. Then, the bsRICs were conjugated with S-2-(4-Isothiocyanatobenzyl)-1,4,7-triazacyclononane-1,4,7-triacetic acid (p-SCN-bn-NOTA) before radiolabeling with ^{64}Cu. A one-point *in vitro* competition binding assay was performed to examine the binding specificity of ^{64}Cu-bsRICs to MDA-MB-231 (EGFR+/HER2-), 231-H2N (EGFR+/HER2+), and SKOV3(EGFR-/HER2+). Pharmacokinetic study was performed in healthy BALB/c mice to evaluate the whole-body transport of bsRICs and monospecific RICs (^{64}Cu-NOTA-EGF and ^{64}Cu-NOTA-Fab) between 0 and 42 hours post injection. MicroPET/CT was performed in NOD-SCID mice bearing subcutaneous 231-H2N (EGFR+/HER2+) human BC xenografts at 24 and 48 h post intravenous tail injection of ^{64}Cu-bsRICs (25-30 MBq; 10 μg). Tumour and normal tissue uptake were quantified by *ex vivo* biodistribution studies and compared to those for monospecific RICs.

Results: The binding of bsRICs to MDA-MB-231 cells was reduced to 24.5 ± 5.2% by excess EGF. The binding of bsRICs to SKOV3 cells was displaced to 38.6 ± 5.4 % by excess Fab. Calculated pharmacokinetic parameters (AUC_{total}, V_1, V_{dss}, CL_{total}) revealed that ^{64}Cu-bsRICs were eliminated more slowly from the blood than ^{64}Cu-bsRICs without PEG spacer, and much more slowly than both ^{64}Cu-NOTA-Fab and ^{64}Cu-NOTA-EGF. Tumour uptake of ^{64}Cu-bsRICs in 231-H2N xenografts was 5.1 ± 0.05 %ID/g at 48 hours post injection. Significant differences were observed in tumour uptake of bsRICs when compared to ^{64}Cu-NOTA-Fab (1.9 ± 0.3 %ID/g; $p = 0.002$) and ^{64}Cu-NOTA-EGF (0.68 ± 0.2 %ID/g; $p = 0.0005$).

Conclusions: New ^{64}Cu-labeled bsRICs were successfully constructed which exhibited specific binding to EGFR and HER2 *in vitro*. These bsRICs exhibited better accumulation in tumours *in vivo* co-expressing EGFR and HER2 than monospecific RICs, permitting tumour visualization by microPET/CT.

Supported by grants from the Ontario Institute for Cancer Research (OICR Smarter Imaging Program) and the Canadian Institutes of Health Research .

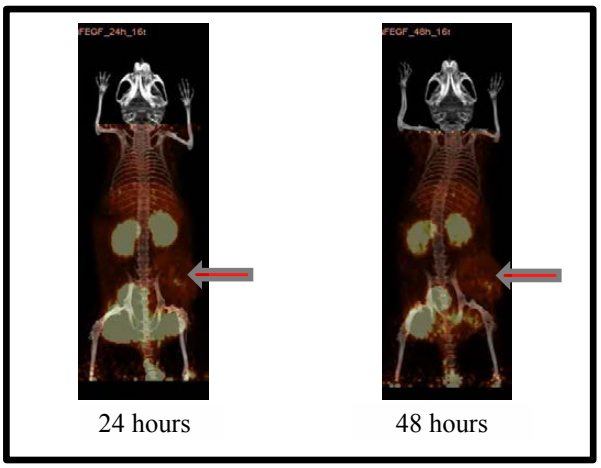

Figure 1. MicroCT/PET imaging with ^{64}Cu-NOTA-Fab-PEG$_{24}$-EGF in 231-H2N (EGFR+/HER2+) xenograft (shown in red arrow) at 24 hours and 48 hours post injection.

Remote Monitoring of Image Quality for Mammography Stations in the Ontario Breast Screening Program

Stephanie Langton[1*], Gord Mawdsley[1], Sam Shen[1], Aili Maki[1], Roy Yu[1], and Martin J. Yaffe[1,2]
[1]Sunnybrook Research Institute, Toronto, Ontario, Canada
[2]Dept. of Medical Biophysics, University of Toronto, Toronto, Ontario, Canada

Introduction. Consistently high technical quality of mammography is necessary in a breast screening program if the mortality reduction associated with screening is to be achieved. For this reason, quality control is mandated under federal and provincial legislation as well as for accreditation of mammography facilities. Quality control programs require that certain tests, including imaging of phantoms, be conducted on a daily, weekly, and monthly basis, with results analyzed and tracked over time. Technologists subjectively look at the images and have significantly different thresholds of acceptability. Until recently, the medical physicist's quality control testing in The Ontario Breast Screening Program (OBSP) has been conducted semi-annually on site at each of the participating screening centres. As a result, the analyses that can be performed on a day to day basis are limited, and post processing of the results is difficult. To address these concerns, a remote system for monitoring the imaging performance of all screening sites is being developed and implemented. The system supervises collection of QC images, data analysis, data collection, and display of results for central monitoring and for the radiological technologist.

Methods. The remote monitoring program consists of several stages. First the quality control images acquired at each site are transmitted to a central monitoring location via a secure DICOM server. Once received, the images are automatically sorted, regions of interest on the images are identified automatically and the appropriate image analysis is performed. The results of the image processing are then stored in a database and displayed on a web page accessible by the mammography technologists at each site, allowing them to review the results. The tests that have been incorporated in the program assess spatial resolution, uniformity, signal-to-noise ratio and artefacts and the tests have been designed to be conducted under conditions similar to those of imaging a real breast.

Results. The remote QC program is currently being activated at the OBSP sites. To date approximately 65 sites have successfully sent images to the centralized DICOM server, and can now review results on the web page. Fig. 1(a) shows results of the analysis of a flat field phantom that is imaged daily. The graph displays the average signal in a region of interest on the image. The remote monitoring processing program has the advantage of being able to show specially-processed versions of the image that can help detect subtle problems that may not be obvious from cursory inspection of the original image. Fig. 1(b) shows one of several thumbnail images that the technologists can view on the web page, in this case giving the peak variance deviation, an indicator of spatial nonuniformity. In the figure, the small dark specks could be caused by dust or non-functioning detector elements, and the technologist is prompted to investigate further.

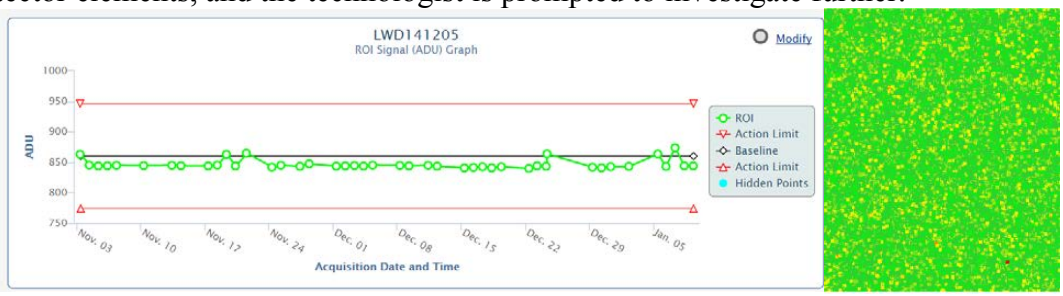

Figure 1. (a) ROI signal in a daily uniformity phantom **(b)** Peak variance deviation of daily uniformity phantom

Conclusions. Centralizing the data collection and analysis of the quality control imaging performed by locations involved in the OBSP allows for consistent and extensive analysis of the image quality. By moving to a single system that performs the same analysis on all mammography units and stores all of the results in a single database, a comparison across sites can easily be performed and retrospective analysis of results spanning a large period of time can be used to guide improvement of the quality control testing procedures and analysis.

References. [1] Jacobs *et al.* One year experience with remote quality assurance of digital mammography systems in the Flemish Breast Cancer Screening Program. Proc. IWDM LNCS 5116, pp. 703-710 (2008).

Linearized Johnson-Wilson approach for modelling dynamic contrast enhanced studies

Fiona Li* and Ting-Yim Lee
Robarts Research Institute, Western University, London, Ontario, Canada
Lawson Health Research Institute, London, Ontario, Canada

Introduction

The standard two compartment (2-C) model, consisting of vascular and tissue compartments, is frequently used to fit tissue time density curves (TDCs) from dynamic contrast enhanced (DCE) CT or MR studies. However, the compartmental assumption for the vascular space means that the finite vascular transit time is ignored. As image acquisition speed increases beyond 0.5 Hz, parameters estimated without accounting for the finite vascular transit time could be biased. Also, 2-C model is unable to estimate blood flow (F), it estimates Ktrans instead, which is the flow extraction efficiency product. On the other hand, fitting tissue TDC using the Johnson-Wilson model with the adiabatic approximation (aaJW) will provide estimates of both Ktrans and F that are independently important for investigations of tumor associated angiogenesis. Current applications of the aaJW model use non-linear curve fitting methods to estimate Ktrans and F. These methods are prone to be trapped in local minima while searching for the optimal fit to the tissue TDC resulting in erroneous estimates of model parameters. The main aim of this project is to develop a method to linearize the fitting of DCE tissue TDC with the aaJW model and compare the method's sensitivity to model parameters and covariances of estimated parameters with non-linear fitting methods

Method

Linearization of 2-C model fitting of tissue TDC has been published before but no attempts to-date have been made for linearization of aaJW model fitting. The method we developed to linearize aaJW model fitting of the tissue TDC is based on time integrals of the arterial TDC ($C_p(t)$) and the tissue TDC ($Q(t)$). The stability of the linear and non-linear fitting methods were analyzed using sensitivity analysis which calculated the changes in the fitted tissue TDC with changes in the model parameters or sensitivity functions of both fitting methods. The sensitivity functions were used to estimate the covariances of the estimated parameters for both methods.

Results

The equations for tissue TDC fitting with the aaJW model are:

Non-linear: $Q(t) = F\cdot[D(t-t_o)-D(t-t_o-W)]+K_1\cdot C_p(t-t_o-W)*\exp(-k_2\cdot(t-t_o-W))$

Linear: $Q(t) = F\cdot[D(t-t_o)-D(t-t_o-W)]+K_1\cdot D(t-t_o-W)+F\cdot k_2\cdot[E(t-t_o)-E(t-t_o-W)]- k_2\cdot G(t)$

where * is convolution operator, t_o is the delay between $Q(t)$ and $C_p(t)$, W is the vascular transit time, K_1=Ktrans, k_2 is backflux rate constant, $D(t)$ is the integral of $C_p(t)$, $E(t)$ is the integral of $D(t)$ and $G(t)$ is the integral of $Q(t)$. The sensitivity functions for the linear fitting method were ~ 5 times larger than those of the non-linear fitting method resulting in the covariances of estimated parameters from the linear fitting method > 1.3 times less than those of the non-linear fitting method.

Conclusions

Unlike the non-linear fitting method, the linear method estimates model parameters at the unique global minimum sum of squared deviations between the fitted and the measured tissue TDC. More importantly, the covariances of the estimated model parameters are significantly less for the linear method than the non-linear method. This would lead to more precise quantitative functional maps from DCE studies and more reliable diagnosis.

Metal chelating polymers (MCPs) harbouring multiple pendant PEG_{2K} chains linked to panitumumab $F(ab')_2$ fragments for microPET/CT imaging of patient-derived pancreatic cancer xenografts in mice

Amanda Boyle[1], **Yijie Lu[2]**, Ping-Jiang Cao[3], David Hedley[3], Raymond M. Reilly[1], and Mitchell Winnik[2]
Departments of Pharmaceutical Sciences[1] and Chemistry[2], University of Toronto; Ontario Cancer Institute/Princess Margaret Hospital[3], Toronto, ON, Canada

Background: Pancreatic cancer (PC) is the 4th leading cause of cancer related death in Canada and has the highest mortality rate of all cancers. ^{64}Cu-labeled panitumumab F(ab')$_2$ fragments (PmabFab2) which target human epidermal growth factor receptor (EGFR) overexpressed on >90% of PC have potential as combined PET imaging and therapeutic agents ("PET theranostics"). Our objective was to conjugate metal-chelating polymers (MCPs) via bis-aromatic hydrazone formation chemistry to PmabFab2 for labeling with ^{64}Cu to amplify their sensitivity for imaging and potency for cancer treatment. This study examines three MCPs with 19 repeat units and with different numbers of pendant PEG chains, $2PEG_{2K}$, $4PEG_{2K}$, and $8PEG_{2K}$, and examines their *in vitro* and *in vivo* characteristics, as well as their potential for PET/CT imaging linked to PmabFab2.

Methods: Unconjugated MCPs were ^{64}Cu-labeled then injected intravenously by tail-vein injection into non-tumour bearing BalbC mice and biodistribution was evaluated at 48 h post-injection for *in vivo* assessment of blood residence and normal tissue uptake with regards to the number of PEG_{2K} pendant chains per MCP. PmabFab2 fragments were conjugated to MCPs via bis-aromatic hydrazone formation. PmabFab2-MCPs were ^{64}Cu-labeled for *in vitro* assessment of their EGFR immunoreactivity using a 1-point binding assay and PANC-1 human PC cells (4 x 10^5 EGFR/cell). MicroPET/CT imaging and biodistribution studies were performed at 48 h post-injection in NOD-scid mice engrafted orthotopically with patient-derived OCIP23 PC tumours.

Results: For unconjugated ^{64}Cu-labeled MCPs in BalbC mice, the amount of radioactivity accumulated in each organ at 48 h increased with increasing numbers of PEG_{2K} pendant chains (Fig. 1A). The proportion of specific binding *in vitro* to EGFR for PmabFab2-$2PEG_{2K}$, PmabFab2-$4PEG_{2K}$, and PmabFab2-$8PEG_{2K}$ was 90.7±0.2%, 47.2±4.2%, and 56.0±0.8%, respectively. PmabFab2-$8PEG_{2K}$ was selected for microPET/CT imaging and biodistribution studies in tumour-bearing mice due to its enhanced stealth effects (longer residence time in the blood) which may promote tumour uptake. Uptake in orthotopic OCIP23 at 48 h p.i. was 4.9±0.5% ID/g (Fig. 1 B) and tumours were visualized by PET/CT (Fig. 1C). Liver and spleen uptake was moderate indicating the stealth properties of the MCPs and kidney uptake was relatively low.

Conclusions: Stealth properties demonstrated by longer residence in the blood were increased *in vivo* with increasing numbers of PEG_{2K} pendant chains. The proportion of specific binding to EGFR was retained for PmabFab2-$2PEG_{2K}$, while it was reduced to 50% for PmabFab2-$4PEG_{2K}$ and PmabFab2-$8PEG_{2K}$. Orthotopic PC xenografts were visualized by PET/CT imaging. Further investigation of the MCPs with lower PEG modification is planned to determine if $8PEG_{2K}$ is optimal for constructing the radioimmunoconjugates.

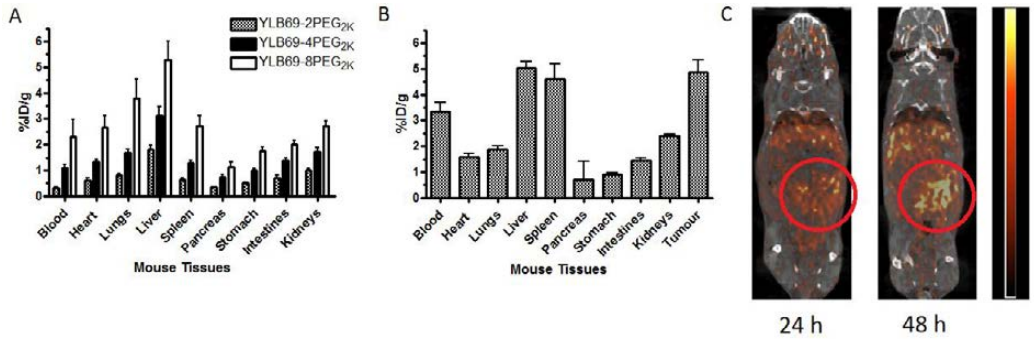

Figure 1. Normal tissue distribution of unconjugated ^{64}Cu-MCPs in BalbC mice at 48 h p.i (A), ^{64}Cu-PmabFab2-$8PEG_{2K}$ in tumour-bearing mice at 48 h p.i (B), and PET/CT imaging in orthotopic pancreatic patient-derived xenograft mouse models at 24 and 48 h p.i (C).

Supported by a grant from the Canadian Cancer Society Research Institute.

T_1 Nuclear Magnetic Relaxation Dispersion of Hyperpolarized ^{13}C Cesium and Sodium Bicarbonate

Francisco M. Martínez[1], Thien Phuoc Dang[1], Heeseung Lim[1], Albert P. Chen[3], and Timothy J. Scholl[1,2]
[1] Department of Medical Biophysics and [2] Robarts Research Institute, Western University, London, ON Canada
[3] GE Healthcare, Toronto, ON Canada
OICR Smarter Imaging Program

Introduction: Hyperpolarized bicarbonate has been demonstrated as a contrast agent for *in vivo* pH estimation in tissue, and as a valuable tool to study the tumour microenvironment [1-3]. As with other hyperpolarized contrast agents, ^{13}C-enriched bicarbonate compounds have a spin lattice relaxation time (T_1) on the order of tens of seconds, which provides enough time for rapid *in vivo* MR spectroscopic imaging. The T_1 of hyperpolarized media can be readily measured at standard magnet field strengths (1.5T, 3T, 9.4T, etc.) but no such data are available at low field strengths where T_1 can be significantly shorter. This information is required to determine the significant loss of polarization as the agent is transported from the polarizer, where it is dispensed near the earth's field, to that of the scanner for injection. In this work, we address this problem and also we compare the differences between cesium and sodium bicarbonate preparations previously reported in the literature.

Methods: Stock solutions of ^{13}C-sodium and ^{13}C-cesium bicarbonate dissolved in glycerol were prepared following the formulations proposed by Wilson *et al.* [3] and Gallagher *et al.* [1], respectively. The final concentrations of the ^{13}C-enriched stock solutions were 1.82M for sodium bicarbonate and 6.8M for cesium bicarbonate. From these stock solutions, individual samples were placed in a sample cup and then hyperpolarized using a HyperSense Dynamic Nuclear Polarizer (DNP) (Oxford Instruments, Abingdon, UK).

To investigate the effects of dipolar relaxation, for the sodium bicarbonate samples, two different dissolution media were used to achieve a final ^{13}C bicarbonate concentration of 60 mM. One dissolution using water/EDTA solution (100 mg/L) and the other one using deuterium oxide (heavy water) with the same EDTA weight-per-volume ratio. For the cesium formulation, only the water/EDTA solution was used to get the same final ^{13}C bicarbonate concentration as for sodium.

After dissolution with one of the two available dissolution media, a 1-mL sample of the hyperpolarized solution was withdrawn, placed in an NMR tube and quickly transferred to a fast field-cycling NMR relaxometer (Spinmaster FFC2000 1.0T C/DC, Stelar s.r.l., Mede, Italy). Different hyperpolarized samples were used to cover relaxation fields (B_{RLX}) in the range of 0.41mT to 0.55T. T_1 relaxation times were determined from the Spinmaster relaxation curves at different B_{RLX} using non-linear least-square estimation as presented in [4].

Results: Figure 1 shows the T_1 nuclear magnetic relaxation dispersion of ^{13}C-enriched cesium and sodium bicarbonate from 0.41mT to 0.55T for both EDTA-buffered water and EDTA-buffered heavy water. As a reference and given that pyruvate is a commonly used hyperpolarized ^{13}C compound, a similar plot for this substrate is also shown [4].

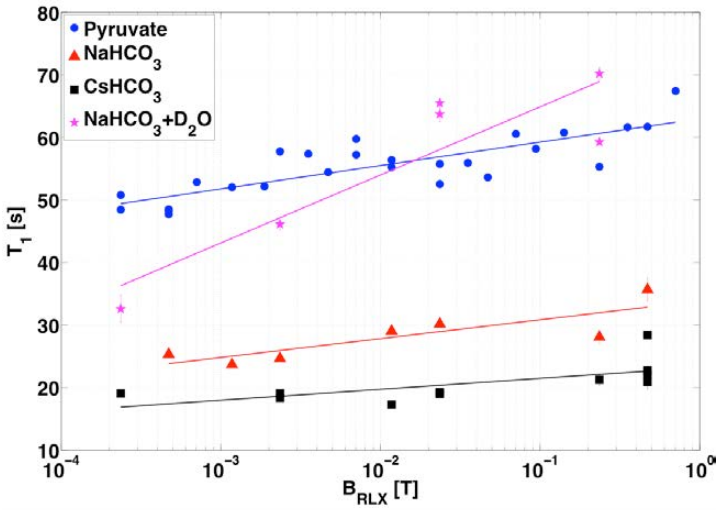

Figure 1. T_1 Measurements of Hyperpolarized ^{13}C Pyruvate and Bicarbonate Substrates

Conclusions: These preliminary results show that the T_1s of hyperpolarized ^{13}C-enriched cesium or sodium bicarbonate substrates are significantly lower than that of [1-^{13}C]pruvate making their use more challenging as NMR probes for *in vivo* studies. The use of deuterium oxide (D_2O) significantly increases T_1, although further studies are required to investigate the metabolic implications of injecting small quantities of D_2O into animal models. Our results suggest that the cesium bicarbonate formulation provides even shorter T_1 values than the sodium bicarbonate counterpart and therefore removing the cesium and radical from the hyperpolarized solution may be a requirement not only to reduce its toxicity but also to increase T_1 and make a more viable substrate for *in vivo* studies.

References: [1] Gallagher FA, *et al.*, Nature 2008;453(7197):940. [2] Gallagher FA, *et al.*, NMR Biomed 2011; **24**(8):1006. [3] Wilson DM, *et al.*, J Magn Reson 2010; 205(1):141. [4] Chattergoon N, *et al.*, Contrast Media Mol I 2013;8(1):57.

Data Collection For Multi-disciplinary Cancer Research

Chun Nim Li, Gord Mawdsley, Sharmila Balasingham,
Anne Martel, Sonal Gandhi, Kathleen I. Pritchard, Martin J. Yaffe
OICR Smarter Imaging Program
Sunnybrook Research Institute, Toronto, Ontario, Canada

Introduction. Data from clinical research projects are often stored in specific-formatted computer files, spreadsheets or in hardcopy form. In addition to being susceptible to loss, this can make quantitative analysis very difficult and often makes it impractical to bring data from one study into another. Data collected frequently include demographic information, imaging data, pathology reports, and information on treatment, response and outcome. Collecting such data reliably in a consistent format across the spectrum of cancer trials could provide important synergies and would greatly facilitate the ability to conduct currently uncontemplated future studies. It is also essential to maintain security and privacy standards compatible with the regulatory environment. To make it valuable for future researchers with different expectations, the database schema needs to be flexible and expandable. Our solution is to develop a centralized system that allows various groups to process their research data simultaneously. Customized user interfaces can be provided for study groups with different needs and goals. Through the back-end database, records from various studies for each patient can be connected and processed. It is also able to communicate with other hospital systems and can export anonymized data. At Sunnybrook Research Institute (SRI), we have been developing such a system called the Biomatrix. Here, we describe the system development process and demonstrate its value to participating research groups.

Methods. Following User-Centred Design Process, we work with individual research teams on the system development. After we study their research processes, objectives, metadata and needs, we enhance the existing database scheme and program functions to help them accomplish their goals. Open Source database PostgreSQL is used in the back-end. ASP.Net MVC is used to develop a web application to address the needs of the studies following the Agile Programming Approach. As each research study is incorporated into the Biomatrix, we either create new, or improve existing database structure and/or system functions. After the application becomes stable for one group, we repeat the development process with another in order to incorporate new study data into our existing system. Along the development, we also identify the common information participating research groups may want to share.

Results. To date, thirteen research studies have been incorporated into the Biomatrix with over 6600 patient records. A companion digital image database that can be linked to the data from radiology report allows correlation with quantitative data extracted from medical images. Linkage that provides automatic acquisition of data from pathology lab reports of consenting patients is currently underway. Projects supported by the Biomatrix span a wide range of questions and investigator disciplines. A data dictionary carefully defines variables which are then enforced in data entry to maximize compatibility across the Biomatrix. Some examples of projects currently underway include: 1) the use of breast MRI image data and diagnoses to develop computer-assisted detection algorithms for improving the specificity and efficiency of the imaging methods, 2) developing and testing methods for assessing tumour response to neoadjuvant therapy in locally-advanced breast cancer, 3) development of risk assessment tools, 4) validating biomarkers that predict the recurrence of breast cancer following an initial diagnosis of DCIS, 5) assessing factors associated with side effects in radiation therapy, 6) collecting data for a randomized trial of digital breast tomosynthesis versus digital mammography for breast cancer screening.

Conclusions. Developing a technical platform that allows multiple research groups to store and share study data individually or collectively, securely and dynamically can reduce duplicated effort of data entry - improving cost effectiveness, as well as facilitating collaboration opportunities among different researchers. Central collection and anonymization of data permits future studies which were not part of the original study plans.

In Vivo Sodium MRI of Human Prostate Cancer

Justin Charles Peterson[1], Adam Farag[2], Trevor Szekeres[2], Eli Gibson[2,3], Aaron Ward[2,3], Joseph Chin[4], Stephen Pautler[5], Glenn Bauman[4], Cesare Romagnoli[4], Robert Bartha[1,2], and Timothy J. Scholl[1,2]

[1]Medical Biophysics, Western University, London, Ontario, Canada, [2]Robarts Research Institute, Western University, London, Ontario, Canada, [3]Biomedical Engineering, Western University, London, Ontario, Canada, [4]London Health Sciences Centre, Ontario, Canada, [5]St. Joseph's Health Care, Ontario, Canada

INTRODUCTION: One in seven men will develop prostate cancer (PCa) in their lifetime and most of these men will die with prostate cancer, rather than of it. Since the introduction of the prostate specific antigen test, there has been a trend toward overtreatment of the disease. Placing patients in proper treatment streams according to tumour grade ('active surveillance' or 'immediate treatment') could save the Canadian healthcare system $100 million, annually [1]. Multi-parametric magnetic resonance imaging (MRI) is emerging as an improved method for imaging PCa. Unfortunately, current techniques alone are unable to differentiate lesion grade. The overall goal of this study is to determine whether tissue sodium concentration (TSC) is related to tumour grade in patients with PCa.

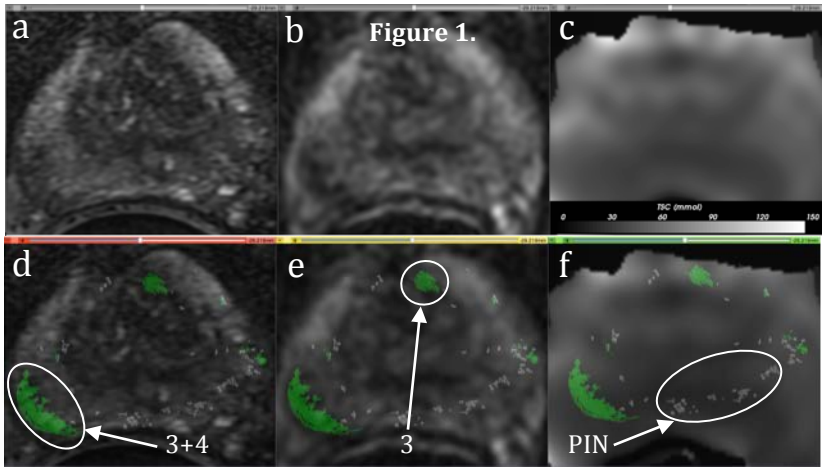

Figure 1.

METHODS: ***MRI***: ^{23}Na images were acquired using custom-built ^{23}Na-tuned endorectal receive-only surface and asymmetric transmit-only birdcage RF coils, operating in transmit-only/receive-only mode interfaced to a 3T GE scanner. Three vials (1mL volume) that span the entire length of the receive loop were incorporated into the endorectal coil as reference standards with varying NaCl concentrations.

Patients: Four male patients were recruited as part of a multi-modality, image-guided prostate cancer study. Each patient was imaged with both ^{23}Na MRI and multi-parametric ^{1}H MRI protocols.

Registration: The registration pipeline included *in-* and *ex-vivo* volumes, T_2- and T_1-weighted contrasts, and tumour grading from high-resolution histology. Accurate registration of the histopathology slices and the TSC data were made possible through a deformable extension for 3DSlicer (E. Gibson, 2014).

Figure 2.

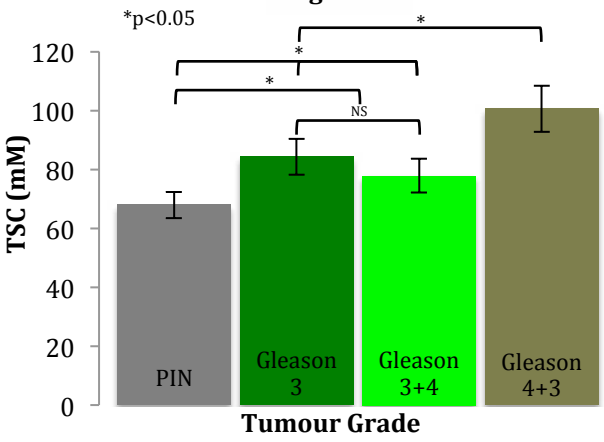

RESULTS: **Figure 1**, shows a high-resolution T_2-weighted ^{1}H Cube image (a), an axially acquired ^{1}H T_2-weighted image (b), and the distribution of endogenous sodium concentration (c) with corresponding histology contours overlaid (d-f) of an oblique slice through a prostate with biopsy-proven cancer. Green contours represent Gleason 3 and Gleason 3+4 lesions; grey contours represent prostatic intraepithelial neoplasia (PIN, a possible precursor to cancer). **Figure 2**, shows preliminary quantitative analysis of a single patient with biopsy-proven prostate cancer. The error bars represent one standard deviation.

DISCUSSION: TSC was measured using sodium MRI within the prostate including the peripheral and central zones. Preliminary data show a significant difference ($p<0.05$) in TSC between high and low grade tumours within the prostate, which is consistent with studies in brain and breast cancer [2,3]. Future analysis will determine the relationship between normal prostatic tissue and cancerous lesions.

CONCLUSION: These encouraging preliminary results motivate the potential utility of sodium MR in addition to other multi-parametric contrasts as a tool to aid with the grading of prostate cancer and ultimately the reduction of its overtreatment.

ACKNOWLEDGEMENTS: Ontario Institute for Cancer Research, Smarter Imaging Program

REFERENCES: [1] Dragomir, A., Cury, F. L., & Aprikian, A. G. *CMAJ Open* (2014). *2*(2), 60–68; [2] Ouwerkerk, *et al*., *Radiology*, (2003), *23*(10), 529–537; [3] Ouwerkerk *et al*., *Breast Cancer Res Treat*, (2007), *106*(2), 151–60.

Evaluation of CT Perfusion as an Imaging Biomarker of Tumour Hypoxia

Qi Qi[a], Timothy Pok Chi Yeung[a,d], Ting-Yim Lee[a-c], Glenn Bauman[a,b,d], Cathie Crukley[c], Laura Morrison[b], Slav Yartsev[a,b,d]

[a]Western University, [b]Lawson Health Research Institute, [c]Robarts Research Institute, [d]London Regional Cancer Program, London Health Sciences Centre, London, Ontario, Canada
Research Supervisor: Dr. Slav Yartsev

Purpose: Tumour hypoxia is associated with treatment resistance to cancer therapies. Hypoxia can be investigated by immunohistopathologic methods but such procedure is invasive. A non-invasive method to interrogate tumour hypoxia is an attractive option as such method can provide information before, during, and after treatment for personalized therapies. Our study aimed to evaluate the correlations between computed tomography perfusion (CTP) parameters and immunohistopathologic measurement of tumour hypoxia.
Methods: Wistar rats (N = 14) implanted with the C6 glioma tumour were imaged using CTP every 5 days (range: 1 – 7) to monitor tumour growth. A final CT perfusion scan and the brain were obtained on average 14 days (8 – 22 days) after tumour implantation. Tumour hypoxia was detected immunohistopathologically with pimonidazole. The tumour, necrotic, and pimonidazole-positive areas on histology samples were measured. Percent necrotic area and percent hypoxic areas were calculated. Tumour volume (TV), blood flow (BF), blood volume (BV), and permeability-surface area product (PS) were obtained from the CTP studies. Correlations between CTP parameters and histological parameters were assessed by Spearman's rho correlation. A Bonferroni-corrected P value $\leqslant 0.004$ was considered significant.
Results: TV and BV showed significant correlations with percent necrotic area, while BF and BV showed significant correlations with percent hypoxic area (Table 1 and Figure 1). PS was not correlated with either percent necrotic or percent hypoxic areas.
Conclusions: Percent hypoxic area provided a better overall correlation with BF and a significant correlation with BV, suggesting that CT perfusion is a potential non-invasive imaging biomarker of tumour hypoxia.

Table 1. Spearman's rho correlation between CTP parameters and histology

	Tumour volume (mm^3)	Blood flow (ml/min/100g)	Blood volume (ml/100g)	Permeability-surface area (ml/min/100g)
% Hypoxia area	0.54*	-0.81†	-0.77†	-0.10
% Necrosis area	0.79†	-0.71†	-0.65*	-0.10

† indicates a statistical significance ($P \leqslant 0.001$) and * indicates marginal significance ($0.01 \leqslant P \leqslant 0.05$)

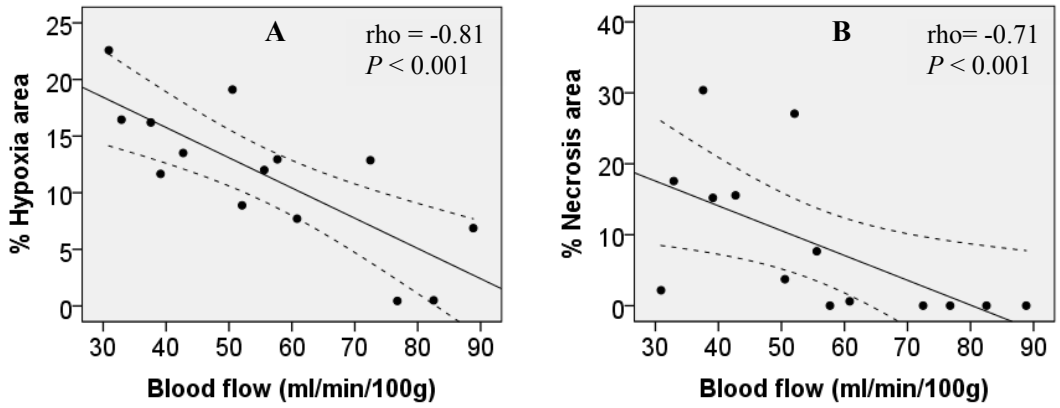

Figure 1: Percent hypoxic area vs. tumour blood flow (A) and percent necrotic area vs. tumour blood flow (B). Solid line shows the line of best fit and dotted lines denote the 95% confidence intervals.

3D Prostate MR-TRUS Non-linear Registration with Volume Preserving Prior

Wu Qiu*, Jing Yuan, Yue Sun, and Aaron Fenster
Robarts Research Institute, University of Western Ontario, London, Ontario, Canada.

Introduction: Magnetic Resonance Imaging (MRI) is considered to be a promising imaging modality for non-invasive identification of prostate cancers because of its high sensitivity and specificity for detecting early stage prostate cancer. However, it cannot replace transrectal ultrasound (TRUS) guided needle biopsy, which is the standard approach for definitive diagnosis of prostate cancer and for guiding biopsy needles to suspicious regions in the prostate, even though the lack of contrast of prostate tumors in TRUS results in an increasing number of repeat biopsies. The fusion of MR-TRUS prostate images is an effective way to enjoy the advantages of both modality images. However, the accurate registration of the 3D MR-TRUS images may suffer from large non-linear deformations due to different patient positioning, bladder filling, rectal wall motion, and the transducer probe pressure shifting. Thus, the challenging non-rigid image registration technique is of great interests for compensating these deformations in clinical use.

Methods: In this work, we study the deformable registration of the input 3D prostate MR image, with the pre-segmented prostate region as prior knowledge, to its corresponding TRUS image, by imposing the global volume invariance of the pre-segmented prostate region. The introduced region-based volume preserving constraint describes a global geometrical prior knowledge about registering the prostate regions within the two input image modalities. Specifically, we developed a sequential convex optimization method to optimize the proposed nonlinear multi-channel modality independent neighborhood descriptor (MIND) based image fidelity function, across the two modality images, which is subject to the linear equality constraint resulted from the preserving volume prior.

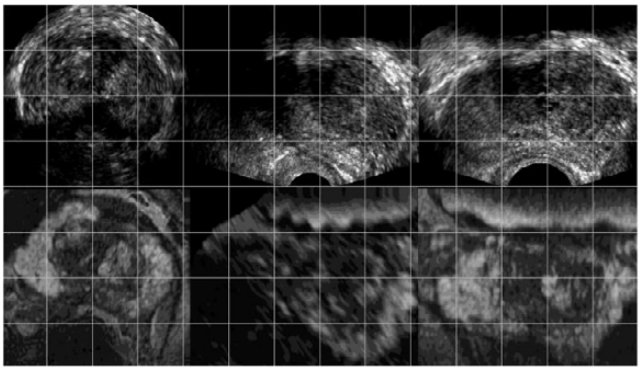

Fig. 1. Examples of one registered MR (bottom row) and 3D TRUS (top row) images. Left - right columns: axial, sagittal, and coronal views.

Ten subjects suspected to have tumors identified by multi-spectral MR imaging were involved in this study. The T2-weighted MR images were obtained at an image size of 512 × 512 × 36 voxels with a voxel size of 0.27 × 0.27 × 2.2 mm^3. The 3D TRUS images were acquired at an image size of 448×448×350 voxels with a voxel size of 0.19×0.19×0.19 mm^3. The registration accuracy was evaluated by calculating the target registration error (TRE) using manually identified corresponding intrinsic fiducials in the whole prostate gland, and also comparing the MR and TRUS manually segmented prostate surfaces in the registered images, using Dice similarity coefficient (DSC), the mean absolute surface distance (MAD) and maximum absolute surface distance (MAXD).

Table 1. Registration results of 10 patient images in terms of TRE, DSC, MAD, and MAXD, using the proposed algorithm with (NR_{VP}) and without (NR) region-based volume preserving prior.

	TRE (mm)	DSC (%)	MAD (mm)	MAXD (mm)
Before registration	3.8 ± 1.5	81.5 ± 4.5	2.0 ± 0.8	7.6 ± 4.5
NR	2.2 ± 0.7	83.5 ± 3.8	1.6 ± 0.8	7.0 ± 4.0
NR_{VP}	$\mathbf{1.7 \pm 0.7}$	$\mathbf{87.3 \pm 3.4}$	$\mathbf{1.3 \pm 0.6}$	$\mathbf{6.4 \pm 3.3}$

Results: Figure 1 shows one algorithm registered prostate. Table 1 shows the mean quantitative registration results for 10 patient images. More specifically, the proposed non-rigid registration algorithm with the volume-preserving prior improved the accuracy by 3.8% in terms of DSC compared to the registration algorithm without using the volume-preserving prior, by 5.8% compared to before registrations. The mean registration time of the proposed non-rigid registration approach was 8 ± 2.5 minutes excluding the rigid registration time.

Conclusions: A new convex optimization-based MR-TRUS deformable registration approach is proposed in this paper, which incorporates a novel volume preserving prior into a sequential convex optimization non-linear registration framework using the MIND descriptor. The experiments show that the proposed registration algorithm capture the nonlinear deformation between 3D MR and TRUS image pairs accurately and efficiently, in terms of metrics of TRE, DSC, MAD, and MAXD. Its performance also suggests that it may be suitable for the clinical use involving the image guided prostate biopsy procedures.

Inter-operator variability of 3D prostate magnetic resonance image segmentation using manual and semi-automatic approaches

Maysam Shahedi*, Derek W. Cool, Cesare Romagnoli, Glenn Bauman, Matthew Bastian-Jordan, Eli Gibson, George Rodrigues, Belal Ahmad, Michael Lock, Aaron Fenster†, and Aaron D. Ward†
(*Primary author, †Co-supervisors)

OICR Smarter Imaging Program
London Regional Cancer Program; Graduate Program in Biomedical Engineering, Robarts Research Institute, Department of Medical Imaging, Department of Oncology, Department of Medical Biophysics, The University of Western Ontario, London, Ontario, Canada

Introduction: Three dimensional (3D) prostate image segmentation is useful for cancer diagnosis and therapy guidance. However, it is time-consuming to perform manually and subject to inter-operator variability [1]. The levels of difficulty and inter-operator variability vary across the prostatic base, mid-gland and apex. Our goal is to measure accuracy and inter-operator variability of a semi-automatic prostate segmentation method for T2-weighted endorectal magnetic resonance (MR) imaging.

Methods: MR images from 42 prostate cancer patients were acquired. Manual border delineation was performed by one observer on all the images and by two other observers on a subset of 10 images. Simultaneous truth and performance level estimation (STAPLE) [2] segmentation was calculated from all three segmentations. Our algorithm calculated inter-subject prostate shape and local boundary appearance similarity during its training phase. To initiate the segmentation, the operator indicated the anteroposterior prostate orientation and selected the prostate centre on the most-superior, mid-gland, and the most-inferior slices. These inputs were used to identify candidate prostate boundary points using learned appearance characteristics, which were regularized according to learned prostate shape information to produce the final segmentation. On all subjects, we evaluated our method against the manual reference segmentations using complementary boundary-, region- and volume-based metrics: mean absolute distance (MAD), Dice similarity coefficient (DSC), recall rate, precision rate, and volume difference (ΔV). On 10 cases, we measured the inter-operator variability of manual segmentation by comparing the reference segmentations to the STAPLE segmentation, and conducted a multi-operator study to measure inter-operator variability of the semi-automatic algorithm.

Results: Table 1 shows our results on our 42 subjects with a single operator. Table 2 compares the consistency of manual and semi-automatic segmentations on 10 cases. The variability of all of the metrics resulting from the semi-automatic segmentation was reduced, compared to the manual segmentation.

Conclusions: We observed substantial inter-operator variability in manual segmentation and reduced variability in semi-automatic segmentation. In studies evaluating prostate segmentation algorithm accuracy using a single-operator reference standard, it is important to consider the measured errors in the context of inter-operator manual segmentation variability.

Table 1: Accuracy and variability for semiautomatic segmentation: mean ± standard deviation of MAD, DSC, recall, precision, and ΔV for different regions of interest (ROI).

ROI	MAD (mm)	DSC (%)	Recall (%)	Precision	ΔV (cm^3)
Whole gland	2.0±0.5	82±4	77±9	88±6	-4.6±7.2
Mid-gland (1/3)	1.6±0.5	90±3	90±7	91±6	-0.1±2.0
Apex (1/3)	2.0±0.7	79±6	82±14	80±13	0.1±3.3
Base (1/3)	2.6±0.8	73±10	61±14	93±6	-4.5±3.7

Table 2: Consistency of manual and semi-automatic segmentation: average of means (average of standard deviations) of the metrics across three manual and three semi-automatic segmentations by three expert operators. (N: number of images, reference: STAPLE segmentation).

Method	N	ROI	MAD	DSC (%)	Recall (%)	Precision	ΔV (cm^3)
Manual segmentation	10	Whole gland	1.3 (1.6)	90 (11)	88 (19)	94 (6)	3.9 (10.1)
		Mid-gland	0.8 (0.9)	95 (5)	93 (10)	97 (2)	0.8 (2.1)
		Apex	1.4 (1.8)	86 (15)	85 (24)	93 (8)	1.4 (3.3)
		Base	1.6 (1.9)	86 (14)	86 (22)	91 (11)	1.6 (4.8)
Semi-automatic segmentation	10	Whole gland	1.9 (0.3)	80 (4)	75 (7)	88 (3)	-3.2 (2.9)
		Mid-gland	1.5 (0.3)	90 (2)	90 (3)	91 (2)	0.2 (0.7)
		Apex	1.8 (0.4)	82 (4)	87 (8)	80 (8)	0.8 (1.2)
		Base	2.7 (0.5)	68 (7)	57 (12)	93 (6)	-4.2 (2.5)

References:

[1] Smith, W.L., *et al.*, Int J Radiat Oncol Biol Phys, 2007. **67**(4): p. 1238-47.
[2] Warfield, S.K., *et al.*, IEEE Trans Med Imaging, 2004. **23**(7): p. 903-21.

The Effect of the Chemotherapy Agent Methotrexate on the Developing Brain

Leigh Spencer Noakes[1], Ellen van der Plas[3], Shoshana Spring[1], Russell Schachar[3], Brian J. Nieman[1,2]
[1]Mouse Imaging Centre, Hospital for Sick Children, Toronto, ON, Canada; [2]Medical Biophysics, University of Toronto; [3]Psychiatry, University of Toronto

Introduction. Acute lymphocytic leukemia (ALL) is the most common childhood cancer and is commonly treated with a cocktail of chemotherapy agents. This treatment has improved survival to 90%. However, up to 50 % of those that recover are left with side effects, including "late effects" which can impair cognitive ability. These "late effects" are accompanied by changes in brain structure volume.[1] In this study, we aimed to determine if treatment with MTX at an infant stage of development in mice has consequences for brain development, measured by volume of MRI images later in life.

Methods. C57Bl/6 mice were treated with 20 mg/kg of MTX (n=13) or saline (CTL, n=9) intraperitoneally on postnatal day (P) 17. At P42, mice were perfusion fixed with gadolinium contrast agent (Prohance) included in the perfusate. Ex vivo images were collected with a T_2-weighted fast spin-echo sequence with k-space dimensions 360x360x450, an echo train length of 6, echo spacing of 11.8 ms, with three averages, a resolution of 56 μm and total time of 14 hours and 24 minutes. Images were registered together nonlinearly through a series of iterative steps to produce an unbiased average.[2] Volumetric changes were computed by registering a structural atlas with 159 structures to the unbiased average image. The volume of each structure was fit with a linear model, including an intercept and a categorical treatment group (MTX or CTL). The model also included a normalizing volume term accounting for the pre-treatment brain volume, obtained from in vivo MRI data.

Results. Of the 159 structures we tested, 25 (or 16%) showed significant volumetric differences ($p<0.05$, uncorrected). In Figure 1, the structures that achieved significance are colored based on their relative volume change. The majority (21/25) of the differences we observed represented volume decreases in the MTX-treated group relative to the control group, with magnitude on the order of 7%. Interestingly, several cortical regions are among those changed, even though emphasis in the clinical literature has been on changes in the white matter.

Conclusion. MRI of the mouse brain detects changes in development induced by early treatment with MTX. Most of these changes represent impaired growth, and gray matter regions may be particularly affected. Further adaptation of the treatment regimen to match that of the clinic, experiments in genetically-engineered mice and testing of additional chemotherapy agents will allow a complete mouse model of chemotherapy effects on the brain to be developed. In the long-term, this will allow adaptation of treatments to minimize cognitive late effects that affect survivors' quality of life.

References. (1) Zeller, B. *et al. J. Clin. Oncol.*, **2013**, *31*, 2078-2086. (2) Lerch, J. P. *et al. Methods Mol. Biol.*, **2011**, *711*, 349-361.

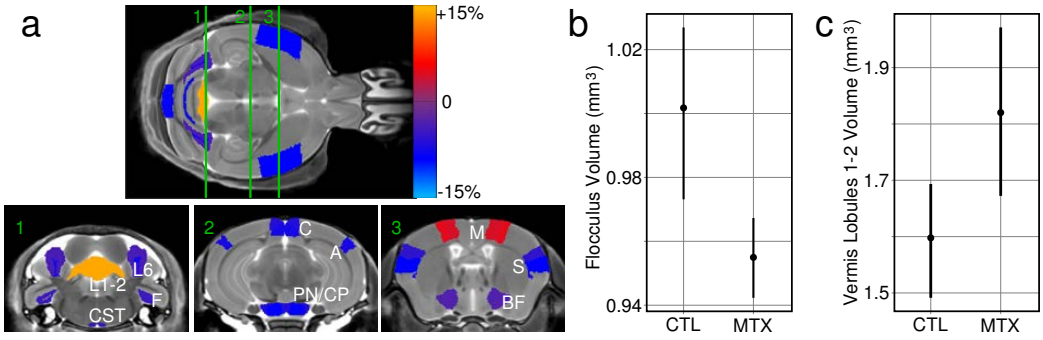

Figure 1: Structural volume differences in MTX-treated vs CTL mice. (a) Map of significant structure differences ($p<0.05$, uncorrected) with the color scale indicating percent volume change. Labeled structures include the basal forebrain (BF), somatosensory cortex (S), motor cortex (M), auditory cortex (A), cingulate cortex (C), pontine nucleus and cerebral peduncle (PN/CP), cerebellar lobule 6 (L6), lobules 1-2 (L1-2), corticospinal tract (CST) and flocculus (F). The flocculus and lobules 1-2 of the cerebellar vermis are plotted separately in (b) and (c) respectively with error bars showing 95% confidence intervals.

Evaluation of deformable image registration accuracy using virtual phantoms

Jason Vickress[1], Rob Barnett[1,2,3], Jerry Battista[1,2,3], Slav Yartsev[1,2,3]
Departments of [1]Medical Biophysics and [2]Oncology, Western University, London, Ontario
[3]London Regional Cancer Program, London Health Sciences Centre, London, Ontario
OICR Smarter Imaging Program

Introduction: Deformable image registration is currently being introduced into image-guided radiation therapy to model the anatomical deformation and indicate when plan adaptation is required [1]. This tool has worked well in image registration applications but has not been tested for dose registration and accumulation. The efficacy of deformable image registration has been the subject of much scrutiny, particularly in the application of industry-protected "black box" algorithms. In this study, the suitability of deformable image registration for accurate dose accumulation over fractionated radiation therapy is tested using a simple cubic virtual phantom with different levels of inhomogeneity.

Methods: The virtual phantom consists of a 30 mm cube with a fixed CT number (50 HU) centered in a 250 mm water cube (0 HU).Voxel size was 1×1×3 mm^3. For all dose distribution comparisons, the same single 7×7 cm^2 6 MV radiation field was used. Gradual deformations were introduced by only moving the inner cube in the anterior direction, parallel to the central axis depth dose gradient by 2, 4, 6, 8, and 10 mm. 3D slicer software (demons algorithm) and MIM Software Inc. deformable registration algorithms were tested. Less than 30 seconds were required for deformable image registration for both algorithms. The inner cube was modified by adding feature patterns of greater contrast using Gaussian HU distributions with increasing standard deviations (SD). Gaussian noise was also included in the image through the addition of random pixel values. The registration accuracy was evaluated by comparing (i) the absolute mean error in displacement of each voxel and (ii) the overall mean dose change.

Results: The resulting image from each deformation vector field appeared correct from visual inspection. However, the internal deformation vectors were mapped incorrectly as illustrated in Fig. 1 (b) for a homogenous case (SD = 0). For inner cube displacement of 2 to 10 mm, the error in voxel displacement and percent mean dose increased from 0.24 to 1.8 mm and from 11% to 18%, respectively, for 3D slicer, and from 0.09 to 0.24 mm and from 3% to 2%, respectively, for MIM software. Significant improvement was observed in Fig. 1 (c) with the introduction of contrast features into the homogenous cube. Figure 2 illustrates the improvement in deformation accuracy with increased contrast for two deformable registration algorithms. Image noise had no substantial effect on the "per voxel" deformation accuracy, even as the signal to noise ratio approached one.

Conclusions: Our simulation demonstrated the limitations of deformable registration algorithms and the variation of results produced by different providers for a simple test object. More realistic phantoms for radiation therapy applications, both virtual and physical, will be required for evaluation of propriety "black box" software before any full scale clinical implementation should be attempted.

References: [1] Lim K et al. Int J Radiat Oncol Biol Phys 2014;90:47-154

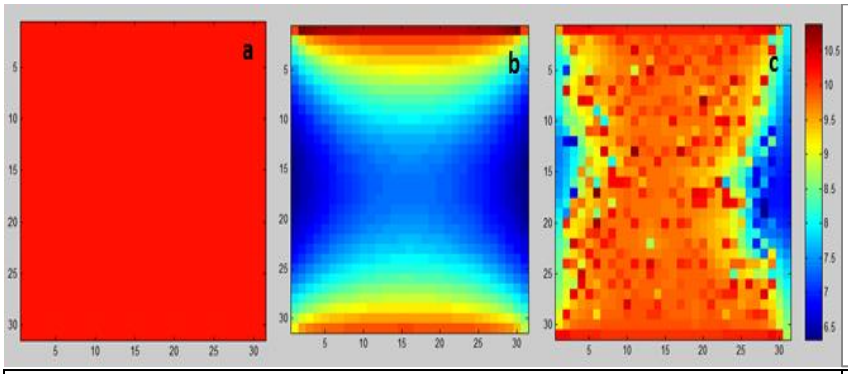

Figure 1: Voxel displacements (mm) in the A/P direction of the inner cube for (a) true displacement by shift of 10 mm; (b) as calculated using 3D slicer for homogeneous 50 HU case and (c) with added inhomogeneous feature (SD = 0.5)

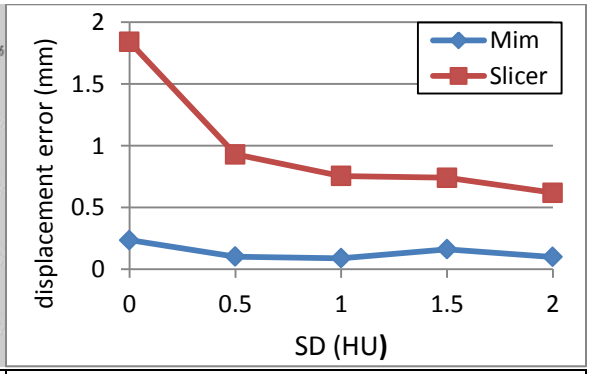

Figure 2: Mean absolute error (mm) of displacement vector lengths for different levels of contrast features

Adaptive Denoising in Breast Tomosynthesis Filtered Back Projection Reconstruction

Xinying Wang [a], James G. Mainprize [a] and Martin G.Yaffe [a, b]

[a]Sunnybrook Research Institute, 2075 Bayview Ave., Toronto, Ontario, Canada, M4N 3M5;
[b]Dept. of Medical Biophysics, University of Toronto, 2075 Bayview Ave., Toronto, Ontario, Canada, M4N 3M5

Introduction. Early detection of breast cancer has been shown to save lives. Currently, breast cancer screening is largely performed using digital mammography. Unfortunately, mammography is an imperfect test. Because mammography is a 2D projection image, surrounding health tissue can often obscure lesions or mimic a lesion that is not present. Digital breast tomosynthesis (DBT) is a novel advance that attempts to address the limitations of mammography, by producing quasi-3D images that give cross-sectional slices at multiple depths in the breast. Because of limitations imposed on the radiation dose, however, the images often appear noisy which can be distracting to the radiologist and may obscure the presence of micro-calcifications. DBT slices are created by a reconstruction step. One method for reconstruction is by the use of filtered back projection (FBP). Because of the strong enhancement by the reconstruction filters, noise at high spatial frequencies can be greatly increased. Apodization filters are used to reduce this enhancement, but overly aggressive filtering can degrade the appearance of fine details..

Methods. An optimal filter is needed to suppress the noise with minimal loss of detail. An adaptive Wiener filter is presented in this paper. The Wiener filter requires a good estimate of the noise which will be image dependent. The noise in the projection images is estimated using a neighbourhood wavelet coefficient window technique[1] modified to include an adaptive threshold for estimating the noise floor in the wavelets by 'wavelet shrinkage'[2]. From the noise-estimate, the resulting Wiener filter is applied to each of the projection images. Image quality of a FBP reconstruction with and without Wiener filtering is investigated using a non-prewhitening observer SNR (d') that assesses the detectability of objects.

Results. We evaluated the performance in simple simulations with homogeneous (Fig 1a-a″) and textured backgrounds mimicking breast tissue structure (Fig 1b-b″) containing low-contrast masses. Further examples on clinical images containing small microcalcifications will also be presented. The detectability improved in all cases. Examples of the increase in SNR(d') are shown in Fig. 1c

Conclusion. Wiener filter improved image quality and increase detectability in the reconstructed slices. And the fuzzy logic Wiener filter based on wavelet method is more efficient for small lesions, and weak signal.

References. [1] GY Chen, TD Bui, A Krzyzak, "Image denoising using neighbouring wavelet coefficients," *IEEE International Conference on Acoustics, Speech, and Signal Processing*, pp. ii-917-20, 2004.

[2] S Schulte, B Huysmans, A Pižurica, EE Kerre, W. Philips "A New Fuzzy-Based Wavelet Shrinkage Image Denoising Technique," *ACIVS 2006, LNCS 4179*, pp. 12-23, 2006.

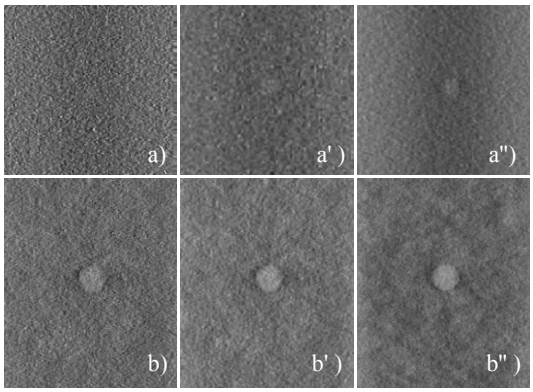

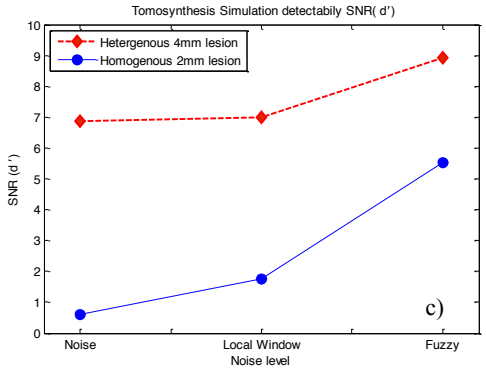

Fig.1 (The central slices of DBT reconstructions of simulated 2mm spherical lesions in a uniform background and bottom row are 4mm textured background. a) and b) correspond to standard FBP reconstruction filters, a') and b') using Wiener filters estimated with the standard (local-window) neighbourhood wavelet technique, and a") and b") use the improved Wiener filter approach with adaptive (fuzzy) threshold wavelet shrinkage. Total exam air kerma is 0.29 mGy Contrast settings are identical for each image. c) The detectability SNR(d') in original reconstruction and with the two denoising approaches for the images in (a)-(b).

Adaptive Denoising in Breast Tomosynthesis Filtered Back Projection Reconstruction

Xinying Wang [a], James G. Mainprize [a] and Martin G.Yaffe [a, b]

[a]Sunnybrook Research Institute, 2075 Bayview Ave., Toronto, Ontario, Canada, M4N 3M5;
[b]Dept. of Medical Biophysics, University of Toronto, 2075 Bayview Ave., Toronto, Ontario, Canada, M4N 3M5

Introduction. Early detection of breast cancer has been shown to save lives. Currently, breast cancer screening is largely performed using digital mammography. Unfortunately, mammography is an imperfect test. Because mammography is a 2D projection image, surrounding health tissue can often obscure lesions or mimic a lesion that is not present. Digital breast tomosynthesis (DBT) is a novel advance that attempts to address the limitations of mammography, by producing quasi-3D images that give cross-sectional slices at multiple depths in the breast. Because of limitations imposed on the radiation dose, however, the images often appear noisy which can be distracting to the radiologist and may obscure the presence of micro-calcifications. DBT slices are created by a reconstruction step. One method for reconstruction is by the use of filtered back projection (FBP). Because of the strong enhancement by the reconstruction filters, noise at high spatial frequencies can be greatly increased. Apodization filters are used to reduce this enhancement, but overly aggressive filtering can degrade the appearance of fine details..

Methods. An optimal filter is needed to suppress the noise with minimal loss of detail. An adaptive Wiener filter is presented in this paper. The Wiener filter requires a good estimate of the noise which will be image dependent. The noise in the projection images is estimated using a neighbourhood wavelet coefficient window technique[1] modified to include an adaptive threshold for estimating the noise floor in the wavelets by 'wavelet shrinkage'[2]. From the noise-estimate, the resulting Wiener filter is applied to each of the projection images. Image quality of a FBP reconstruction with and without Wiener filtering is investigated using a non-prewhitening observer SNR (d') that assesses the detectability of objects.

Results. We evaluated the performance in simple simulations with homogeneous (Fig 1a-a″) and textured backgrounds mimicking breast tissue structure (Fig 1b-b″) containing low-contrast masses. Further examples on clinical images containing small microcalcifications will also be presented. The detectability improved in all cases. Examples of the increase in SNR(d') are shown in Fig. 1c

Conclusion. Wiener filter improved image quality and increase detectability in the reconstructed slices. And the fuzzy logic Wiener filter based on wavelet method is more efficient for small lesions, and weak signal.

References. [1] GY Chen, TD Bui, A Krzyzak, "Image denoising using neighbouring wavelet coefficients," *IEEE International Conference on Acoustics, Speech, and Signal Processing*, pp. ii-917-20, 2004.

[2] S Schulte, B Huysmans, A Pižurica, EE Kerre, W. Philips "A New Fuzzy-Based Wavelet Shrinkage Image Denoising Technique," *ACIVS 2006, LNCS 4179*, pp. 12-23, 2006.

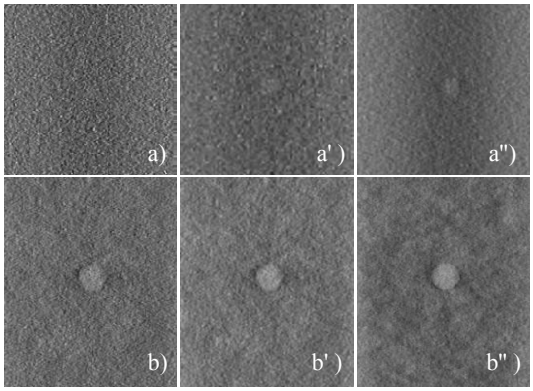

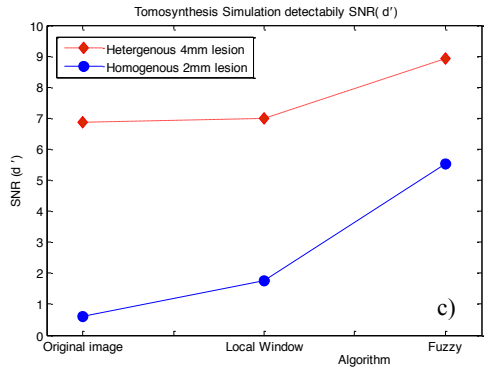

Fig.1 (The central slices of DBT reconstructions of simulated 2mm spherical lesions in a uniform background and bottom row are 4mm textured background. a) and b) correspond to standard FBP reconstruction filters, a') and b') using Wiener filters estimated with the standard (local-window) neighbourhood wavelet technique, and a") and b") use the improved Wiener filter approach with adaptive (fuzzy) threshold wavelet shrinkage. Total exam air kerma is 0.29 mGy Contrast settings are identical for each image. c) The detectability SNR(d') in original reconstruction and with the two denoising approaches for the images in (a)-(b).

Ontario Preclinical Imaging Consortium

OPIC

Oral Presentation and Poster Abstracts

Comparison of small (~800 Da) and large (65,000 Da) contrast agent CT perfusion to quantify blood-tumor-barrier permeability following focused ultrasound and microbubble treatment in a C6 rat glioma model

[1,2,4]**H. Ahmed**, [3]R. Chopra, [3]K. Hynynen, [1,2,4]TY Lee
[1]Department of Medical Biophysics, The University of Western Ontario, [2]Imaging Research Laboratories, Robarts Research Institute, [3]Sunnybrook Health Research Institute, [4]Lawson Health Research Institute.

Introduction: The purpose of this study is to quantitatively evaluate BTB permeability using a standard Isovue contrast agent and a much larger agent, Exia (~65,000 Da).

Material: A stereotactic frame was used to surgically implant 1 x 10^6 C6 glioma cells in the right cerebral hemisphere of six rats. At 10-15 days post treatment, when the tumor diameter was greater than 5mm, the tumor was trans-cranially sonicated with a 10ms burst length and a 1 Hz repetition frequency for 120s, at an acoustic power of 0.5W using a 0.563-MHz FUS system. Definity microbubbles at a dose of 2 µl/kg were administered simultaneously with each sonication. Baseline, 1, 24, and 72-h post CT perfusion scans were performed with Isovue (~800 Da), and eXia (~65,000 Da) contrast agents, and blood flow (BF), blood volume (BV), and PS permeability surface area) maps were computed.

Results: When measured with a standard Isovue contrast agent (~800 Da), instead of a transient increase in BBB permeability that is seen in the normal brain, FUS and MB demonstrated a gradual decrease in BTB permeability in the hours following treatment ($p < 0.05$). An acute vascular shutdown, drop in CBF and CBV ($p < 0.05$), was also observed immediately following treatment, as previously reported in other tumor models. The drop in PS persisted at 24 h post ($p < 0.05$), returning at 72 h post, whereas the CBF and CBV returned back to baseline levels by 24 h post. A trend of increasing eXia permeability at 24 h post suggests that the decrease in BTB PS alleviates the elevated IFP that results from vasogenic edema and improves the penetration of larger drugs or molecules that are unable to diffuse across the BTB. When plotted against the MTT, which is the inverse of perfusion pressure, BTB PS (isovue) shows a moderate positive correlation ($r^2 = 0.71$), whereas BTB PS (eXia) shows a weak negative correlation ($r^2 = - 0.50$).

Conclusions: Our findings indicate that although FUS and MB treatment at our parameters may not necessarily be useful for increasing the delivery of small molecule drugs, it may be more useful for increasing the delivery of larger molecules where the IFP is a barrier.

Development of fast 3D photoacoustic imaging

Jeffrey J.L. Carson
Imaging Program, Lawson Health Research Institute, London, Ontario N6A 4V2
Department of Medical Biophysics, the University of Western Ontario, London, Ontario

Photoacoustic imaging is a powerful technique that can be used to obtain images of thick tissues and small animals that have both spectrally dependent optical contrast and high resolution (< 100 μm in some scanner designs). Optical contrast can reveal haemoglobin concentration and oxygen saturation of tissues, which are important indicators of tissue health and useful for detection of disease (e.g. ischemia and cancer). In photoacoustic imaging, ultrasound is generated by objects (e.g. blood vessels) that preferentially absorb energy delivered by a short laser pulse (~ 10 nanoseconds). Detection of the ultrasonic pressure waveform from many viewing perspectives (i.e. projections) followed by reconstruction of the projection data results in a 3D image. This process is inherently slow since each projection must be acquired by translation of a single ultrasound transducer (or transducer array) through many positions or sequential (or multiplexed) digitization of a high-density 2D transducer array. In either case, a minimum of one laser pulse is required for each projection. To overcome this speed limitation, my research group with ORF-OPIC funding has been developing a method to capture 3D photoacoustic images using a limited number of sparsely arranged transducers [1]. The sparse array detection scheme relies on a one-time calibration of the transducer array using a robotically scanned photoacoustic point source that provides an estimate of the imaging operator [2]. This prior knowledge of the transducer array response is then used to interpret the ultrasound projection data by an iterative or psuedoinverse image reconstruction algorithm [3,4]. The reconstructed 3D photoacoustic images are then displayed. These advancements have enabled the acquisition of a complete 3D photoacoustic image of optically absorbing objects using only a single laser pulse [1,4]. Building upon this capability, we have been able to capture a sequence of 3D frames at 10 frames per second with up to two distinct colors, demonstrating the feasibility of 4D and 5D photoacoustic imaging [5]. Recently, we modified our photoacoustic imaging system with fast mechanical scanning capabilities, which has increased the field of view of our sparse array and enabled 3D photoacoustic imaging of very large specimens (up to 8 cm in diameter) in less than 5 minutes.

References:

1. Ephrat, P., Keenliside, L., Seabrook, A., Prato, F.S., & J.J.L. Carson. Three-dimensional photoacoustic imaging by sparse-array detection and iterative image reconstruction. J Biomed Opt 13(5): 054052 (2008)
2. Roumeliotis, M., Ephrat, P., Patrick, J., & J.J.L. Carson. Development and characterization of an omni-directional photoacoustic point source for calibration of a staring 3D photoacoustic imaging system. Opt Express 17(17): 15228-15238 (2009)
3. Roumeliotis, M., Stodilka, R.Z., Anastasio, M.A., Chaudhary, G., Al-Aabed, H., Ng, E., Immucci, A.N., & J.J.L. Carson. Analysis of a photoacoustic imaging system by the crosstalk matrix and singular value decomposition. Opt Express 18(11): 11406-11417 (2010)
4. Roumeliotis, M., Stodilka, R.Z., Anastasio, M.A., Ng, E., & J.J.L. Carson. Singular value decomposition analysis of a photoacoustic imaging system and 3D imaging at 0.7 FPS. Opt Express 19(14): 13405-13417 (2011)
5. Kosik, I., & J.J.L. Carson. Real-time multispectral 3-D photoacoustic imaging of blood phantoms. Proc. SPIE 8581: 85811V-1-85811V-8 (2013)

Hyperpolarized 13C Imaging: from Rats to Humans

Charles Cunningham

Sunnybrook

Research Institute

Abstract:

Rapid imaging of biochemical reactions within tissue using MRI has recently become possible through the use of the Dynamic Nuclear Polarization (DNP) and dissolution method. DNP-dissolution, pioneered in Malmo, Sweden [1], results in an intravenous contrast agent that is ``hyperpolarized'', producing a magnetic signal that is enhanced by up to 100,000 fold. This enhanced signal enables the time-resolved imaging of the reaction between substrates such as 13C-labeled pyruvate and enzymes within cells.

Over the course of a project funded by OPIC, a pre-clinical 13C imaging system based on MDA-MB-231 xenografts in nude rats was developed, and was used to advance 13C imaging technology towards application in the first patient studies. In this presentation I will outline some of the advances achieved using this model and describe the integration of these methods in upcoming patient studies.

[1] Ardenkjær-Larsen, Jan H., et al. "Increase in signal-to-noise ratio of> 10,000 times in liquid-state NMR." Proceedings of the National Academy of Sciences 100.18 (2003): 10158-10163.

Optimizing optical transmission of nano-hole arrays for multispectral imaging

Kieffer Davieau[a,b,c], Mohamadreza Najiminaini[a,c], Mahi Singh[b], and Jeffrey J.L. Carson[a,c]
[a] Imaging Program, Lawson Health Research Institute, St. Joseph's Health Care, London, ON, Canada
[b] Department of Physics and Astronomy, University of Western Ontario, London, ON, Canada
[c] Department of Medical Biophysics, Schulich School of Medicine and Dentistry, University of Western Ontario, London, ON, Canada
(Corresponding author: Jeffrey J.L. Carson, jcarson@lawsonimaging.ca)
Ontario Pre-Clinical Imaging Consortium

Introduction. A nano-hole array (NHA) consists of a periodic array of nano-holes perforated in an optically thick metallic film. The optical transmission characteristics of NHAs can be tuned by changing the nano-hole diameter as well as the periodicity between the nano-holes. Our group has investigated the use of NHAs to construct a pixelated colour filter array (CFA) for multispectral imaging applications [1]. Colour filter arrays have long been used in digital cameras to separate the red, green and blue colour channels. We have recently demonstrated snapshot and near video rate multispectral imaging with the use of 4-colour CFA fabricated from pixelated NHAs [2]. The main objective of this work was to investigate through numerical simulations the effect of periodicity and nano-hole size on the transmission characteristics of NHAs, which will enable us to improve NHA-based CFAs for multispectral imaging applications.
Method. In order to simulate the effects of various nano-hole diameters and periodicities of a NHA on the optical transmission spectrum, we used a finite-difference time-domain (FDTD) method to numerically solve Maxwell's equations (FDTD Solutions, Lumerical Inc., Vancouver, Canada). Using FDTD Solutions, a script was written to loop through a series of periodicities with constant nano-hole diameter as well as through a series of nano-hole diameters for a constant periodicity.
Results. The results from the simulations are shown in Figure 1, which illustrate the relation between nano-hole diameter, periodicity and optical transmission of each NHA. In Figure 1 (a) it can be seen that an increase in the periodicity of 10 nm resulted in a red-shift in the optical transmission spectrum of approximately 10 nm. In Figure 1(b) it can be seen that an increase in the nano-hole diameter resulted in an increase in the optical transmission as well a red-shift in the spectrum. The increase in optical transmission was non-linearly dependent on nano-hole diameter. The large peaks in each spectrum were related to the (-1,0) resonance related to the SPP modes.

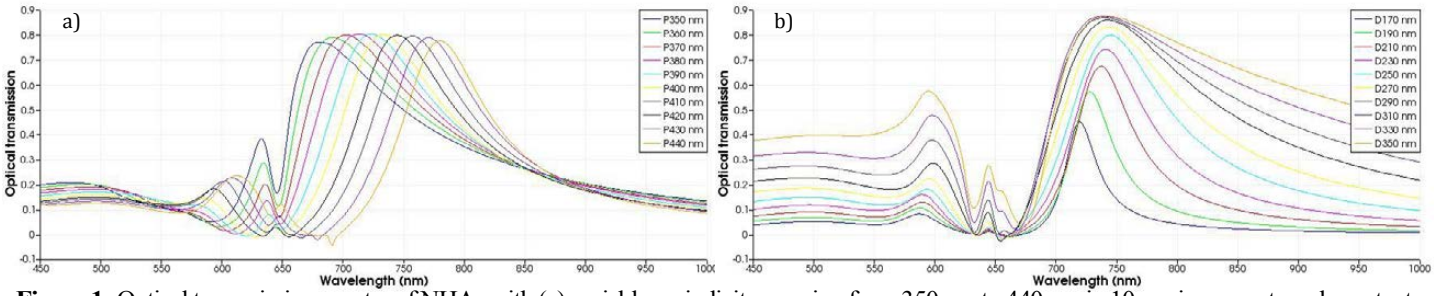

Figure 1: Optical transmission spectra of NHAs with (a) variable periodicity, ranging from 350 nm to 440 nm in 10 nm increments and constant nano-hole diameter of 250 nm, and (b) variable hole diameter, ranging from 150 nm to 330 nm in 20 nm increments and constant periodicity of 400 nm.

Discussion. An optical filter that utilizes the optical transmission peak due to the (-1,0) SPP resonance can be fabricated by choosing a specific combination of periodicity and nano-hole size. Transmission efficiency can be improved by increasing the nano-hole diameter and the resonance wavelength can be tuned by selecting the periodicity. For example, for an optical filter in the near infrared region with a centre wavelength of 730 nm, a NHA array with a periodicity of 400 nm would be optimal. The bandwidth of the filter could be tuned at the expense of transmission efficiency by selecting an appropriate nano-hole diameter. For high transmission efficiency, but poor spectral selectivity a large nano-hole diameter could be selected. While a smaller nano-hole diameter could result in a much more discriminating optical filter.
Conclusion. By utilizing a strategy of selecting the periodicity and nano-hole diameter for each NHA in a pixelated CFA, we will be able to tailor the pixelated CFA to specific color bands. Furthermore, the selectivity of each color band can be tuned. This for example could have implications for biomedical multispectral imaging applications, where the spectral characteristics of a series of simultaneously injected contrast agents differ not only in wavelength, but also bandwidth.
References. [1] Najiminaini et al. Nano-hole-array-based device for 2D snapshot multispectral imaging. Scientific Reports 3(2589): 1-7 (2013). **[2]** Najiminaini et al. Bolus tracking with nanofilter-based multispectral videography for capturing microvasculature hemodynamics. Scientific Reports 4(4737): 1-9 (2014).

Optimized 3-point IDEAL for MRI of Hyperpolarized ^{129}Xe in the Gas and Tissue Phases of the Lung

Ozkan Doganay[1,2], Elaine Hegarty[2,4], Rolf F. Schulte[3], Charles McKenzie[1,2], and Giles Santyr[1,2,4]

[1]Department of Medical Biophysics, Western University, London, Ontario, Canada, [2]Imaging Research Laboratories, Robarts Research Institute, London, Ontario, Canada, [3]GE Global Research, Munich, Germany, [4]Peter Gilgan Centre for Research and Learning, The Hospital for Sick Children, Toronto, Ontario, Canada

Introduction: MRI of hyperpolarized (Hp) ^{129}Xe promises to provide unique functional information for diagnosis of lung diseases, including measurement of size and exchange between the gas phase compartment (*G*) (ie. alveolar air space, the lung tissue compartment (*T*) and the red blood cell compartment (*RBC*) [1]. While most of the inhaled Hp ^{129}Xe remains in the gas compartment, approximately 2% dissolving in the tissue and compartments and these can be spectrally resolved using IDEAL (Iterative Decomposition of water and fat with Echo Asymmetry and Least-square estimation) approach [2, 3]. The signal-to-noise ratio (SNR) of Hp ^{129}Xe IDEAL images significantly depends on the MRI parameters including the choice of RF pulse flip angles for both tissue (α_T), and gas (α_G), pulse repetition time (*TR*) and echo-time spacing (ΔTE). In this study, an optimized single-shot spiral IDEAL approach [4] for Hp ^{129}Xe imaging of *G* and *T* was implemented. The new approach was tested in healthy rat lungs with a view toward mapping the kinetics of gas exchange *in vivo*.

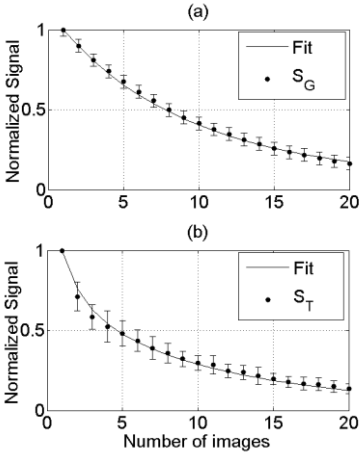

Figure 1: Experimentally measured gas (a) and lung tissue (b) signals as a function of image number. The solid line shows the theoretical best fit to the data.

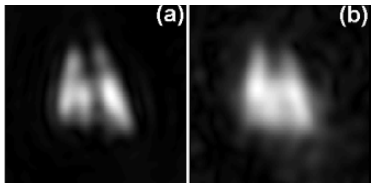

Figure 2: Coronal gas (a) and lung tissue (b) images of rat lungs.

Methods: Theoretical *G* and *T* signal strength (S_G, S_T) equations as a function of image number and flip angles (α_G, α_T) were derived from appropriate coupled Bloch equations including the exchange of magnetization between the G and T compartments. ΔTE was calculated based on the known chemical shift differences and T_2* values of the gas and tissue compartments using the effective number of signal averages approach [4], yielding a value of 50 us.All experiments were conducted using a 3T MRI system (MR750 GEHC, Wisconsin) with a custom-built transmit-only/receive-only birdcage coil and high performance insertable gradient system. Three healthy Sprague Dawley rats were ventilated with enriched Hp ^{129}Xe (85%) polarized to ~10% (Polarean, Durham NC). A set of coronal projection *G* and *T* images were obtained using single-shot 3-point IDEAL technique using three RF pulses and echo images (*m*=3) with echo-times of $\Delta TE \times m$. A non-selective RF excitation pulse was used with a pulse width of 180μs centered on the tissue resonance. To estimate α_G and α_T, 20 pairs of IDEAL images were acquired with *TR* fixed at 30 ms within 1.6 s and fitted to the S_G, S_T equations. *TR* was varied between 30 ms and 200 ms to investigate the effect of gas exchange.

Results: Figure 1 (a) and (b) shows the experimental $\boldsymbol{S_G}$ and $\boldsymbol{S_T}$ as a function of number of 20 IDEAL images as well as the best fit to the data based on the theoretical equations, yielding flip angles of 18^o and 60^o for α_G and α_T respectively. The measured α_T was found to be 60^o, which corresponded to the use of 90% of available tissue signal. Figure 2 shows coronal IDEAL *G* (a) and *T* (b) images from the lungs of a representative rat after average of 20. An increase of approximately 38% in S_T was observed at *TR*=200 ms compared to *TR*=30 ms due to replenishment from the gas phase.

Discussion: This study shows that the spiral IDEAL approach can efficiently separate the *G* and *T* ^{129}Xe lung signals over a range of *TR* values within a rat breath-hold. This dependence of the tissue signal on *TR* should allow mapping of the kinetics of gas exchange in lung. This approach is also expected to be useful for imaging the size and kinetics of the ^{129}Xe in the RBC compartment.

Acknowledgements: This work was supported by NSERC, CIHR and OPIC. O.D. was supported by a CaRTT studentship. **References:** [1] M. Fox Medical Physics 2014, 41(7):072302 [2] O. Doganay. et al., ISMRM 2015, Abstract:5591; [3] K. Qing et al., MRI 2013, 30(2):1134–42; [4] F. Wiesinger et al., MRM 2012, 68(1):8-16;

Development of Gd-free Blood-Pool T_1 MRI Contrast Agents for High-Field Applications

Shili Dong[1], Weiran Cheng[1,2], Feng Xu[1], Tameshwar Ganesh[4,5], Francisco Martinez[6,7], Timothy J. Scholl[6,7], Hai-Ling Margaret Cheng[4,5,8,9] and Xiao-an Zhang[1,2,3]

[1]Department of Physical and Environmental Sciences, [2]Department of Biological Sciences, University of Toronto Scarborough, [3]Department of Chemistry, [4]Department of Pharmaceutical Sciences, Leslie Dan Faculty of Pharmacy, University of Toronto, [5]Physiology & Experimental Medicine, Hospital for Sick Children, [6]Imaging Research Laboratories, Robarts Research Institute, [7]Department of Medical Biophysics, The University of Western Ontario, [8]The Edward S. Rogers Sr. Department of Electrical & Computer Engineering, [9]The Institute of Biomaterials and Biomedical Engineering, University of Toronto, ON, Canada

Introduction. Blood pool agents (BPA) are a class of contrast media designed for MR angiography (MRA). Typical BPAs require long circulation in the vascular system and high relaxivity, which can extend the time window for imaging and enable better signal-to-noise ratio to highlight the vasculature. Currently, the only clinically approved BPA is Ablavar®, a Gd-based contrast agent (GBCA) elegantly designed to bind to human serum albumin (HSA) reversibly, thus to achieve long vascular retention. There are, however, a few challenges associated with GBCAs, particularly, release and accumulation of free toxic Gd ions *in vivo* and decreased sensitivity at high magnetic field. To address these issues, a new class of Gd-free BPAs is designed with better biocompatibility and high sensitivity at both clinical and higher magnetic field strengths.

Methods. Due to several advantages of manganese(III) porphyrin (MnP) platform, a water-soluble MnP dimer, MnP_2, was designed as a Gd-free BPA.[1] Mn is an endogenous micronutrient, which is much more tolerable than free Gd^{III} and has shown prominent stability within porphyrin chelates at physiological pH.[2] Moreover, with rational ligand design, MnP can reach high relaxivity at high field. Two selected MnP units are connected with a biphenyl linker (Fig. 1a), which also promote non-covalent interaction with HSA, allowing MnP_2 to retain within the vasculatures.[1] MnP_2 was prepared through multiple-step synthesis, and characterized by HPLC, NMR, UV-Vis and MS. The binding of MnP_2 to HSA was evaluated by different optical spectroscopic methods, including UV- Vis absorption, circular dichroism (CD), and fluorescence spectroscopies. The field-dependent relaxivity of the MnP_2–HSA complex was measured in comparison with that of free MnP_2. Implications of HSA-binding in the pharmacokinetics of MnP_2 were evaluated in rats.[1, 3] Based on the results of MnP_2, the second generation dimer, *m*-MnP_2 was designed, synthesized and evaluated similarly.

Results. Successful synthesis of MnP_2 was achieved with four major steps: synthesis of porphyrin, coupling reaction, sulfonation and Mn insertion. MnP_2 was structurally confirmed by NMR, MS, and HPLC.[1] It exhibits extended high relaxivities up to 3 T, tight HSA binding and drastically elevated contrast in the vascular compartment (Fig. 2).[3] The HSA binding studies suggest that the MnP_2 may be buried in the hydrophobic protein pocket, hindering water access to the Mn^{III} ion, leading to a slight decrease in relaxivity.[1] In an attempt to avoid potential water access hindrance, a kinked version of MnP_2, *m*-MnP_2, was designed (Fig. 1b). Having the biphenyl linking group connected at the *meta*-positions, *m*-MnP_2 is expected to interact differently with HSA and result in improved relaxivity upon binding. The binding of *m*-MnP_2 to HSA was evaluated by UV-visible absorption and results suggest that *m*-MnP_2 has stronger and more specific binding to HSA than MnP_2.

Conclusion. With high relaxivity at high clinical field, high stability and long circulation, MnP_2 and *m*-MnP_2 are ideal Gd-free BPAs. Herein, the synthesis, characterization and protein binding properties of MnP_2 and *m*-MnP_2 will be presented.

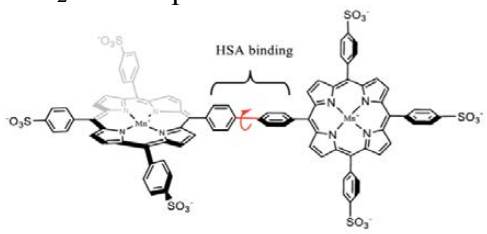

Figure 1 (a). MnP_2

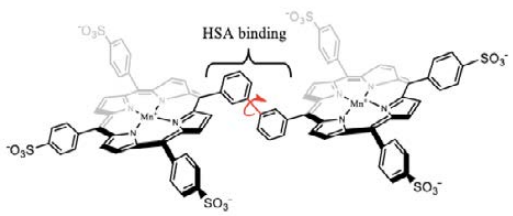

Figure 1 (b). *m*-MnP_2

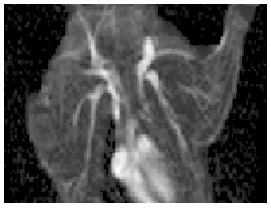

Figure 2

References

[1] Cheng, W. *et al. J. Med. Chem*. **2014**, *57,* 516-520. [2] Lyon, R. C. *et al. Magn. Reson. Med.* **1987**, *4*, 24.
[3] Cheng, W. *et al. J. Biol. Inorg. Chem*. **2014**, *19*, 229-235.

Ultra low dose CT myocardial perfusion imaging with compressed sensing based image reconstruction

[1]Esmaeil Enjilela, [1,2]Ting-Yim Lee, [3]Jiang Hsieh, [4]Kelley Branch,

[5]Robb Glenny and [1,2]Aaron So

[1]Imaging Research Laboratories, Robarts Research Institute;

[2]Imaging Program, Lawson Health Research Institute;

[3]CT Engineering, GE Healthcare;

[4]Division of Cardiology, University of Washington Medical Center;

[5]Division of Pulmonary and Critical Care Medicine, University of Washington

Computed tomography (CT) perfusion is a process by which perfusion to an organ is measured by CT images. This technique requires repetitive scanning together with injection of contrast agent resulting in high radiation dose (~5 to 20 mSv). We have developed a low x-ray dose method for quantitative CT perfusion imaging. It relies on reconstructing dynamic contrast-enhanced (DCE) CT images from sparsely sampled x-ray projections using a compressed sensing (CS) based algorithm. The feasibility of this approach is demonstrated in the myocardial perfusion imaging of a pig. For this purpose, we performed prospectively ECG triggered dynamic CT imaging on a 70 kg farm pig at 140 kV and 80 mA (28 mAs) with a GE Healthcare (GE) CT750 HD scanner with contrast injection (0.7 mgI/kg) at 3 ml/s. DCE images were then reconstructed from all (984) and one-third (328) of available projection views with filtered backprojection (FBP) and CS respectively. Myocardial perfusion (MP) maps from five consecutive 5 mm slices of the porcine heart generated with CT Perfusion (GE) using CS image sets were compared with those from full view FBP reconstruction and also with microsphere MP measurements. Compared with full view FBP MP measurements, CS maps had biases of -0.01 mL/min/g (95% CI -0.05 – 0.03). When measurements from CS MP maps were compared against ex-vivo fluorescent microspheres technique, the mean bias was -0.12 mL/min/g (95% CI -0.26 – 0.03). This animal study demonstrated that the proposed sparse view coupled with CS image reconstruction is able to generate MP maps with one-third of projection views (sparse-views) required in the conventional FBP technique, resulting in 66.67% reduction in radiation dose.

OPIC and the Development of a Commercialized Photoacoustic Imaging Platform

F. Stuart Foster

The Ontario Preclinical Imaging Consortium (OPIC) aimed to develop and commercialize the next generations of preclinical imaging technology, applications, and services for bioresearchers around the world. It has driven the evolution of new technologies and deepened our understanding of the imaging of complex biological targets. Instead of focusing on the individual imaging technologies, the proposed research and development was driven by goal oriented research on the origins of disease, imaging and biomarker validation, and development of new treatment strategies. Each of these themes brang significant commercial potential that was leveraged by our industrial partners and an aggressive commercialization strategy. The commercial partners ranged from large multinational corporations such as GE Healthcare, Bayer and Pfizer, to Ontario success stories like VisualSonics, and other fledgling Ontario start-ups. Thirteen interlinked projects across 5 institutions have been completed. Many of the projects involve multi-institution collaborations and involve younger principal investigators who will form the future of the Ontario's success in this field. The substantial progress achieved over the seven year history of OPIC will be summarized in this session and elsewhere in the program by the project PI's. This presentation will focus on the development, under OPIC, of a commercialized imaging platform for simultaneous high frequency ultrasound and photoacoustic imaging of mice and other small animals. The design and implementation of the new scanner will be described and its performance quantified. Beamforming techniques and signal processing will be presented, along with in vivo PA images of normal subcutaneous mouse tissue and selected tumour models. In particular, the use of the system to estimate the spatial distribution of oxygen saturation (sO2) in blood and co-registered with B-Mode images of the surrounding anatomy will be highlighted.

A Linear RF Birdcage Coil For Higher Frequencies For Rat Lung Imaging At 3T.

Gowtham Gajawada[1,2], Tao Li[1], Marcus J. Couch[1,2], Matthew S. Fox[3,4], Mitchell Albert[1,2]

1. Thunder Bay Regional Research Institute, Thunder Bay, Ontario. 2. Lakehead University Thunder Bay, Ontario. 3.Imaging Department, Robarts Research Institute, London, Ontario. 4. Department of Medical Biophysics, The University of Western Ontario, London, Ontario.

Introduction: Inhaled inert fluorinated gas magnetic resonance imaging (MRI) is a promising technique for anatomical and functional lung imaging. In order to better understand and develop this novel technique, a vast number of pre-clinical animal experiments are required for validation and optimization of radio frequency (RF) coils. Before the advent of dual-tuned coils, multinuclear studies required more than one RF coil in order to capture all the desired information. Since the subject needs to be moved in order to switch the RF coils, image registration (co-alignment of separate images) may be required for correct image interpretation. The purpose of this study was to develop a proton (^{1}H) and fluorine-19 (^{19}F) dual-tuned coil and co-registration of the images can be done easily while post processing.

Methods: A birdcage coil inherently has two orthogonal channels that are electrically invisible to each other. Since ^{19}F and ^{1}H nuclei have close resonant frequencies at 3 T (127.74 MHz and 120.15 MHz, respectively), one can take advantage of these two channels and tune each of them to a different resonant frequency assuring identical B_1 field profiles for the two nuclei resulting in an improved SNR. The size of the coil was chosen for rodent imaging, and the coil was constructed on an 88.3 mm diameter acrylic tube. The ^{1}H channel was at 0° and the ^{19}F channel was at 90°. An isolation of -17 dB was achieved at the ^{1}H frequency, and -30 dB at the ^{19}F frequency. In order to quantitatively study the field homogeneity for both nuclei, ^{1}H B_1 field mapping was performed using a dual-TR method and a 30 mL syringe of mineral oil. ^{19}F B_1 field mapping was performed using Dual Angle Method and a 30 mL syringe of sulfur hexafluoride (SF_6). 3D rat lung imaging was then performed on a healthy male Sprague-Dawley rat (348 g) using an animal care protocol approved by the local animal care committee. The rat was ventilated with a custom-built MR-compatible ventilator using a mixture of 80% SF_6 and 20% O_2. ^{19}F imaging was performed using TR=4ms, TE=0.85ms, 400 signal averages with a resolution of 64x64. The total scan time to acquire the images was 4 minutes and 42 seconds.

Results: Figure 1 shows the B_1 field mapping for both coil channels and the corresponding histograms. A 15 x 15 x 30 mm^3 field of view was considered for the ^{19}F for B_1 map, and a 16 x 16 x 20 mm^3 field of view was considered for Proton for B_1 and histogram. The mean normalized B_1 for the ^{1}H and ^{19}F frequencies (± standard deviation) were 0.819 ± 0.105 and 0.947 ± 0.019, respectively. Figure 2 shows *in vivo* rat lung images in the coronal and axial planes. The top row shows the ^{1}H images acquired using a turbo spin echo sequence during free breathing (no gating). The second row shows the ^{19}F images acquire during free breathing (no gating).

Discussion and Conclusions: The completed coil has exhibited satisfactory electrical performances as well as good B_1 field homogeneity for both nuclei. The rat lung images demonstrate a sufficient signal to noise ratio for ^{19}F MRI studies of animal models of pulmonary diseases.

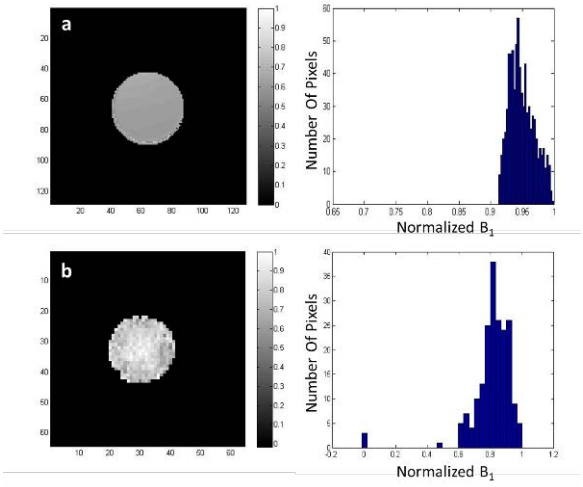

Figure 1: (a) A B_1 field map for the ^{1}H channel and the corresponding histogram. (b) The B_1 field map for the ^{19}F channel and its corresponding histogram.

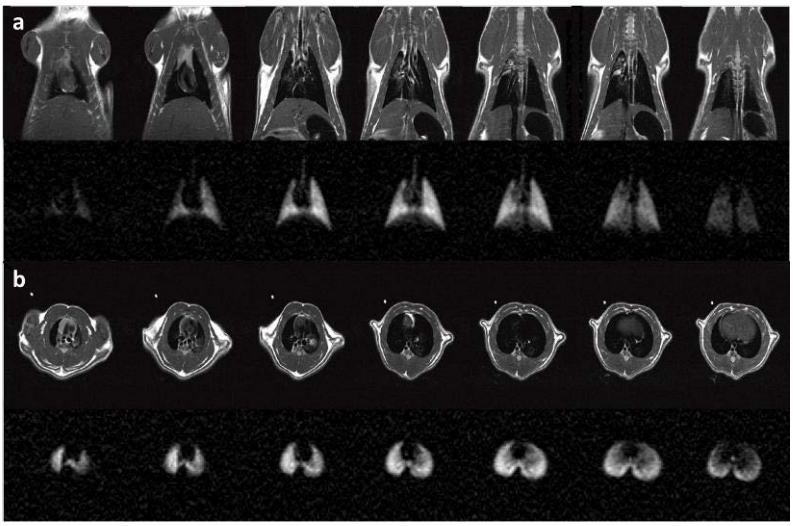

Figure 2: (a) Coronal and (b) axial views of the ^{1}H and ^{19}F MR lung images acquired in the lungs of a healthy rat.

Hyperpolarized ^{129}Xe Magnetic Resonance Imaging of Radiation-Induced Lung Injury with Correlation to Histology

Elaine Hegarty[1, 2], Ozkan Doganay[1, 3], Brandon Zanette[2, 4], Andras Lindenmaier[2, 4], Giles E. Santyr[1, 2, 3, 4]

[1]Imaging Research Laboratories, John. P. Robarts Research Institute, London, [2]Peter Gilgan Centre for Research and Learning, The Hospital for Sick Children, Toronto, [3]Department of Medical Biophysics, Western University, London, [4]Department of Medical Biophysics, University of Toronto, Toronto, Ontario, Canada.

Introduction: Early detection of radiation-induced lung injury (RILI) is important for improving outcome of radiation treatment of thoracic cancer. It has previously been shown that Magnetic Resonance Imaging (MRI) with hyperpolarized ^{129}Xe can detect changes in both lung tissue signal as well as exchange between gas and tissue (ie. pneumonitis) as early as two weeks following whole thorax irradiation in rats[1]. In this study, hyperpolarized ^{129}Xe MRI lung tissue imaging was performed in a rat model of RILI involving single-lung irradiation and compared to a cohort of non-irradiated rats. The ^{129}Xe lung tissue signal was correlated with tissue area (TA) and mean linear intercept (MLI) measured using quantitative histology.

Methods: Six Sprague Dawley rats were prepared following a Western University AUS approved protocol previously described[1]. Two weeks prior to imaging, three rats were irradiated with 18 Gy to the right thorax. Lung tissue images and lung gas images were obtained using spiral IDEAL[2] MRI during a 6s breath-hold. For each rat, the ^{129}Xe signal from the lung tissue was normalized to the gas to account for differences in polarization and ventilation. Following imaging, the lungs were removed, fixed in 10% formalin, and embedded in paraffin wax. The tissue was then cut into 5 μm thick tissue sections and stained with haematoxylin-eosin (H&E). TA was calculated as a fraction of the entire area by creating a binary image, which separated the tissue from the gas space. MLI was calculated using the method described in Knudsen et al[3].

Results: Figure 1 shows the normalized ^{129}Xe tissue signal acquired using MRI versus TA measured by quantitative histology for all rats/lungs. A positive correlation between normalized tissue ^{129}Xe signal and TA was observed (R^2 = 0.65, p-value = 0.13). Furthermore, the irradiated rats had significantly a higher ^{129}Xe tissue signal and TA: 0.26 (0.08) and 0.28 (0.02) respectively, compared to the non-irradiated rats: 0.17 (0.03) and 0.22 (0.03) respectively, with respective p-values of 0.02 and 0.003, consistent with pneumonitis. The un-irradiated left lung of the irradiated rats also showed an increase in ^{129}Xe tissue signal and TA. The correlation between ^{129}Xe tissue signal and MLI was less significant.

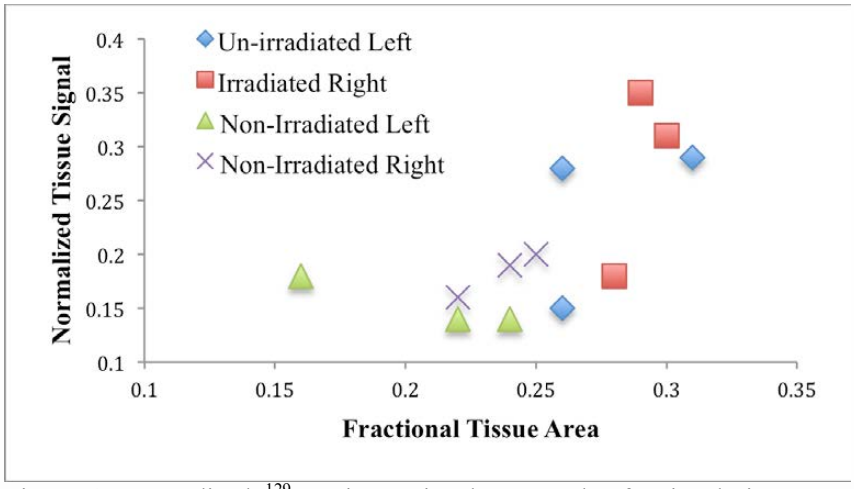

Figure 1: Normalized ^{129}Xe tissue signal versus the fractional tissue area measured by quantitative histology. The triangular and x symbols represent the left and right lung respectively of the non-irradiated cohort. The diamond and square symbols represent the un-irradiated left lung and irradiated right lung respectively of the irradiated cohort.

Conclusion: Both ^{129}Xe tissue signal and TA can detect early changes associated with irradiation compared to a non-irradiated cohort. These methods should be translatable to human subjects in future given the growing availability of hyperpolarized gas technology in the clinic. Early detection of pneumonitis may allow adjustment to the radiotherapy plan and/or the application of alternate therapies to mitigate RILI.

References: [1]Fox M. S. et al. Medical Physics 2014 [2]Wiesinger F. et al., MRM 2012 [3]Knudsen L. et al., J Appl Physiol 2010

Acknowledgements: We would like to thank Dr. Parraga and her lab members for assistance in polarization of ^{129}Xe and Dr. Wong for his assistance with irradiations. We would also like to acknowledge our funding sources: CIHR, NSERC, OPIC and the Hospital for Sick Children.

Mouse Models of Human Diseases

R. Mark Henkelman and the Mouse Imaging Centre (MICe)

Within the context of OPIC, the Mouse Imaging Centre was committed to developing three-dimensional imaging methods and automated analysis technologies, and to apply these to mouse models of human diseases. Over the course of the grant, we have investigated 36 different gene knockout mice with phenotypes related to 13 different diseases. This has required imaging of ~3,500 mice and has resulted in 59 publications.

In terms of methods development, we have worked out techniques for three-dimensional imaging of mutant mouse embryos that are embryonic lethal, using optical projection tomography (OPT) at E9.5 and X-ray micro CT at E15.5. Based on these images, we have developed automated computer techniques for identifying phenotypic deficits.

Another area of concentration has been Autism Spectrum Disorder where we have taken a series of 26 genes that have been identified through human GWAS studies, obtained brain MRI images for each of the corresponding mouse model and asked how the phenotypic neuroanatomical differences cluster as a way of identifying subtypes of autism.

Pre-Clinical Imaging for Models of Musculoskeletal Disease

David W. Holdsworth and Maria Drangova
Robarts Research Institute
Western University, London ON

Small-animal models and human cadaveric testing are commonly employed in basic research related to musculoskeletal conditions – such as arthritis, osteoporosis, degenerative disk disease, and cartilage degeneration. As part of the Ontario Pre-Clinical Imaging Consortium (OPIC), our group has developed novel techniques to acquire and analyze 3D micro-CT images of rodents and human cadaveric specimens, with the goal of improving our knowledge of the anatomy and function of musculoskeletal tissue, in health and disease. For studies of anatomy and micro-structure, we have developed techniques for body composition analysis, which have been applied to knock-out models of spine degeneration, and also for dual-energy micro-CT analysis of vascular micro-architecture near bone. For biomechanical analyses, we have developed CT-compatible devices that facilitate real-time 3D micro-imaging of animals and tissue specimens during dynamic material testing. We have also developed techniques to extend high-speed, slip-ring based volumetric micro-CT for investigations of knee function, using intact human cadaveric specimens. Another new capability that has been made possible with OPIC support is the development of new techniques for image-based advanced manufacturing, where micro-CT is used for high-resolution non-destructive analysis of clinical orthopaedic components, and as the basis for the design and fabrication of functional orthopaedic implants for a rat model of hip arthroplasty.

Altered angiotensin II AT_1 receptor binding in a renal hypertension rat model is normalized with enalapril: PET study with [^{18}F]FPyKYNE-Losartan

B. Ismail[1,2], T. Hadizad[2], RA. deKemp[2], RS. Beanlands[1,2], J N. DaSilva[1,3]

(1) University of Ottawa Heart Institute, Cellular and Molecular Medicine Department, Ottawa, Canada
(2) University of Ottawa Heart Institute, Ottawa, Canada
(3) University of Montreal Hospital Research Centre (CRCHUM), Department of Radiology, Radio-Oncology and Nuclear Medicine, University of Montreal, Ottawa, Canada

Introduction: Renal Hypertension is associated with increased cardiovascular morbidity and mortality. Subtotal nephrectomy leads to a chain of events that culminates in hypertension and chronic kidney disease. The renin angiotensin system (RAS) is known to be dysregulated, specifically AT_1 receptor plays a major role in progression of the disease. However, conflicting results have been reported on intrarenal AT_1 receptor levels and the impact of antihypertensive drugs on RAS signaling is poorly understood.
Methods: Male SD rats underwent 5/6 nephrectomy (5/6Nx) or sham operations. At 8-10 weeks post-surgery, a subset of animals was sacrificed; and the remaining 5/6Nx rats either received no treatment or ACEI, enalapril (10 mg/kg/d). The following were measured at ~10 and ~20 weeks post-surgery: systolic blood pressure (SBP), plasma creatinine, [^{13}N]NH3 PET renal and myocardial blood flow (RBF, MBF) and LV EF. Renal AT_1 receptor levels were assessed with our novel [^{18}F] FPyKYNE-Losartan and PET.
Results: Around 10 weeks post-surgery; 5/6Nx rats compared to shams developed hypertension, elevated plasma creatinine, increased MBF (188.4±15.6 vs 145.7±18 mmHg; 1.36±0.17 vs 0.67±0.3 mg/dl; 4.1±0.78 vs 2.7±0.75 ml/min/g, respectively; $p<0.05$) and LV hypertrophy. PET [^{18}F]FPyKYNE-Losartan distribution volume (DV) determined by Logan analysis was reduced in the remnant hypertrophied left kidney cortex of 5/6Nx rats vs shams (2.3±0.4 vs 2.78±0.5 ml/cm3, respectively; $p<0.05$). At ~20 weeks (table), enalapril significantly decreased SBP and creatinine back to normal levels and normalized MBF and RBF. Changes in LV EF and DV values in the 5/6Nx rats were normalized by enalapril treatment.
Conclusion: Progressive structural and functional changes in kidney and heart occurred as early as 10 weeks post-subtotal nephrectomy. Normalization of renal AT_1 receptor DV by enalapril was accompanied by restored renal and cardiac functions. *In vivo* PET imaging with [^{18}F]FPyKYNE-Losartan enables non-invasive identification of AT_1 receptor expression abnormalities. This approach holds promise as an aid to understand disease and guide therapy.

	SBP (mmHg)	Plasma Creatinine (mg/dl)	LV EF (%)	DV (ml/cm3)
Sham	**147±14.9**	**0.5±0.07**	**73±5.3**	**2.78±0.48**
5/6Nx	**189±17.3†**	**0.75±0.08†**	**62±8.3†**	**1.99±0.33**
5/6Nx-Enalapril	**151±9.4‡**	**0.4±0.04‡**	**74±6.2‡**	**2.76±0.49**

†Significant from sham, ‡ significant from 5/6Nx ($p<0.05$).

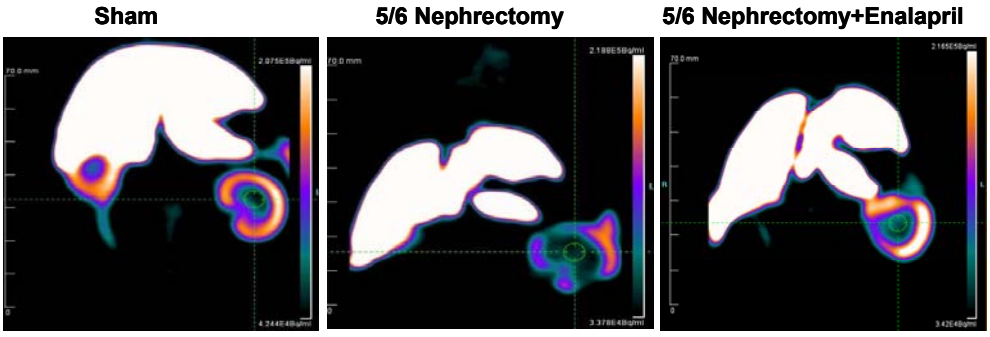

Coronal view microPET scans showing liver and kidneys obtained at 5-10 min post-injection of [^{18}F]FPyKYNE-Losartan.

Development of a photoacoustic imaging system for intraoperative breast lumpectomy characterization

Ivan Kosik, Philip Wong, Muriel Brackstone and Jeffrey JL Carson
Ontario Pre-Clinical Imaging Consortium
Imaging Program, Lawson Heath Research Institute, University of Western Ontario, London, Ontario, Canada

Introduction: Lumpectomy surgery is recommended for women diagnosed with early breast cancer, however, about 1 in 5 procedures will fail to completely remove all cancer and a second surgery becomes necessary. This situation, resulting from a lack of rapid and specific 3D tumour imaging technology, strains both patients and resources. Deep tissue Photoacoustic Imaging (PAI), shows great promise as a diagnostic tool for cancer detection because it is able to visualize optical contrast based on biomarkers such as hemoglobin and lipid concentration, as well as oxygen saturation (SO_2). Abnormal concentrations of blood and lipid, as well as low SO_2, have been linked to both tumor malignancy and reduced treatment efficacy (1). Unfortunately, available PAI systems are not optimized to visualize these biomarkers in deep tissue. The objective of this project is to develop a new PAI system utilizing specialized ultra-broadband transducer technology capable of distinguishing cancerous from normal tissue at clinically relevant depths.

Methods: A raster scanning 3D PAI system was constructed on a portable transport cart. The system was comprised of a laser tunable in the 680 nm - 950 nm range, a 4-axis robot, and a 16-channel transducer array connected to a 50 MHz data acquisition system (DAQ). The DAQ, robot and laser were controlled with LabVIEW and the image reconstruction was performed in Matlab. A 30 cm x 60 cm x 30 cm glass tank was used to contain imaging specimens and degassed water was used as an acoustic coupling medium. Preliminary imaging tests were performed on fresh lumpectomy specimens obtained immediately following excision in coordination with surgical staff (Fig 1a). 3D photoacoustic scans were performed using 690 nm and 930 nm wavelengths of light. For qualitative comparison a 2D ultrasound (US) image was also acquired (Fig 1b).

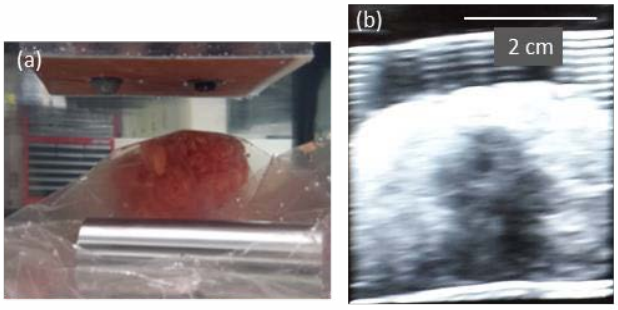

Fig 1(a) Photograph of lumpectomy specimen mounted beneath 10 cm x 10 cm custom built 16-channel, receive only, US transducer array. (b) Clinical US system image showing suspicious mass (dark region) inside lumpectomy.

Results: The image acquisition procedure took less than 10 minutes to complete for both laser wavelengths and resulted in 3D imaging volumes measuring 16 cm x 16 cm x 6 cm. Compared to imaging at 930 nm (Fig. 2), images reconstructed using 690 nm light (Fig. 3), show significantly more high-contrast areas. Furthermore, 690 nm light was able to provide a high signal-to-noise-ratio (SNR) at deeper locations inside the lumpectomy specimens, with signals originating at up to 6 cm from the light entry point.

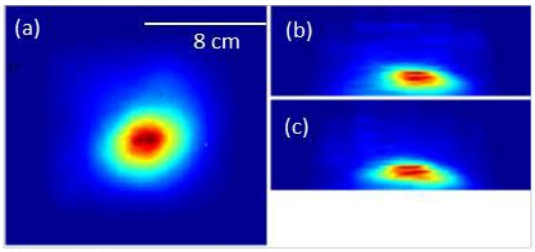

Fig 2. PA images of Maximum Intensity Projections (MIPs) along (a) Z-axis, (b) Y-axis and (c) X-axis imaged using 930 nm light.

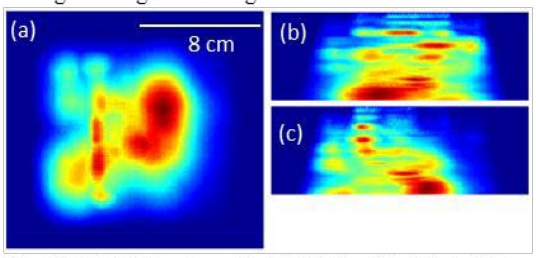

Fig 3. PAI MIPs along (a) Z, (b) Y and (c) X at 690 nm.

Conclusions: A 3D photoacoustic imaging system specialized for breast lumpectomy imaging was designed, constructed and tested. Preliminary imaging results showed better deep tissue SNR at 690 nm where breast tissue optical absorption is lower compared to 930 nm, allowing deeper light penetration (2). Also consistent with literature was the presence of numerous high-contrast areas, found in images acquired using 690 nm wavelength light. These volumes of increased absorption likely originate from increased concentrations of deoxyhemoglobin commonly associated with malignant angiogenic tumours, however, further imaging using co-registered 3D ultrasound as well as comparison with histology will be carried out to make conclusions.

References: [1]Wang *et al*. Science 2012;6075:1458-1462. [2]Cerusi *et al*. J. Biomed. Opt. 2006;11(4) 044005.

Quantitative functional and molecular imaging in cardiac and cancer studies

Ting-Yim Lee, PhD, Aaron So, PhD, James Koropatnick, PhD, Robert Hudson, PhD, Len Luyt, PhD, Michael Kovacs, PhD, Songju Chu, PhD, Lihai Yu, PhD
Lawson Health Research Institute and Robarts Research Institute
Medical Imaging and Chemistry, University of Western Ontario
London, Ontario

Although Cardiac CT angiography (CTA) has increasingly become the modality of choice to investigate acute chest pain, it remains a morphological technique that assesses the degree of stenosis in 'large' epicardial blood vessels which may not be related to the tissue ischemia causing the symptoms. We have developed a quantitative CT method to measure not only myocardial perfusion but also contrast distribution volume. Normal myocytes are impermeable to contrast agent but becomes permeable when injured by ischemia. This would lead to an increase in the contrast distribution volume. It follows that quantitative assessment of both perfusion and contrast distribution volume may allow discrimination among normal, at risk and infarcted myocardium as shown in a porcine acute myocardial infarction model.

Recent studies indicate that epigenetic regulation of genes is as important to tumorigenesis as altered gene sequence. Epigenetics refers to changes in gene expression that are independent of changes to DNA sequence. These changes can be grouped into three broad categories – methylation of DNA, covalent histone modifications, and expression of non-coding RNAs (miRNA) as opposed to the extensive array of genetic mutations present in subsets of tumor cells from a common progenitor. As such, epigenetics could be a common pathway of tumorigenesis. We have developed a F-18 probe, F-18 FAHA, for imaging of histone deacetylase activity in tumors. Results of F-18 FAHA PET imaging in xenograft tumor (MDA-MB-468) in nude mice will be presented and their implications for personalized cancer treatment discussed.

Dependence of Hyperpolarized ^{129}Xe Lung MRI Morphometry on the Free Diffusion Coefficient of Xenon Gas

Andras Lindenmaier[1,2], Elaine Hegarty[2,3], Ozkan Doganay[3,4], Alexei Ouriadov[3], Giles Santyr[1,2,3,4]

1. Department of Medical Biophysics, University of Toronto, Toronto, ON
2. Physiology and Experimental Medicine, The Hospital for Sick Children, Toronto, ON
3. Imaging Research Laboratories, Robarts Research Institute, Western University, London, ON
4. Department of Medical Biophysics, Western University, London, ON

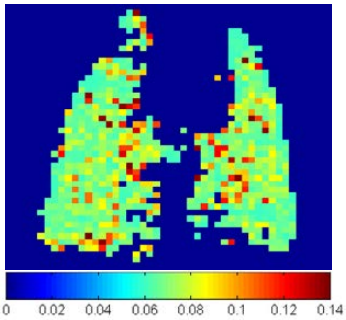

Fig. 1: Sample D_0 map of a rat lung calculated using the variable D_0 morphometry method.

Introduction: Hyperpolarized ^{129}Xe MRI has been previously shown to provide not only high resolution ventilation mapping, but also detailed anatomical and functional information that allows differentiation of various lung pathologies[1].
In particular, apparent diffusion coefficient (ADC) mapping, combined with morphometry, can be used to track microstructural (ie. alveolar) disease effects.[2] Traditionally, clinical ADC imaging, is preformed using a single breath-hold of xenon, during which the patient is imaged with a fast diffusion-weighted sequence. The ADC signal vs. b value can then be used in conjunction with morphometry to extract lung microstructural parameters such as the alveolar radius (r), airway radius (R), alveolar sleeve depth (h) and mean linear intercept (L_m). The conventional assumption has been that the free diffusion coefficient of xenon (D_0) does not vary significantly within the lungs and so D_0 was considered a constant in morphometry calculations[1]. However, due to the small inhaled dose (500 mL) and the large volume of air present in the lungs and due to potentially uneven mixing in various pathologies, D_0 has been shown to vary[2]. To further explore this dependence, we adapted the Yablonskiy morphometry model to account for variable D_0 within the lungs, similar to Ouriadov et al[2]. We investigate the effect of varying D_0 on measured lung morphometry parameters using multiple pre-breaths in a rat.

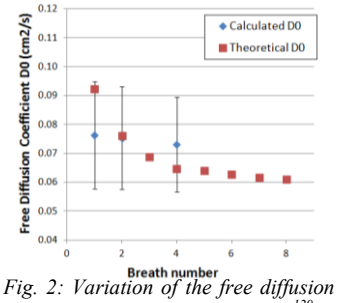

Fig. 2: Variation of the free diffusion coefficient (D_0) as a function of ^{129}Xe breath number. Red squares show the theoretical values, while the blue diamonds represent data obtained using the novel variable D0 morphometry algorithm. Error bars show ± 1 SD.

Methods: 4 Sprague-Dawley male rats were imaged using a protocol approved by Western University's Animal Use Subcommittee. As part of a larger study investigating radiation induced lung injury (RILI), the rats had partial irradiation of the right thorax, and a total delivered dose of 18Gy, after which they were incubated for two weeks. The rats were anesthetized, tracheostomized, placed within the MRI system, and mechanically ventilated using an MR-compatible ventilator[3]. Following 1, 2 or 4 breaths of ^{129}Xe (effectively changing D_0 in the lungs), MRI images of the lungs were acquired in breath-hold fashion using a 2D diffusion-weighted sequence on a 3T GE MRI system, with FOV = 5x5cm, matrix size of 64x64, TE= 9.6ms, TR = 11ms, BW = 2kHz and an averaging of 3 images to boost SNR. An insert gradient coil was used to ensure a range of b-values (0, 2.2, 8.9, 20.0, 35.6, 55.6, 80.1, 109.0 s/cm^2) at a diffusion time of 1.62ms. Morphometry was performed using the Yablonskiy method[1] with D_0 as a fifth parameter in the fitting algorithm.

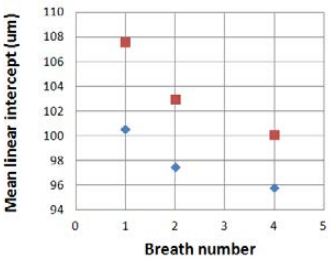

Fig. 3: Lung mean linear intercept calculated with the improved variable D_0 morphometry (diamonds) and fixed D_0 (squares).

Results and Discussion: Fig. 1 is a representative D_0 map obtained using the variable D_0 morphometry approach, showing the extent of variability throughout the lung. Fig. 2 shows the expected theoretical[3] dependence of D_0 on breath number as well as the average D_0 values measured from the rat morphometry experiments. As expected, a trend of decreasing D_0 was observed with increasing number of breaths, consistent with increasing ^{129}Xe concentration in the lung. More significantly however, as seen in Fig. 3, was the effect of breath number on L_m. All structural parameters were observed to vary 5-10% on average. Since the effects of disease may change lung microstructure subtly and heterogeneously, a variability of 10% in the morphometry parameters may mask pathological changes. This work shows that it is important to explicitly account for variations in D_0 throughout the lungs, particularly since D_0 depends on lung volume, ventilation and the gas mixture used. In future, a dedicated breath-hold (at short diffusion time) could be used to map the D_0 variability and to better account for this confounding effect. On the other hand, D_0 may be diagnostic in its own right as it has been shown to depend on disease[2].

References: 1) Yablonskiy, et al. MRM 67, (2012). 2) Ouriadov, et al. MRM epub (2014). 3) Couch, et al. MRM 68, (2012).

Acknowledgements: The authors would like to thank Andrew Wheatley for polarization of ^{129}Xe and Dr. Wong for his help with irradiations. We would also like to acknowledge our funding sources: CIHR, NSERC, OPIC, OGS and the Hospital for Sick Children.

A practical platform for real-time imaging of live cells during dynamic fluid shear

Lorusso, D.[1,2,3], Nikolov, H.[3], Milner, J.S.[3], Sims, S.M.[2], Dixon, S.J.[2], Holdsworth, D.W.[3,4,5]

1. Western's Bone & Joint Initiative; Schulich School of Medicine & Dentistry, The University of Western Ontario, London, ON, Canada.
2. Department of Physiology & Pharmacology; Schulich School of Medicine and Dentistry, The University of Western Ontario, 1151 Richmond Street, London, ON, Canada. N6A 3K7
3. Imaging Research Laboratories, Robarts Research Institute; Schulich School of Medicine and Dentistry, The University of Western Ontario, 100 Perth Drive, London, ON, Canada. N6A 5K8
4. Department of Medical Biophysics; Schulich School of Medicine and Dentistry, The University of Western Ontario, 1151 Richmond Street, London, ON, Canada. N6A 3K7
5. Department of Surgery; Schulich School of Medicine and Dentistry, The University of Western Ontario, 1151 Richmond Street, London, ON, Canada. N6A 3K7

Introduction: Mechanotransduction is the process by which cells sense – and respond to – the local mechanical environment. This ability to react to external loads and forces is a critical component of mammalian physiology and is essential for normal functioning of our bones, lungs, and blood vessels; yet, the underlying mechanisms are still poorly understood. A form of mechanical stimulation that is commonly implicated in mechanotransduction is shear stress due to fluid flow. Our goal is to observe the immediate responses of cells to pulsatile fluid shear. Here, we describe the development of a microfluidic chamber for live cell cultures, which is compatible with real-time optical microscopy.

Methods: A microfluidic chamber was designed and fabricated from polydimethylsiloxane (PDMS) using a replica molding technique. Thin PDMS membranes were applied to a cell-culture dish with a thin glass-bottom window. Chambers were then cast and sealed to this base membrane, creating a microfluidic chamber with channels from about 1500-µm wide by 100-µm tall to 500-µm wide by 100-µm tall. A saline solution containing 6-µm diameter beads was pumped through the chambers. Imaging of the channels under flow was performed using an inverted microscope and high-speed digital camera (1200 FPS). Flow parameters were calculated by micro-particle imaging velocimetry, using the polystyrene beads as markers. Chambers were disinfected, sterilized, and subsequently pretreated to enhance cell attachment. MC3T3-E1 osteoblast-like cells were then seeded into the chamber and imaged. In addition, cells were treated with fluorescent calcium dye fura-2 and exposed to shear stress during photometry.

Results: Several prototype microfluidic flow chambers have been successfully fabricated in a reproducible manner. Steady flow rates up to 30 µL/min have been introduced into the chambers, generating a range of shear stresses from 1 to 3 Pa. In addition, MC3T3-E1 cells adhered and survived within the microfluidic chamber for at least 24 hours. Calcium photometry shows an increase in intracellular Calcium levels in response to fluid shear stimulus.

Conclusions: We have developed, fabricated and tested a microfluidic system capable of delivering physiologically relevant fluid shear stresses, under steady flow conditions. Such stresses can be applied to a chamber capable of hosting live cells, which can be imaged while subjecting cells to controlled flow-induced shear stress. Further development of the platform will enable application of high-frequency oscillatory stimuli.

These studies are supported by the Canadian Institutes of Health Research.

1

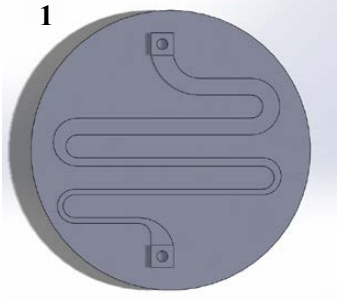

Figure 1. A CAD drawing of the mold to be CNC milled for the production of PDMS microfluidic chips

2

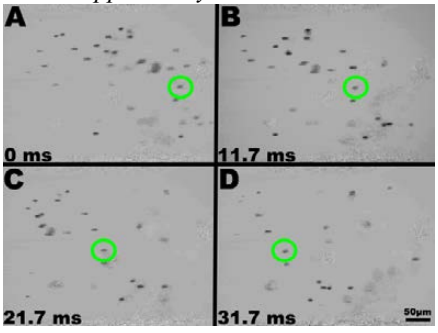

Figure 2. Frames (A) 1, (B) 7, (C) 13, and (D) 19 of a 600 FPS video, showing particle flow over time within a prototype channel

3

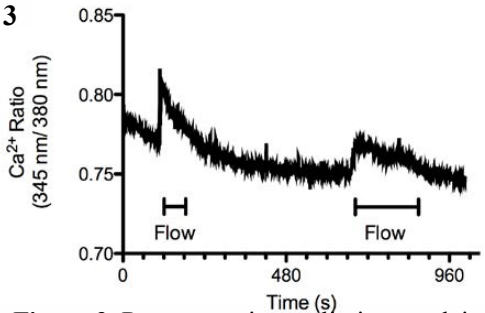

Figure 3. Representative preliminary calcium response plotted as the ratio of the fluorescence intensities at 345 nm / 380 nm. Flow was introduced at 30 µL/min where indicated for the bars below the trace.

In vivo tracking of iron labeled tumour-associated macrophages with MRI

A V Makela & P J Foster
Ontario Pre-Clinical Imaging Consortium
Robarts Research Institute, The University of Western Ontario, London, Ontario

Introduction: Macrophages are the main stromal cells in tumours. These are referred to as tumour-associated macrophages (TAMs). The cellular composition of some tumours is known to be up to 50% TAMs.[1] The presence and density of TAMs have been linked with tumour aggressiveness, metastatic spread and poor outcomes.[2] There is a pressing need for reliable methods to image cells of the tumour microenvironment at multiple time points, in vivo during cancer progression and metastasis. Our research addresses this need, using emerging in vivo cellular magnetic resonance imaging (MRI) techniques that we will advance in our lab to detect, monitor and measure TAMs. Previous imaging studies have demonstrated that the intravenous (IV) administration of iron oxide nanoparticles (USPIO) can be used to label TAMs in vivo and that MRI can be used to detect and monitor the accumulation of iron-positive TAMs.[3]

Methods: We used two cancer models (1) human breast cancer cells (231) implanted orthotopically into the mammary fat pad in nude mice and (2) mouse melanoma cells (B16F10) implanted subcutaneously into the flank in syngeneic C57Bl/6 mice. Whole body images were acquired weekly using a 3D-balanced steady state free precession (bSSFP) sequence. At 3 weeks post cell implantation mice received an IV injection of USPIO nanoparticles and then images were acquired ~24 hours later. Image data was assessed for regions of signal void within the tumour. Tumours were sectioned and stained with H&E and with Perl's Prussian Blue (PPB) to detect iron-labeled cells. The number of iron positive cells were counted to determine the average number of PPB-positive cells for all tissue sections for each tumour type. The spatial distribution of PPB-positive cells was recorded for all tumours.

Results: For both types of tumours, images obtained 24hrs after IV USPIO showed clear regions of signal loss within the tumour mass (**Figure 1**). The signal loss was much more substantial in 231 mammary fat pad tumours compared to B16F10 melanoma tumours. For 231 tumours signal loss was often prominent near the periphery of the tumours (peritumoural) but was also visible throughout the tumour mass. B16F10 tumours showed signal loss centrally. Our analysis of PPB-stained tissue sections agreed with the MRI data (**Figure 2**). There were approximately 10x more PPB+ cells in the breast cancer sections; average of 30.6 for breast cancer vs. 3.1 for melanoma.

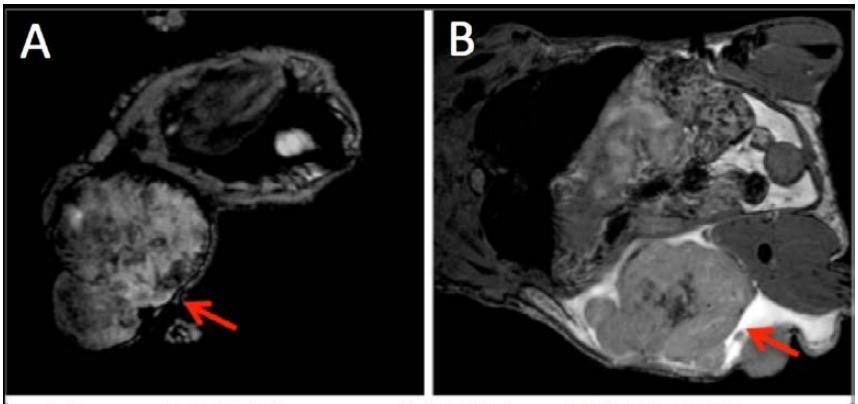

Figure 1: MRI images of A) 231 and B) B16F10

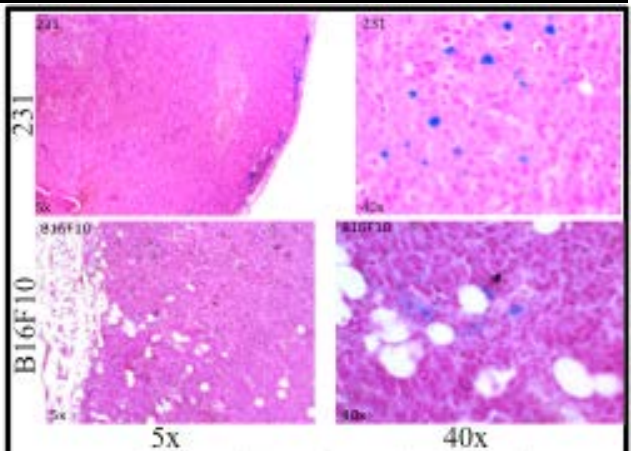

Figure 2: 5x and 40x views of PPB sections of 231 and B16F10 tumours

Additional studies using three different types of breast cancer cell lines representing different phenotypes in terms of aggressiveness, propensity to metastasize and growth rates are underway.

Conclusions: TAMs play multiple roles in cancer progression and metastasis. The results of our study confirm the value of IV USPIO and MRI as a diagnostic tool for assessing TAMs. To the best of our knowledge, this is the first direct comparative study of the density and distribution of TAMs in different tumour models by USPIO and MRI.

References:

1. Kelly PM et al, Br J Cancer, 1988; **2.** Obeid E et al, Int J Oncol, 2013; **3.** Daldrup-Link HE et al, Clin Cancer Res, 2011

Longitudinal MRI tracking of brain metastasis development and dormancy after radiotherapy

Donna H. Murrell[1,2], N Zarghami[2], MD Jensen[2], AM Hamilton[1], AF Chambers[2,3], E Wong[2,3], PJ Foster[1,2]

Ontario Preclinical Imaging Consortium

1. Imaging Research Laboratories, Robarts Research Institute, London, ON
2. Department of Medical Biophysics, Western University, London, ON
3. London Regional Cancer Program, London, ON

INTRODUCTION: Breast cancer is the most commonly diagnosed cancer in Canadian women [CCS Canadian Cancer Statistics, 2013]. Brain metastases occur in about half of metastatic breast cancer patients who over express the human epidermal growth factor receptor 2 (HER2) [Lai *et. al*., Cancer, 2004] and the prognosis for this is poor; the median survival time is 4-6 months and only 20% of patients can expect to live to one year [Clayton *et. al.,* Brit J Cancer, 2004]. Improved therapies are desperately needed for these patients. Preclinical studies play a crucial role in understanding metastasis progression and investigating responses to treatment.

When a cancer cell spreads to a distant site, it may experience one of three fates: (1) it may die, (2) it may proliferate to form tumours, or (3) it may remain viable but nonproliferative ('dormant'). Our lab has developed high-resolution anatomical and iron-labeled cellular MRI techniques [Heyn *et al.,* Magn Reson Med, 2006] to monitor cancer cell fate *in vivo* during brain metastatic development in animal models. Here, we use this in addition to image-guided micro-irradiation technology developed in the Wong lab [Jensen *et al.,* Med Phys, 2013] to investigate the growth of brain metastatic breast cancer and concurrent responses of metastases and dormant cancer cells to WBRT.

METHODS: Two animal experiments were performed. Female nude mice were given intracardiac injections of 100,000 MDA-MB-231-BR-HER2 cells and brain metastatic development was monitored using MRI. At endpoint, brains were excised for histology and immunohistochemistry. The first experiment (n=12) investigated 'late' WBRT (20Gy/2fx) delivered when MRI-detectable tumours had developed; this is similar to the case of clinical diagnosis [*preliminary results presented last year at ImNO*]. The second experiment (n=12) used iron-labeled cells and investigated 'early' WBRT (20Gy/2fx) given following initial cancer cell arrest in the brain, prior to tumour growth.

RESULTS: 'Late' WBRT was able to halt tumour growth. At 11 days post-therapy, the average volume of a treated tumour was significantly smaller than untreated ($p<0.01$); however, the number of MRI-detectable tumours did not decrease and some tumours continued to grow. 'Early' WBRT was able to eradicate nearly all tumours. The number of metastases and total tumour volume in treated brains were significantly less than untreated ($p<0.05$). There was a reduction in the number of MRI signal voids (representing dormant cancer cells) over time, but no significant difference between groups was observed at any time point.

CONCLUSION: 'Early' WBRT is more effective than 'late' for mitigating tumour burden observed by MRI. Early therapy provides good tumour control and improved survival, yet dormant cancer cells can persist even when treatment is delivered very early in cancer progression. Further investigation of the dormant cell population is warranted to confirm viability and determine if they may respond to proliferation signals causing future recurrence.

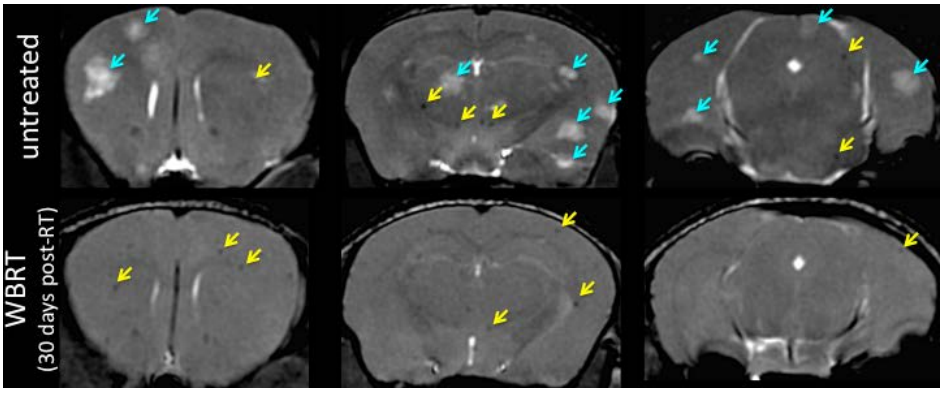

Figure: MR images of mouse brain *in vivo* 32 days after cancer cell injection. 'Early' WBRT provides good control of tumour growth, as seen by lack of metastasis development in treated brains (tumours are indicated by blue arrows in untreated brain); however, dormant cancer cells (indicated by yellow arrows) persist in both treated and untreated brain.

Non-invasive live insect imaging made possible using CO_2 general anesthesia and micro-CT

Danny Poinapen[*1,3], Joanna K Konopka[2,3], Jeremy N McNeil[2], Joseph U Umoh[1], Chris JD Norley[1], Daniel CW Brown[4], David W Holdsworth[1]

Ontario Pre-Clinical Imaging Consortium

[1]Robarts Research Institute; [2]Department of Biology, University of Western Ontario; [3]Southern Crop Protection & Food Research Centre, Agriculture & Agri-Food Canada, London, ON, Canada; [4]Canadian Centre for Agri-Food Research in Health &Medicine, Winnipeg, MB.

Introduction. To overcome the difficult technical demands in live insect imaging (e.g. absolute unrestricted immobilization of insects (< 5 µm), adequate quality to distinguish *in situ* structures, and repeated scanning of same individuals), two inherent characteristics of insect adaptive physiology and their cellular biochemistry are exploited. First, insects can withstand hypoxic environments, and keeping them under carbon dioxide (CO_2) leads to temporary full immobilization as CO_2 plays an anesthetic role, interfering with the neuromuscular junction (NMJ)[1,2]. Second, insects are radio-tolerant, and can survive very high radiation doses (>200 Gy) via highly efficient oxidative stress and DNA damage repair mechanisms[3,4]. Based on these two properties, we pioneered the combination of CO_2 anesthesia and X-ray micro- computed tomography (micro-CT) to image live insects. We aim at optimizing the conditions for full unrestricted immobilization of insects without concerns of potential impact of radiation on the subsequent life history of scanned individuals or biological processes under investigation.

Methods. We demonstrated this new method on two insect species: *Leptinotarsa decemlineata* and *Pseudaletia unipuncta*. The adult insects were immobilized by CO_2 anesthesia (constant flow of 5 psi) in a specially designed tube (Fig.1), and placed in a GE explore Locus scanner (80 kV; 0.45 mA). Then, 900 X-ray projections were acquired at 0.4° increments around the individuals to create 3D CT reconstruction at 20 µm isotropic pixel size. The entrance dose in 5 protocols of different scan times (0.33, 1.40, 2.68, 3.96, and 6.53 h) was measured at the isocenter of an ionization chamber coupled to an electrometer (Keithley, models 96035B and 35614, respectively). Noise, in each protocol, was calculated as the standard deviation in a water phantom image in 5 specific ROI locations (20^3 pixels each). A dose-noise relationship was then established to yield the optimal scanning conditions.

Results. An inverse-square, dose-noise relationship was obtained (Fig. 2). The optimal scanning condition resulted in an entrance dose of 6.2 ± 0.04 Gy and produced images with a 129.6 ± 5.1 HU noise level during a 2.68 h scan (i.e. the amount of time the insects were maintained under CO_2 anesthesia). Under these conditions, the insects attained full recovery (moved in a coordinated fashion) within 40 min post-anesthesia. Overall, the insects received radiation doses ranging from 0.58 to 15.5 Gy (i.e. corresponding to a noise range of 445.3 to 79.1 HU) depending on the imaging protocols used (or combination, in case of repeated scanning). Although in the 6.5 h scan a 15.5 ± 0.10 Gy entrance dose may seem high (~2.5 times greater than the optimal 2.68 h scan; Fig. 3), it is still at least 13 times less than the required dose for insect sterilization[3]. Moreover, after longer scans, the insects took longer (> 90 min) to fully recover post-anesthetic.

Conclusions. Live CO_2-anaesthetized insect imaging is feasible using micro-CT. This cost-effective and accessible method (as compared to synchrotron beams) enables routine scanning of live insects to extract biologically relevant information in any time-course study on the same individuals in insect development, parasitology, forensic and medical entomology.

References. [1]Nicolas and Sillans 1989 Annual Review of Entomology 34:97-116. [2]Badre *et al.* 2005 Comparative Biochemistry and Physiology Part A 140: 363-376. [3]Bakri *et al.* 2005. In: V.A. Dyck; J. Hendrichs & A.S. Robinson, (Eds.), 233-269, Springer.[4]Cheng *et al.* 2009 Mutagenesis 24:259-269.

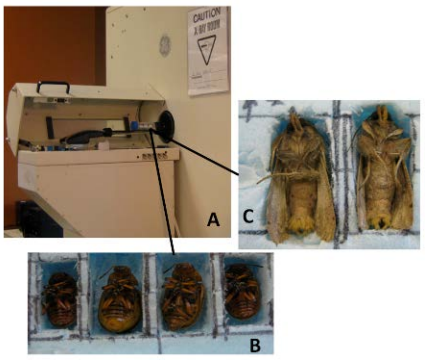

Fig. 1: Set-up for insect live scan(A). Anesthetized *L. decemlineata* (B), and *P. unipuncta* (C) adults.

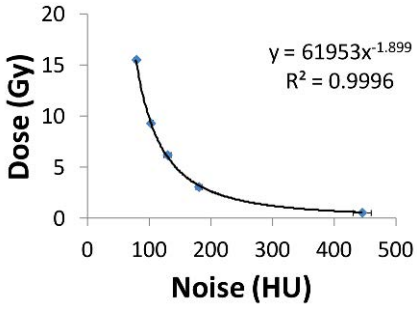

Fig. 2:Dose-noise relationship. Points represent mean±SD.

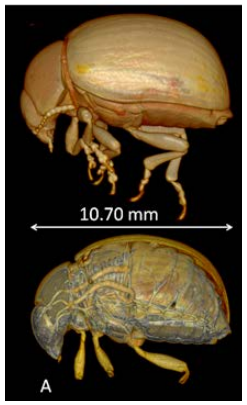

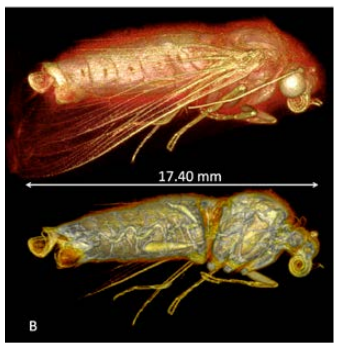

Fig. 3: 3D reconstruction of live anesthetized 1-wk-old *L. decemlineata* (A; 6.53 h scan), and 1-d-old *P. unipuncta* (B; 2.68 h scan) at 20 µm isotropic resolution depecting the tracheal system.

Anatomical, Functional and Metabolic MRI of Lung Injury using Hyperpolarized Nuclei

Giles Santyr

Peter Gilgan Centre for Research & Learning, Hospital for Sick Children, Toronto, Ontario, Canada.

Imaging Research Laboratories, Robarts Research Institute, Western University, London, Ontario, Canada.

With the advent of hyperpolarized nuclei, namely 129Xe and 13C, Magnetic Resonance Imaging (MRI) has the ability to measure anatomical, functional and metabolic changes in the lung not previously possible. For example, gas exchange and metabolic changes associated with inflammation may be reflected by changes in 129Xe tissue signal and 13C lactate-to-pyruvate signal ratio respectively in rodent models of lung injury. These imaging biomarkers are seen to correlate well with blood gas analysis as well as tissue morphology and cell counting approaches based on histology. In this presentation, hyperpolarized MRI methods are introduced and the application of these approaches to early detection of radiation-induced lung injury (RILI) is described. The translation of these approaches to human applications is also discussed.

Magnetic resonance imaging of growth restricted fetal guinea pigs due to placental insufficiency

Kevin J Sinclair[*,1], Lanette J Friesen–Waldner[1], Colin M McCurdy[1], Curtis N Wiens[2], Trevor P Wade[1,3], Barbra de Vrijer[4], Timothy RH Regnault[4,5], Charles A McKenzie[1,3]
Ontario Pre-Clinical Imaging Consortium
[1]Medical Biophysics, Western University, London, Ontario, Canada, [2]Radiology, University of Wisconsin, Madison, Wisconsin, United States, [3]Robarts Research Institute, Western University, London, Ontario, Canada, [4]Obstetrics and Gynaecology, Western University, London, Ontario, Canada, [5]Physiology and Pharmacology, Western University, London, Ontario, Canada

Introduction: Intrauterine growth restricted (IUGR) fetuses are at an increased risk for later life metabolic and cardiovascular disease. IUGR caused by placental insufficiency reduces nutrient and oxygen transport to the developing fetus. Brain growth is often prioritized at the expense of abdominal organs and muscle tissue, leading to asymmetrical growth restriction. Adaptations to this suboptimal *in utero* environment, such as altered fat storage, can persist into postnatal life, setting up the offspring for later life disease. MRI is a useful tool for studying fetal anatomy due to its excellent soft tissue contrast. It is especially useful in studying fat deposition as its ability to separate water from fat signals allows for analysis of adipose tissue volumes as well as organ fat content. Thus, we sought to utilize MRI to observe developmental abnormalities such as asymmetrical growth and altered fat deposition *in utero*.

Methods: Pregnant guinea pigs were anaesthetized and scanned ~60 days into an ~68 day gestation. Two maternal groups were scanned: a uterine artery ablation group (N = 7, 24 pups) and a Sham Control group (N = 3, 13 pups). T_1- and T_2-weighted images were acquired with voxel dimensions = 0.875x0.875x0.9mm^3 for both acquisitions. IDEAL water-fat images were also collected for each guinea pig with voxel dimensions = 0.933x0.933x0.9 mm^3. The T_1- and T_2-weighted images (Figure 1a,b) were used to segment fetal liver, brain, and total fetal volumes. IDEAL fat-only images (Figure 1c) were used to segment total and visceral fetal adipose volumes. Proton density fat fraction maps (Figure 1d) were used to obtain liver fat fractions.

Results: To represent 25% of the study population, IUGR was defined as having a brain to liver volume ratio above 0.80. Thus, the study population consisted of 8 IUGR and 28 normal pups. Expressed as a percent of fetal volume, IUGR fetuses had significantly smaller livers (5.3±0.8% vs 6.3±1.1%, p=0.03) but larger brains (4.7±0.8% vs 3.6±0.5%, p<0.001) than the normal group. IUGR fetuses had less total adipose tissue as a percent of fetal volume than normals (9.0±3.9% vs 13.6±4.0%, p=0.04), but no difference was seen in the proportion of adipose tissue deposited in visceral depots (p=0.99). Furthermore, liver fat fraction was not significantly different between groups (22±9% vs 23±5%, p=0.66).

Conclusions: We have demonstrated the use of MRI for detecting developmental differences in IUGR fetuses in guinea pigs *in utero*. Future studies relating the differences seen *in utero* to those seen after birth, as well as translation to human imaging, are possible.

Acknowledgements: GE Healthcare, NSERC, CIHR, ORF and the Canada Research Chairs Program.

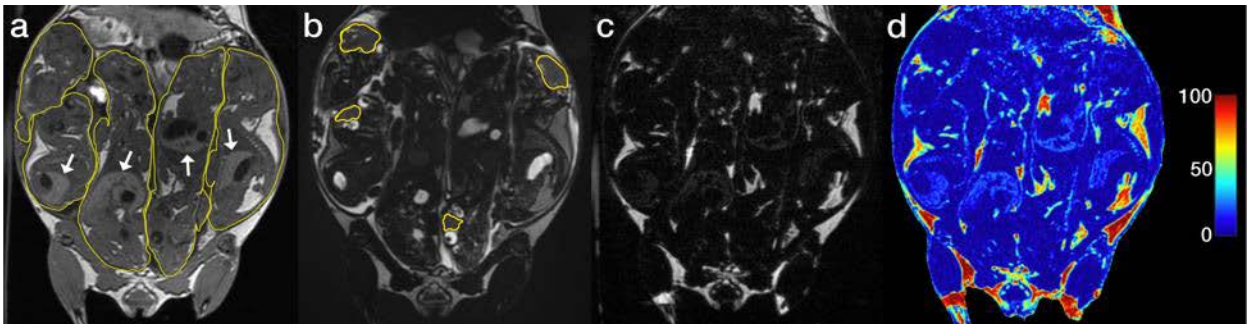

Figure 1: Coronal T_1- (a), T_2-weighted (b), IDEAL fat-only (c), and IDEAL fat fraction (d) images of a pregnant guinea pig that had undergone ablation of the uterine arteries to promote IUGR. Fetuses are contoured in yellow in (a) and fetal livers are denoted by white arrows. Fetal brains are contoured in yellow in (b). Images have been cropped to highlight fetuses only.

The study of scattering cross section of light in metallic nano-hole structures

Mahi R. Singh[1], M. Najiminaini[2,3], Shankar Balakrishnan[1,2] and J. J. L. Carson[2,3]
[1] *Department of Physics and Astronomy, The University of Western Ontario, London N6A 3K7, Canada*
[2] *Lawson Health Research Institute, 268 Grosvenor Street, London N6A 4V2, Canada*
[3] *Department of Medical Biophysics, The University of Western Ontario, London N6A 3K7, Canada and*
(corresponding author: Mahi R. Singh, msingh@uwo.ca)

Introduction: There is an interest to study the optical properties of metallic nano-hole structures experimentally and theoretically. They provide new and simple way to excite SPPs at perpendicular incidence without varying the angle of the incident beam. These structures transmit more radiation than that of incident light due to the presence of SPPs in these structures. Recently it has been found that metallic nano-hole structures are now considered as new plasmonic metamaterials.

Theoretical Formulations: The theory of the scattering cross section of light from the nano-hole structure ,using the quantum scattering theory and Green's function method, is expressed as

$$\left.\frac{d\sigma}{d\Omega}\right|_{spp} = \sum_n \frac{4\pi \mathbf{d}_n^2 \rho_{spp}\left(\varepsilon_n^{sp}\right)}{\epsilon_0 \hbar}\left(\frac{\Gamma_n}{\left(\varepsilon_p - \varepsilon_n^{sp}\right)^2 + \Gamma_n^2}\right) \tag{6}$$

Results and Discussion: Experimental parameters for the nano-hole structure are given as $r_r = 60nm$, $a_p = 400nm$ and $l_r = 100nm$. The results are plotted in fig.1. The circle denoted the experimental points and the solid curve represents theoretical results. The first two peaks correspond to n=0 and n=1 SPP modes. The first peak is located at SPP energy $\varepsilon_0^{sp} = 1.8eV$ and the second peak is found at SPP energy $\varepsilon_1^{sp} = 2.25eV$. The third peak is located at $\varepsilon_{pl} = 2.45eV$ and it corresponds to the bulk plasmon of the nano-hole structure. It is because of the decay rate (Γ_p) of plasmons due to the plasmon-phonon scattering in metals.

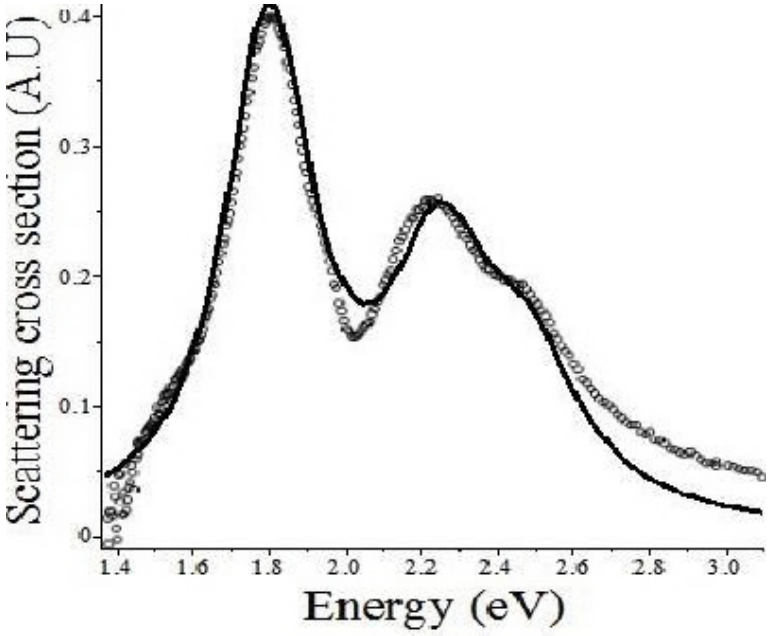

Fig. 1 The scattering cross section in arbitrary units (A.U) is plotted as a function of energy (eV). The third hidden peak is for the bulk plasmon located at 2.45 eV.

Conclusions: We have investigated theoretically and experimentally the scattering cross section of light through metallic nano-hole structures. Transmission through the nano-hole structure is measured by varying the radius of nano-holes and also by modifying the periodicity of the nano-hole structure. The dispersion relation and effective dielectric constant are calculated by using the TL theory. We have found that the energies of SPPs are quantized and systems can have several SPPs depending on the radius and periodicity of the structures. It is proposed that these systems can be used as sensors and switches for medical and engineering applications.

Preclinical microPET assessment of an In-Vivo Imaging Contrast Agent Targeting Cathepsin D in Alzheimer's disease mouse models.

Jonatan A. Snir[1,2], Mojmir Suchy[2,3], Geron A. Bindseil[4], Blaine A. Chronik[4], Robert H.E. Hudson[3], Stephen H. Pasternak[5,6] and Robert Bartha [1,2]

[1]Department of Medical Biophysics, University of Western Ontario, London, Ontario, Canada,
[2]Centre for Functional and Metabolic Mapping, Robarts Research Institute, University of Western Ontario, London, Ontario, Canada,
[3]Department of Chemistry, University of Western Ontario, London, Ontario, Canada,
[4]Department of Physics and Astronomy, University of Western Ontario, London, Canada
[5]J. Allyn Taylor Centre for Cell Biology, Molecular Brain Research Group, Robarts Research Institute, University of Western Ontario, London, Ontario, Canada,
[6]Department of Clinical Neurological Sciences, Schulich School of Medicine, University of Western Ontario, London, Ontario, Canada

Introduction: Early detection of Alzheimer's disease pathology is a serious challenge for both diagnosis and experimental therapy testing. Cathepsin D (CatD), a lysosomal aspartyl protease has been shown to be over-expressed in AD pathology and therefore may be used as a potential biomarker. A major obstacle for the delivery of drugs and contrast agents (CA) to the brain is the Blood Brain Barrier (BBB). To overcome the BBB, Cell Penetrating Peptides (CPP), which have been shown to enter and exit cells with ease and deliver cargoes of a variety of sizes into cells, have been suggested as delivery vehicles. Previously, we developed a cell-penetrating fluorescence probe based on a reduced kinetics strategy to detect Alzheimer's disease-associated protease activity in-vitro. We have shown the CA to be non-toxic, preferentially taken up by CatD over-expressing cells and able to transverse across the BBB according to in-vitro and ex-vivo confocal microscopy measurements. A modified version of the CA that fluoresced in the Near Infrared region (to reduce auto fluorescence and increase tissue penetration) demonstrated significant differences in-vivo in the washout kinetics of the probe in 5 and 12 months old transgenic (Tg) AD mice compared to age matched wild type (WT) controls. Herein, we present our findings of a third generation CA labeled with ^{68}Ga isotope. This minor modification produced a probe that allowed us to further study CA uptake and retention in different organs longitudinally using dynamic micro Positron Emisstion Tomography (microPET) imaging. **Methods:** The probe developed consists of a CPP HIV-1 Tat peptide conjugated to a CatD cleavage sequence that was flanked by a green fluorescent dye and a DOTA conjugate chelating Gadolinium. Once exposed to CatD, the recognition sequence becomes cleaved, resulting in separation of the CPP from the imaging probe. For this study, 8 mice (5XFAD Tg AD model mice and non-Tg age matched littermates) were administered with our CatD targeted CPP agent at 2, 4.5 months of age and scanned using the Siemens Inveon dedicated microPET scanner. All mice were scanned under isofluorane anesthesia after an intravenous tail vein CA injection of ~12 MBq suspended in ~200 μL saline adjusted to pH~7. Reconstructed images were used to measure the uptake and washout of the CA in the brain, liver, kidneys and bladder. **Results:** The Tg mice demonstrated significantly greater rate of uptake ($p<0.05$) of the CA in the brain in the first two hours following injection at 4.5 months but not 2 months of age compared to controls. No differences in uptake were observed in other organs. **Conclusions:** This preliminary work further supports the capacity of this CA to help differentiate between AD mice and controls.

Feasibility of Arterial Spin Labeling for Detection of Low Frequency Activation

Tracy Ssali*[1,2], Udunna Anazodo[1,2],, Yves Bureau[1,2], John Butler[1], Matthias Günther[3], and Keith St Lawrence[1,2]
[1]Laswon Health Research Institute, London, Ontario, Canada, [2]University of Western Ontario, London, Ontario, Canada, [3]Fraunhofer Institute for Medical Image Computing MEVIS, Bremen, Germany

Introduction: The ability of arterial spin labeling (ASL) to measure cerebral blood flow (CBF) independent of task frequency makes it attractive for longitudinal studies to study changes in brain function, particularly in chronic pain[1–3]. However, ASL's poor spatial resolution makes image alignment between separate sessions difficult. The resulting registration errors can reduce sensitivity by increasing variance and potentially lead to greater Type I errors. Additionally, variations in basal CBF due to physiological and transient effects (ex. arousal, mood, and caffeine-intake) can further reduce reproducibility over longer periods of time[4]. The aim of this study was to quantify between-session variance and demonstrate that with the appropriate steps, ASL has the sensitivity to detect activation-induced changes in regional CBF over periods extending up to a month.

Methods: Seven right-handed volunteers (22.7 ± 1.3 years, 2 male) were scanned during three sessions separated by a week (7.0 ± 0.5 days) and a month (28.9 ± 2.5 days). Imaging was performed on the Siemens 3.0T Biograph system. To minimize registration errors between-session, immobilization head molds were created for each subject during the first session and reused in the following sessions to replicate head position. Each session consisted of two 6-min sets of rest and sequential finger tapping tasks, during which ASL images were continuously acquired (48 images per task). Variability and reproducibility of baseline CBF (within and between-session) were assessed using within-session coefficient of variance (wsCV) and intra-class correlation coefficient (ICC). Image analysis software, SPM8, was used to generate statistical parametric maps (a) using rest and task data from the same session and (b) using data from different sessions (i.e. task and rest periods separated by a week and a month). To remove the variability in basal CBF, data were scaled by their respective resting gray matter CBF. Areas of activation were identified after correction for multiple comparisons using the family wise error rate ($p < 0.05$).

Results: Within and between-session resting gray matter CBF had reproducibility: ICC = 0.863 and 0.625 and variability: wsCV = 9.07% and 10.04% respectively (Fig 1,i). After intensity normalization ICC within and between session increased to 0.873 and 0.781 and wsCV decreased to 4.71% and 5.74% respectively (Fig 1,ii). Absolute and normalized gray matter CBF activation maps from within and between-session analyses are shown in Figure 2.

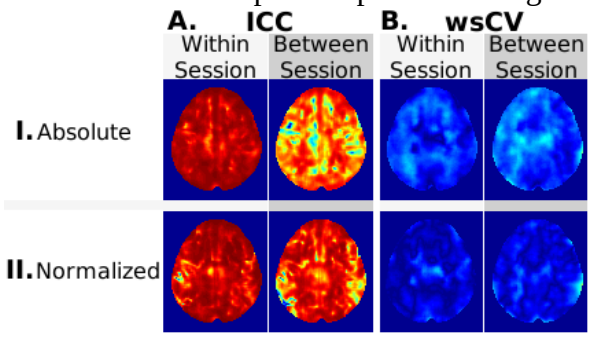

Figure 1: Within and between session (a) reliability and (b) variance in (i) absolute CBF and (ii) CBF normalized by resting grey matter flow.

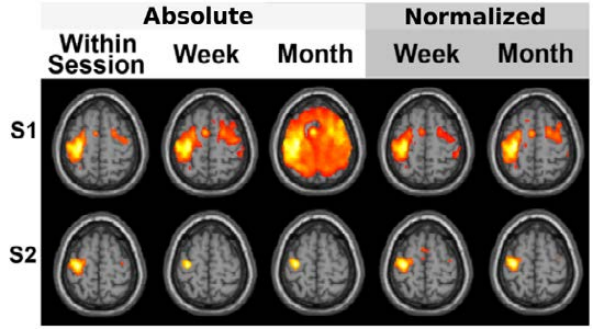

Figure 2: Within and between-session motor activation with absolute and normalized CBF

Discussion and Conclusion: Variance and reproducibility values were similar to other ASL studies[4,7]. Spatial representation of wsCV (Fig. 1b) shows some regional heterogeneity, but only a marginal increase when compared to the between-session images. This is reflected in the comparison of activation maps generated from rest and activation images from the same session and maps generated from rest and activation images from separate days (Fig. 2). The remarkable similarity in the maps after removing the effects of variations in resting CBF indicates that registration errors between sessions were minimal. This is also visible in the improved ICC after normalization (Fig. 1a). These results demonstrate the feasibility of conducting voxel-wise analysis of CBF images acquired on different days (in this case, up to a month apart) and highlight the potential of this technique for longitudinal studies. Future work will be to repeat the comparison with a functional task, such as experimental pain, that contains activation in multiple brain regions.

References:[1] Borogovac et al. *J. Cereb. Blood Flow Metab.* 2010; 30, 1721–33. [2] Detre, et al. *J. Radiol.*1999; 30,115–24. [3] Owen, D et. al. *Pain.* 2010; 148, 375–86. [4] Chen et al. *J. Magn. Reson. Imaging.* 2011; 33, 940–9 [5] Günther et al. *Magn. Reson.Med.* 2005; 54, 491–8. [6] Wang, Z. et al., *Magn. Reson. Imaging.* 2009. 26, 261–269, [7] Mezue et al. *J. Cereb. Blood Flow Metab.* 2014; 163, 1-9

A production method of customized in-bore epoxy resin filters for gantry-based micro-CT scanners

Justin J Tse*[a,b], Joy Dunmore-Buyze[a], Maria Drangova[a,b], and David W Holdsworth[a,b]
Ontario Pre-Clinical Imaging Consortium
[a]Imaging Research Laboratories, Robarts Research Institute, University of Western Ontario, London, Ontario, Canada. [b]Department of Medical Biophysics, University of Western Ontario, London, Ontario, Canada

Introduction: The ability to tailor output x-ray spectra of micro-computed tomography (micro-CT) machines allows one to visually isolate chemically similar structures, from within a sample, using dual-energy computed-tomography (DECT). For low-contrast objects, such as blood vessels, an exogenous contrast agent is still required. High-Z elements can provide sufficient contrast to make these structures visible, but require proper x-ray filtration through custom and expensive. We present a method for the production of custom sized and composition in-bore x-ray filters for gantry-based micro-CT machines. This will allow users to tailor the output x-ray spectrum without opening or modifying their CT machine.

Methods: A master Al filter was machined to act as a positive for a silicone mold. A mixture of resin with a homogeneous distribution of Er_2O_3 nanoparticles was poured into the resulting negative silicone mold.

Results: The results of our custom filter making process are presented in Fig. 1, including our master Al filter, Er-embedded resin filter, and Cu filter. The results of their implementations in DECT are demonstrated in Fig. 2. One can observe the minimal differences between a low and high energy scans; however, after the application of decomposition algorithms, separate and distinct images of bone and perfused vasculature can be visualized. The interplay between the vasculature and bone can be further observed in Fig. 2A and 2B, with 3D renderings of perfused vasculature in red and bone in white.

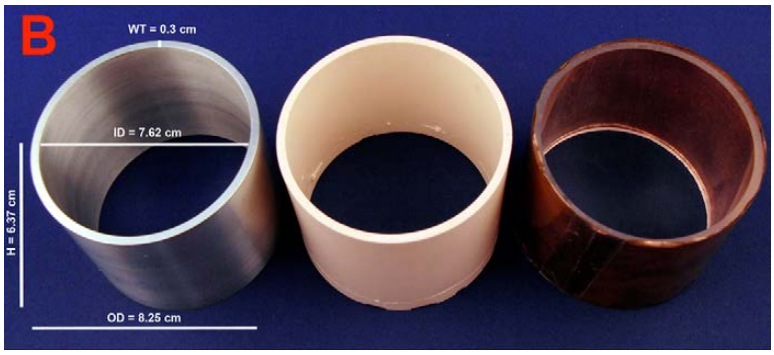

Fig. 1. (Left) Master Al filter with its outlined dimensions. (Middle) Custom casted Er-based filter for our low energy scans. (Right) A Cu filter used for our high-energy scans.

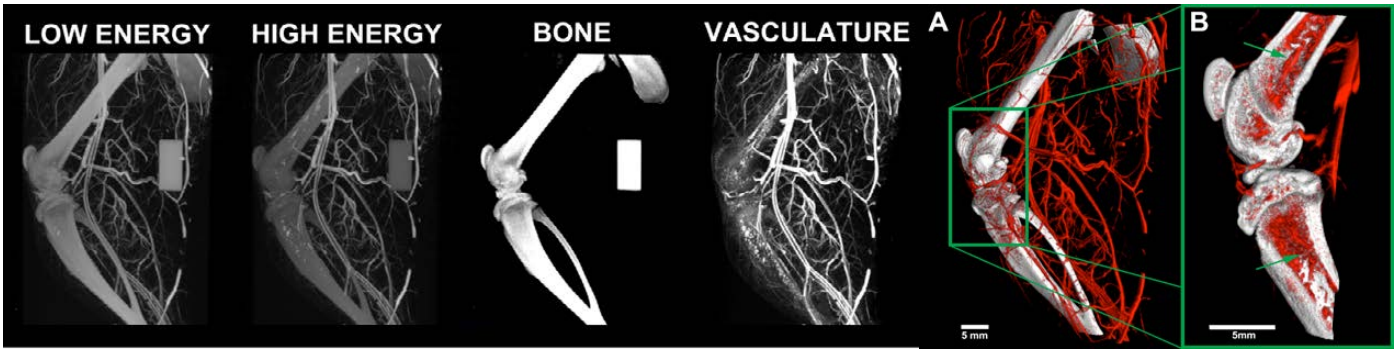

Fig. 2. Results of DECT, dual-energy images decomposed into their respective perfused vasculature and bone images. (A) 3D visualization of the interaction between vasculature (red) and bone (white). (B) Slice through the area outlined by the green box in (A), demonstrating the highly vascularized interior of the bone.

Conclusion: The results of the dual-energy decomposition demonstrate our method's success in the homogeneous incorporation of Er_2O_3 powder into a resin, to produce a functional in-bore x-ray filter for gantry-based micro-CT machines. With our custom filter we were able to decompose a rat hindlimb, perfused with our own custom Er-based vascular perfusion contrast agent, into a separate image of the perfused vasculature and its surrounding skeletal structure. With this technique, researchers that are interested in performing DECT on other elemental compositions are able to construct the needed custom filters without buying expensive foils and/or opening or modifying the CT machine.

The Determination of the Relationship Between Mouse Visceral Adipose Tissue and Whole-Body Adipose Tissue Using Micro-Computed Tomography

Joseph U. Umoh[1], A. Burke[2], E. Turley[2], C. Norley[1], S. Pollmann[1], J. Dunmore-Buyze[1], M. Drangova [1,3], M. Huff[2], and D.W. Holdsworth[1,3]
Ontario Pre-Clinical Imaging Consortium
[1]Preclinical Imaging Research Centre, Robarts Research Institute, [2]Dept. of Medicine and Biochemistry, [3]Depts. of Medical Biophysics and Surgery, Western University, London, ON, Canada

Introduction: Adipose tissue stores energy and provides insulation for some organs. However, the accumulation of excess visceral adipose tissue is linked to different risks of obesity or diabetes. Research interest in adipose tissue is growing not only because investigators are seeking solutions to the problem of obesity but also because of the realization that adipose tissue in human is a potential reservoir of adult stem cells (1), which could be used in tissue repairs and engineering. In this study, the volume and mass of visceral adipose tissue (VAT) in the abdominal cavity as well as the volume and mass of the whole-body adipose tissue (WAT) were computed. The computation of VAT involves more processing time. The objective of this study was to determine an empirical relationship between the mass of VAT and that of WAT in a mouse model, which will enable the former to be estimated from the latter.

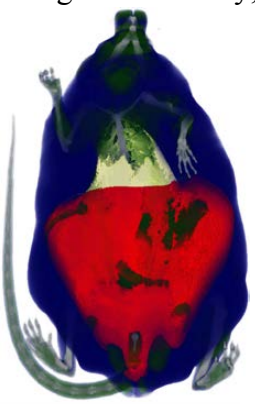

Figure 1: Micro-CT image of a whole mouse showing the volume of the visceral adipose tissue (red).

Methods: A diverse population of 61 mice was used in this study. The group consisted of males and females; wild-types and knockouts; high-fat-diet-fed mice and normal-diet-fed mice; mice of age from 2 weeks to 88 weeks; and with weight from 2 g to 54 g. The animals were imaged using a *GE Locus Ultra* micro-CT scanner, with the same scan protocol and reconstruction parameters: x-ray tube voltage 80 kV, tube current 55 mA, 1000 projections, exposure time 16 s, and 154 μm 3D image voxels. Using the 3D micro-CT images, the abdominal cavity was segmented out for each mouse. Lower and upper image threshold values of the adipose tissue were determined from the histogram plots of the whole mouse image values. A software program was written to compute the volume and mass of the adipose tissue. Volume was calculated using pixel values between the two thresholds; and mass was calculated by multiplying the volume by a pre-determined density (0.90 g cm^{-3}) for adipose tissue. Using the image of the whole-body mouse, the program computed the mass of WAT. Similarly, using the segmented image of the abdominal cavity, the program computed the mass of VAT (Fig. 1). A linear regression analysis was performed between VAT and WAT to determine the relationship between the two.

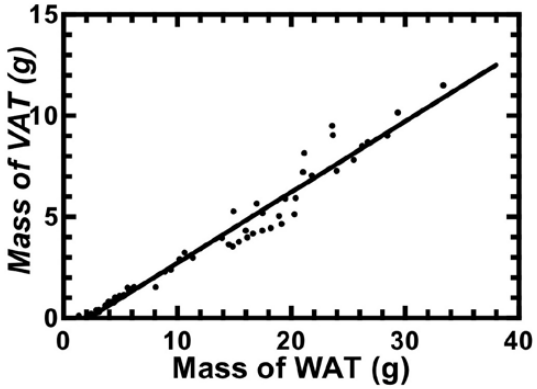

Figure 2: Plot of the mass of mouse whole-body adipose tissue (WAT) against the mass of the visceral adipose tissue (VAT) showing the linear regression line.

Results: Image values corresponding to adipose tissue were between -30 HU and -380 HU. A linear regression model between VAT (V) and WAT (W) showed (Fig. 2) that the two quantities could be expressed as $V = a\,W - b$ where $a = 0.35 \pm 0.01$ and $b = 0.77 \pm 0.04$ ($r^2 = 0.96$, $p<0.0001$). The root-mean-square error between the model and observations was 0.6 g.

Conclusions: This study has determined, for the first time, a strong correlation between the mouse visceral adipose tissue and the whole-body adipose tissue. Knowing the mass of a whole-body adipose tissue (which is more readily computed using threshold segmentation method), this relationship could be used to predict the mass of visceral adipose tissue.

References: [1] Zuk *et al.* Molecular Biology of the Cell 2002; 13: 4279-4295.

New Approaches for Functionalizing and Targeting Ultrasound Microbubbles

John Valliant, PhD, McMaster University

A new approach to developing molecular imaging probes using bioorthogonal chemistry will be presented. Notably, the rapid and highly selective coupling between transcyclooctene and tetrazines was used to develop targeted microbubbles for molecular imaging applications using ultrasound and radiopharmaceuticals for nuclear imaging. This collaborative research spans new synthesis and radiochemistry through in vitro and in vivo validation studies using a number of different oncologic biomarkers. The new targeting and bioconjugation strategies have applications beyond ultrasound and nuclear medicine imaging which will also be discussed during the presentation.

The effect of matching layers as an acoustic lens in a staring transducer array in photoacoustic imaging

Madeleine Van de Kleut[a,b], Philip Wong[a,b], Avery Raess[a,b], Ivan Kosik[a,b], and Jeffrey J.L. Carson[a,b]
[a]Imaging Program, Lawson Health Research Institute, London, ON, Canada
[b] Medical Biophysics, Schulich School of Medicine and Dentistry, University of Western Ontario, London, ON, Canada
(Corresponding author: Jeffrey J.L. Carson, jcarson@lawsonimaging.ca)
Ontario Pre-Clinical Imaging Consortium

Introduction: Photoacoustic imaging utilizes transducers to acquire acoustic waves generated by thermoelastic effects inside tissue due to absorption of light. Matching layers are often applied to each transducer face with the purpose of minimizing acoustic attenuation, in addition to acoustic impedance matching between the coupling medium and the transducer element. Application of a convex epoxy matching layer to the face of individual transducers is proposed to increase the acoustic angular acceptance in comparison to flat-faced counterparts (Figure 1). When incorporated into an array, the increased angular acceptance of each transducer should result in an increase in the field of view of the photoacoustic imaging system. The objective of this work was to compare flat-faced and convex epoxy-coated transducers using simulation and experiment.

Method: Flat and convex epoxy matching layers were applied to transducers by hand. Each transducer was comprised of a disc-shaped 3-mm diameter piezoelectric element. The angular acceptance of each transducer was measured by scanning a photoacoustic point source located 3 cm from the face of the transducer at angles with respect to the normal to the piezoelectric element ranging from ±80°. Signal intensity recorded on the transducer was plotted as a function of angle, and the response of each transducer to a photoacoustic point source was simulated using a model that incorporated the angular acceptance of the transducer. These responses were then aggregated into an imaging operator (IO). Experimental IOs were computed using the measured response to each transducer. Sensitivity maps for the simulated and experimental response were obtained by computing the cross-talk matrix of each IO, respectively.

Results: The sensitivity of the system was quantified using the full width at half maximum as a function of signal intensity through three orthogonal planes. Simulated responses gave an average of 5.7 mm and 20.3 mm for flat and convex matching layers, respectively, whereas the experimental results gave average values of 5.9 mm and 14.2 mm, respectively.

Discussion and Conclusion: Application of a convex matching layer to the transducer face results in an effective increase in the field of view of the array of approximately three times compared to that of an array with transducers having flat matching layers. The simulated response is in close agreement with the experimental data for the flat matching layer case, although the sensitivity is less uniform compared to the convex case, as shown in the sensitivity maps (Figure 2). Convex matching layers increase the angular acceptance of the transducers, increasing the imaging volume.

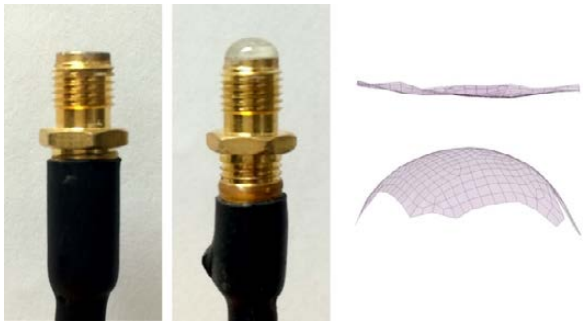

Figure 1 showing transducers with flat and convex matching layers and their respective 3D renderings.

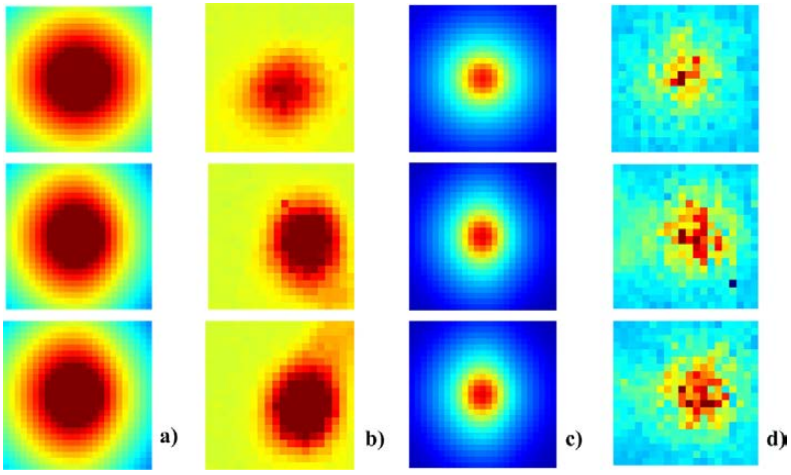

Figure 2 showing sensitivity maps computed from the diagonal of the cross-talk matrix for **a)** simulated convex matching layer, **b)** experimental convex matching layer, **c)** simulated flat matching layer, and **d)** experimental flat matching layer.

Objective Assessment and Design Improvement of a Staring, Sparse Transducer Array by the Spatial Crosstalk Matrix for 3D Photoacoustic Tomography

Philip Wong[a, b,*], Ivan Kosik[a, b], Avery Raess[a, b], and Jeffrey J.L. Carson[a, b]
Ontario Pre-Clinical Imaging Consortium
[a]Imaging Program, Lawson Health Research Institute, London, ON, Canada
[b]Schulich School of Medicine and Dentistry, University of Western Ontario, London, ON, Canada

Introduction: Accurate reconstruction of 3D photoacoustic (PA) images requires detection of photoacoustic signals from many angles. Several groups have adopted staring ultrasound arrays, but assessment of array performance has been limited. We previously reported on a method to calibrate a 3D PA tomography (PAT) staring array system and analyze system performance using singular value decomposition (SVD). The developed SVD metric, however, was impractical for large system matrices, which are typical of 3D PAT problems. The present study consisted of two main objectives. The first objective aimed to introduce the crosstalk matrix concept to the field of PAT for system design. The second objective aimed to utilize the figures-of-merit to characterize and improve the performance of a near-spherical staring array design.

Method: Figures-of-merit (FoM) utilized in this study were root mean square error, peak signal-to-noise ratio, mean absolute error, and a three dimensional structural similarity index, which were derived between the normalized spatial crosstalk matrix and the identity matrix. The applicability of this approach for 3D PAT was validated by observing the response of the FoM in relation to well-understood PAT sampling characteristics (i.e. spatial and temporal sampling rate). Staring array design parameters (transducer arrangement, array radius, and array angular coverage) were then examined in a simulation study.

Results: The top row of Fig. 1 shows the sensitivity maps (i.e. diagonal elements of the crosstalk matrix) for 3 planes of our 3D PAT system. The region with highest system sensitivity occurred near the center of the array and decreased with distance from the center. Improved system performance near the center was also reflected in the aliasing maps (i.e. off-diagonal elements of the crosstalk matrix) where there was reduced aliasing for the center voxel and increased aliasing for an edge voxel in the same plane (middle and bottom rows in Fig. 1). The measured FoM scores improved as a function of spatial and sampling rate and optimal values for the three staring array design parameters were found.

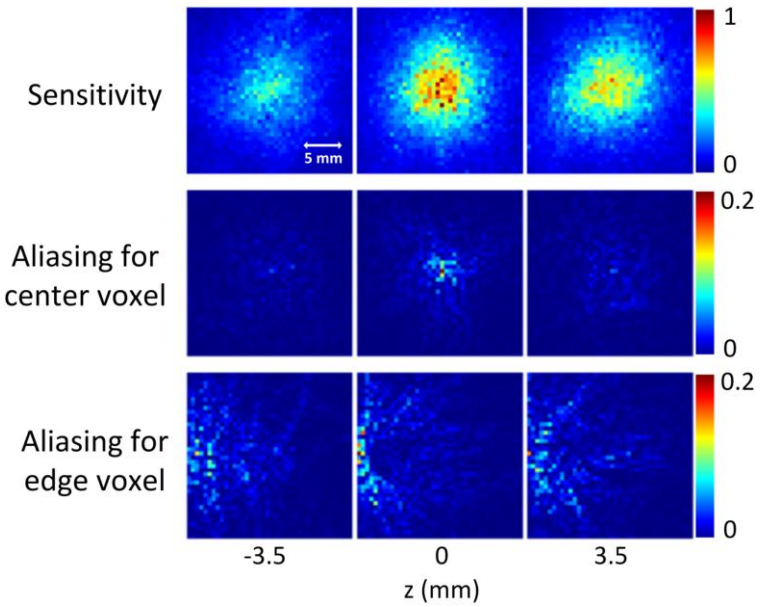

Figure 1. Top row: Normalized 3D PAT system sensitivity maps of the xy-plane 3.5 mm below center (left column), center plane (middle column), and xy-plane 3.5 mm above center (right column). Middle row: Aliasing maps for the center voxel. Bottom row: Aliasing for a voxel near the edge. Object space was 20 cm x 20 cm x 20 cm.

Discussion: We observed that the spatial crosstalk matrix qualitatively reflected changes in system performance. The spatial crosstalk matrix provided insight into the contribution from each voxel to the pressure data as well as how unique each voxel contribution was from the other voxels. These insights can be visualized as sensitivity and aliasing maps as shown in Fig. 1. The changes were quantified using the FoM with respect to an ideal system response. The design and performance of a 129-element staring transducer array for 3D PAT was studied and the results suggested that the developed formulation would enable the development of efficient strategies for future system design optimization.

Conclusion: Four FoM from the spatial crosstalk matrix were introduced as a tool to objectively assess 3D PAT system design. The FoM were applied to study the staring array design of a 129-element 3D PAT system. The transducer arrangement, array radius, and array angular coverage were studied and improved values were found.

Effect of Gas Phase Replenishment on Dissolved Phase Hyperpolarized ^{129}Xe MRI

Brandon Zanette[1,2], Ozkan Doganay[3,4], Elaine Hegarty[1,3], Giles Santyr[1,2,3,4]

1. Peter Gilgan Centre for Research and Learning, The Hospital for Sick Children, Toronto, ON, Canada. 2. Department of Medical Biophysics, University of Toronto, Toronto, ON, Canada. 3. Imaging Research Laboratories, Robarts Research Institute, London, ON, Canada. 4. Department of Medical Biophysics, University of Western Ontario, ON, Canada.

Introduction: Magnetic Resonance Imaging (MRI) using hyperpolarized ^{129}Xe has emerged as a promising tool for the quantification of gas exchange between airspaces and dissolved phases of xenon, specifically lung tissue (T) and red blood cells (RBC), by exploiting chemical shift differences between each of these three compartments[1]. Differences in dissolved phase signals have been measured using whole-lung MR spectroscopy in models of lung injury, including Radiation-induced Lung Injury (RILI)[3]; however, imaging of the dissolved phases represents a significant challenge due to the small amount of ^{129}Xe that dissolves in lung tissue (~2%). One approach to increase dissolved signal is to selectively excite the dissolved phase, while the gas phase acts as a reservoir, leading to signal replenishment[2]. With appropriate choice of sequence repetition time (TR), optimization between signal accumulation and acquisition time may be achieved. Depending on disease model, choice of TR may act as a mechanism of contrast due to compartmental saturation of gas or attenuated gas transfer times. The purpose of this work was to explore the effect of TR on spectrally resolved regional dissolved phase (T and RBC) quantification in a RILI model involving irradiation of the right lung.

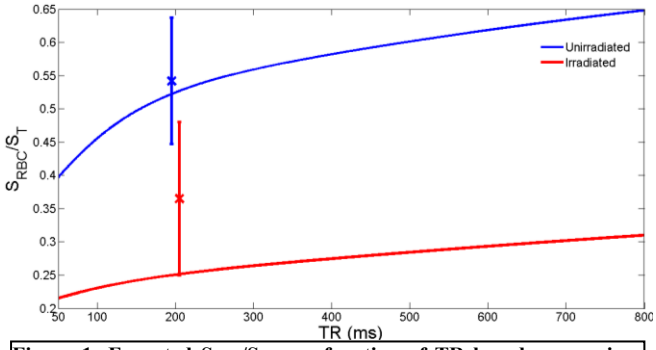

Figure 1: Expected S_{RBC}/S_T as a function of TR based on previous work[3]. Points at TR=200ms are mean ± sdev of S_{RBC}/S_T in the right

Methods: Sprague Dawley rats were used following Western AUC approved protocols. One cohort was irradiated with 18Gy to the right thorax and incubated for two weeks, while the other served as unirradiated controls. Chemical Shift Imaging (CSI) was used to obtain localized dissolved phase ^{129}Xe spectra in the coronal plane with a matrix size of 8×8, FOV=5×5cm^2, BW=±2.5kHz, with the RF transmit pulse centred at the tissue frequency. From previous whole-lung irradiation work[3], expected signal curves for T and RBC as a function of TR were calculated for healthy rats and irradiated rats. It was determined that TR=200ms would be sufficient enough for signal accumulation in the dissolved compartments and generate contrast between them, while maintaining an acceptable acquisition time. Spectra were reconstructed and processed as described in previous work[4]. Summed T and RBC signals (S_T and S_{RBC}, respectively) were acquired for the right and left lungs for each rat. S_{RBC}/S_T was computed in individual lungs for each rat, and then the ratio of right to left S_{RBC}/S_T (R/L) was taken as a measure of regional lung injury. The lungs were then removed, fixed, and stained for histological analysis.

Results: Eight rats were analyzed (three irradiated, five unirradiated). Figure 1 shows experimentally measured S_{RBC}/S_T in the right lung at TR=200 ms as well as the expected curve based on whole lung irradiation. R/L was significantly different between the two rat cohorts (p=0.009) with mean values of 0.91±0.08 and 0.69±0.07 for the unirradiated and irradiated cohorts, respectively. Unirradiated and irradiated individual lung S_{RBC}/S_T showed less significance in the left lung (p=0.056) versus the right lung (p=0.019), while whole lung S_{RBC}/S_T was intermediate (p=0.022). These were consistent with increases in lung tissue area measured by histology.

Discussion: Dissolved phase ^{129}Xe S_{RBC}/S_T was able to distinguish irradiated rat lungs from unirradiated rat lungs at a TR of 200 ms which were largely consistent with expected values for the unirradiated rat cohort. For the irradiated rat cohort, measured S_{RBC}/S_T was ~50% higher compared to expectation based on whole-lung irradiation. This may be a result of reduced injury in this single-lung irradiation model of RILI, suggesting less inflammatory response due to the reduced radiation field. The R/L values in the irradiated cohort revealed greater asymmetry in S_{RBC}/S_T than present in the unirradiated cohort. We hypothesize that the combination of increased inflammation and direct vascular damage due to radiation contribute to asymmetric changes in R/L. The ability to resolve early regional changes associated with irradiation may be helpful for adjustment of the therapy plan to avoid RILI. In future, advanced techniques such as Dixon-based or Spectral-spatial techniques may permit mapping of gas exchange times as well as dissolved tissue signal changes in human lung injury.

References: 1. Sakai et al., J Magn. Reson. B. (1996). 2. Kaushik et al., J. Appl. Physiol. (2014). 3. Fox et al., Med. Phys. (2014). 4. Thind et al., Radiother. Oncol. (2014). **Acknowledgments:** The authors would like to thank the following sources of funding: The Hospital for Sick Children, CHIR, NSERC, and OPIC.

The Second Generation Gd-free Extracellular MRI Contrast Agents Based on Mn-Porphyrin

Yong Le Zhu,[a,b] Weiran Cheng,[a,b] Tameshwar Ganesh,[d,e] Taleen Karnieg,[b] Inga E. Haedicke,[a,b] Hai-Ling Margaret Cheng,[d,e, f, g] and Xiao-an Zhang[a,b,c]

[a]Department of Chemistry, University of Toronto,[b]Department of Physical and Environmental Sciences and [c]Department of Biological Sciences, University of Toronto Scarborough, [d]Department of Pharmaceutical Sciences, Leslie Dan Faculty of Pharmacy, University of Toronto, [e]Physiology & Experimental Medicine, Hospital for Sick Children, , [f]The Edward S. Rogers Sr. Department of Electrical & Computer Engineering, [g]The Institute of Biomaterials and Biomedical Engineering, University of Toronto, ON, Canada

Introduction. MRI is a non-invasive imaging modality that mainly relies on the ^{1}H-NMR signal of water in the body. Contrast agent (CA) can shorten the relaxation time of surrounding water protons, which enhances the sensitivity and tissue contrast. The contrast enhancement efficiency of a CA is termed as relaxivity. The non-selective extracellular fluid (ECF) agents based on Gd complexes dominate in clinical application. Despite their tremendous success in diagnostic medicine, Gd-based ECF agents have two limitations. First, the relaxivity of a typical Gd CA is relatively low and decreases gradually at high field, which constraints their future applications with high-field clinical scanners. Second, toxicity associated with free Gd arise as a major concern: in vivo Gd dissociation can cause a lethal adverse effect called Nephrogenic Systemic Fibrosis (NSF). To overcome these issues, our research group focuses on the development of Gd-free CAs based on water-soluble Mn(III)porphyrin (MnP). As a micronutrient, Mn ion is less toxic than Gd. Moreover, the high stabilities, unique electron relaxation properties, and backbone rigidity make MnP an ideal molecular platform to design Gd-free CAs with lower toxicity and higher relaxivity.[1,2] We have developed two novel MnPs, MnTCP and MnP2 (Fig. 1), based on two distinct objectives. MnTCP, a small and highly polar compound, was designed as an ECF agent with fast renal clearance.[3] MnP2, a dimeric porphyrin, was designed as a blood-pool agent with high relaxivity and long circulation time, due to non-covalent binding with serum albumin (SA).[2] For current study, our goal is to develop a 2nd generation ECF agent with higher relaxivity while maintaining the rapid renal clearance.

Methods. A novel MnTCP analog, MnTrCP2, was designed to improve the relaxivity as a dimeric MnP. By removal of bipenyl bridge as used in MnP2, it prevented the SA-binding and achieved fast clearance. MnTrCP2 was synthesized in an optimized protocol with 8 steps. The NMRD profile of MnTrCP2 was measured by a field cycling relaxometer up to 1 T and in vivo assessment was performed under a 3 T MRI scanner.

Results and Conclusion. At 1 T, higher relaxivity of MnTrCP2 ($12mM^{-1}s^{-1}$ per Mn) was obtained compared to monomeric MnTCP ($10mM^{-1}s^{-1}$ per Mn). In HSA binding studies, MnTrCP2 was found to have no HSA affinity using UV-Vis and CD spectroscopies. In conclusion, our results suggested that MnTrCP2 is an improved Gd-free ECF agent, compatible for high field application.

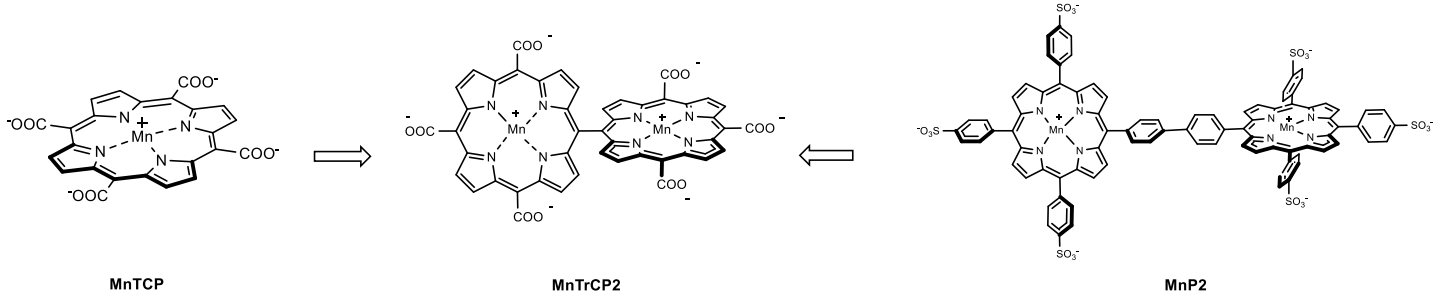

Figure 1: Scheme of Molecular Design of MnTrCP2 from MnTCP and MnP2

1. Koenig, S. H.; Brown, R. D., III.; Spiller, M. *Magn. Reson. Med.* **1987,** *4*, 252.
2. Cheng, W.; Haedicke, I. E.; Nofiele, J.; Martinez, F.; Beera, K.; Scholl, T. J.; Cheng, X. L.; Zhang, X. A. (2014) *J Med Chem.* **57**, (2), 516.
3. Nofiele, J. T.; Haedicke, I. E.; Zhu, Y. L.; Zhang, X. A.; Cheng, H. L. (2014) *J Magn Reson Imaging.* [Epub ahead of print]

Effective Systems for Procedure Specific Healthcare Simulation

Simulation

Oral Presentation and Poster Abstracts

Phantom Echogenicity and Ease-of-Segmentation: Effects on Ultrasound Calibration

Golafsoun Ameri*, John SH Baxter, Jonathan McLeod, Elvis CS Chen, and Terry M Peters
Robarts Research Institute, The University of Western Ontario, London, Ontario, Canada

Introduction: Many image-guided interventions are leaning towards the use of ultrasound as the sole or a complementary inter-operative imaging modality because of its capability to visualize tissues without direct line of sight[1]. One crucial element of the use of ultrasound imaging in these procedures, particular those that make use of tracking or augmented reality environments, is that of ultrasound calibration, which relates the location of structures on the ultrasound image to a common co-ordinate system with the ultrasound probe and any tracked surgical tools. Currently, the state-of-the-art in ultrasound segmentation uses dedicated calibration phantoms. However, there has yet to be a systematic evaluation of the materials used in said phantoms, and the effect this has on segmentation and the overall accuracy of ultrasound calibration.

Hypothesis: We hypothesize that larger phantoms with lower echogenicity will allow for easier automatic segmentation and as a result, lower calibration error.

Methods: Experiments were performed using the phantomless calibration approach[2], where a long, cylindrical object, normally a needle or other surgical tool, is used as a calibration phantom. Four experimental phantoms were used, two plastic straws of differing diameter, and two tubes with differing diameter made from polyvinyl alcohol cryogel (PVA-C) using one freeze-thaw cycle. An automatic segmentation algorithm was designed to segment the ultrasound images, and isotropic Procrustes analysis was used to determine the calibration transform.

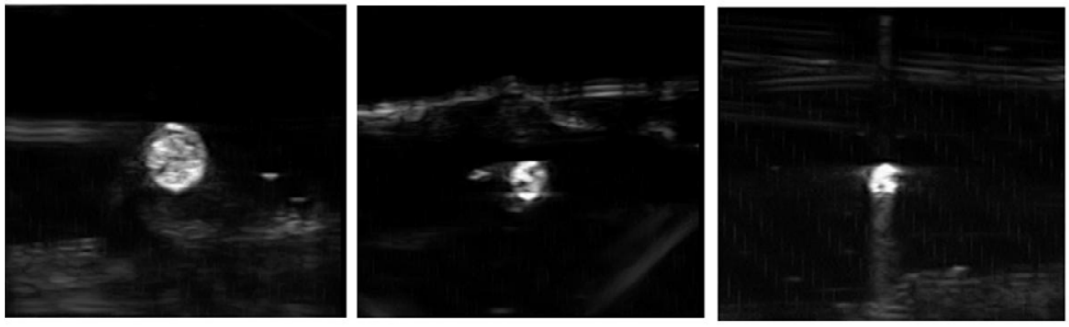

Large PVA rod | Small PVA rod | Surgical Needle

Results: Larger phantoms with lower echogenicity were indeed easier to segment automatically. Quantitative analyses concerning calibration accuracy is still in progress. If this analysis reports better calibration accuracy, it would have a profound effect on the design and evaluation of ultrasound calibration phantoms.

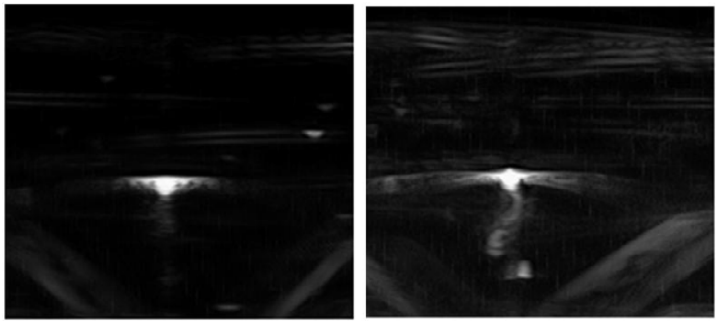

Trilene Fish Wire | Braid Fish Wire

References: [1] T. Peters and K. Cleary, Springer, 2008. [2] A. Khamene et al., MICCAI, 2005.

Optimal Supervised Parameter Selection in Continuous Max-Flow Image Segmentation

John SH Baxter*, Martin Rajchl, Jonathan McLeod, Jing Yuan, and Terry M Peters
Robarts Research Institute, The University of Western Ontario, London, Ontario, Canada

Introduction: As medical image segmentation algorithms become increasingly complex, they suffer increasingly from issues associated with initialization and parameterization. Global optimization based segmentation approaches such as discrete graph cuts and continuous max-flow have largely addressed the issue of initialization sensitivity. However, to incorporate them into more complex, multi-region image segmentation, many convex functionals are simultaneously weighted and employed.[1] The increasing number of these parameter necessitates a mathematically rigorous approach to weighting parameter selection. [2]

Methods: The context of this approach is supervised parameter selection, where a single gold standard labeling is provided to a parameter selection algorithm. The algorithm then solves an inverse problem, finding the weighting parameters which imply the global optimality of the provided gold standard in the context of the unweighted convex functionals in the segmentation algorithm.

The algorithm maintains an 'estimate set' of possible optimal weighting parameters. At each iteration, it prunes this set by generating a competing 'optimal' segmentation. By ensuring the gold standard has a lower energy than the competing segmentation, a linear inequality is created, pruning the estimate set.

Compute $E_D(u^G)$, $E_S(u^G)$, and $E_D(u^*(\infty))$
Set $P_{-1} \leftarrow \emptyset$, $P_0 = \{\alpha | \alpha \geq 0, \alpha \in C(u^*(\infty))\}$, $t \leftarrow 0$
while $P_t / P_{t-1} \neq \emptyset$ **do**
  $Q \leftarrow$ the vertices of P_t
  $M \leftarrow$ mean(Q)
  if M is $\geq \epsilon$ away from any prior evaluated α **then**
    $u' \leftarrow$ output of solver with parameters M
    Update $P_{t+1} \leftarrow P_{t+1} \cap C(u')$
  else
    Remove any of P_{t-1}'s vertices from Q
    Set $P_{t+1} \leftarrow P_t$
    for $\forall \alpha' \in Q$ **do**
      $u' \leftarrow$ output of solver with parameters α'
      Update $P_{t+1} \leftarrow P_{t+1} \cap C(u')$
    end for
  end if
  Set $t \leftarrow t + 1$
end while
Return P_t

Results: The algorithm shown was proven to be mathematically correct. For empirical validation, the BrainWeb[3] MRI simulator was used. Realistic functionals were created using a mixed intensity/spatial model.[4] After four iterations, the parameter selection algorithm found the closest segmentation to the gold standard with only 2% of voxels mislabelled compared to 5% from thresholding. Furthermore, the 'competing' optimal segmentation indicate insufficiencies in the data costs and/or gold standard, which opens avenues for further research in optimization-based image segmentation.

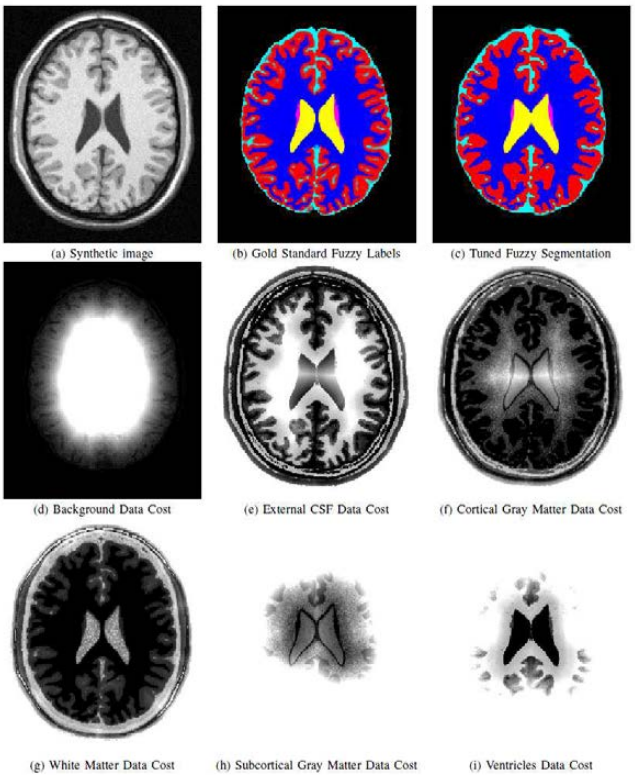
(a) Synthetic image
(b) Gold Standard Fuzzy Labels
(c) Tuned Fuzzy Segmentation
(d) Background Data Cost
(e) External CSF Data Cost
(f) Cortical Gray Matter Data Cost
(g) White Matter Data Cost
(h) Subcortical Gray Matter Data Cost
(i) Ventricles Data Cost

References: [1] McIntosh & Hamarneh, *Advances in Visual Computing*, 2009; 1079-1088. [2] Szummer et al., *ECCV*, 2008; 582-595. [3] Cocoso et al., *NeuroImage*, 1997. [4] van der Lijn et al., *NeuroImage*, 2008; 43.4, 708-720.

Validation of automated bundle extraction in DTI tractography

Kaiyue Diao[1, 2], Sandrine de Ribaupierre[3], Terry M. Peters[3], Ali R. Khan[3]
[1] Robarts Research Institute, the University of Western Ontario, London, Ontario, Canada
[2]West China School of Medicine Sichuan University, Sichuan University, Chengdu, China
[3] Department of Medical Biophysics, Western University, London, Canada.

INTRODUCTION: Diffusion tensor imaging (DTI) tractography is a non-invasive MRI technique to delineate white matter (WM) bundles in vivo. However, conventional manual extraction of bundles is tedious and time-consuming. Existing automated approaches have lacked efficiency and have not been validated on all functionally relevant WM bundles. Thus we hypothesize that our recently developed hybrid atlas- and cluster-based automated DTI tractography method can extract the major WM bundles with higher accuracy as validated with quantitative metrics and visual comparison.

METHODS: Diffusion weighted data (2.5mm isotropic, 41 directions, 4 b0) were from 15 healthy volunteers. 3D slicer 4.3.1 was used to delineate and extract WM bundles manually for comparison against the automated approach. We extracted the following 18 WM bundles following existing protocols: corpus callosum, left/right: arcuate fasciculus, cingulum, fornix, corticospinal tract, inferior longitudinal fasciculus, inferior fronto-occipital fasciculus, uncinate fasciculus, and inferior/middle/superior cerebellar peduncles.

The automated approach used ROIs non-rigidly warped from an atlas to generate the initial bundles. A set of representative streamlines were then extracted from these using spectral clustering, and fed into an affinity-based cost function to label every streamline in the brain.

We computed modified Hausdorff distances (MHD) to measure the difference between the manual and automated fiber bundles. Accuracy of the initial atlas-based bundles were compared with the affinity-based bundles (at various thresholds) to validate the affinity-based approach. We also performed qualitative comparisons to visualize false positive and false negative tracts.

RESULTS: Our manually-extracted bundles were verified by an experienced neurosurgeon. By running our protocol, we got the corticospinal tracts with its lateral connections to the face motor area. The MHD comparison showed the hybrid affinity-based approach with an affinity threshold (at 0.75) significantly improves the accuracy of the automated approach for 12 of the 18 WM bundles. The hybrid approach with an optimal threshold chosen for each bundle had significant improvement for 15 of the 18. The manual bundle extraction performed for this study can be used to validate additional automated techniques or to generate an atlas for improving automated labeling.

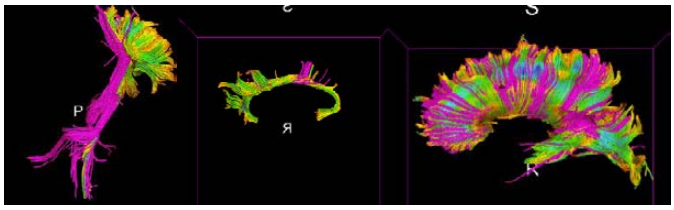

Figure 1. Overlap views of corticospinal tract, cingulum and corpus callosum, from left to right. (Red: automated; colored: manual made)

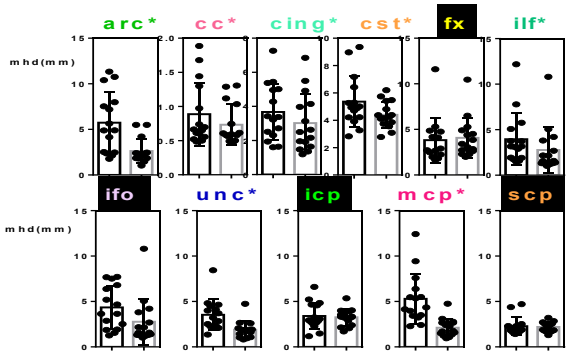

Figure 2 Mean Hausdorff Distances of the initial (left) and the affinity-based (right) bundles compared against the manually-extracted bundles. Statistically significance indicated by (*).

CONCLUSION: Our experiment showed the hybrid approach of combining atlas and cluster-based automated tractography can improve the accuracy significantly for most fiber bundles. Choosing affinity thresholds specific to a fiber bundle further improved accuracy, suggesting that an adaptive threshold should be used in future work.

Automatic Real-Time Intra-Operative 2D Biplane Ultrasound Calibration during *in situ* Minimal Invasive Heart Surgery

Azhar Hosein Faraz[1], Terry M. Peters[1,2], Elvis C. S. Chen[1,2]
[1]Biomedical Engineering Graduate Programe, Western University, London, ON, Canada
[2]Imaging Research Laboratories, Robarts Research Institute, London, ON, Canada

Introduction: Accurate ultrasound (US) calibration is essential for the navigated trans-apical mitral valve repair surgery, where the traditional 2D single/bi-plane and real-time 3D US volume are used throughout the procedure. Augmenting both the trans-apical sugical tool and the TEE probe with magnetic tracking system allows performing this beating-heart procedure in an Augmented Virtuality envirnemnt. We propose an *in situ* calibration using high-quality 2D bi-plane US images, accounting for the speed of sound in an US medium (i.e. primarily composed of blood poll and myocardium). In addition, by applying the intrinsic relationship between 2D US and 3D US volume, we are able to achieve more accurate real-time 3D US calibration.

Methods: We extended the "phantom-less calibration" proposed by Khamene and Sauer[1] to operate in bi-plane ultrasound images. The ultrasound calibration we seek is the anisotropic scales, followed by rotation and translation. A Philips 3D TEE transducer (X7-2t) capable of operating in single-plane, bi-plane, and real-time 3D mode was used. A pre-calibrated trans-apical surgical tool (Neochord DS1000) was used as the calibration tool. A 6DOF magnetic tracking sensor (Aurora, NDI, Canada) is rigidly attached to each of the TEE probe and Neochord tool. The ultrasound reflection of the cylindrical Neochord tool (i.e. partial arc of an ellipse) was automatically segmented using a custom Randomized Hough Transform algorithm[2]. The centroids of the ellipses from each pair of the bi-plane US, and the orientation of tracked Neochord tool, serve as the basis for solving the ultrasound calibration. The intrinsic relationship between bi-plane and real-time 3D ultrasound was determined from the internal coordinate system. Tracked stylus with spherical tip was used for validation: the tip of the stylus was imaged using the tracked real-time 3D ultrasound, and the centroid of the imaged tip was used as the basis for Target Registration Error (TRE) validation experiment.

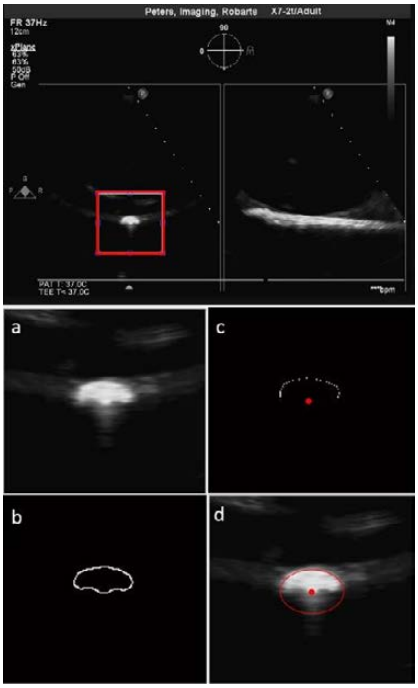

Figure 1 Automatic centroid identification of the surgical tool in US images. (a) Smoothing, (b) edge detection, (c) centroid identification (d) and overlay of the estimated ellipse.

Results: In a laboratory setting, our method achieved a TRE of 0.96±0.08mm based on 17 data acquisition (i.e. 34 tracked images). The reproducibility of the system was also confirmed by performing additional US calibration acquisitions at different setting/time. The automatic partial-ellipse detection algorithm works well in the acquired images, removing the need to the laborious and error-prone process of manual segmentation. The machine-dependent intrinsic calibration between 2D and real-time 3D ultrasound was also determined. We are planning to perform ultrasound calibration in a simulated surgical environment which requires the precise spatial pose between TEE probe and Neochord tool.

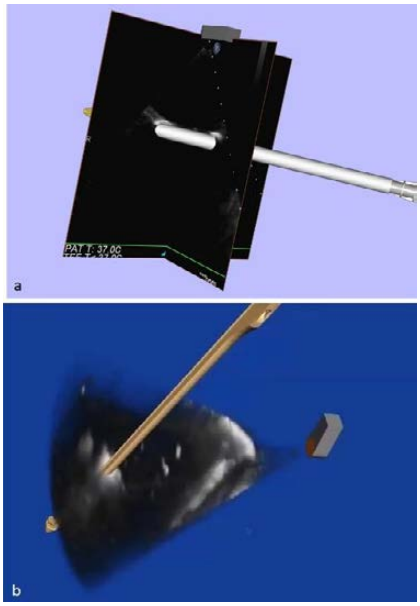

Figure 2. Qualitative validation by virtual representation of the tool overlaid within (a) bi-plane US images as well as (b) 3D US volume post applying intrinsic transform.

Conclusion: We developed a fast and accurate in situ ultrasound calibration paradigm using a surgical tool, to perform during the beating-heart trans-apical mitral valve repair surgery. The primary goal is to recover proper speed-of-sound parameters in the ultrasound calibration, since the intended target-site is primarily composed of blood pool and myocardium with the speed-of-sound potentially higher than the assumed 1540m/s. Our approach allows an accurate ultrasound calibration using the high-quality 2D-US, and apply the calibration parameters to the real-time 3D ultrasound. Animal study is being planned to test the feasibility of our approach and determining the minimal number of data-acquisition required.

References: [1] Khamene A, *et al*. MICCAI 2005.pp 6572. [2] Lu W, *et al.* Pattern Recogn. 2008 41:12681279.

Graphical Interface for Interactive Parameter Selection in Radiation Therapy Treatment Planning

Danielle A. Ripsman[1], Kimia Ghobadi*[,1], Dionne M. Aleman[1], David A. Jaffray[2]
(1) Department of Mechanical and Industrial Engineering, University of Toronto, Toronto
(2) Radiation Oncology, Princess Margaret Hospital, University Health Network, Toronto
Cancer Imaging Network of Ontario Consortium

Introduction. Radiation therapy is a commonly used clinical treatment for patients with cancer and tumours. Treatment plans aim to satisfy the competing goals of delivering the prescribed dose to cancer cells while sparing the healthy surrounding tissue. Inverse treatment plans, such as continuous path algorithm for Elekta's Leksell Gamma Knife® Perfexion™, can be produced automatically using clinical guidelines [1]. The quality of such inverse plans, however, are heavily influenced by the selection of input weighting parameters that must be chosen *a priori*. Common methods of parameter value selection include experimental adjustment and utility assessment, which often fail to fully address the complex nature of the problem's tradeoffs [1, 2].

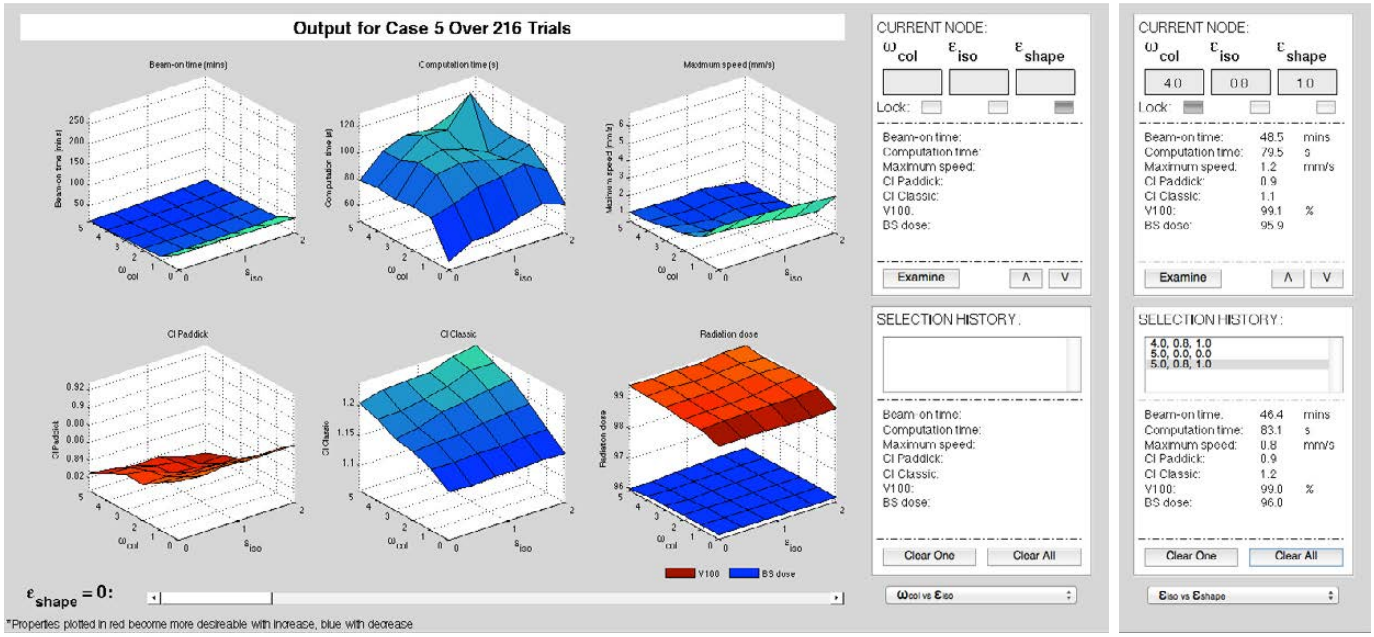

(a) Initial GUI setup, no interactive selections (b) Selected plans

Figure 1: A screen shot of the interface displaying output values for three varied weighting parameters (ω_{col}, ε_{iso} and ε_{shape}), incremented over six trials each; (a) shows the interface's initial setup, while (b) demonstrates the populated Current Node and Selection History panels after interactive selections have been performed.

Methods. In this work, we develop the graphical visual interface, depicted in Figure 1, using MATLAB® software. The interface demonstrates fundamental planning tradeoffs by varying input parameters to generate a diverse set of potential plans. After generation, the plans are displayed as a single node on quality metric plots (Figure 1a) and users may interactively select and compare the different plans based on their metrics, populating the right panels (Figure 1b).

Results. Using the enhanced flexibility of the visual display, users can quickly and efficiently find plans with high conformity metrics and reasonably short delivery times. We tested the interface to compare over 300 inverse plans for 7 clinical cases generated by continuous path algorithm. High-quality plans that meet the soft-clinical guidelines for each patient could be quickly identified in each case. For example, a plan that delivers over 99% of the prescribed dose within 12 minutes, without over-dosing sensitive organs is discovered, while plans with good conformity but long-treatment times or plans with poor metrics are ignored.

Conclusions. Through visualization, it is possible to better understand and identify the tradeoffs involved in radiation therapy treatment planning and to choose high quality plans that are difficult to reproduce using traditional selection methods.

References. [1] K. Ghobadi, H. Ghaffari, D. Aleman, D. Jaffray, and M. Ruschin. *Medical Physics* 2012; 39(6):3134-3141. [2] Y. Yu. *Medical Physics* 1997; 24(9): 1445-1454.

Development and Evaluation of an Open-Source 3D Virtual Simulator with Integrated Motion-Tracking as a Teaching Tool for Pedicle Screw Insertion

Stewart McLachlin*, Brendan Polley, Mirza Beig, Jeremie Larouche, and Cari Whyne
Effective Systems for Procedure Specific Healthcare Simulation
Sunnybrook Research Institute, Toronto, Ontario, Canada

Introduction. Pedicle screw insertion techniques are traditionally taught with limited hands-on training, using artificial or cadaveric models, prior to guided supervision within the operating room. As residency programs move to competency-based curricula, more authentic and accessible teaching tools are required to train next generation spine surgeons. Virtual simulation can provide a valuable tool for practicing challenging surgical procedures; however, its potential depends on effective integration into student learning (1). The objectives of this work were to develop a freely accessible virtual pedicle screw simulator and to improve the clinical authenticity of the simulator through integration of low-cost motion tracking.

Methods. The open-source medical imaging and visualization software, 3D Slicer, was used as the development platform for the virtual simulation. 3D Slicer contains many features for quickly rendering and transforming 3D models of the bony spine anatomy from patient-specific CT scans. The virtual simulation needed to include both pre-operative planning and intra-operative pedicle screw insertion workflows. Pre-operative planning utilizes CT imaging to identify the vertebral levels requiring instrumentation and take anatomic measurements. The intra-operative screw insertion workflow requires identification of the correct entry point and trajectory to create a safe screw tract with a pedicle probe. This requires skill in complex 3D spatial perception and interpreting 2D images into real-world 3D positioning. To address this required skill development, virtual monitoring of the surgeon's simulated tool was assessed with a low-cost motion tracking sensor in real-time (~$80, LeapMotion, San Francisco). This allowed a physical screw surrogate to be tracked as the surgeon defined the virtual screw's trajectory on a 3D spine model.

Results. Using a combination of existing and custom-written 3D Slicer Python scripts, an interactive virtual pedicle screw simulator was created. The surgical planning and operative screw insertion were simulated in a six step workflow: (1) identify vertebral levels on CT imaging, (2) choose the surgical region of interest, (3) select screw entry points (Figure 1), (4) take anatomic measurements (Figure 2), (5) define screw trajectory via the LeapMotion (Figure 3), and (6) grade final screw positioning (Figure 4). Surgeon feedback of the virtual simulator with integrated motion tracking was positive, with no noticeable lag and high accuracy between the real and virtual environments.

Conclusions. The 3D Slicer-based virtual pedicle screw simulation overcomes accessibility issues of previously developed simulators by allowing distribution without the need for expensive commercial software (2). This will enable trainees to practice instrumentation techniques anywhere they have access to a computer. Further the interactivity provided by the low-cost LeapMotion represents a significant advancement in terms of the simulator's task authenticity. Future work will evaluate the benefit of this simulation platform with use over the course of resident spine rotations to improve planning and surgical competency and in quantitatively evaluating performance.

References. [1] Gallagher *et al*. Ann Surg 2005;241:364-72. [2] Podolsky *et al*. J Spinal Disord Tech 2010;23(8):e70-4.

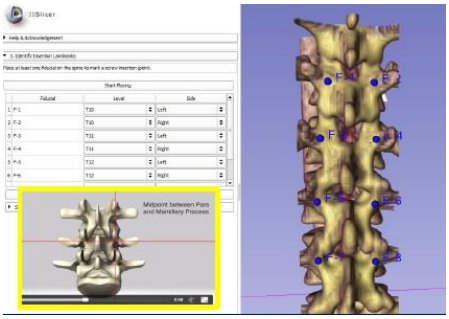

Figure 1: The user identifies screw entry points via fiducial markers (optional training video).

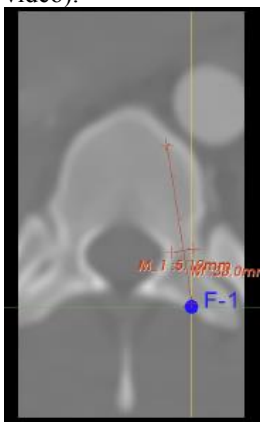

Figure 2: Anatomic ruler measurements are added to determine screw sizing.

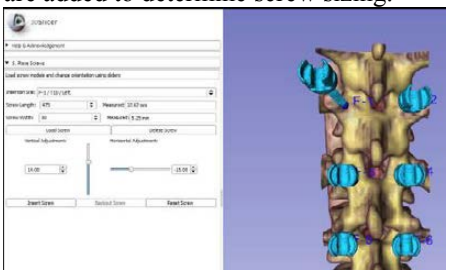

Figure 3: Virtual screw trajectory is determined from a physical screw surrogate tracked via the LeapMotion.

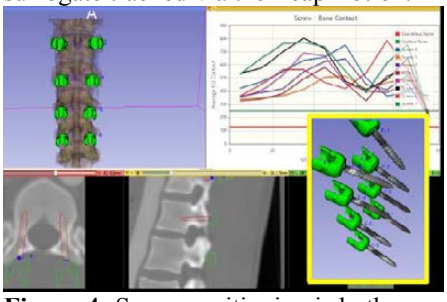

Figure 4: Screw positioning is both qualitatively and quantitatively evaluated. The intersection of the screw on the CT images is shown and the bone density along the screw length reported for breaches.

Ultrasound video processing for identification of dural pulsation in the lumbar spine

Jonathan McLeod, John Baxter, Golafsoun Ameri, Sugantha Ganapathy, Terry Peters, Elvis Chen
Effective Systems for Procedure Specific Healthcare Simulation
Robarts Research Institute, Western University, London Ontario Canada

Introduction: Anesthesiologists increasingly rely on ultrasound imaging to guide epidural injections; however, reaching the epidural space frequently requires multiple attempts and can result in injury to the spinal cord. [1] Dural pulsation is a subtle cue anesthesiologists can use to find safe needle trajectories to the epidural space. We propose a method for real time identification of dural pulsation from ultrasound video.

Methods: A video processing algorithm was developed that used extended Kalman filtering to fit a periodic model to pixel intensities. The estimated frequencies and amplitudes were then used to locate the pulsating dura in the ultrasound video and a heat-map showing the strength of pulsation was displayed to the user. The software was developed to run in real-time on a commercial ultrasound system (SonixTouch, Ultrasonix) and was evaluated by retrospectively analyzing human ultrasound video and by performing mock epidural procedures in a phantom environment. The retrospective human analysis consisted of running the software on ultrasound videos of the lumbar spine acquired from two healthy volunteers. The mock epidural procedures used a model of the lumbar spine designed for training spine needle interventions.[2] The dura was actuated at 60bpm using an external device to simulate dural pulsation and an anesthesiologist performed 12 simulated injections with and without the video processing for dural pulsation. During each injection the position of the needle was continuously recorded using a magnetic tracking system allowing for evaluation on the basis of needle path length, number of attempts and time. In both experiments, images were acquired from a paramedial view that is used clinically for guiding epidural injections.

Results: The human data showed good detection of the pulsating dura (fig 1a). When this method was used by the anesthesiologist in the mock procedures it resulted in a reduced normalized path length (3.0 vs 5.4) $p<0.05$ and fewer average number of attempts (1.7 vs 2.7) $p<0.05$. It also resulted in an insignificant reduction in the time required per injection (12.0s vs 15.7s).

Conclusion: The proposed method was able to accurately identify the pulsating dura in human and phantom videos. This method is computationally lightweight and can run in real-time on commercial ultrasound systems. When used to guide mock procedures, this new visualization was able to reduce the path length and number of attempts required to reach the epidural space. By helping to identify a clear path to the dura, and avoiding multiple needle insertions, this method could improve patient comfort as well as reduce the risk of potentially serious complications including nerve damage and injury to the spinal cord. This new visualization can be incorporated into a mixed reality environment to further improve image guidance (fig 1b).

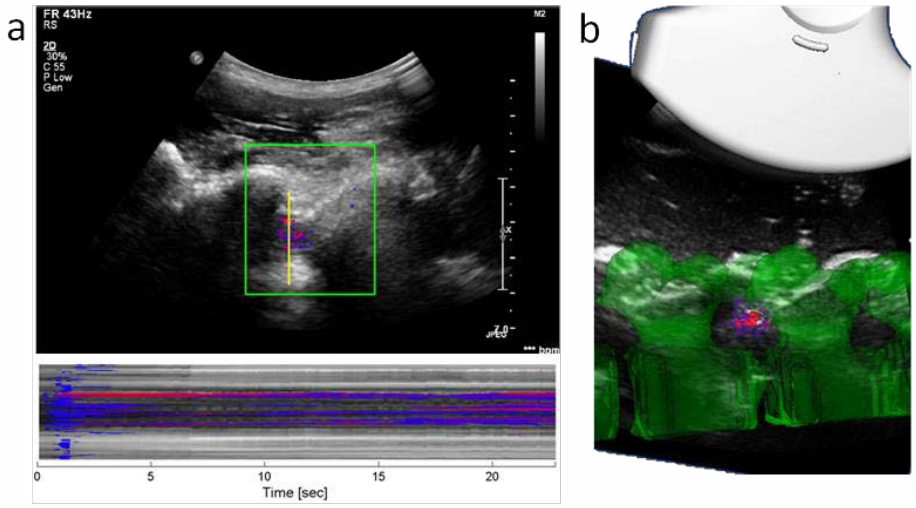

Figure 1: Dural pulsation detection algorithm running on retrospective human data (a). The time profile taken across the yellow line shows the dura was detected in the first five seconds. The algorithm ran in real time on a spine phantom and can be included in more advanced guidance systems (b).

References:

[1] Conroy, P., Luyet, C., McCartney, C., McHardy, P.: Real-time ultrasound-guided spinal anaesthesia: a prospective observational study of a new approach. Anesthesiology research and practice (2013)
[2] Chen, E.C.S., Ameri, G., Li, H., Sondekoppam, R.V., Ganapathy, S., Peters, T.M.: Navigated simulator for spinal needle interventions. Studies in health technology and informatics (2014).

Acoustic characterization of various tissue mimicking materials for medical ultrasound

Audrey Thouvenot [a,b,c], Terry M. Peters[b,c] (research supervisor), Tamie Poepping[c] and Elvis Chen[b,c]
Consortium affiliation: simulation
[a] Institut Supérieur d'Ingénieurs de Franche Comté, Besançon, France
[b] Robarts Research Institute, London, Canada
[c] Western University, London, Canada

1. INTRODUCTION

Prior to any animal or human testing, medical practitioners often use phantoms (constructed with tissue mimicking material, TMM) to perform procedural planning, surgical training, medical imaging research, and machine calibration. Depending on the intended application, phantoms for ultrasound imaging must exhibit desirable acoustic properties, such as speed of sound and attenuation coefficient, similar to those of soft tissue. By convention, the average speed of sound and attenuation for human tissues is assumed to be 1540 m.s^{-1} and 0.54 dB.cm^{-1}.MHz^{-1}, respectively.
Phantoms are also used for ultrasound-guided needle interventions, such as epidural injection and lumbar puncture. However, previous needle insertion reduces the realism and the useful lifespan of the phantom due to the presence of needle tracks. Ideally, TMM would also demonstrate a tensile strength similar to tissue, and if possible a self-healing ability to alleviate the effects of needle tracks.
The purpose of this planned study is to add different chemical compounds to polyvinyl chloride (PVC) and silicone TMM in order to increase the speed of sound and attenuation, and to provide self-healing capabilities. These experiments will study the conflicting results about these parameters existing in the current literature.

2. METHODS

Additives, such as PVC powder, graphite, and PVC hardener incorporated into PVC ; and mineral oil or room temperature vulcanizing into silicone, will increase the speed of sound and attenuation in their respective materials.
In the pulse transmission technique, the speed of sound and attenuation coefficient of a material are determined by measuring the time delay and amplitude for an ultrasound pulse traveling a known distance with and without a sample placed between two transducers in a water bath (see Figure 1).
The speed of sound, c, is a function of the zero-crossing time shift, Δt, and sample thickness, ds, according to the following equation:

$$c = \frac{c_w}{1 + \frac{c_w \Delta t}{d_s}}$$

where the speed of sound in pure water c_w at 22°C is 1488.3 m/s.
The attenuation coefficient, $\alpha(f)$, is frequency dependent and thus measured for frequencies between 1 to 9 MHz, for 5 different thicknesses from 1.5 cm to 4 cm, and calculated according to the following equation:

$$\alpha(f) = a.f^b$$

where a (dB.cm^{-1}.MHz^{-b}) and b are fitting parameters and f (MHz) is frequency. The fit parameters were derived from the intercept and slope of a linear regression fit to the log-log plot of the attenuation coefficient vs. frequency.

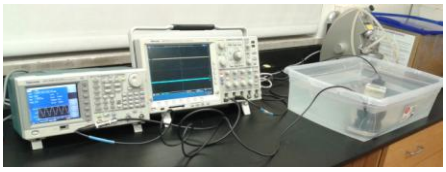

Figure 1. Equipment setup including a function generator, an oscilloscope, a water bath with two transducers and PVC in the sample holder.

Needle insertion will be then performed in these materials and will be imaged daily to investigate self-healing capability.

3. RESULTS

We expect to investigate speed of sound and attenuation of PVC and silicone, and compare to current literature. The acoustic properties will be altered with the addition of hardener giving a stiffener material. Based on our experience with PVC, we also expect to find a silicone compound mixture with the desired self-healing property.

4. CONCLUSIONS

Phantoms are designed with desired properties, such as imaging characteristics, mechanical properties, durability, shelf-life, and cost. For needle interventions, self-healing materials with appropriate acoustic properties are desired, saving both time and money. By optimizing the recipes of PVC and self-healing silicones, phantoms made with these tissue-mimicking materials can be incorporated into surgical simulators for ultrasound-guided spine needle interventions.

INDEX

INDEX CONTINUED

INDEX CONTINUED

INDEX CONTINUED

ImNO Thanks Our Corporate Sponsors

Commercialization Session Sponsor

CIMTEC®

Silver Sponsors

VISUALSONICS
FUJIFILM

GE Healthcare

SHELLEY
MEDICAL
IMAGING
TECHNOLOGIES

SIEMENS

Bronze Sponsors

PHILIPS

Educational CT Scanner
DESKCAT
by Modus

Exhibitor

UNIVERSITY OF
CALGARY

CIPAC